Czech Technical University in Prague

Faculty of Nuclear Sciences and Physical Engineering

DISSERTATION THESIS

Study of Accelerator-Driven Subcritical Setups Determined for Testing of Transmutation Possibilities

Prague 2020

Pavel Tichý

Bibliografický záznam

Autor	Ing. Pavel Tichý České vysoké učení technické v Praze Fakulta jaderná a fyzikálně inženýrská Katedra jaderných reaktorů
Název práce	Studium urychlovačem řízených podkritických sestav určených pro testování možností transmutace
Studijní program	Aplikace přírodních věd
Studijní obor	Jaderné inženýrství
Školitel	RNDr. Vladimír Wagner, CSc. Akademie věd ČR Ústav jaderné fyziky Oddělení jaderné spektroskopie
Akademický rok	2019/2020
Počet stran	154
Klíčová slova	Urychlovačem řízené systémy, Energie a transmutace radioaktivních odpadů, produkce a transport neutronů, neutronová aktivační analýza, spektrometrie gama záření, simulace Monte Carlo

Bibliographic Entry	
Author	Ing. Pavel Tichý Czech Technical University in Prague Faculty of Nuclear Sciences and Physical Engineering Department of Nuclear Reactors
Title of Dissertation	Study of Accelerator-Driven Subcritical Setups Determined for Testing of Transmutation Possibilities
Degree Programme	Application of Natural Sciences
Field of Study	Nuclear Engineering
Supervisor	RNDr. Vladimír Wagner, CSc. Czech Academy of Sciences Nuclear Physics Institute Department of Nuclear Spectroscopy
Academic Year	2019/2020
Number of Pages	154
Keywords	Accelerator-driven systems, Energy and Transmutation of Radioactive Waste, production and transport of neutrons, neutron activation analysis, gamma-ray spectrometry, Monte Carlo simulations

Author’s declaration

I declare that I elaborated the submitted dissertation thesis individually and that I stated all the used information sources in accordance with the Guidelines for the ethical preparation of university theses. The dissertation thesis was elaborated in the internal and combined form of postgraduate study at the Department of Nuclear Reactors at the Faculty of Nuclear Sciences and Physical Engineering of the Czech Technical University in Prague and has not been submitted to acquire another qualification at this or any other university. The dissertation thesis was created thanks to the collaboration between the Nuclear Physics Institute of the Czech Academy of Sciences and the Joint Institute for Nuclear Research Dubna (Russia).

In Prague, _____________ __________________________

Ing. Pavel Tichý
(author of the thesis)

Supervisor’s declaration

The author, in collaboration with his collaboration colleagues, worked out an extensive study of a lead target and two setups E+T and QUINTA aimed at testing of possibilities of accelerator-driven transmutation systems. The experimental data were compared with simulations acquired with the MCNPX program. Another significant outcome of the dissertation thesis is the simulation performance of future experiments with the big uranium target BURAN.

Albeit all the work was carried out in the framework of the broad collaboration, I declare, that the author’s contribution was always significant and is clearly stated in the thesis text.

In Prague, _____________ __________________________

RNDr. Vladimír Wagner, CSc.
(supervisor and responsible member for the authors collective)

Acknowledgements

First of all, I would like to express my sincere gratitude to my supervisor RNDr. Vladimír Wagner, CSc., who was always ready to discuss problems, help or give advice. Equally, I wish to thank the leader of our workgroup at the Joint Institute for Nuclear Research (JINR), prom. fyz. Jindřich Adam, CSc., for valuable discussions and comments. I also thank my colleagues at JINR and the Nuclear Physics Institute of the Czech Academy of Sciences, in particular, Ing. Lukáš Závorka, PhD, for valuable discussions, comments, and for the guidance during my beginnings at JINR.

I gratefully acknowledge the financial support from the Educational Programme of the Director of JINR and Plenipotentiary of the Government of the Czech Republic in JINR and funds allocated in the grants of the Plenipotentiary of the Government of the Czech Republic in JINR and the grants 3+3.

Abstrakt / Abstract

Spolupráce “Energie a transmutace vyhořelého jaderného paliva” se zabývá studiem sestav, složených ze spalačního terče a podkritického blanketu, které jsou ozařovány svazky vysokoenergetických protonů a deuteronů. Experimenty jsou velmi důležité k získání nových experimentálních dat a poznatků, které umožní realizaci větších projektů zaměřených na výzkum urychlovačem řízených transmutačních systémů.

Autor disertace se v rámci spolupráce zabýval výzkumem produkce různých radionuklidů a studiem generovaného neutronového, protonového a deuteronového pole v experimentálních sestavách E+T, QUINTA a BURAN. Zvláštní zřetel věnoval studiu centrálních oblastí těchto sestav, kolem průchodu primárního svazku částic. Ke svému výzkumu využil experimentální metodu jaderné gama spektrometrie a výpočetní metodu Monte Carlo.

Autor provedl Monte Carlo simulace na sestavách E+T a QUINTA a srovnal výsledky s experimentálními hodnotami. Na základě získaných dat vypracoval citlivostní analýzu nepřesností popisu geometrie primárního svazku na sestavě QUINTA a analyzoval přesnost a možnosti využití a testování kódu MCNPX 2.7.0 v centrálních oblastech i mimo ně. Zhodnotil možnosti použití kódu pro budoucí experimenty na sestavě BURAN a simuloval její chování. Na základě výsledků ocenil možnosti provádění budoucích experimentů. Provedl také benchmark testy kódu MCNPX 2.7.0 na experimentu ozařování olověného spalačního terče, určeného pro sestavu BURAN.

The “Energy & Transmutation of Radioactive Waste” collaboration is involved in the study of setups, composed of a spallation target and subcritical blanket, which are irradiated by high-energy proton and deuteron beams. The experiments are significant for the acquirement of new experimental data and knowledge, which are supposed to enable a realisation of larger-scale experiments on accelerator-driven transmutation systems research.

In the framework of the collaboration, the author of the thesis was involved in research on the production of various radionuclides and study of the neutron, proton, and deuteron fields generated inside the experimental setups E+T, QUINTA, and BURAN. Special attention was paid to the investigation of the setups central regions along the primary beam passage. The method of nuclear gamma spectrometry and Monte Carlo computational method were used.

The author performed simulations at the setups E+T and QUINTA and compared the results with experimental values. Based on the acquired data, he worked out a sensitivity analysis of the primary beam geometry description inaccuracies on the QUINTA setup and analysed the accuracy and possibilities of usage and benchmarking of the MCNPX 2.7.0 code in the central regions, but also beyond them. He assessed the code usage possibilities for future BURAN experiments and simulated the setup behaviour. Based on the results, he evaluated the possibilities of future experiments performances. He also carried out the MCNPX 2.7.0 benchmark tests in the experiment of irradiation of lead spallation target designated for the BURAN setup.

Contents

List of Abbreviations

ABC – Accelerator-Based Conversion of Plutonium

ADANES – Accelerator-Driven Advanced Energy System

ADB – Accelerator-Driven System Burner

ADEP – Accelerator-Driven Energy Production

ADRUF – Accelerator-Driven Recycle Used Fuel

ADS – Accelerator-Driven System

ADTT – Accelerator-Driven Transmutation Technologies

APT – Accelerator Production of Tritium

ATW – Accelerator Transmutation of Waste

CC – experiment at the QUINTA setup (660 MeV proton beam irradiation, samples positioned Closer to Centre)

CDT FASTEF – Central Design Team for the design of a Fast-Spectrum Transmutation Experimental Facility

CERN – Conseil Européen pour la Recherche Nucléaire

CIADS – China Initiative Accelerator-Driven System

CONFIRM – Collaboration on Nitride Fuel Irradiation and Modeling

CSNS – China Spallation Neutron Source

d4GeV – experiment at the QUINTA setup (4 GeV deuteron beam irradiation)

d8GeV – experiment at the QUINTA setup (8 GeV deuteron beam irradiation)

DEP – Double-Escape Peak

E+T – Energy plus Transmutation

E+Tp0.7GeV – experiment at the E+T setup (0.7 GeV proton beam irradiation)

E+Tp1GeV – experiment at the E+T setup (1 GeV proton beam irradiation)

E+Tp1.5GeV – experiment at the E+T setup (1.5 GeV proton beam irradiation)

E+Tp2GeV – experiment at the E+T setup (2 GeV proton beam irradiation)

E+Td1.6GeV – experiment at the E+T setup (1.6 GeV deuteron beam irradiation)

E+Td2.52GeV – experiment at the E+T setup (2.52 GeV deuteron beam irradiation)

E+Td4GeV – experiment at the E+T setup (4 GeV deuteron beam irradiation)

E&T RAW – Energy & Transmutation of Radioactive Waste

EFNUDAT – European Facilities for Nuclear Data Measurements

EUROPART – European Research Programme for the Partitioning of Minor Actinides

EUROTRANS – European Research Programme for the Transmutation of High Level Nuclear Waste in an Accelerator-driven System

ESS – European Spallation Source

FAIRFUELS – Fabrication, Irradiation and Reprocessing of Fuels and Targets for Transmutation

HINDAS – High and Intermediate Energy Nuclear Data for Accelerator-driven System

HPGe – High-Purity Germanium detector

ISNS – Indian Spallation Neutron Source

J-PARC – Japan Proton Accelerator Research Complex

JINR – Joint Institute for Nuclear Research

JIPNR – Joint Institute for Power and Nuclear Research

KIPT – Kharkiv Institute of Physics and Technology

LANL – Los Alamos National Laboratory

MEGAPIE – MEGAwatt PIlot Experiment

MOX – Mixed Oxide Fuel

MYRRHA – Multi-purpose hYbrid Research Reactor for High-tech Applications

NPI – Nuclear Physics Institute of the Czech Academy of Sciences

nps – number of source particles

nTOF – Neutron Time-of-Flight Facility

ORNL – Oak Ridge National Laboratory

PIE – Post-Irradiation Examination

PSI – Paul Scherrer Institut

RED IMPACT – Impact of Partitioning, Transmutation and Waste Reduction Technologies on the Final Waste Disposal

SCK CEN – Belgian Nuclear Research Centre

SEP – Single-Escape Peak

SNS – Spallation Neutron Source

SSNTD – Solid State Nuclear Track Detectors

TEF – Transmutation Experimental Facility

TEF-P – Transmutation Physics Experimental Facility

TEF-T – ADS Target Test Facility

UA – experiment at the QUINTA setup (660 MeV proton beam irradiation, Usual Arrangement of samples)

WS – experiment at the QUINTA setup (660 MeV proton beam irradiation, QUINTA Without lead Shielding)

List of Tables

List of Figures

1 Introduction

Our group at the Joint Institute for Nuclear Research (JINR) in Dubna, Russia, is a member of the "Energy & Transmutation of Radioactive Waste" (E&T RAW) international collaboration which is formed by members from 15 countries. The collaboration is involved in experiments with subcritical transmutation setups. Such research is significant for the accelerator-driven system (ADS) and fast nuclear reactor development. The setups are composed of a lead or uranium spallation target and uranium (natural or depleted) subcritical blanket. They are irradiated by relativistic proton or deuteron beams. At JINR, there is a possibility to use the proton beam of energy 660 MeV from the Phasotron accelerator and also both proton and deuteron beams of energies from 1 GeV up to 8 GeV from the Nuclotron accelerator. These beams are aimed at the subcritical targets where neutrons are created mostly by spallation reactions. These neutrons are consequently multiplied in the setup blanket by fission and spallation reactions. In this way, intense neutron fields are formed inside the setups.

The neutron, proton and deuteron spatial and energy distributions inside the setups can be effectively measured by activation detectors. The activation detectors have an advantage is their small dimensions so they can be easily inserted into the setups in various positions. Their longer evaluation time can be considered as a disadvantage.

Performance of Monte Carlo simulation programs benchmarks is essential concerning experiments with subcritical targets. The need for the benchmarks stems from the importance of using such codes in advanced nuclear system research, where precise simulations of production and transport of neutrons may be necessary. The results of the experiments with subcritical assemblies performed at JINR are usually compared with Monte Carlo simulations.

The main objective of my work was to focus on ADS experiments performed at JINR, especially experiment preparation, measurement and evaluation of irradiated activation samples by gamma spectrometry methods, and Monte Carlo simulations of particle flux and radionuclide production inside the experimental setups. I analysed the results of already realised experiments with individual setups simulating ADS technologies. Of these, I focused on the E+T (Energy plus Transmutation) assembly, consisting of a lead target and natural uranium blanket, whose systematical study was completed in recent years. By comparing obtained experimental data and simulations, it is possible to analyse the predictive ability of Monte Carlo simulation programs. I got involved in experiments with the QUINTA setup. I focused mainly on the determination of the influence of beam position and beam geometry on the obtained data and their accuracy. The uncertainties in the positioning and overall geometry of the beam proved to be the primary sources of experimental uncertainties. Based on the experience gained in the study of previous setups, I focused on the preparation of experiments with the new large uranium assembly BURAN.

1.1 Goals of the thesis

1. To work out an overview of current accelerator-driven system research focusing on target setups.
2. To carry out an analysis of existing experiments realised at JINR Dubna aimed

especially at target setups and production and transport of neutrons inside the setups. To focus especially on the experimental setup QUINTA.

3. To perform simulations of the setups using Monte Carlo program MCNPX and compare the simulation results with obtained experimental data. To focus mainly on the last QUINTA experiments carried out at the Phasotron accelerator. To assess the simulation results accuracy and possibilities of the program use in the preparation of the future experimental setups.

4. Based on the knowledge gained in the previous parts, to simulate the behaviour of the new setup BURAN and describe its characteristics related to future irradiation experiments. To assess its possibilities and recommend options for experiment performances.

5. To assess how the realised and prepared experiments can contribute to accelerator-driven transmuters realisation. Based on experimental and simulation results comparison, to judge the prediction accuracy enabled by the MCNPX program.

1.2 ADS research - current state in the world

Efforts to introduce advanced nuclear technologies based on accelerator-driven transmutation have a long-term history. The excellent review of history, current state-of-the-art accelerator-driven research and a wide range of references are in [1]. They should help to solve several key problems of nuclear power. The main examples are

- More efficient use of nuclear fuel reserves
- Reducing the volume and danger of nuclear waste
- Increasing the safety of nuclear technologies

The method is based on an external neutron source and a subcritical blanket of fissile material. Relativistic proton or light ion spallation reactions are usually used as a source of neutrons.

Right from the beginning, different ADS or ADTT (Accelerator-Driven Transmutation Technologies) research studies have had different priorities, and there have been a number of different projects

- Accelerator Transmutation of Waste (ATW)
- Accelerator-Driven Energy Production (ADEP)
- Accelerator-Based Conversion of Plutonium (ABC)
- Accelerator Production of Tritium (APT)

Before discussing the different variants of accelerator-driven transmutation technologies in more detail, let us mention the most important technological problems to be solved.

- A sufficiently reliable relativistic ion accelerator with very high beam intensity needs to be developed

- It is necessary to solve the effective target cooling
- To find a suitable target material
- To provide an accurate description of the production and transport of neutrons and radionuclides inside subcritical assemblies. We need to prepare codes that can accurately describe the spallation reactions in the target and the reactions of neutrons in the target and blanket. It is necessary to know the production of various radionuclides, and the efficiency of transmutation of nuclear fuel and waste in the blanket.
- The knowledge of thermodynamic and mechanical behaviour of individual parts of assemblies is equally important

Let us now look at the specific research projects in the world.

The ATW project has been performed mostly at the Los Alamos National Laboratory (LANL) under the supervision of C. D. Bowman [2]. The aim of the project is to shorten the necessary time needed for spent nuclear fuel storage by means of transmutations.

The ADEP is the CERN (Conseil Européen pour la Recherche Nucléaire) project initially started by C. Rubbia [3]. Considering that the world's supplies of thorium are on a high level, commercial use of thorium in nuclear power engineering would be very beneficial. ^{233}U is supposed to be gained by the reactions

$$n +^{232} Th \longrightarrow^{233} Th + \gamma \tag{1}$$

$$^{233}Th \overset{22.3min}{\longrightarrow} {}^{233}Pa + e^- + \nu^- \tag{2}$$

$$^{233}Pa \overset{27d}{\longrightarrow} {}^{233}U + e^- + \nu^- \tag{3}$$

and then it should be fissioned.

The ABC project serves for the transmutation of long-lived isotopes [4]. Formerly, it was performed primarily for the reduction of ^{239}Pu supplies that were primarily meant for use in nuclear weapons. Today, the technology is not that common because of MOX (Mixed Oxide Fuel) fuel production and new types of reactors.

The APT project concentrates on the production of tritium by (n,^{3}H) reactions that can arise in certain materials while irradiated by dense neutron fields [5]. Once, tritium was expected for hydrogen bombs manufacture. At present, the research is significant for fusion reactors.

The ADS concept demands investigation in several research directions that are crucial

- Development of accelerators with high beam intensities
- Development of beam targets for neutron production
- Enhancement of nuclear data, especially the investigation of neutron cross-sections
- Development and benchmarks of Monte Carlo simulation codes
- Shielding of high-energy neutrons

Research programme Euratom [6] for nuclear research and training covered under the European Fifth Framework Programme (1998 - 2002) [7] the following nuclear data research projects

- Neutron Time-of-Flight Facility (nTOF) [8]
- High and Intermediate Energy Nuclear Data for Accelerator-Driven System (HINDAS) [9]
- Nitride Fuel Irradiation and Modeling (CONFIRM) [10]
- Thorium Cycle Project [11]

The consecutive Sixth Framework Programme (2002 - 2006) [12] covered projects as

- European Facilities for Nuclear Data Measurements (EFNUDAT) [13]
- European Research Programme for the Transmutation of High-Level Nuclear Waste in an Accelerator-driven System (EUROTRANS) [14]
- European Research Programme for the Partitioning of Minor Actinides (EUROPART) [15]
- Impact of Partitioning, Transmutation and Waste Reduction Technologies on the Final Waste Disposal (RED IMPACT) [16]

Important projects related to transmutation, of the Seventh Framework Programme (2007 - 2013) [17] were

- Central Design Team for the design of a Fast-Spectrum Transmutation Experimental Facility (CDT FASTEF) [18]
- Fabrication, Irradiation and Reprocessing of Fuels and Targets for Transmutation (FAIRFUELS) [19]

The newest programme is Horizon 2020 (2014 - 2020) [20]. The current Euratom work programme for the year 2020 can be found in [21]. A more detailed description of the projects is given in [22].

An intensive neutron source plays a vital role in ADS research. The most powerful pulsed neutron source (started to operate in 2006) in the world is SNS [23, 24] (Spallation Neutron Source) at ORNL (Oak Ridge National Laboratory). The accelerator delivers a 695 ns proton pulse onto a mercury target. The repetition rate is 60 Hz and the average power is 2 MW. The need for slow neutrons for material science research is ensured by neutron moderators around the target. The facility is able to provide 18 neutron beamlines.

In Europe, construction of the intense neutron source ESS [25] (European Spallation Source) is in progress. The source is situated in Lund in Sweden. It is supposed to use a 5 MW accelerator delivering 2 GeV proton beam, and tungsten target wheel cooled by helium. The neutron source is planned to be operational in 2023. In the ESS project, thirteen European countries are involved, including the Czech Republic. The Czech representation is lead by the Nuclear Physics Institute of the Czech Academy of Sciences (NPI).

Another significant neutron source which has already come into operation in August 2018 is CSNS [26, 27] (China Spallation Neutron Source) and another neutron source is planned to be built in India (ISNS, Indian Spallation Neutron Source [28, 29]).

There are four significant projects related to ADS. The aim of the PSI (Paul Scherrer Institut) MEGAPIE project (1999 - 2015) [30-32] (MEGAwatt PIlot Experiment) was to prove safe operation and usefulness of liquid Pb-Li spallation target. The irradiation of the target with a 590 MeV proton beam of 0.77 MW power took place during 2006. After the successful irradiation phase, the extended Post-Irradiation Examination (PIE) program [33, 34] began. The objective of this phase was to study the irradiated target material structure and the accumulated radionuclide content and its behaviour. The results and experience obtained during the MEGAPIE project are now being a significant aid in the realisation of the MYRRHA project.

The MYRRHA project [35-38] (Multi-purpose hYbrid Research Reactor for High-tech Applications) started in 1997 at SCK CEN (Belgian Nuclear Research Centre) in Mol. MYRRHA is planned to be a flexible fast-spectrum research reactor (50 - 100 MW_{th} power) coupled with a high-intensity proton accelerator. It is supposed to demonstrate the full ADS concept and to provide neutron and proton beams for various applications, and for transmutation studies of minor actinides. Because MYRRHA is the biggest world's project of an accelerator-driven nuclear reactor, it deserves more attention.

The main MYRRHA components are the 600 MeV proton accelerator and a liquid Pb-Bi spallation target placed in a pool-type subcritical reactor. The reactor vessel is situated underground and is coated with biological shielding. The vessel height is 7 m and its inner diameter is 4.4 m. The reactor core is composed of a lattice with 183 hexagonal channels. The lattice contains 68 Pu-enriched MOX fuel pins of 0.6 m in length. The level of Pu-enrichment is about 30 %. The coolant of the core is also the liquid Pb-Bi eutectic which flows in a separate circuit. Irradiation stations are located in and around the core with neutron spectrum ranging from thermal to fast neutron energies.

MYRRHA will be an outstanding research device enabling to perform new research in various fields of physics such as, e.g. nuclear physics, atomic physics, reactor physics, material physics and medical physics. It will help to develop and innovate transmutation technologies for nuclear waste management, conduct material testing and development for new Generation IV, fission and fusion reactors, and open the door to new radioisotopes production for medical applications allowing less invasive cancer treatment.

Recently, in September 2018, the MYRRHA project's financing was approved. Also, the planning and the preliminary dates became more specific. At the first stage of the planning in 2017, construction of a 100 MeV proton accelerator has begun. The accelerator is supposed to be operational at the second stage in 2026. Right after that, its extension phase into the 600 MeV accelerator begins. Simultaneously in 2026 the third stage, the reactor construction, is being launched. MYRRHA is expected to be finished and fully operational in 2033, which is deemed as a fourth and final stage of the project.

In Japan, there is an important ADS project called TEF [39] (Transmutation Experimental Facility), which is realised at J-PARC (Japan Proton Accelerator Research Complex). It is divided into two research facilities: TEF-P (Transmutation Physics Experimental Facility), which deals with ADS dynamic and physical properties engaging a 600 MeV proton beam of 10 W power, and TEF-T (ADS Target Test Facility) focused on experiments for material and thermo-hydraulics. Liquid Pb-Bi eutectic will be used both as a spallation target and a coolant and irradiated with a 600 MeV proton beam of 200 kW power.

The Chinese ADS project ADANES [40, 41] (Accelerator-Driven Advanced Energy System) will be composed of the ADB facility (Accelerator-Driven system Burner) and the ADRUF facility (Accelerator-Driven Recycle Used Fuel). The ADANES system is supposed to utilise around 95 % of its nuclear fuel and giving nuclear waste comprising primarily of fission products. ADANES includes the CIADS project (China Initiative Accelerator-Driven System) which will be a 500 MeV proton accelerator coupled with a fast-spectrum reactor of 10 MW_{th} power using Pb-Bi eutectic as a coolant.

1.3 ADS research at the Joint Institute for Nuclear Research

The ADS research at the Joint Institute for Nuclear Research in Dubna has a long tradition. Already in the 1960s, R. G. Vasilkov studied neutron production in spallation reactions in very large lead targets irradiated with relativistic protons [42]. Its new stage started in the 1990s and continues up to now. Experiments are usually performed on subcritical setups, which are irradiated by relativistic proton or deuteron beams of the Nuclotron or Phasotron accelerators. A brief review of the experimental assemblies is given in this section.

1.3.1 GAMMA-2

GAMMA-2 (see Fig. 1) was one of the first ADS research setups of the above mentioned new stage of experiments at JINR. The setup was composed of a lead target with a diameter of 8 cm and length of 20 cm (prolonged to 50 cm later) and a paraffin blanket of 6 cm thickness, which served as a neutron moderator. The aim of the GAMMA-2 experiments was the study of spallation reactions, production, transport, moderation and capture of neutrons arising in the setup, and transmutation of long-lived isotopes like ^{129}I, ^{139}La and ^{237}Np. The results of the GAMMA-2 irradiation by relativistic proton beams of energies ranging from 0.5 GeV to 4.15 GeV can be found in [44]. The authors of [45] irradiated the prolonged version of the setup by 1 GeV, 1.5 GeV and 2 GeV proton beams.

Figure 1: GAMMA-2 setup: lead target and part of its paraffin moderator [43].

1.3.2 GAMMA-3

The GAMMA-3 assembly (see Fig. 2) is composed of a 60 cm long lead target with a diameter of 8 cm. The target is surrounded by a massive graphite square moderator of dimensions 60×110×110 cm^3. Inside the moderator, there are four removable cylinders of different diameters. During the experiments, transmutation samples were placed into the cylinder holes. The setup was primarily used for studies of radioisotope transmutation in the moderated neutron field. The results of the setup irradiation by 2.33 GeV deuteron beam from March 2011 (when the distribution of neutron field inside the setup was studied) are given in [46]. The last experiment with the GAMMA-3 setup took place in 2012.

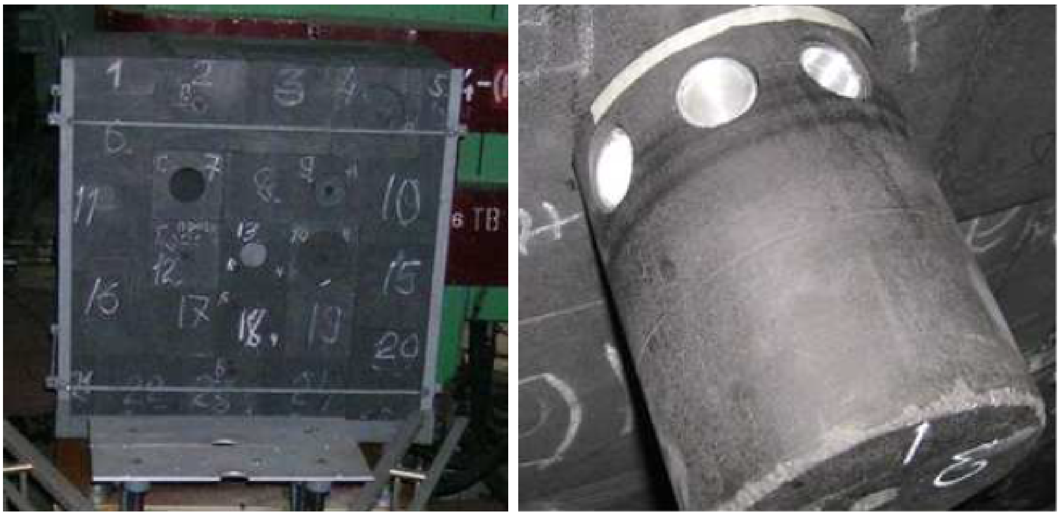

Figure 2: GAMMA-3 assembly and detail of the cylinder for samples placement [47].

1.3.3 Energy plus Transmutation (E+T)

The setup is composed of a lead target 480 mm long and 84 mm in diameter with a mass of 28.66 kg and a hexagonal blanket with a mass of natural uranium of 206.4 kg. E+T is divided into four sections, which are composed of 30 uranium rods. Each rod is 104 mm long, 36 mm in diameter and 1.72 kg in weight, and is encapsulated in an aluminium casing. Between every two sections, there is an 8 mm gap for detectors placement. The E+T assembly is shown in Figs. 3, 4 and. 5.

The setup is surrounded by a wooden shielding with dimensions 1000×1060×1100 mm^3 (see Figs. 4 and 5). Inside the wooden box walls, there are granulated polythene with boron carbide, and on the inner walls, there is a cadmium layer of 1 mm thickness. On the box floor, there is a 30 mm-thick textolite layer. The polythene moderates fast neutrons escaping the setup. After the moderation, they can be absorbed in boron or in the cadmium layer.

A more detailed description of the E+T assembly is given, e.g. in [49].

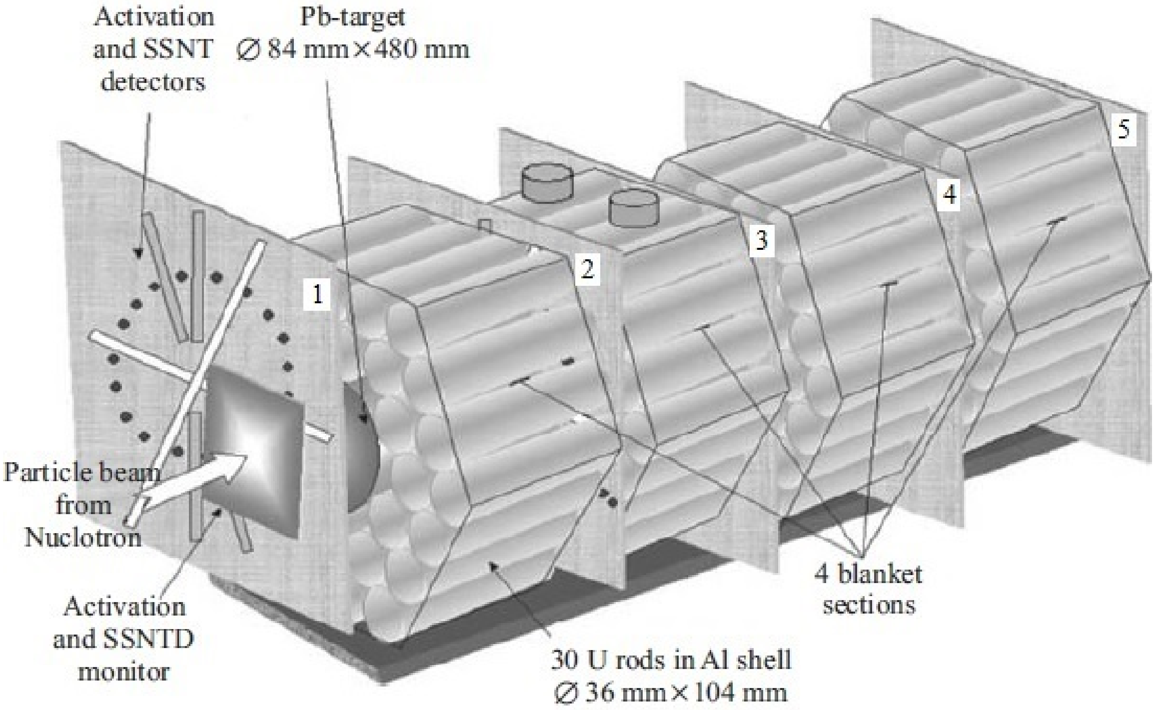

Figure 3: Schematic drawing of the E+T setup [48]. Numbers 1-5 represent locations for activation detectors placement, i.e. no. 1 is the location in front of the target, no. 2-4 are the gaps between the sections and no. 5 is the location behind the target.

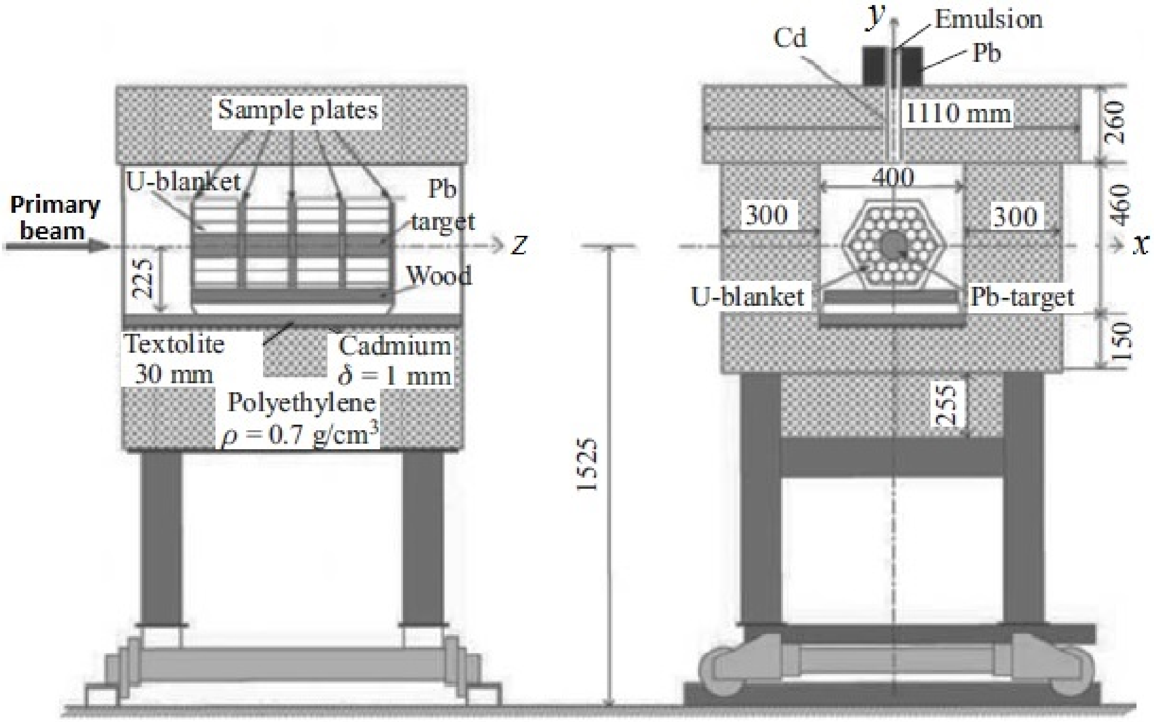

Figure 4: Cross-cut of the E+T setup with the biological shielding (side and front view) [48]. Dimensions are in mm.

Figure 5: E+T setup with the biological shielding (left) and view of the uranium blanket (right) [47].

The Energy plus Transmutation project, introduced by M.I. Krivopustov et al. [50-52], started in 1999. Until 2004, the setup was irradiated with the relativistic proton beams of Nuclotron with kinetic energies in the range from 0.7 GeV to 2 GeV [53-61]. Since then, the experiments were performed using the Nuclotron deuteron beams with energies in the range from 1.6 GeV to 4 GeV [62-68]. The last E+T experiment was carried out in November 2009, when the setup was irradiated by the 4 GeV deuteron beam [66]. Production and transport of neutrons, their spatial and energy distribution inside the setup, production of other secondary particles and transmutation of long-lived actinides were being investigated by the broad E&T RAW collaboration.

While the workgroup at JINR was highly focused on transmutations of radioactive waste using the neutron field generated in the E+T setup [67-70], the NPI group was highly focused (and is still focused) on neutron generation and transport, spatial and energy distribution of neutrons inside and around the setup, and the benchmark studies of Monte Carlo simulation codes. The neutron flux was usually measured using various activation materials and evaluated by the activation technics.

A list of performed E+T setup irradiations at Nuclotron by the proton and deuteron beams is given below. I_p and I_d are the integral numbers of protons and deuterons, respectively, impinging on the target. E_n stands for the energy of neutrons and E_{thr} for the effective energy threshold.

List of E+T experiments at Nuclotron - irradiations with proton beams:

- 0.7 GeV proton beam irradiation [58] - I_p = 1.52(15)E13. Activation samples used in the experiment were: Al, Au, Bi, Co and Y situated both in longitudinal and radial directions. Simulations were performed in MCNPX version 2.6.E [71]. Neutron field produced in the setup was studied via (n,γ), (n,xn) and (n,α) reactions. Experimental yields of ^{198}Au, ^{196}Au, ^{194}Au, ^{192}Au, ^{24}Na, ^{204}Bi, ^{203}Bi and ^{202}Bi were observed and compared to the Monte Carlo simulations. The simulations sufficiently well described the trends of the experimental data. It was noticed that experiment-to-simulation ratios are very dependent on the accuracy of the beam intensity determination and also on used cross-sections. Neutron multiplicity (integral number of neutrons produced in the setup) was investigated by the modified method [72] of the Water Bath Activation Foil Method [73]. The multiplicity was assed to 24 ± 2.4 neutrons per one 0.7 GeV proton.

- 1 GeV proton beam irradiation [59] - I_p = 3.30(7)E13. Activation samples used in the experiment were: Al, Au, Bi and Co. Simulations were performed in MCNPX version 2.4.0 [74] and MCNPX version 2.6.C [75]. The authors studied the intensity and shape of the generated neutron field by the activation techniques. Neutron-induced reactions with high-energy thresholds up to $E_{thr} \sim 60$ MeV were observed. The intensity of the fast neutrons ($E_n > 1$ MeV) had its maximum in the first setup gap (see Fig. 3). Hard neutron spectrum part was more dominant at the setup ends. The experiment-to-simulation agreement was relatively good with the maximum disagreements around 50 %, but a bit steeper decrease of the simulated yields in the radial direction was observed compared to the experimental values. The disagreement was increasing with higher energy thresholds.

- 1.5 GeV proton beam irradiation [57, 60] - I_p = 1.14(6)E13. Spatial and energy distribution of the neutron field was measured by Al, Au, Bi, Co and Cu threshold activation samples. Simulations were performed by the LAHET code [76] in combination with MCNP version 4B [77], and also in MCNPX version 2.3.0 [78] and version 2.4.0 [74]. As in the 1 GeV proton experiment, the fast neutron field intensity was measured in the first setup gap and the hardest neutron spectrum part was situated at the setup ends. Also, a steeper decrease in the radial direction of the simulated yields over the experimental yields for the high-energy threshold products was found out, compared to the 1 GeV proton experiment. This trend was much greater than in the 1 GeV proton experiment. Effect of the polythene shielding was also studied using the simulations. Neutron spectra in the first setup gap were simulated with no shielding, with the shielding but without its cadmium layer on the inner walls, and with the full-equipped shielding. The results showed that the shielding considerably increases the thermal, epithermal and resonance neutron spectrum part and that the cadmium acts as an absorber of the thermal neutron part. Transmutation of radioactive waste by irradiation ^{129}I and ^{237}Np samples was also studied [69].

- 2 GeV proton beam irradiation [61] - I_p = 1.25(6)E13. The neutron field inside the setup was studied using Al, Au, Bi activation samples and the Monte Carlo simulations were performed in MCNPX version 2.6.C [75]. The reactions with energy threshold $E_{thr} \sim 60$ MeV were observed. The maximum of the fast neutron spectrum intensity was detected in the first setup gap. The simulated yields of the threshold reactions were generally in a good agreement with the experimental values in the longitudinal direction, but in the radial direction, the similar effect as in the 1.5 GeV proton irradiation was observed. In the radial direction from the target axis, the simulations became even few times underestimated in some cases.

List of E+T experiments at Nuclotron - irradiations with deuteron beams:

- 1.6 GeV deuteron beam irradiation [65] - I_d = 2.45(10)E13. Spatial and energy distribution of neutron field was measured by Al, Au, Bi, Y, In and Ta activation foils. The results were compared to the Monte Carlo simulations performed in MCNPX version 2.7.A [79]. Radionuclide production both in threshold and non-threshold reactions, were relatively well described by the simulations. Neutron multiplicity was investigated by the modified Water Bath method. The multiplicity ranged between 68 and 101 neutrons per one 1.6 GeV deuteron depending on the used MCNPX intranuclear and evaporation models. Transmutation in ^{232}Th and ^{nat}U samples was also studied during this experiment [68].

- 2.52 GeV deuteron beam irradiation [65] - I_d = 6.45(13)E12. As in the 1.6 GeV deuteron experiment, the generated neutron field was investigated by Al, Au, Bi, Y, In and Ta activation foils and the samples were positioned almost in the same way. Simulations in MCNPX 2.7.A well described the experimental data. Neutron multiplicity was investigated by the modified Water Bath method. The multiplicity ranged between 68 and 108 neutrons per one 2.52 GeV deuteron depending on the MCNPX model. Investigation on the transmutation of radioactive waste was also carried out [67]. Radioactive samples of ^{129}I, ^{237}Np, ^{238}Pu and ^{239}Pu were irradiated and studied.
- 4 GeV deuteron beam irradiation [66] - I_d = 1.99(25)E13. This was the last irradiation which concluded the series of the E+T experiments. Neutron field inside the setup was studied using Al, Au, Bi, Co, In and Ta activation foils. Simulations in MCNPX version 2.7.0 [80] were performed and compared to the experimental results. Reactions with high-energy thresholds up to $E_{thr} \sim 106$ MeV were observed during this experiment. Generally, the simulations well described the radionuclide production along both longitudinal and radial axes. Better simulation results were provided for neutron low threshold reactions. For high thresholds (above $E_{thr} \sim 55$ MeV), the simulations were generally more than two times underestimated. The highest experiment-to-simulation ratio coefficient reached almost the value of 5. Neutron multiplicity was assessed using the modified Water Bath method. The multiplicity ranged between 120 and 210 neutrons per one 4 GeV deuteron depending on the MCNPX models and used activation foils.

The highest intensity of the generated fast neutron spectrum was found in the first setup gap. The major contribution to the epithermal and resonance part of the neutron spectrum was caused by escaping neutrons moderated in the biological shielding and backscattered to the setup. It causes almost homogenous low-energy part ($E_n < 0.1$ MeV) of the neutron spectrum in the setup. A bit greater multiplicity was found for the deuteron irradiations than for the proton irradiations. Simulated multiplicity was underestimated up to 40 % [81, 82].

Generally, the simulations well describe the experimental data, but the experiment-to-simulation agreement was worse for the 1.5 and 2 GeV proton irradiations, where the simulations were often few times underestimated. It was observed that the simulations usually got worse with growing threshold energy of the reactions and also the radial distance of the setup. The knowledge of cross-sections for neutron-induced reactions with higher energy thresholds ($E_{thr} > 30$ MeV) is often insufficient. The cross-sections are also being investigated by our group at NPI [83-88]. The precision of the simulations is also dependent on neutron data libraries and physics models engaged in simulation codes.

Considering that the simulations in the above-mentioned works were performed in various versions of MCNP code, various physics models and neutron data libraries were engaged, and also various versions of TALYS for calculation of cross-sections (needed for convolutions with simulated neutron flux, see section 2.3) were used, a new systematics of the experiments is now being prepared (chapter 3). I have already performed new simulations in MCNPX 2.7.0 [80] for threshold neutron reactions on activation foils of aluminium, gold and bismuth both from the proton and deuteron E+T experiments, and compared the simulation results with the experimental ones. The E+T experiments were also a topic of Master and Dissertation Theses [47, 49, 88-92].

The research with the Energy plus Transmutation assembly was more or less successfully completed and provided us with much valuable experience and knowledge. The QUINTA irradiation was the next logical step. The main difference between the two assemblies is that QUINTA is not equipped with the lead target but is made entirely from natural uranium.

1.3.4 QUINTA

QUINTA is a setup similar to E+T. QUINTA is also composed of hexagonal sections with gaps for activation detectors placement. The main difference is that the setup target is not lead like in the E+T case, but it is made from natural uranium (as well as the cylindrical rods forming the QUINTA blanket).

There are two versions of the setup. The earlier version was composed of three hexagonal sections (see Fig. 6) and the later version was composed of five sections (see Figs. 7 and 8). The very front hexagonal section of the prolonged setup differs from the other sections by having a free space in the middle for beam passage.

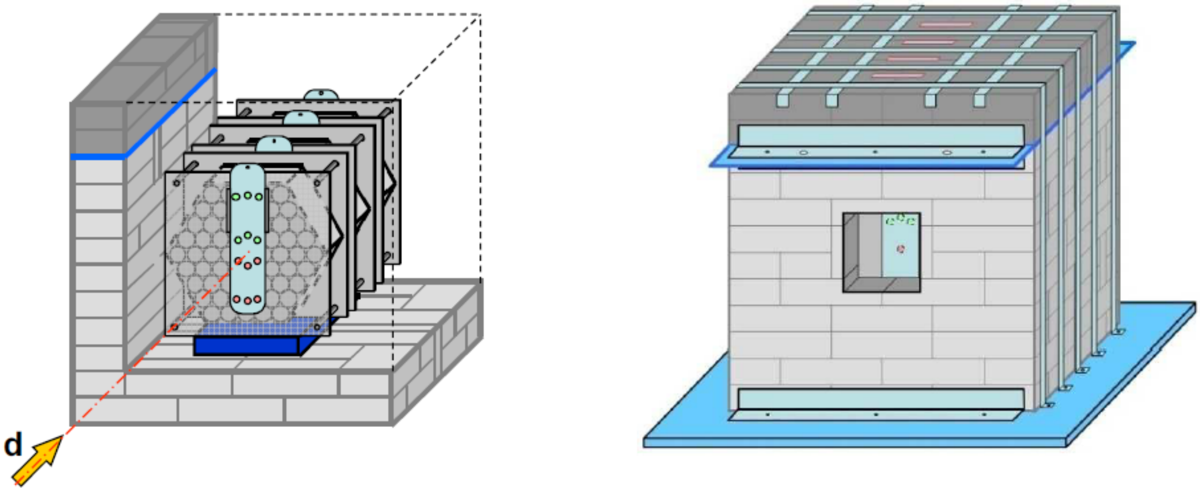

Figure 6: Scheme of the QUINTA setup composed of three hexagonal sections. The setup covered by lead shielding is in the right picture [87].

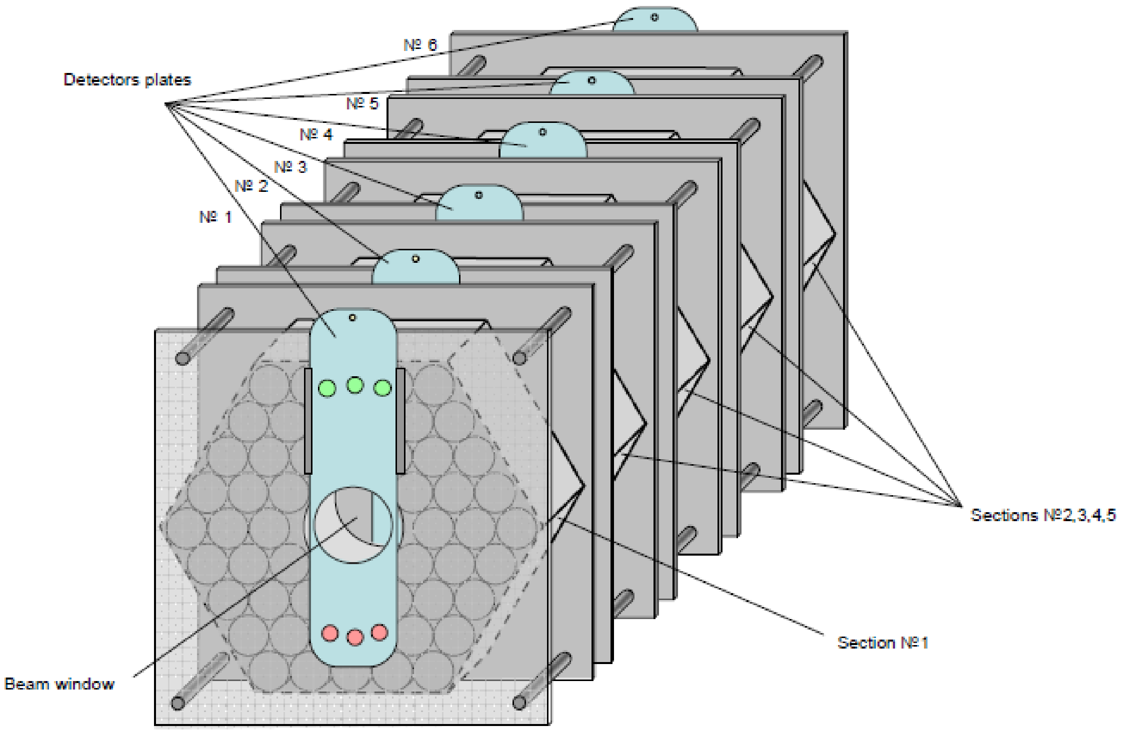

Figure 7: Scheme of the QUINTA setup composed of five hexagonal sections [93]. Dimensions are in mm.

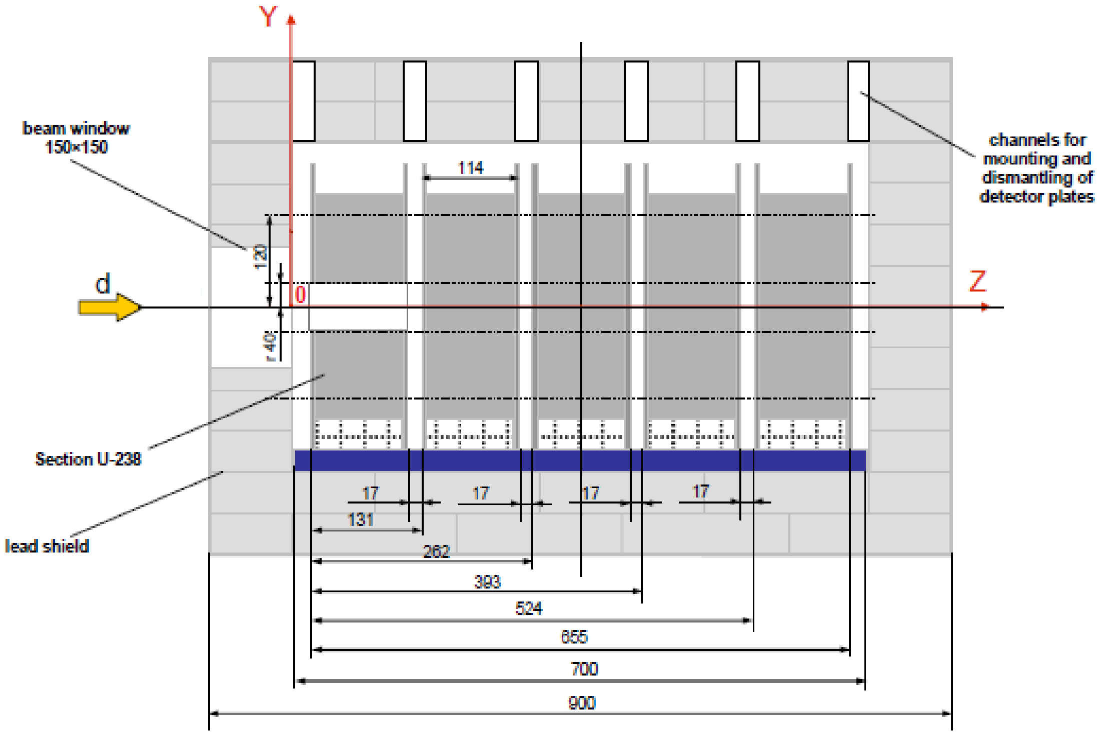

Figure 8: Cross-cut of the setup with lead shielding [93]. Dimensions are in mm.

Every section is 114 mm long, and between the sections, there are 17 mm air gaps for activation detectors placement. The uranium rods forming the sections are enclosed in aluminium plates of dimensions 350×350×5 mm^3. The first section contains 54 rods while the other sections contain 61 rods. The uranium rods are 104 mm long, and their diameter is 36 mm. The weight of a single rod is 1.72 kg, and it is encapsulated in an aluminium cover. The weight of the QUINTA assembly is 540 kg, and it is shielded by the lead box of 100 mm wall thickness. The real view of QUINTA is in Fig. 9.

A more detailed description of the QUINTA assembly is given, e.g. in [93].

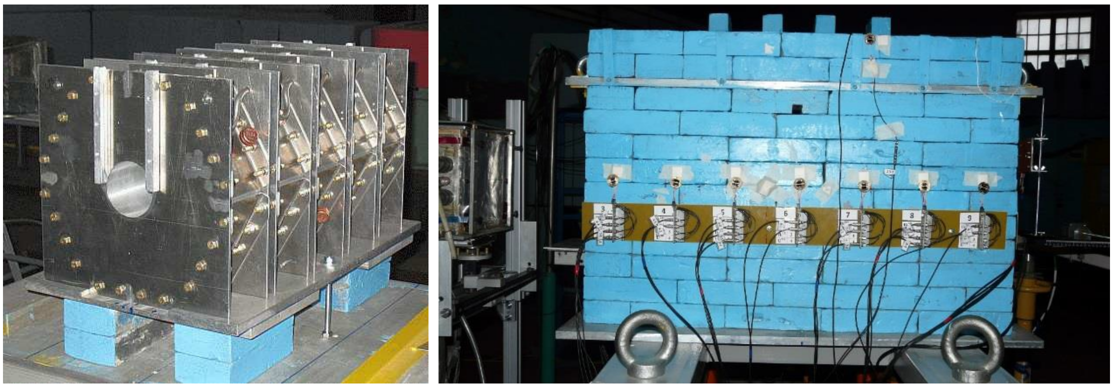

Figure 9: QUINTA setup without (left) and with (right) the lead shielding [93, 94].

Irradiation of QUINTA started in 2009, and up to 2010, it was composed of three hexagonal sections. Then the next two uranium sections were added, and the prolonged version was operational until 2017 when the experiments ended. The lead shielding of QUINTA was added in 2012.

The QUINTA experiments were performed at the JINR Nuclotron accelerator where the setup was irradiated by 1 - 8 GeV deuteron beams, and by 24 and 48 GeV ^{12}C ion beams [95]. By the end of 2014, the setup was moved to the Phasotron accelerator. At Phasotron, QUINTA was irradiated by the 660 MeV proton beam with the intensity of two orders of magnitude higher than the intensity of the deuteron beams of Nuclotron. Such a high intensity enables a more detailed investigation of nuclear reactions induced by spallation neutrons and the determination of neutron energy distribution by means of the activation techniques.

In the frame of the E&T RAW collaboration, the international groups were responsible for specific tasks to ensure a smooth course and evaluation of the performed experiments. The JINR team was responsible for online beam monitoring using a system based on the ionisation chamber and scintillation telescope [96]. The Czech NPI, the Ukraine KIPT (Kharkiv Institute of Physics and Technology) and also the JINR teams were responsible for offline beam monitoring using aluminium and copper activation detectors [88, 93, 97]. The Belarus JIPNR (Joint Institute for Power and Nuclear Research) team measured beam profiles of the primary deuterons on the beam entrance to QUINTA using Solid State Nuclear Track Detectors (SSNTD) [98, 99].

Among the main research objectives of the QUINTA experiments belonged:

- Measurement of neutron spatial and energy distribution and radionuclide production inside the setup [100-105]

- Transmutation of uranium and thorium, fission products and higher actinides [106-109]
- Measurement of cross-sections important for ADS [110-112]
- Benchmark tests of Monte Carlo method based simulation codes [113-116]

Significant research was also the determination of the number of escaping spallation neutrons lead by J. Adam [117]. Since the end of 2015, the JINR team also started to carry out research on neutron flux determination by temperature differences using thermocouples (TC) lead by J. Svoboda [118-120]. Master and Dissertation Theses were also written about QUINTA [87, 88, 94, 121, 122]. A list of performed QUINTA irradiations at Nuclotron and Phasotron is presented below [93, 100, 123-127]. I_p, I_d and I_{12C} are integral numbers of protons, deuterons and carbon nuclei, respectively, impinging on the target. E_p, E_d and E_{12C} are energies of the proton, deuteron and carbon nuclei beams, respectively.

List of QUINTA experiments at Nuclotron:

- 2009 - First two pilot experiments of the setup irradiation by 1 and 4 GeV deuteron beams. QUINTA was composed of three hexagonal sections and was not equipped with the lead shielding.
- March 2011 - Deuteron beam, three irradiations without the lead shielding: 1) E_d = 2 GeV, I_d = 1.69(8)E13; 2) E_d = 4 GeV, I_d=1.41(7)E13; 3) E_d = 6 GeV, I_d = 1.94(10)E13
- December 2011 - Deuteron beam, three irradiations: 1) E_d = 1 GeV, I_d = 1.50(4)E13; 2) E_d = 4 GeV, I_d = 1.94(5)E13; 3) E_d = 8 GeV, I_d = 0.063E13 (this value was measured only with ionisation chamber)
- March 2012 - Deuteron beam, three irradiations: 1) E_d = 1 GeV, I_d = 1.86(5)E13; 2) E_d = 4 GeV, I_d = 2.72(7)E13; 3) E_d = 8 GeV, I_d = 0.539(17)E13
- December 2012 - Deuteron beam, three irradiations: 1) E_d = 2 GeV, I_d = 3.052(9)E13; 2) E_d = 4 GeV, I_d = 3.569(15)E13; 3) E_d = 8 GeV, I_d = 0.91(4)E13
- March 2013 - Deuteron beam, three irradiations: 1) E_d = 1.3 GeV, I_d = 0.906(5)E13; 2) E_d = 2 GeV, I_d = 4.01(4)E13; 3) E_d = 4 GeV, I_d = 1.861(19)E13
- November 2013 - Deuteron beam, E_d = 4 GeV, I_d = 2.12(3)E13, samples: 33 Al, 12 Pb, 10 Bi, 4 Co, 6 Au, 10 ^{235}U, 10 ^{nat}U
- December 2013 - Deuteron beam, E_d = 8 GeV, I_d = 6.11(8)E12, samples: 33 Al, 12 Pb, 10 Bi, 10 Co, 6 Au, 10 ^{235}U, 10 ^{nat}U
- December 2013 - Carbon beam, E_{12C} = 24 GeV, I_{12C} = 2.14(15)E11, samples: 10 Al, 10 ^{nat}U
- December 2013 - Carbon beam, E_{12C} = 48 GeV, I_{12C} = 6.18(44)E10, samples: 10 Al, 10 ^{nat}U

List of QUINTA experiments at Phasotron (irradiation with the 660 MeV proton beam):

- November 2014 - $I_p = 8.60(40)E14$, samples: 10 Al, 10 Co, 10 Au, 10 Bi, 10 Y, 5 ^{232}Th, 24 ^{nat}U
- February 2015 - $I_p = 2.40(12)E15$, samples: 47 ^{232}Th
- April 2015 - $I_p = 2.50(10)E15$, samples: 6 Co, 6 Au, 6 Bi, 44 Mn
- May 2015 - $I_p = 2.43(10)E15$, samples: 19 Au, ^{127}I(NaI), ^{129}I(NaI)
- November 2015 - $I_p = 3.38(40)E15$, samples: 36 Co, 28 Pb, 6 Au, 5 Y, ^{232}Th, 2 TC
- December 2015 - $I_p = 4.16(47)E15$, samples: 29 Co, 25 Mn, 2 Ta, 16 ^{232}Th, 6 ^{235}U, 4 ^{nat}U, 15 TC
- May 2016 - $I_p = 4.88(31)E15$, samples: 12 ^{235}U, 12 TC
- June 2016 - $I_p = 4.95(32)E15$, samples: 36 Al, 36 In, 9 Co, 13 Mn, 1 Pb, 1 W, 1 ^{232}Th, 3 TC
- December 2016 - $I_p = 4.84(31)E15$, samples: 12 Co, 12 Pb, 9 Y, 12 ^{235}U, 2^{nat}U, 1 ^{237}Np, 1 ^{241}Am, 16 TC
- December 2016 - $I_p = 1.51(14)E15$, samples: 10 Pb, 1 ^{232}Th, 50 ^{nat}U
- June 2017 (QUINTA without lead shielding) - $I_p = 1.52(16)E15$, samples: 40 ^{nat}U, 88 TC
- June 2017 (QUINTA without lead shielding) - $I_p = 1.43(15)E15$, samples: 50 Co, 12 Pb, 36 Al, 2 Au, 2 Bi, 36 In, 36 Mn, 40 ^{nat}U, 40 TC

Due to the similar QUINTA construction and arrangement like the E+T setup, there can be found similarities. The maximum flux of fast neutrons in QUINTA was measured in the air gap between the second and third sections, while in E+T between the first and second sections. This was caused by the air space in the first QUINTA section. The neutron flux was typically higher in QUINTA because of the natural uranium spallation target. Like in the E+T case, the experiment-to-simulation ratios were worse for higher energy thresholds of the (n,xn) reactions due to insufficient knowledge of cross-sections for high energies. Generally, the experiment-to-simulation agreement was found worse in the QUINTA case. There exist a suspicion that it could be caused by the worse primary beam geometry description. QUINTA was during each experiment 2 degrees tilted (see Fig. 24 and section 4.1.1), what could be a possible extra source of the beam geometry uncertainties.

My particular task in the framework of our team was to concentrate on the investigation of the central region along the primary beam passage and to assess the suitability of the Monte Carlo code MCNPX 2.7.0 usage for simulations of radionuclide production in this region (chapter 4). To deeper investigate the beam geometry uncertainties, I worked out a sensitivity analysis of simulation results, which is given in chapter 5.

1.3.5 BURAN

The BURAN assembly is a QUINTA successor (see Fig. 10) [93]. BURAN is supposed to be a “quasi-infinite“ spallation target, which means that there should be a minimum neutron leakage from the assembly. According to my simulations in MCNPX 2.7.0, the neutron leakage in the case of BURAN irradiated with the 660 MeV protons is around 15 %, while the leakage in the case of QUINTA is around 75 % (see chapter 7). Experiments of BURAN irradiation with the 660 MeV proton beam of Phasotron are now in the preparatory phase at JINR.

Figure 10: Photograph of the BURAN setup.

The BURAN setup consists of a large depleted uranium (containing 0.3 % of ^{235}U) blanket of 1200 mm in diameter and 1000 mm in length with a total uranium mass of 20 tons (see Fig. 11). The cylinder has a 200 mm in diameter air opening in its centre in which a spallation target can be inserted. The target can be of different spallation materials like lead, carbon or uranium. The blanket is shielded with a 100 mm steel layer, having a 200 mm in diameter beam window. The primary beam is aimed perpendicularly to the window. Then it enters the spallation target channel, which is supposed to have an adjustable length, e.g. 0, 100 or 200 mm. Also, the target dimensions can be changeable. Monte Carlo simulations for various spallation target materials and various high-energy particle beams are presented in chapter 6. About an experiment with a potential lead spallation target for BURAN is dealt with in chapter 8.

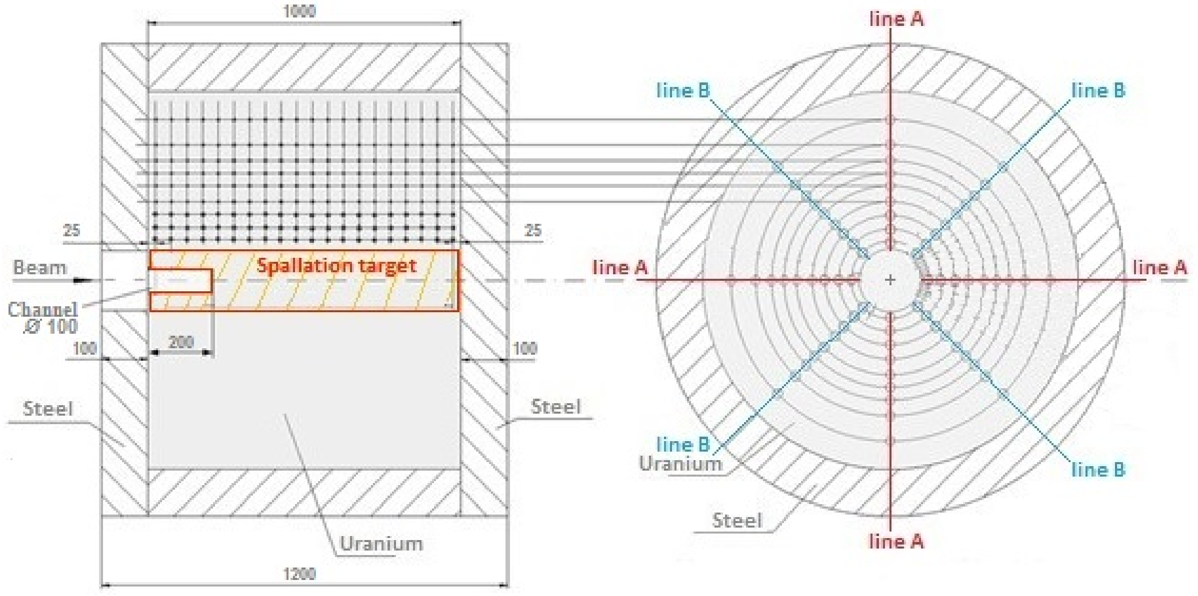

Figure 11: Schematic drawing of the BURAN setup [93].

The blanket is equipped with 72 air channels of 30 mm in diameter parallel to the beam axis, and 20 measuring positions are defined in every channel. The first position is located at the 25 mm distance from the uranium blanket edge. Each next position is in the 50 mm distance from the previous one. Totally 1440 positions are supposed to enable outstanding flexibility in neutron spatial and spectral distribution measurement. The radial distances of the air channels from the BURAN central longitudinal axis are: 140, 180, 220, 260, 300, 340, 380, 440 and 520 mm (lines A), and 120, 160, 200, 240, 280, 320, 360, 400 and 480 mm (lines B). The model of BURAN visualised in Vised 24E [128] is given in Fig. 12. In the figure, a depleted uranium spallation target of 1000 mm in length and 200 mm in diameter, and equipped with the target channel of 200 mm in length and 100 mm in diameter, is taken into consideration.

The experimental research at BURAN will be focused on the study of generated neutron field inside the setup, its spatial and energy distribution, study of fission reactions and leakage of neutrons from the setup. Further, it will be used for the investigation of transmutation of long-lived isotopes and fission of ^{239}Pu, acquiring of nuclear neutron data, research of optimum dimensions of ADS core and suitable energy of primary proton or deuteron beams. Last but not least, the experiments at BURAN are supposed to be very useful for verification of Monte Carlo simulation codes.

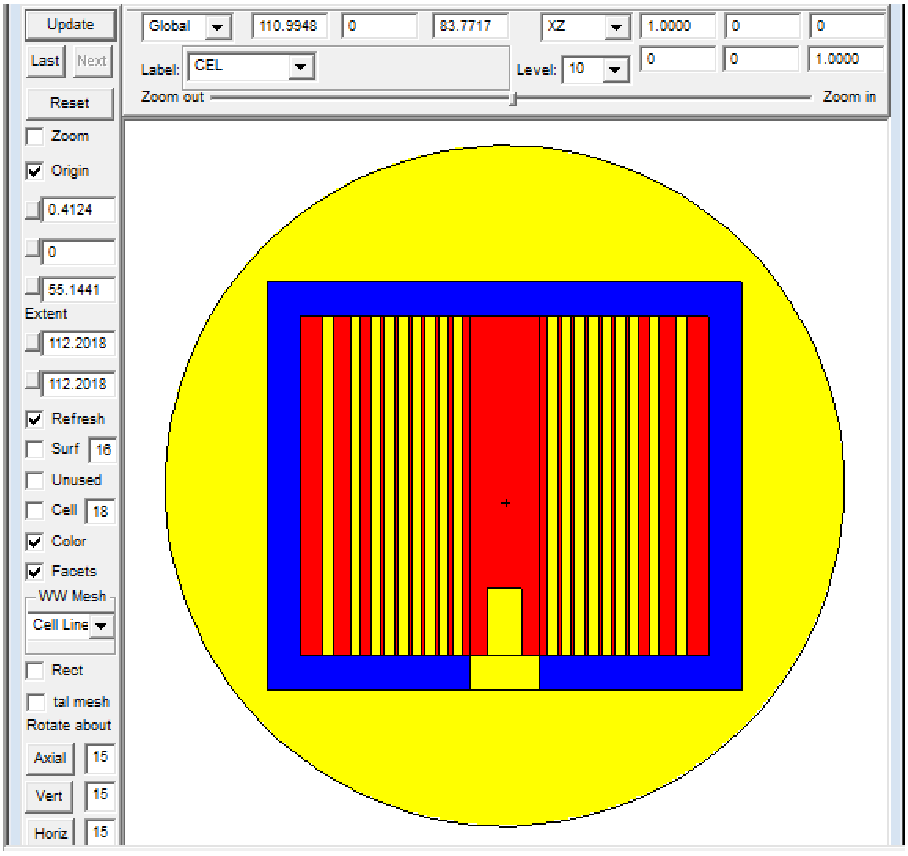

Global 110.9948 0 83.7717
XZ 1.0000 0 0
0 0 1.0000
Label: CEL
Level: 10
☐ Zoom
☑ Origin
0.4124
0
55.1441
Extent
112.2018
112.2018
☑ Refresh
☐ Surf 16
☐ Unused
☐ Cell 18
☑ Color
☑ Facets
WW Mesh
Cell Line
☐ Rect
☐ tal mesh
Rotate about
Axial 15
Vert 15
Horiz 15

Figure 12: Central slice of the BURAN geometrical model visualised in the Vised 24E editor. Red colour represents the depleted uranium, blue colour represents the steel covering and yellow colour is the air.

2 Data evaluation and simulations

For the experimental data processing and measurement, I used the method of the activation techniques and activation detectors. The method is very suitable for acquiring the data of neutrons and also other particles and has several advantages. Among them belong their small dimensions, zero dead time which is independent on the density of particle flux, and that no electronics is required during irradiation. Nevertheless, there is also a couple of drawbacks like the complexity of the measured gamma spectra, complex and time-consuming evaluation, necessity for a good knowledge of cross-sections of studied reactions and that only the off-line evaluation is possible.

We usually use activation detectors in the form of thin metal foils. They are mono-isotopic or with known isotope composition. The dimensions have to be big enough, so an adequate number of radioactive nuclei can be accumulated. However, simultaneously they have to be small enough not to influence the surrounding particle field significantly.

When a neutron, proton or deuteron impinges on an activation detector, it can induce a nuclear reaction. The reactions are mainly non-threshold, e.g. (n,γ) or (p,γ), or threshold, e.g. (n,xn) or (p,xn). Radionuclides formed are not stable and they tend to decay by β radiation (products of some activation detectors like ^{nat}U or ^{232}Th also decay by α radiation). The process is accompanied by γ radiation, which is consequently measured by high-purity germanium (HPGe) detectors. By analysis of measured spectra and gamma spectrometry methods, it is possible to gain a number of radionuclides created. Energy neutron spectra can also be unfolded based on the methods using different energy thresholds of (n,xn) reactions [129, 130].

I focused on neutron-, proton- and deuteron-induced threshold reactions. By using specific activation materials and by studying specific nuclear reactions, the components of a mixed neutron-proton (-deuteron) field can be separated (described in section 4.1.4).

2.1 Data acquisition

Before each QUINTA experiment, activation samples need to be prepared including their weighting, wrapping (usually into a sheet of paper) and labelling. They are fixed on aluminium holders into proper positions and inserted into the setup (see Fig. 13 and sections 1.3.4 and 4.1.1).

The QUINTA assembly is irradiated by the proton beam of the Phasotron accelerator [131] or the deuteron beams of the Nuclotron accelerator [132, 133]. The number of source particles impinging on the setup is determined by aluminium activation foils. For the protons in the Phasotron experiment, monitoring reaction ^{27}Al(p,3pn)^{24}Na is used. For the deuterons in the Nuclotron experiments, monitoring reaction ^{27}Al(d,3p2n)^{24}Na is used. For more about the beam intensity monitoring, see e.g. [93].

After irradiation, the activation samples are taken away from the QUINTA assembly and transported to the JINR gamma-spectrometry laboratory YASNAPP-2. In the case of the Nuclotron experiments, the transport takes from half an hour to one hour, in the case of the Phasotron experiments, it is usually in the order of minutes. The laboratory is equipped with six HPGe detectors with corresponding electronics, five of the detectors are coaxial (with which the measurements are performed) and one of them is planar. The coaxial detectors are shielded by thick lead, thin copper and thin cadmium layers and the

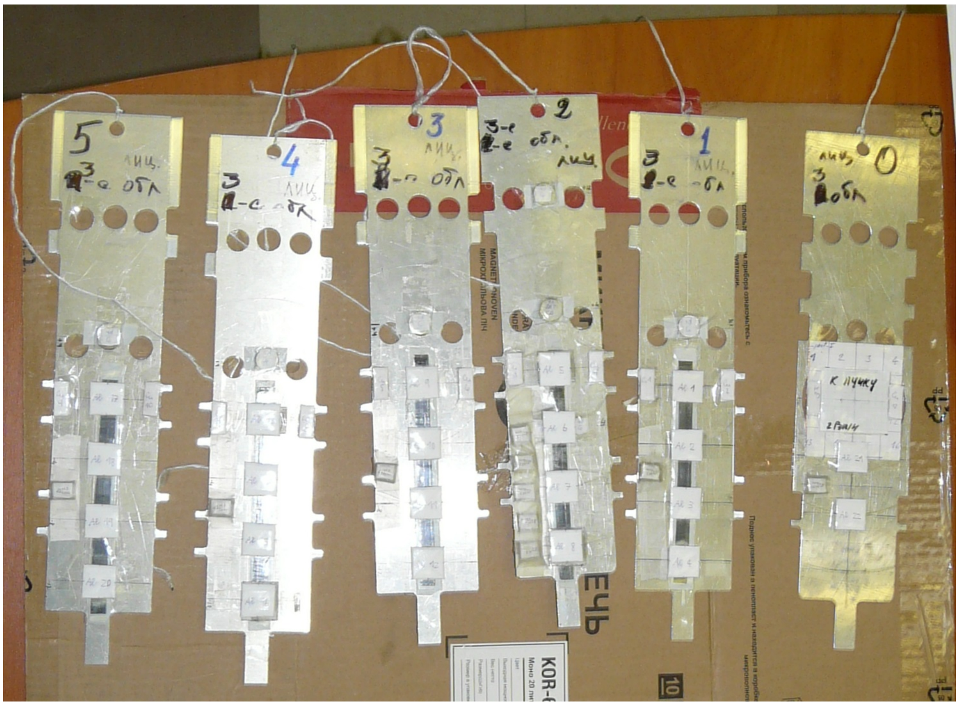

Figure 13: Aluminium plates with activation detectors prepared for insertion into the QUINTA setup and consequent irradiation. (Experiment at Nuclotron from November 2013)

samples are placed on individual plastic plates which are inserted into sample position devices the detectors are equipped with (see Fig. 14). The gamma spectra are recorded using the software programs Genie 2000 [134] (CANBERRA detectors) and Maestro-32 [135] (ORTEC detectors).

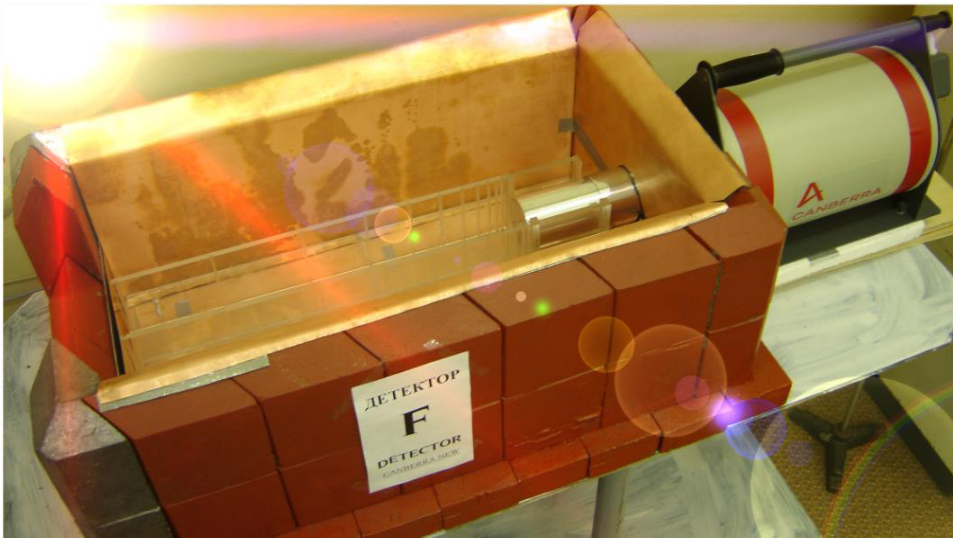

Figure 14: HPGe detector CANBERRA GC3018, its shielding and plastic position device for samples placement. During measurements, the top side is also shielded [122].

Before measurements start, energy and efficiency calibrations of the detectors have to be performed. The energy calibration between the measured spectra and multi-channel analyser channels is linear, described as

$$E(x) = b_0 + b_1 \cdot x \tag{4}$$

where E is the energy of gamma peak, x is the multi-channel analyser channel and b_0, b_1 are the parameters calculated from two selected full-energy peaks with tabulated energies. Usually gamma peaks at energies 122.1 keV of ^{57}Co source and 1332.5 keV of ^{60}Co source are used.

The energy and efficiency calibrations are performed using the set of standard calibration gamma-ray sources: ^{54}Mn, ^{57}Co, ^{60}Co, ^{88}Y, ^{109}Cd, ^{113}Sn, ^{133}Ba, ^{137}Cs, ^{139}Ce, ^{152}Eu, ^{228}Th and ^{241}Am. The sources cover the energy range from 50 to 2610 keV.

For more information about the energy and efficiency calibrations, see e.g. [136].

2.2 Data analysis

For determination of reaction rates R (defined as a total number of nuclei created in an activation sample normalised to one source particle and one atom of the sample), the gamma spectrometry method is used. There exist many programs which enable to analyse measured spectra and provide us with gamma peak areas $S(E_\gamma)$.

The reaction rate R can be calculated as

$$R = N_{yield} \cdot \frac{M}{N_A} \tag{5}$$

where M is the relative atomic mass of the activation sample material, N_A is the Avogadro constant and N_{yield} is the total number of nuclei created in a sample normalised to one source particle and one gram of the sample material. N_{yield} is given by the equation

$$N_{yield} = \frac{S(E_\gamma)}{m_s} \cdot \frac{1}{I_p} \cdot \frac{1}{I_\gamma} \cdot \frac{t_{real}}{t_{live}} \cdot \frac{C_B \cdot C_{abs}}{\varepsilon_p(E_\gamma) \cdot C_g \cdot COI} \cdot \frac{exp(\lambda \cdot t_{delay})}{1 - exp(-\lambda \cdot t_{real})} \cdot \frac{\lambda \cdot t_{irr}}{1 - exp(-\lambda \cdot t_{irr})} \tag{6}$$

where m_s is the sample mass, I_p is the integral number of the source particles, t_{irr} is the irradiation time, t_{delay} is the time between the end of the irradiation and start of the measurement and λ is the decay constant.

In order to gain the number of radionuclides created in the activation samples by nuclear reactions, several corrections have to be made. These corrections are: Intensity of gamma transition I_γ, live measurement time t_{live} ($t_{live} = t_{real} - t_{dead}$, where t_{real} is the real measurement time and t_{dead} is the detector dead time), full-energy peak detector efficiency $\varepsilon_p(E_\gamma)$, beam instabilities during irradiation C_B, self-absorption of gamma photons in samples C_{abs}, sample geometrical correction C_g and cascade coincidence correction COI. TrueCoinc is a program, developed at the University of Debrecen in Hungary by S. Sudár [137], used for the coincidence correction determination. Mathematically, the total correction factor C can be written as

$$C = \frac{C_B \cdot C_{abs}}{I_\gamma \cdot \varepsilon_p(E_\gamma) \cdot C_g \cdot t_{live} \cdot COI} \tag{7}$$

In the equation (6), the

$$\frac{1}{I_\gamma} \tag{8}$$

represents the intensity of gamma line correction,

$$\frac{t_{real}}{t_{live}} \tag{9}$$

represents the detector dead time correction,

$$\frac{exp(\lambda \cdot t_{delay})}{1 - exp(-\lambda \cdot t_{real})} \tag{10}$$

represents the isotope decay from the irradiation end to the measurement start correction, and

$$\frac{\lambda \cdot t_{irr}}{1 - exp(-\lambda \cdot t_{irr})} \tag{11}$$

represents the isotope decay during the irradiation correction.

The derivation of the equations mentioned above can be found, e.g. in [87] or [138].

In case of a set of measured or deduced values x_i (i = 1,2, ... n) of a quantity X with standard deviations σ_i, and under the condition of Gaussian distribution, the mean value can be calculated as a weighted average according to [136]. In this thesis, the weighted average is applied to the determination of reaction rates because the activation samples are usually multiple measured with HPGe detectors and/or the isotopes have more detected lines. The weighted average x^w is given by the equation

$$x^w = \frac{\sum\limits_{i=1}^{n} w_i x_i}{\sum\limits_{i=1}^{n} w_i} \tag{12}$$

where w_i is the weighting factor of x_i given by

$$w_i = \frac{1}{\sigma_i^2} \tag{13}$$

Then the standard deviation $\sigma(x^w)$ of the weighted average x^w is determined as a maximum of the external $\sigma_{ext}(x^w)$ and internal $\sigma_{int}(x^w)$ deviations given by the equations

$$\sigma_{ext}^2(x^w) = \frac{\sum\limits_{i=1}^{n} w_i (x_i - x^w)^2}{(n-1)\sum\limits_{i=1}^{n} w_i} \tag{14}$$

and

$$\sigma_{int}^2(x^w) = \frac{1}{\sum\limits_{i=1}^{n} w_i} \tag{15}$$

2.2.1 Software DEIMOS32 and program package for reaction rate determination

After the QUINTA assembly irradiation, the samples are taken out of QUINTA and gamma spectra are measured with HPGe detectors. DEIMOS32 is a program, developed at NPI Řež by J. Frána [139], which is used for the measured spectra analysis. The spectra analysis is based on the Non-Linear Least Squares Method. The peaks are fitted with a Gaussian function while the background under each peak (parabolic or linear fit) is subtracted. The fitted peaks are visualised in Fig. 15. The Deimos analysis provides us with gamma peak areas S(E_γ), which represent a number of gamma rays detected.

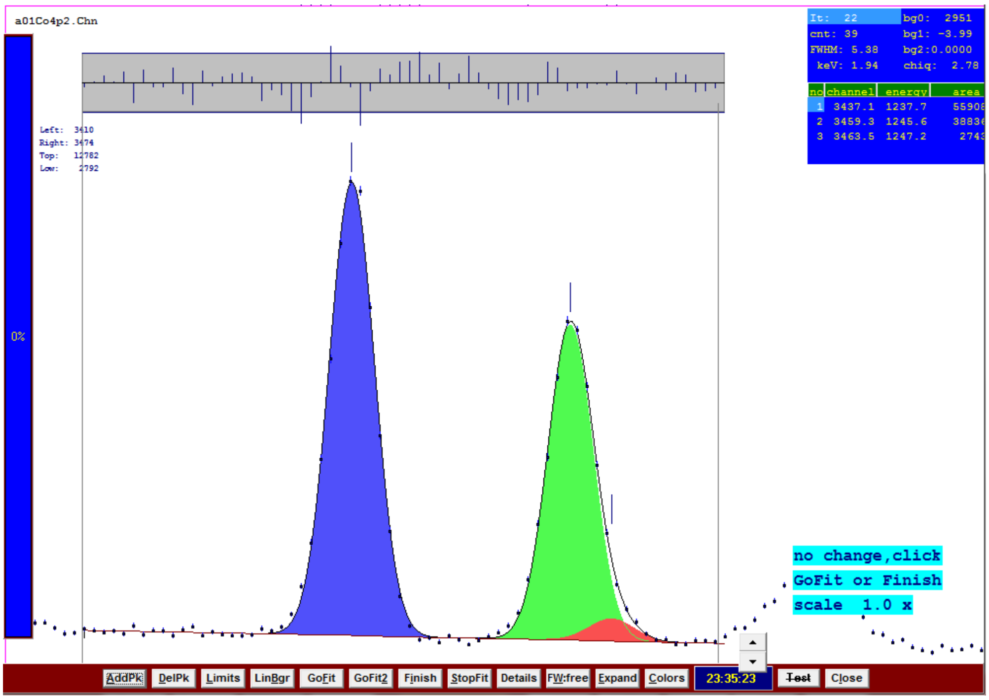

```
a01Co4p2.Chn

Left:   3410
Right:  3474
Top:   12782
Low:    2792

It:   22        bg0:   2951
cnt:  39        bg1:  -3.99
FWHM: 5.38      bg2:0.0000
 keV: 1.94      chiq:   2.78

no channel  energy    area
 1  3437.1  1237.7    55908
 2  3459.3  1245.6    38836
 3  3463.5  1247.2     2743

no change,click
GoFit or Finish
scale   1.0 x
```

Figure 15: Fitting of peaks in DEIMOS32 program. DEIMOS32 informs about energy, area and width of the peaks.

For the reaction rate determination, our workgroup in Dubna uses a special program package [140], based on the previous programs [141], which were innovated in the Ruby programming language [142]. A brief description of the programs is given in Appendix A.

2.3 Simulation procedure

Monte Carlo simulations with the radiation transport code MCNPX version 2.7.0 [80] were performed in this thesis. Both the neutron and proton (and also deuteron in experiments with deuteron beams) flux in activation samples of the studied experiments were simulated employing the intranuclear cascade physics model INCL4.2 [143], fission-evaporation model ABLA-KHSv3p [144, 145], and standard cross-section data library ENDF/B-VII.1 [146]. The cross-sections of the studied neutron- and proton- (and deuteron-) induced reactions were calculated with the deterministic codes TALYS version 1.6 [147] and TALYS version 1.8 [148] using the Constant Temperature and Fermi Gas models (see Fig. 16), and with MCNPX 2.7.0 using the INCL4.2 model and also intranuclear cascade model CEM03 [150]. The simulated reaction rates of the studied radionuclides R_{sim} were then determined by convolutions of the simulated flux and cross-sections according to the following equation

$$R_{sim} = \sum_{i=n,p,d} \sum_{E_{thr}}^{E_{max}} \sigma_i(\Delta E) \cdot \phi_i(\Delta E) \tag{16}$$

where $\sigma_i(\Delta E)$ and $\Phi_i(\Delta E)$ are the reaction cross-section and the flux, respectively, for particles i (neutrons, protons, deuterons) in the energy bin ΔE. The bins ΔE range from the effective reaction threshold energy E_{thr} up to the maximal energy E_{max} (E_{max} = 660 MeV in the case of Phasotron, i.e. the energy of the primary protons impinging at the setup). The authors of [66] studied the effect of using TALYS version 1.6 and version 1.8 on the R_{sim} results during the last E+T experiment. They found out that the difference was only 1-4 % and that using TALYS 1.6 generally provided a little better agreement between the experimental and simulated reaction rates.

The simulations were performed with high statistics with nps (number of source particles [80]) ranging typically between 1E7 and 1E9 in dependence on particular simulation objectives, which resulted in small statistical uncertainties. Therefore the statistical uncertainties of the simulation results could be usually neglected. For example, uncertainties of the simulation results in the experiment with the lead target (see chapter 8) were less than 1 % for the APb and BPb samples, less than 3 % for the CPb sample, and less than 5 % for the DPb sample. However, it was necessary to take into account the uncertainties of the neutron spectra hardness calculations (section 6.4) for the BURAN setup due to low statistics of neutrons in remote longitudinal distances and high-energy intervals. In the energy neutron spectra simulations for BURAN (section 6.3), low statistics for high neutron energies is also visible in the graphs, but the uncertainties were not involved for better readability.

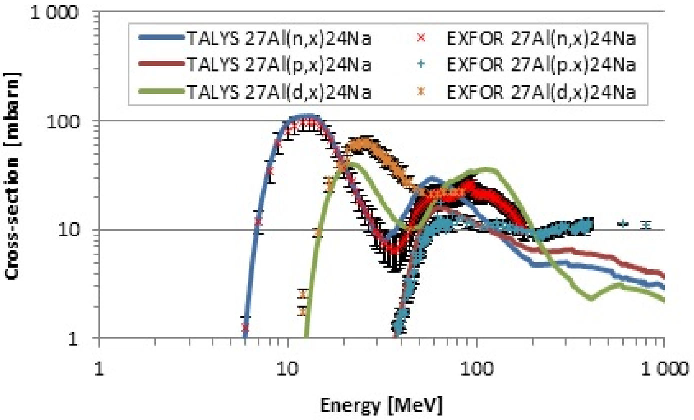

Figure 16: Comparison of cross-sections calculated using TALYS 1.6 with experimental data from the EXFOR database [149] for reactions on aluminium.

All simulations presented in this thesis were performed by myself except the determination of cross-sections with MCNPX 2.7.0 in the E+T experiments (chapter 3), which was performed by M. Suchopár [66]. The MCNPX geometry model of the E+T assembly was created by M. Majerle [91], and the geometry models of the QUINTA and BURAN assemblies by M. Suchopár [88]. The modifications of the MCNPX input files (e.g. the definition of activation samples, source definition, definition of beam parameters, physics definition) were performed by myself. The geometry model of the lead target in chapter 8 was created by myself. An example of the MCNPX input file is given in Appendix B.

3 Experiments with subcritical assembly Energy plus Transmutation

This chapter deals with the experiments of irradiation the E+T assembly by proton and deuteron beams of Nuclotron. As was already mentioned in section 1.3.3, the irradiations of this setup ended in 2009 and the new systematics of the E+T experiments is now being prepared by our workgroup at NPI. My task was to perform new Monte Carlo simulations of the E+T experiments. The meaning of the new simulations is in having them performed with the same "settings" (i.e. to use the same version of MCNPX, same MCNPX physics models and same source of cross-sections) in order the simulation results to be more compatible for comparison between each other throughout the different E+T experiments. Moreover, the old simulations were often performed with less precise beam positions and slightly different E+T simulation models, which is another motivation for performing the simulations again.

3.1 Description and approach

I focused on threshold reactions in the samples of ^{27}Al, ^{197}Au and ^{209}Bi in the E+T irradiations by the 0.7 GeV proton beam (E+Tp0.7GeV) [58], 1 GeV proton beam (E+Tp1GeV) [59], 1.5 GeV proton beam (E+Tp1.5GeV) [60, 89], 2 GeV proton beam (E+Tp2GeV) [61], 1.6 GeV deuteron beam (E+Td1.6GeV) [65], 2.52 GeV deuteron beam (E+Td2.52GeV) [65] and 4 GeV deuteron beam (E+Td4GeV) [66]. I chose these samples because they were all present in the mentioned experiments in the identical or similar positions.

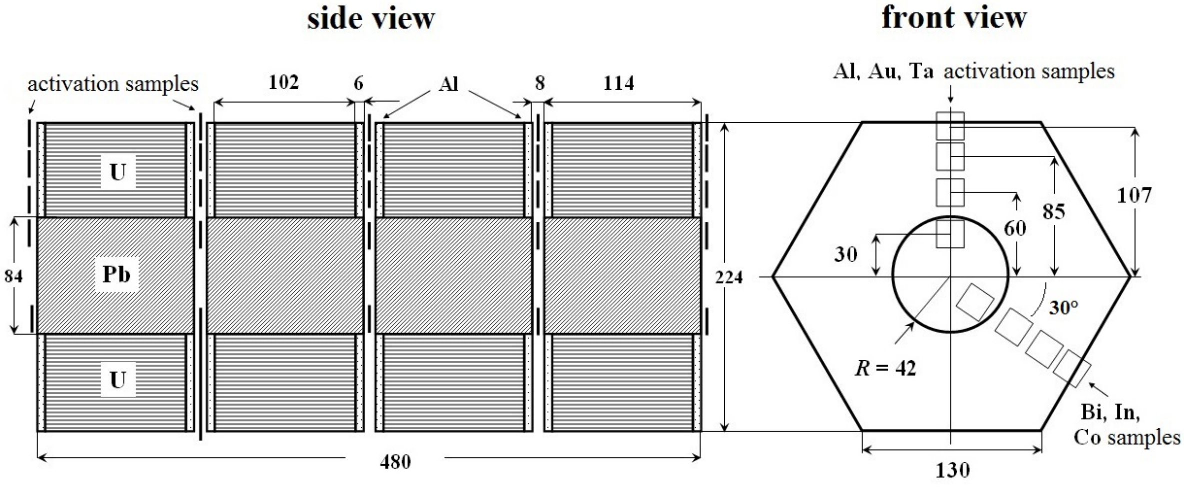

Figure 17: Positions of activation samples in the E+T setup during the 4 GeV deuteron irradiation [66].

The placement of activation samples in the E+Td4GeV experiment is given in Fig. 17. The samples were mounted on plastic plates inserted in front of, behind, and between the E+T sections (see Figs. 3 and 4) at longitudinal distances of 0, 11.8, 24.0, 36.2 and 48.4 cm from the target front. On the plates, samples were placed in radial distances of 3.0, 6.0, 8.5 and 10.7 or 11.5 cm from the central longitudinal axis (axis z in Fig. 4). The first group of samples (^{27}Al, ^{197}Au, ^{181}Ta grouped together) was positioned in the upward direction, and the second group of samples (^{209}Bi + ^{115}In + ^{59}Co) was positioned in the right-down direction. The samples were of a square shape with a side length of 20 mm for ^{27}Al, ^{197}Au and ^{181}Ta samples, 25 mm for ^{209}Bi samples, and 12.5 mm for ^{115}In and ^{59}Co samples. The average weights of the samples were 0.63 g for ^{27}Al, 0.36 g for ^{197}Au, 0.80 g for ^{181}Ta, 6.54 g for ^{209}Bi, 0.56 g for ^{115}In and 1.36 g for ^{59}Co.

In the other experiments, which I was focused on, the samples were situated in the E+T setup similarly. The longitudinal and radial positions of the studied ^{27}Al, ^{197}Au and ^{209}Bi samples are given in Tabs. 9 - 24 in Appendix C. For more detailed information about the irradiated samples and its placement, as well as the course of irradiation, see [58-61, 65, 66, 89].

The simulations were performed in MCNPX 2.7.0 as described in section 2.3. The cross-sections for convolutions with the particle flux up to 200 MeV were extracted from TALYS 1.8. In order to keep consistency with the simulations performed in the last E+T experiment [66], the cross-sections from 200 MeV were extracted from MCNPX 2.7.0 using the INCL4.2 and CEM03 models.

The coordinates of the source beam centre and spatial beam profile on the setup entrance were determined by SSNTD and a set of copper activation foils. The integral number of protons or deuterons impinging on the target was determined using the aluminium and copper activation monitors and concentric aluminium rings. For more detail, see [47, 57, 151, 152]. The beam characteristics on axes x and y on the E+T beam entrance (see Fig. 4) used as input parameters for the simulations are given in Tab. 1.

Table 1: Beam characteristics of the E+T experiments. d$_x$ and d$_y$ are coordinates of the source beam centre on axes x and y on the E+T entrance. FWHM$_x$ and FWHM$_y$ are full widths at half maximums of the 2D Gaussian profile on axes x and y on the E+T entrance.

Experiment	d$_x$[cm]	d$_y$ [cm]	FWHM$_x$ [cm]	FWHM$_y$ [cm]
E+Tp0.7GeV	0.5	-0.4	6.38	5.91
E+Tp1GeV	0.3	0.3	2.4	4.1
E+Tp1.5GeV	0.3	0.1	2.4	3.7
E+Tp2GeV	-1.4	0.3	3.8	5.4
E+Td1.6GeV	-0.64	-0.39	2.87	1.92
E+Td2.52GeV	1.5	-0.3	1.63	1.56
E+Td4GeV	2.4	1.7	2.1	1.8

3.2 Results of the E+T experiments

In this chapter, representative results are presented. The experimental and simulated values of reaction rates are given in Appendix C. The experimental reaction rates were taken from [58-61, 65, 66, 89]. All the simulations in this chapter and Appendix C (except the determination of cross-sections with MCNPX 2.7.0, which was performed by M. Suchopár [66]) were carried out by myself. I did not participate in the E+T irradiations.

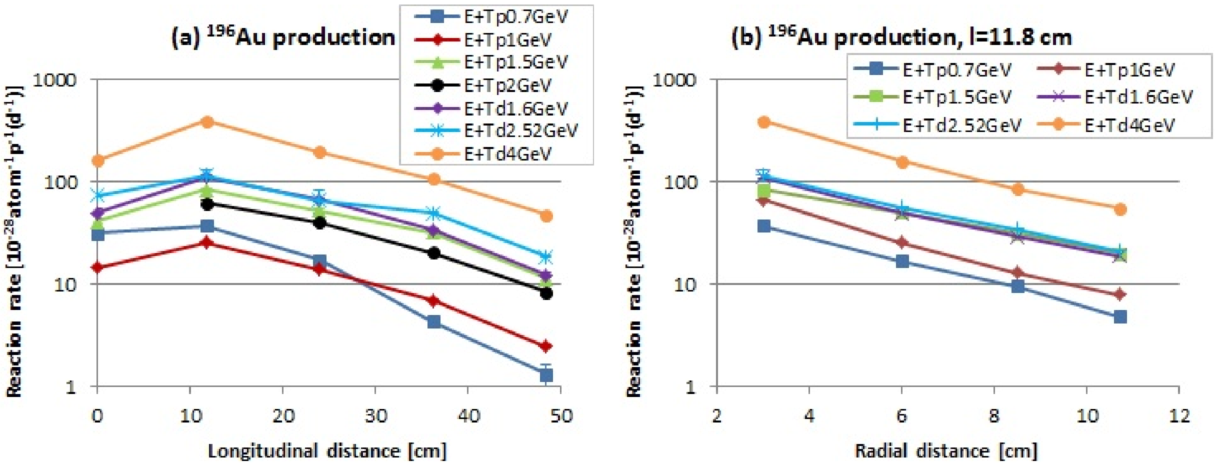

Figure 18: (a) Experimental reaction rates at a radial distance r of ^{196}Au production for the E+T experiments. r = 6 cm for the E+Tp1GeV experiment, r = 5.2 cm for E+Tp2GeV and r = 3 cm for the other experiments. (b) Experimental reaction rates at a longitudinal distance l = 11.8 cm of ^{196}Au production for the E+T experiments. Lines between the points have no physical meaning, and they are present only to guide a reader's eye.

The experimental reaction rates at a radial distance r of ^{196}Au production are given in Fig. 18.a. The experimental reaction rates at a longitudinal distance of l = 11.8 cm (first air gap, see Fig. 17) of ^{196}Au production are given in Fig. 18.b. The experiment-to-simulation reaction rate ratios at a radial distance r of ^{196}Au, ^{24}Na and ^{206}Bi production are given in Fig. 19. Ratios at a longitudinal distance of l = 11.8 cm of ^{196}Au, ^{24}Na and ^{206}Bi production are given in Fig. 20. Ratios for the isotopes of Au and Bi produced in the ^{197}Au and ^{209}Bi samples at a radial distance r are given in Fig. 21. Ratios for the isotopes of Au and Bi produced in the ^{197}Au and ^{209}Bi samples at a longitudinal distance of l = 11.8 cm are given in Fig. 22.

Neutron field inside the setup consists of spallation and fission neutrons. The neutrons are also being moderated, and some of them are back-scattered into the setup. The threshold reactions are caused mainly by the spallation neutrons. In the course of the spallation reaction, the most energetic neutrons are emitted primarily into forward angles during the intranuclear cascade phase. Spallation neutrons from the evaporation and fission phases are emitted isotropically. In Fig. 18.a of the experimental longitudinal distributions, one can see that the longitudinal maximums are located in the first air gap. When the primary charged particles travel through the target, they interact in nuclear reactions and lose their energy by ionisation losses. Hence the flux and energy of spallation neutrons also decrease with increasing longitudinal distance. The neutrons registered at the highest longitudinal distances originate mostly from spallation reactions of high-energy neutrons because their energy is not decreased by ionisation losses. The reactions on the samples in front of the target are caused mostly by spallation neutrons from the evaporation and fission phases. The radial neutron flux in Fig. 18.b, almost exponentially decreases and is the highest near the spallation target.

In Fig. 18, one can also notice that the neutron flux is generally increasing (for the same particles type and the same positions of samples) with the primary beam energy.

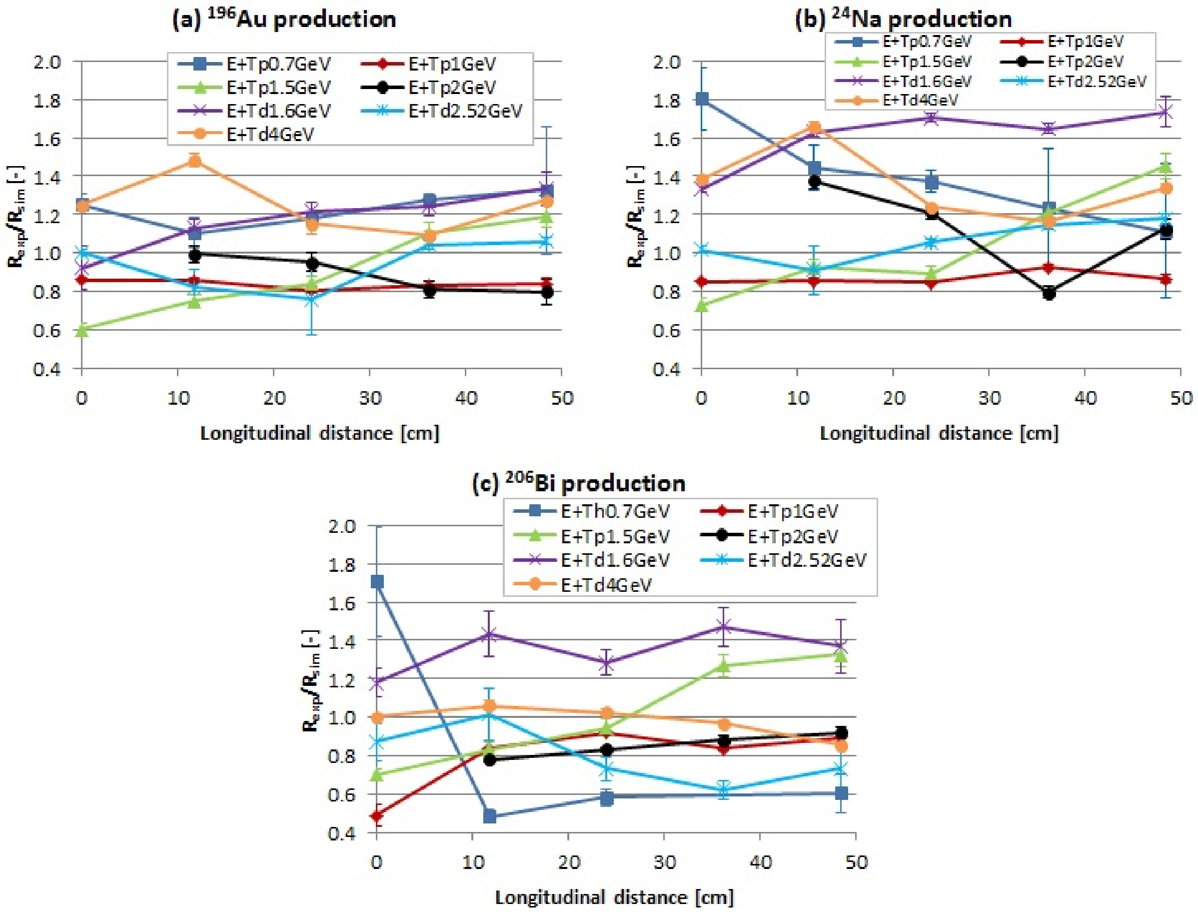

Figure 19: Experiment-to-simulation reaction rate ratios at a radial distance r of ^{196}Au (a), ^{24}Na (b) and ^{206}Bi (c) production for the E+T experiments. r = 6 cm for the E+Tp1GeV experiment, r = 5.2 cm for E+Tp2GeV and r = 3 cm for the other experiments.

Although the radial values of the 1.6 GeV and 2.52 GeV deuteron experiments increase just slightly and the longitudinal values in the 2nd and 3rd air gaps are of the same values (within one sigma). The values of the 4 GeV deuteron experiment rapidly increase compared to the 1.6 GeV and 2.52 GeV deuteron experiments.

In Figs. 19 - 22, one can see that the simulations generally well describe the experimental data and that the simulations typically underestimate the experiments for the deuteron beams. Although the simulations for the 1 GeV proton beam are overestimated, and for the 0.7 GeV proton beam they are underestimated for the Au and Na isotopes and widely overestimated for the Bi production, the situation about the proton beams is in general unclear and will need a further investigation. In Figs. 19 and 20, the experiment-to-simulation disagreement for the studied isotopes describing the longitudinal and radial spatial distributions reaches tens of a per cent typically. But the agreement is worse for the reactions with higher energy thresholds, what can be seen in Figs. 21 and 22. It is caused mainly by the insufficient knowledge of neutron cross-sections for reactions with higher energy thresholds ($E_{thr} > 30$ MeV). Among other factors influencing the simulation data belong used neutron cross-section libraries and physics models.

However, there are other discrepancies present, especially in the results of the E+Tp1.5GeV

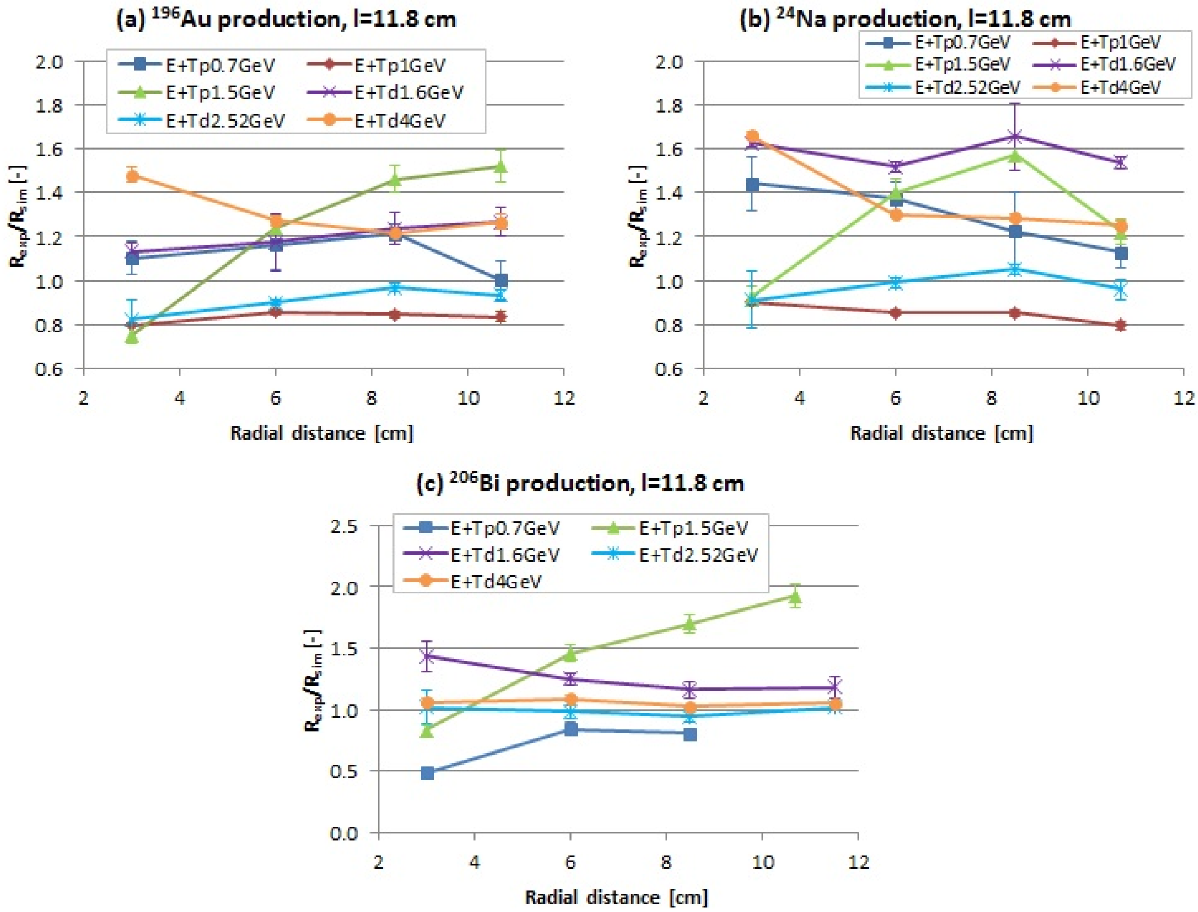

Figure 20: Experiment-to-simulation reaction rate ratios at a longitudinal distance l = 11.8 cm of ^{196}Au (a), ^{24}Na (b) and ^{206}Bi (c) production for the E+T experiments.

experiment. In Fig. 20, one can notice that there is an increasing tendency for the E+Tp1.5GeV ratios. The irradiation by the 1.5 GeV proton beam was the first experiment realised with the E+T setup, and at the time, there was no such knowledge as there is at present. Among that belong, e.g. the effect of beam parameters settings, samples displacement or beam intensity determination on the results [47, 91]. Based on the simulations and analysis of the data, I have already corrected a probable systematical error in the E+Tp1.5GeV experiment. The most remote radial position in which the activation samples were located seems not to be 13.5 cm, as stated in [60, 89], but 10.7 cm. Therefore the new simulations are presented in the new corrected position.

During our work on comparing the experiments and simulations of all the irradiations, we found that the experimental data of bismuth isotopes production in the E+Tp2GeV irradiation published in [61] were systematically overstated. By analysing the original data and their processing, we found a mistake in the evaluation process. It was thus possible to make a correction and obtain the correct experimental values. These values are, therefore, involved in Fig. 19.c and Tab. 16 in Appendix C.

In Figs. 20 and 22, one can see that the experiment-to-simulation agreement is generally worse for low radial positions, i.e. positions close to the central beam axis. Proton- or deuteron-induced reactions, and asymmetry given by the beam position and shape are

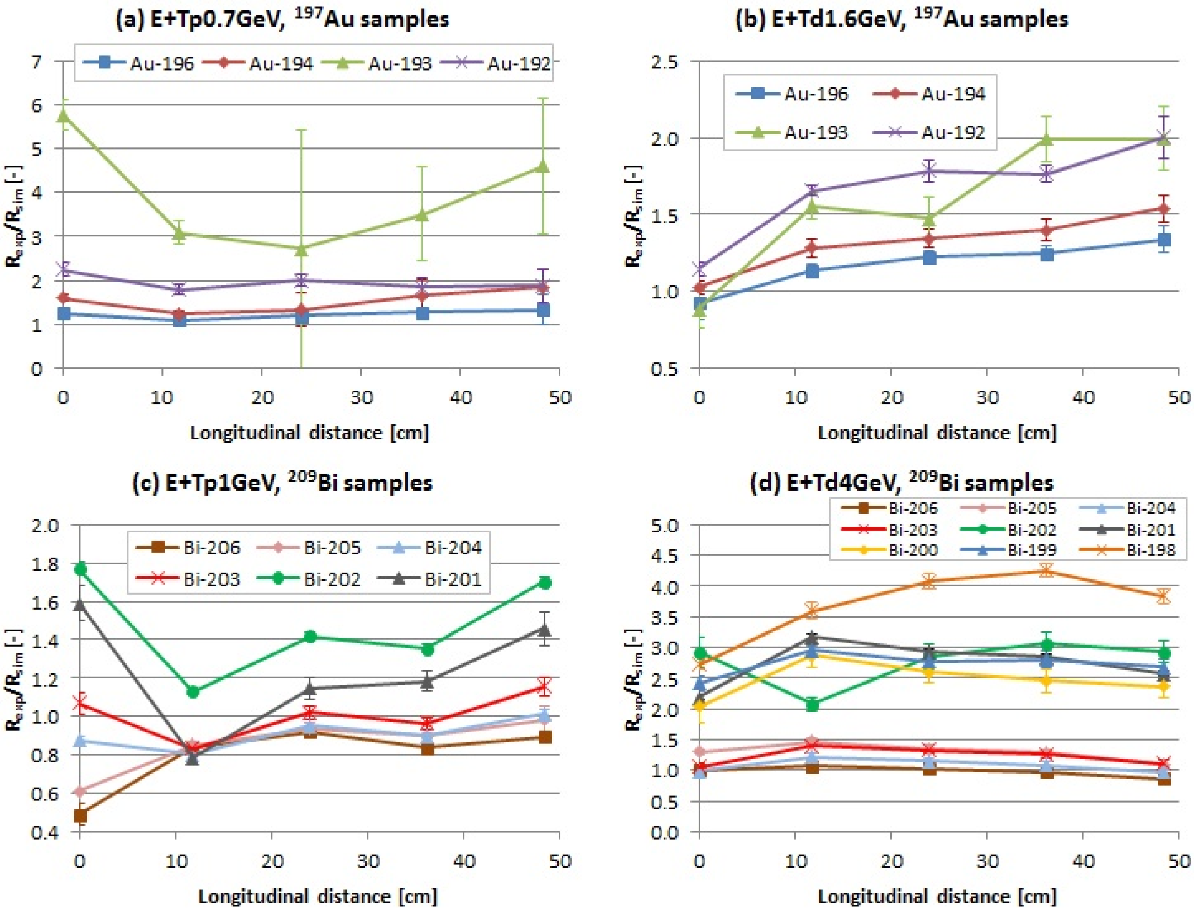

Figure 21: Experiment-to-simulation reaction rate ratios for isotopes of Au and Bi produced in ^{197}Au and ^{209}Bi samples at a radial distance r for selected E+T experiments. (a) E+Tp0.7GeV, ^{197}Au samples, r = 3 cm, (b) E+Td1.6GeV, ^{197}Au samples, r = 3 cm, (c) E+Tp1GeV, ^{209}Bi samples, r = 6 cm, (d) E+Td4GeV, ^{209}Bi samples, r = 3 cm.

mostly present in the beam passage region and close to it. The importance of these reactions and asymmetry fades away with growing radial distance in favor of neutron-induced reactions. It means that samples close to the primary beam passage are sensitive to the precision of the accelerator beam settings more than samples located outside this region. The disagreements of experimental and simulated data in the region close to the beam passage, therefore, indicate that critical factor for the experiments and the consequent simulation benchmarks is the precision of the accelerator beam settings and primary beam geometry description. For this reason, I focused on the investigation of the regions close to the beam passage and study of the beam settings influence in the QUINTA setup experiments, which are dealt with in the following chapters.

The investigation of the E+T experiments is still ongoing, and both the experimental and simulated data will be further analysed in the framework of our group at NPI. A publication in a peer-reviewed journal of the new E+T systematics is being expected in the future.

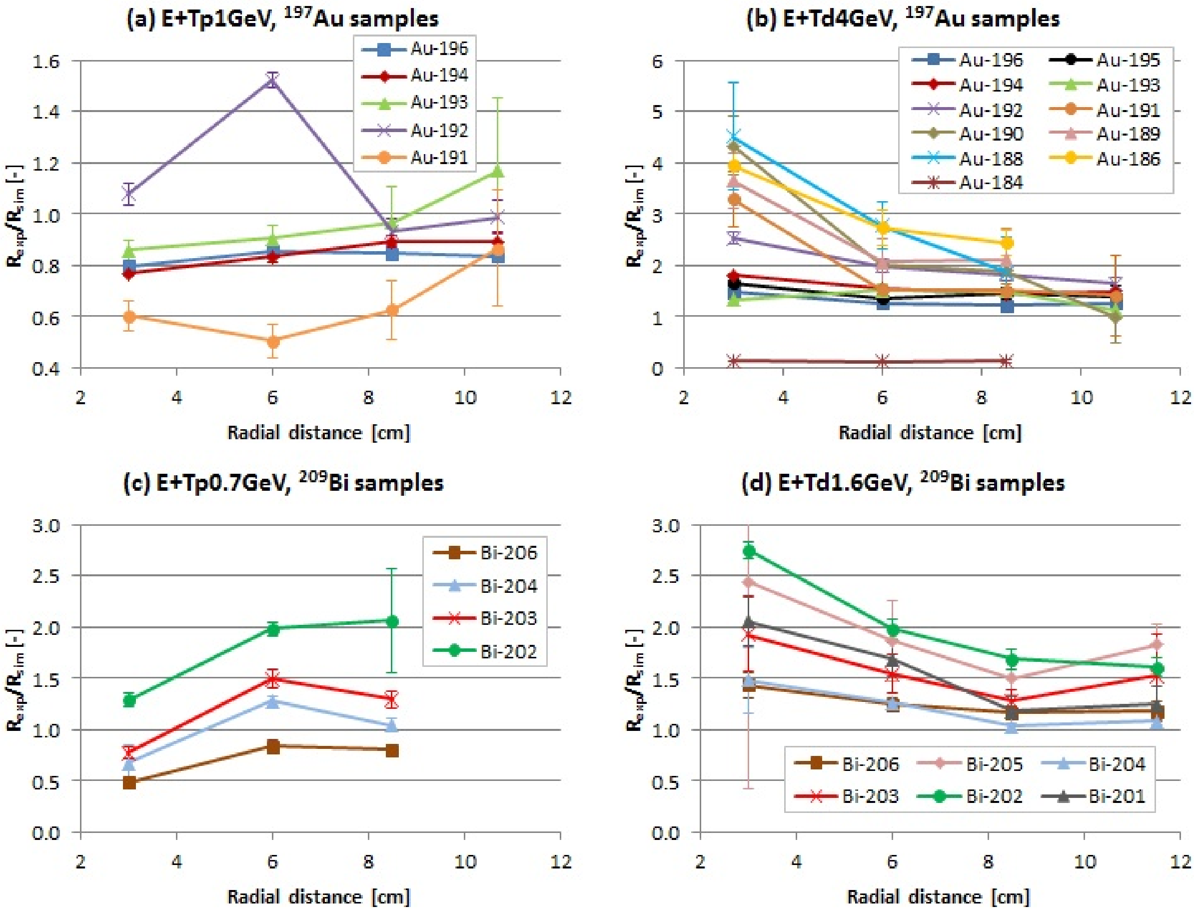

Figure 22: Experiment-to-simulation reaction rate ratios for isotopes of Au and Bi produced in ^{197}Au and ^{209}Bi samples at a longitudinal distance l = 11.8 cm for selected E+T experiments. (a) E+Tp1GeV, ^{197}Au samples, (b) E+Td4GeV, ^{197}Au samples, (c) E+Tp0.7GeV, ^{209}Bi samples, (d) E+Td1.6GeV, ^{209}Bi samples.

4 Experiments with subcritical assembly QUINTA

From a wide range of researches conducted with the QUINTA setup, I focused mainly on the analysis of the aftermath of proton and deuteron reactions with target nuclei, and neutron and proton production in areas close to the centre of the target strongly affected by the primary beam. The neutron, proton and other particle fields are very dependent on the particular beam geometry in these areas. I analysed experimental data and investigated the usage of the Monte Carlo simulation code MCNPX 2.7.0 in the experiments carried out in November 2013, December 2013, November 2015, December 2016 and June 2017 (see section 1.3.4). Description and results of the research are given in this chapter. Some results were also published in [153, 154].

I participated in almost all of the QUINTA experiments at Phasotron during which I also helped with preparation, organisation, activation measurements and data evaluation. I did not participate in the QUINTA experiments at Nuclotron, but I collected measured spectra from the two selected experiments, and all the results presented in this chapter were evaluated and analysed by myself.

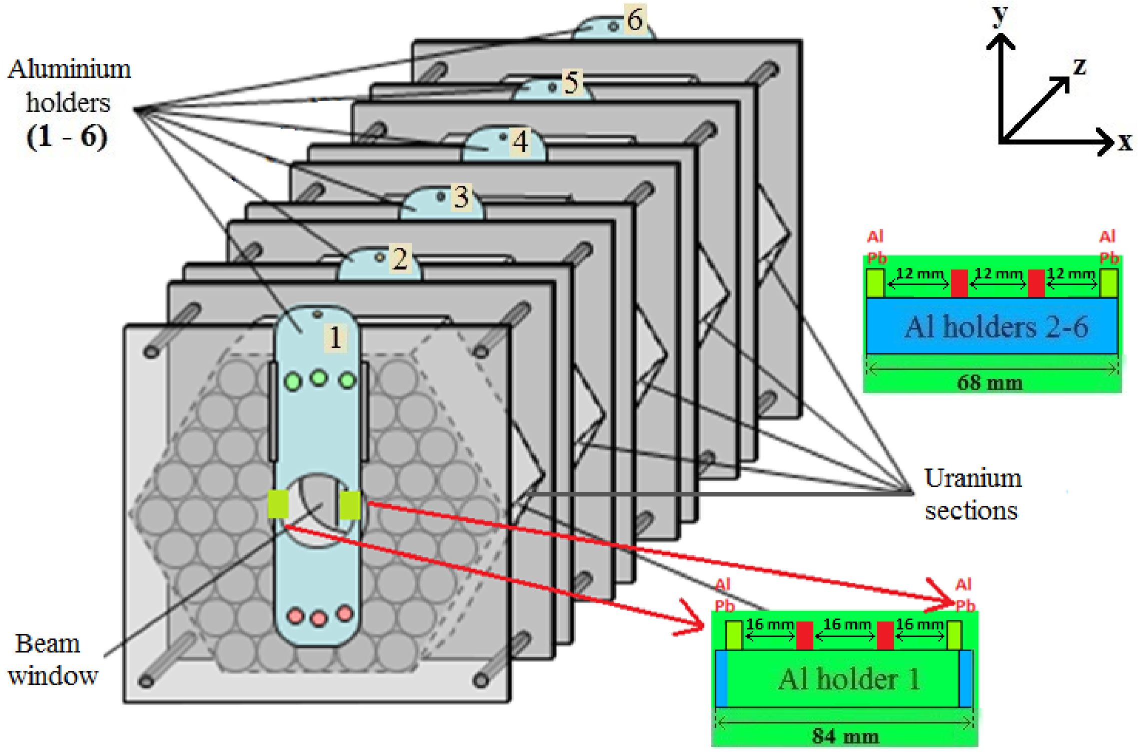

Figure 23: Placement of ^{27}Al and ^{nat}Pb samples in the d4GeV and d8GeV experiments at QUINTA. The samples were placed in front of the aluminium plates, one on another, while the ^{27}Al samples lied on the ^{nat}Pb samples and the ^{nat}Pb samples lied on the aluminium plates. The width of the first plate (the one in the very front) is 84 mm. The width of the other plates is 68 mm. Red rectangles symbolise sample positions of the experiment at Phasotron (CC) held in December 2016 (see section 4.1.2). The distance between the samples on the first plate and the very edge of the first plate is 2 mm [93].

4.1 Description and approach

4.1.1 Experiments at Nuclotron

One of the experiments at Nuclotron, where also the investigation of the central region was performed, was held in November 2013 (d4GeV) and the QUINTA setup was irradiated by a deuteron beam with a total kinetic energy of 4 GeV. The second experiment at Nuclotron I was focused on was held in December 2013 (d8GeV) and the QUINTA setup was irradiated by a deuteron beam with an energy of 8 GeV. In both cases, activation samples of aluminium and lead were irradiated. The samples were placed on the left and right sides on each aluminium plate according to Fig. 23. The particle flux is supposed to be different on the left and right side because QUINTA was tilted from the source beam axis by 2 degrees during each experiment (see Fig. 24).

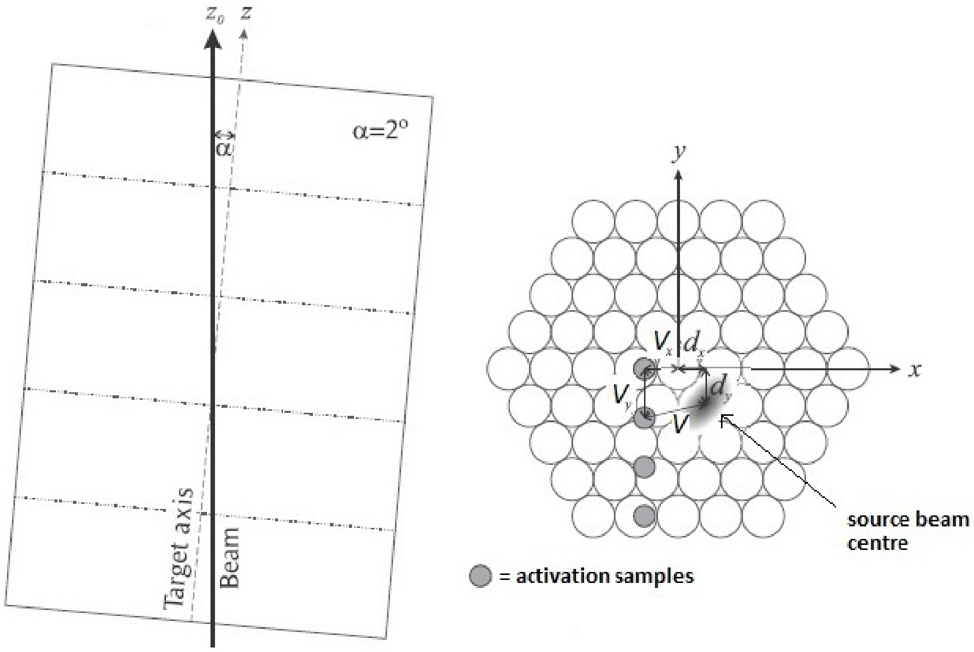

$$V = \sqrt{(V_x - d_x)^2 + (V_y - d_y)^2}, \quad Z \approx Z_0$$

Figure 24: 2-degree QUINTA rotation from the source beam axis (top QUINTA view, left) and position of the source beam centre depending on accelerator settings (front QUINTA view, right). α represents the rotation between the beam axis z_0 and target axis z. V_x and V_y are the coordinates of an activation sample position on the target horizontal axis x and vertical axis y, respectively. d_x and d_y are the beam centre coordinates on given aluminium plates on x and y axes, respectively. V is the radial distance between the activation sample and source beam centre [122].

The beam characteristics of the QUINTA Nuclotron experiments are given in Tab. 2. The coordinates of the source beam centre and spatial beam profile on the setup entrance were measured by SSNTD in case of the Nuclotron experiments. The integral number of deuterons impinging on the target was 2.12(3)E13 for the d4GeV experiment and

6.11(8)E12 for the d8GeV experiment. The numbers were determined using aluminium activation monitors and ^{27}Al(d,3p2n)^{24}Na reaction. The irradiation time was 26 hours for the d4GeV experiment and 27 hours for the d8GeV experiment.

The dimensions of all the samples were 8×20 mm^2. The average weights of the samples in the d4GeV experiment were 0.20 g for ^{27}Al and 0.51 g for ^{nat}Pb and in the d8GeV experiment 0.47 g for ^{27}Al and 0.93 g for ^{nat}Pb. The weights of the individual samples are listed in Tab. 25 in Appendix D.

The distances of the samples from the beam are given in Tab. 3.

Table 2: Beam characteristics of the QUINTA Nuclotron experiments. d_x and d_y are the coordinates of the source beam centre on the QUINTA entrance. FWHM$_x$ and FWHM$_y$ are the full widths at half maximums of the 2D Gaussian profile on axes x and y on the entrance.

Experiment	d_x [cm]	d_y [cm]	FWHM$_x$ [cm]	FWHM$_y$ [cm]
d4GeV	1.4	−1.6	2.7	1.5
d8GeV	−0.2	−0.7	2.3	1.1

Table 3: Distances between the left and right side samples and beam, calculated according to Fig. 24, for the Nuclotron experiments. V is the distance of a sample from the beam located at a longitudinal distance l in QUINTA.

Experiment	d4GeV		d8GeV	
l [cm]	V [cm], left	V [cm], right	V [cm], left	V [cm], right
1.50	4.99	3.29	3.21	4.53
14.75	3.83	2.99	2.00	4.18
27.85	3.41	3.39	1.58	4.64
40.95	3.02	3.79	1.19	5.09
54.05	2.64	4.22	0.86	5.55
67.15	2.30	4.64	0.70	5.99

The reason why aluminium and lead samples were chosen lies in the characteristics of reactions induced by interactions of neutrons, protons and deuterons with aluminium and lead. It is expected that studying of the ^{24}Na nuclei production in ^{27}Al by the activation techniques can provide us with the information about sum of neutron + proton + deuteron flux because ^{24}Na can arise from reactions with neutrons, protons and deuterons: ^{27}Al(n,x)^{24}Na, ^{27}Al(p,x)^{24}Na and ^{27}Al(d,x)^{24}Na. On the other hand, studying of the ^{205}Bi and ^{206}Bi nuclei production in ^{nat}Pb gives the information about sum of proton + deuteron flux because ^{205}Bi and ^{206}Bi can arise only from reactions with protons and deuterons: ^{nat}Pb(p,x)$^{206(205)}$Bi and ^{nat}Pb(d,x)$^{206(205)}$Bi. It is physically impossible for ^{205}Bi or ^{206}Bi to be created by reactions with neutrons because of lead and bismuth proton numbers.

4.1.2 Experiments at Phasotron

There were three irradiations of ^{59}Co and ^{nat}Pb samples situated close to the beam passage by the 660 MeV proton beam of Phasotron (held in November 2015, December 2016 and June 2017). The positions of the samples on the left and right side were identical to the case of the Nuclotron experiments (except for the positions of the December 2016 Phasotron experiment) as described in section 4.1.1, but instead of aluminium samples, cobalt samples were used. The difference between the Phasotron experiments is that in the December 2016 irradiation the samples were put even closer to the central axis (exactly between the samples positions of the other experiments, see Fig. 23), and that the June 2017 irradiation was performed without the lead shielding surrounding QUINTA (see section 1.3.4).

In the following text, let us distinguish the November 2015 experiment by a symbol "UA" (= Usual Arrangement), the December 2016 experiment by a symbol "CC" (= Closer to Centre) and the June 2017 experiment by a symbol "WS" (= Without Shielding).

The beam characteristics of the QUINTA Phasotron experiments are given in Tab. 4. The coordinates of the source beam centre and spatial beam profile on the setup entrance were measured by the ionisation chamber. The integral number of protons impinging on the target was 3.38(40)E15 for the UA experiment, 4.84(31)E15 for the CC experiment and 1.43(15)E15 for the WS experiment. The numbers were determined using aluminium activation monitors and ^{27}Al(p,3pn)^{24}Na reaction. The irradiation time was 5 hours. Unfortunately, the coordinates of the source beam centre and FWHM given in Tab. 4 are missing for the WS experiment due to dosimetry difficulties. Therefore simulations for the WS experiment could not be performed.

Table 4: Beam characteristics of the QUINTA Phasotron experiments. d_x and d_y are the coordinates of the source beam centre on the QUINTA entrance. $FWHM_x$ and $FWHM_y$ are the full widths at half maximums of the 2D Gaussian profile on axes x and y on the entrance.

Experiment	d_x [cm]	d_y [cm]	$FWHM_x$ [cm]	$FWHM_y$ [cm]
UA	1.31	0.76	3.40	3.97
CC	1.40	0.67	3.11	3.60

The production of ^{57}Co, ^{58}Co and ^{60}Co was studied. ^{57}Co and ^{58}Co arise from the reactions with neutrons: ^{59}Co(n,2n)^{58}Co, ^{59}Co(n,3n)^{57}Co, protons: ^{59}Co(p,x)$^{58(57)}$Co and deuterons: ^{59}Co(d,x)$^{58(57)}$Co (deuteron contributions to reaction rate R were negligible for the Phasotron experiments, and therefore they could be neglected, see section 4.3.1). ^{60}Co arises from the reaction with neutrons: ^{59}Co(n,γ)^{60}Co. The production of ^{205}Bi and ^{206}Bi in the ^{nat}Pb activation samples was also studied (see section 4.1.1). The dimensions of the cobalt samples were 8×25 mm^2 and of the lead samples 8×20 mm^2.

The average weights of the samples in the UA experiment were 1.90 g for ^{59}Co and 0.51 g for ^{nat}Pb, in the CC experiment 1.84 g for ^{59}Co and 2.80 g for ^{nat}Pb, and in the WS experiment 1.85 g for ^{59}Co and 2.80 g for ^{nat}Pb. The weights of the individual samples are listed in Tab. 26 in Appendix D.

The distances of the samples from the beam are given in Tab. 5.

Table 5: Distances between the left and right side samples and beam, calculated according to Fig. 24, for the Phasotron experiments. V is the distance of a sample from the beam located at a longitudinal distance l in QUINTA.

Experiment	UA		CC	
l [cm]	V [cm], left	V [cm], right	V [cm], left	V [cm], right
1.50	4.70	3.06	2.23	0.72
14.75	3.47	2.72	1.62	0.85
27.85	3.02	3.17	1.22	1.19
40.95	2.59	3.61	0.88	1.59
54.05	2.15	4.06	0.68	2.02
67.15	1.73	4.51	0.76	2.45

4.1.3 Simulations

After the reaction rates of production of ^{24}Na, ^{57}Co, ^{58}Co, ^{205}Bi and ^{206}Bi were evaluated, simulations were also carried out. The simulations of neutron, proton (and also deuteron flux in case of the QUINTA Nuclotron experiments) in aluminium and cobalt samples, and simulations of proton (and deuteron) flux in lead samples were performed in MCNPX 2.7.0 (see section 2.3). The cross-sections for convolution with the particle flux were extracted from TALYS 1.6. Considering that TALYS calculates the cross-sections up to the energy of 1 GeV, cross-sections above 1 GeV needed for the 4 GeV and 8 GeV Nuclotron experiments were extrapolated by cross-sections calculated with MCNPX 2.7.0 using the INCL4.2 model (see an example in Fig. 25). I also compared the simulated reaction rates to reaction rates using exponential extrapolation of the cross-sections greater than 1 GeV, and even to reaction rates without the contributions from the particles of energy greater than 1 GeV. The reaction rates differed up to 7 % in comparison with reaction rates using the exponential extrapolation, and up to 8 % in comparison with reaction rates when the contributions greater than 1 GeV were excluded. The beam parameters for the MCNPX input files were taken according to Tabs. 2 and 4.

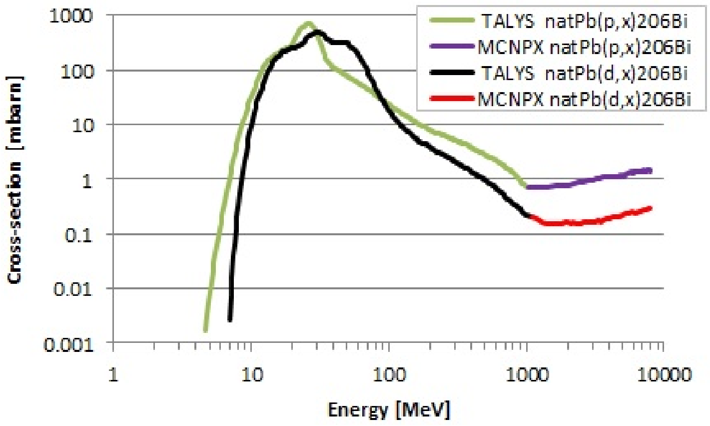

Figure 25: Cross-sections of ^{nat}Pb(p,x)^{206}Bi and ^{nat}Pb(d,x)^{206}Bi reactions extracted from TALYS 1.6 and MCNPX 2.7.0 and connected together.

4.1.4 Neutron flux determination

For the UA experiment, the author suggests determining an approximate neutron flux in the energy interval from 10.63 MeV (threshold of ^{59}Co(n,2n)^{58}Co reaction), alternatively from 19.35 MeV (threshold of ^{59}Co(n,3n)^{57}Co reaction), by the following method [155, 156].

Because the deuteron contributions to reaction rates of ^{57}Co and ^{58}Co production were not more than 0.2 % and the deuteron contributions to reaction rates of ^{205}Bi and ^{206}Bi production were less than 1.3 % (see section 4.3.1), it was possible to neglect the deuteron contributions and assess the experimental neutron flux Φ_n in positions where the samples were placed. The proton flux Φ_p is then given by

$$\phi_p = \frac{R(^{206}Bi)}{\sigma_p^{ef}(^{206}Bi)} \tag{17}$$

where R(^{206}Bi) is the experimental reaction rate for ^{206}Bi production and σ_p^{ef}(^{206}Bi) is the effective cross-section of ^{nat}Pb(p,x)^{206}Bi reaction calculated as

$$\sigma_p^{ef}(^{206}Bi) = \frac{\sum \sigma_i^p \phi_i^p}{\sum \phi_i^p} \tag{18}$$

where σ_i^p is the partial cross-section of ^{nat}Pb(p,x)^{206}Bi reaction for a given energy interval i calculated with TALYS 1.6 and Φ_i^p is the flux of protons for the interval i simulated with MCNPX 2.7.0.

Because the cobalt and lead samples were situated in the same positions inside QUINTA and thus the proton spectra can be considered identical for the cobalt and lead samples, one can write

$$R_p(^{58}Co) = \sigma_p^{ef}(^{58}Co) \cdot \phi_p \tag{19}$$

where R$_p$(^{58}Co) is the reaction rate and σ_p^{ef}(^{58}Co) is the effective cross-section of ^{59}Co(p,x)^{58}Co reaction.

The reaction rate R$_n$(^{58}Co) for ^{59}Co(n,2n)^{58}Co reaction is given by

$$R_n(^{58}Co) = R(^{58}Co) - R_p(^{58}Co) \tag{20}$$

where R(^{58}Co) is the experimental reaction rate for ^{58}Co production. Then the experimental neutron flux Φ_n can be calculated according to the equation

$$\phi_n = \frac{R_n(^{58}Co)}{\sigma_n^{ef}(^{58}Co)} \tag{21}$$

where σ_n^{ef}(^{58}Co) is the effective cross-section of ^{59}Co(n,2n)^{58}Co reaction.

4.2 Results of the Nuclotron experiments

4.2.1 4 GeV deuteron irradiation (d4GeV)

The experimental reaction rates and experiment-to-simulation ratios of nuclei production of ^{24}Na in the ^{27}Al samples and ^{205}Bi and ^{206}Bi in the ^{nat}Pb samples for the left and right side of the QUINTA aluminium plates are given in Figs. 26 and 28. The numerical values of experimental and simulated reaction rates of the studied isotopes are given in Tabs. 28 and 29 in Appendix E. Both statistical and systematical uncertainties of experimental reaction rates are shown in the graphs.

A very good agreement between the experimental and simulated reaction rates of ^{24}Na production was reached as can be seen in Fig. 26.b (average disagreement was around 23 %). The dominant contributions to simulated reaction rates of ^{24}Na production were from neutrons while for protons the contributions were less than 4 % (see Fig. 27.a) and for deuterons, the average contribution was 0.9 % (see Fig. 27.b). In case of the primary deuteron beam of Nuclotron, protons mostly emerge from spallation reactions of deuterons with target nuclei. On the contrary, one can notice high proton contributions for the ^{57}Co and ^{58}Co production from the UA experiment (Phasotron irradiation with the 660 MeV protons). The proton (deuteron) contributions were calculated from the simulated values as ratios of only proton (deuteron) reaction rates and total reaction rates. In Fig. 28.b, one can notice that the simulated reaction rates of ^{205}Bi and ^{206}Bi production on the left side are underestimated compared to experimental reaction rates. The most significant discrepancy is at the first point, which can be problematic (see section 4.3.1). The simulations in the other locations underestimate the experiment by a factor of 3 on average. The agreement is much better on the right side, where the average disagreement is around 42 %. The contributions to reaction rates from deuterons are not over 6 %.

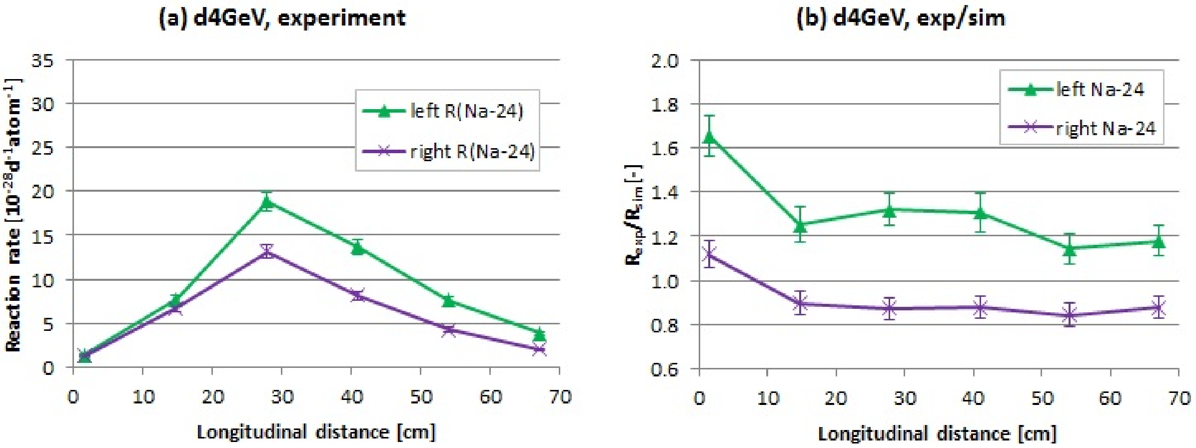

Figure 26: Experimental reaction rates (a) and experiment-to-simulation ratios (b) of production of ^{24}Na for samples on the left and right side (d4GeV).

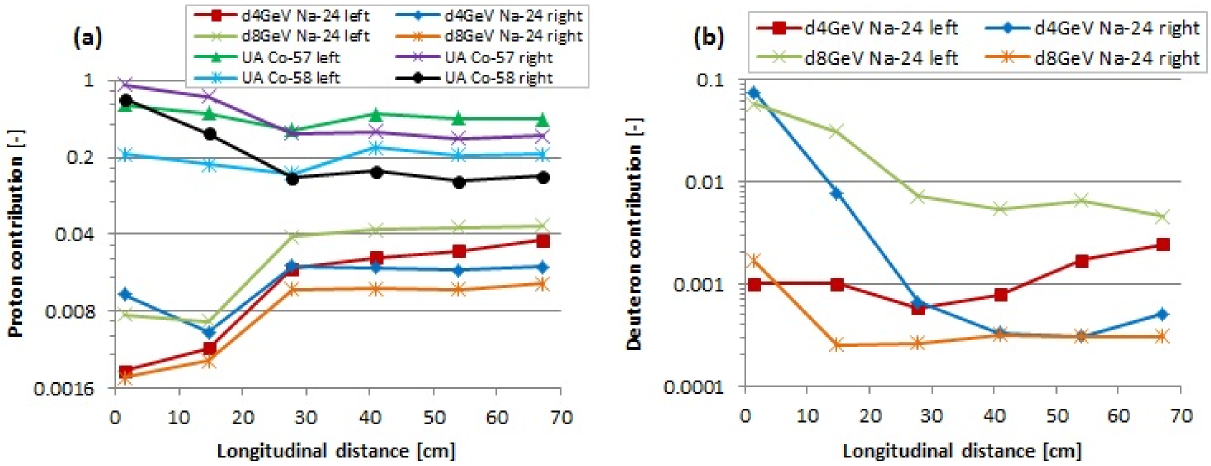

Figure 27: (a) Contribution to reaction rates of ^{24}Na (d4GeV, d8GeV), and ^{57}Co and ^{58}Co (UA) production from reactions induced by protons, (b) Contribution to reaction rates of ^{24}Na production from reactions induced by deuterons (d4GeV, d8GeV).

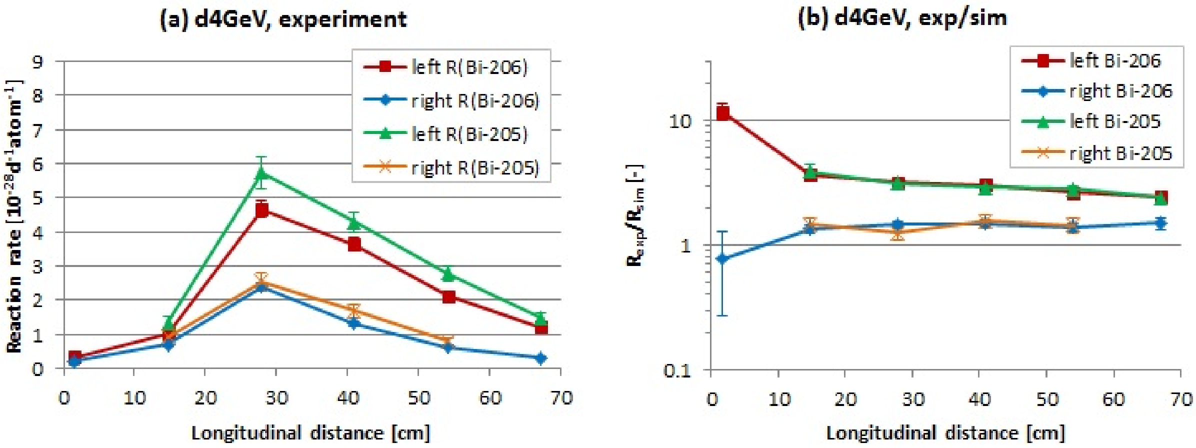

Figure 28: Experimental reaction rates (a) and experiment-to-simulation ratios (b) of production of ^{205}Bi and ^{206}Bi for samples on the left and right side (d4GeV).

4.2.2 8 GeV deuteron irradiation (d8GeV)

The experimental reaction rates and experiment-to-simulation ratios of nuclei production of ^{24}Na in the ^{27}Al samples and ^{205}Bi and ^{206}Bi in the ^{nat}Pb samples are given in Figs. 29 and 30. The numerical values of experimental and simulated reaction rates of the studied isotopes are given in Tabs. 28 and 29 in Appendix E.

In Fig. 29.b of ^{24}Na experiment-to-simulation ratios, one can notice that the simulation gives higher values on the left side in comparison with the d4GeV experiment, where the situation is opposite (see Fig. 26.b). From Fig. 27.b, one can notice that the simulated deuteron contributions for ^{24}Na for the d8GeV experiment are high on the left side compared to the right side (40-times higher on average). This means that the left-side samples were influenced by the position of the primary deuteron beam (Tab. 2) considerably more than the right-side samples. This corresponds to Tab. 3 where one can see shorter distances to the beam axis for the left-side samples. In the d4GeV experiment, the situation is different. The deuteron contributions are higher on the right side for the first two locations (74 and 8-times higher for the first and second locations, respectively). In the third point, the contributions are both around 0.06 % for the left and right sides what corresponds to the similar sample-to-beam axis distance in Tab. 3, and in the last three locations the distance is shorter for the left-side samples, and therefore the deuteron contributions are higher on the left side (4-times on average).

For the ratios of ^{205}Bi and ^{206}Bi (see Fig. 30.b), a good experiment-to-simulation agreement was reached on the left side, where the disagreement was 31 % for ^{206}Bi and 15 % for ^{205}Bi on average. The contributions to simulated reaction rates from deuterons were not over 7 %.

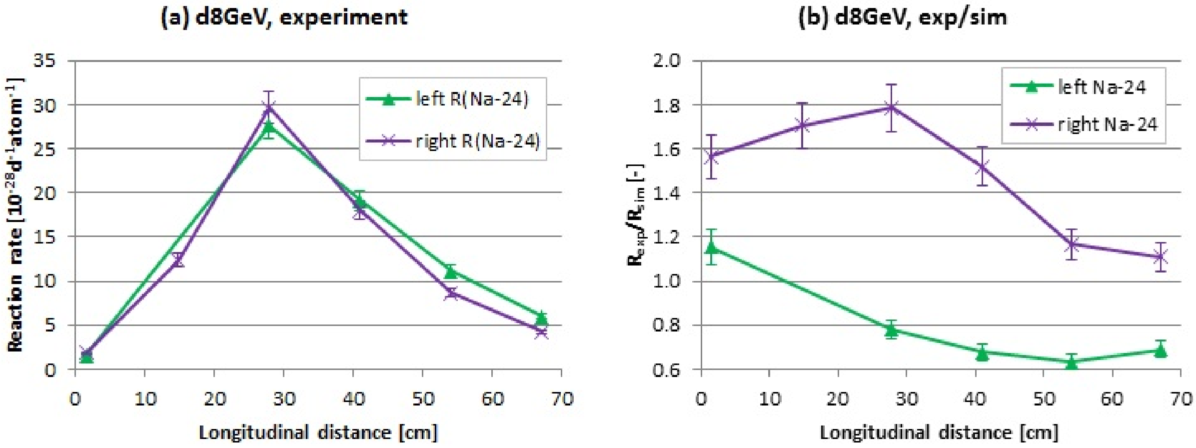

Figure 29: Experimental reaction rates (a) and experiment-to-simulation ratios (b) of production of ^{24}Na for samples on the left and right side (d8GeV).

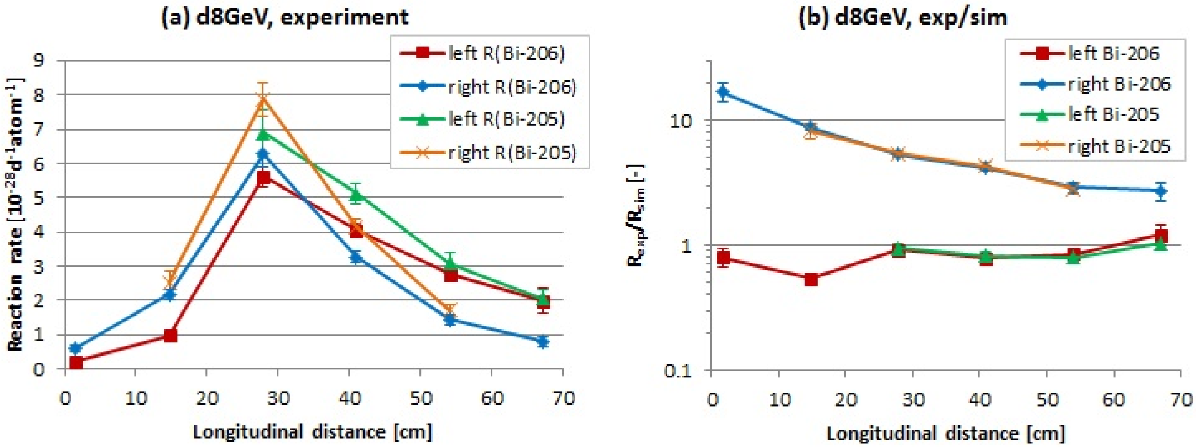

Figure 30: Experimental reaction rates (a) and experiment-to-simulation ratios (b) of production of ^{205}Bi and ^{206}Bi for samples on the left and right side (d8GeV).

The contributions from protons and deuterons to R(^{24}Na) in the d4GeV and d8GeV experiments were less than 5 % for protons and less than 8 % for deuterons (see Fig. 27).

This means that the ^{24}Na production was not influenced in a considerable measure by the primary beam uncertainties. However, one can deduce that there were primary beam uncertainties from the experiment-to-simulation ratios of ^{206}Bi and ^{205}Bi in Fig. 28.b on the left side and Fig. 30.b on the right side. Isotopes of ^{206}Bi and ^{205}Bi are formed only by reactions with protons and deuterons, and therefore they are strongly influenced by the primary beam geometry.

High contributions to R(^{24}Na) from primary deuterons were observed on simulations with MCNPX 2.7.0 by my colleague M. Suchopár [88]. He positioned ^{27}Al samples on the QUINTA holders 2-5 (see Fig. 7) into the direct passage of the primary 2 GeV deuteron beam, and performed simulations. The deuteron contributions to the ^{24}Na production on the holders 2-5 were 33.2 %, 8.4 %, 4.9 % and 2.4 %, respectively. More information about these simulations is given in chapter 5.

4.3 Results of the Phasotron experiments

4.3.1 660 MeV proton irradiation - usual detector positions arrangement (UA)

The experimental reaction rates and experiment-to-simulation ratios of nuclei production of ^{57}Co and ^{58}Co in the ^{59}Co samples and ^{205}Bi and ^{206}Bi in the ^{nat}Pb samples are given in Figs. 31 and 32. The numerical values of experimental and simulated reaction rates of the studied isotopes (including the experimental values of ^{60}Co) are given in Tabs. 30 and 31 in Appendix E. The experimental neutron flux and experiment-to-simulation ratios for the left and right side are given in Fig. 34.

An interesting phenomenon has occurred that the third point of the simulated R(^{58}Co) is higher than the second point of the simulated R(^{58}Co), while for the simulated R(^{57}Co) the situation is opposite (see Fig. 33). The explanation can be derived from chapter 7 and Fig. 64 of simulated neutron flux in the QUINTA uranium part. The gradients around the regions of beginning and end of the second QUINTA uranium section are very steep, and neutron flux (and therefore reaction rate) is extremely sensitive to activation sample longitudinal position.

According to the simulations in Fig. 27.a, the contributions to reaction rates of the ^{57}Co and ^{58}Co production from reactions with protons are high. These high contributions are caused mostly due to primary beam protons from Phasotron (beyond the range of flight of the primary protons, the proton contributions are given by secondary processes), which are substantially represented in the QUINTA central region, and therefore the proton contribution must not be neglected along this region.

The proton contribution for the first point of ^{57}Co and ^{58}Co on the right side reaches almost 90 % and 70 %, respectively. That indicates that, according to simulations, the corresponding ^{59}Co sample was hit by the primary beam in a considerable measure. However, this is not confirmed by the experimental data of ^{205}Bi and ^{206}Bi production from Fig. 32.a. The production of ^{205}Bi and ^{206}Bi in the first position on the right side should, therefore, be much higher than on the left side, which was not observed. This discrepancy corresponds to the experiment-to-simulation ratio in Fig. 32.b for ^{205}Bi and ^{206}Bi on the left side, where the simulation is underestimated by a factor of 13. Isotopes of ^{205}Bi and ^{206}Bi are only produced in proton-induced reactions, and therefore are more sensitive

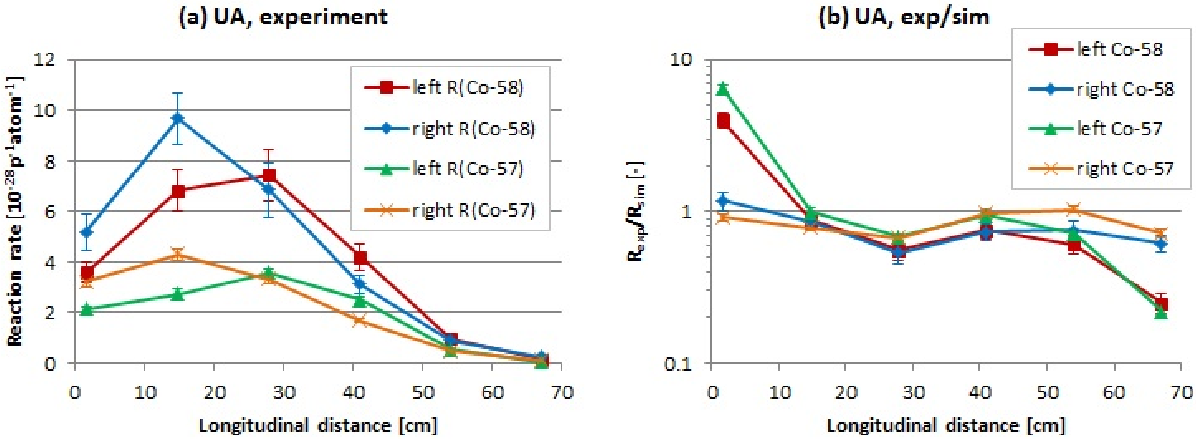

Figure 31: Experimental reaction rates (a) and experiment-to-simulation ratios (b) of production of ^{57}Co and ^{58}Co for samples on the left and right side (UA).

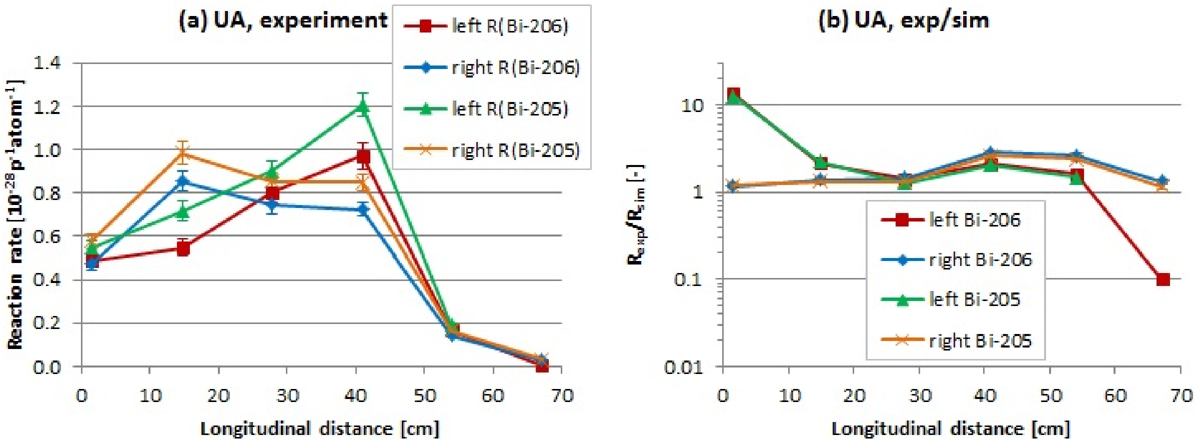

Figure 32: Experimental reaction rates (a) and experiment-to-simulation ratios (b) of production of ^{205}Bi and ^{206}Bi for samples on the left and right side (UA).

to the proton beam settings. This indicates that the beam geometry is not accurately described.

The deuteron contributions (originated predominantly from spallation reactions) to reaction rates of ^{57}Co and ^{58}Co production were not more than 0.2 %. The deuteron contributions to reaction rates of ^{205}Bi and ^{206}Bi production were less than 1.3 %. The deuteron contribution in the Phasotron experiments can be therefore neglected.

The experiment-to-simulation disagreement is high for the first and last points of the cobalt and bismuth isotopes on the left side in Figs. 31.b and 32.b. The edge values are very sensitive not only to inaccuracies of the beam settings but also to systematical and statistical errors. One can notice that the disagreement for the bismuth isotopes (e.g. the simulation of ^{206}Bi underestimates the experiment by a factor of 13 in the first point, and overestimates the experiment by a factor of 10 in the last point) is higher than for the cobalt isotopes (simulation of ^{58}Co underestimates the experiment by a factor of 4 in the first point, and overestimates the experiment by a factor of 4 in the last point). This

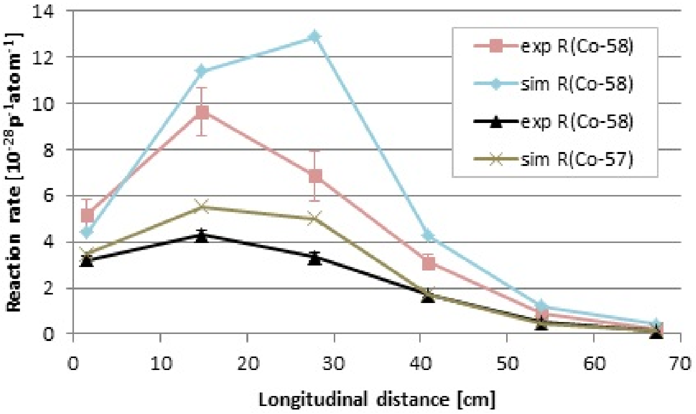

Figure 33: Experimental and simulated reaction rates of production of ^{57}Co and ^{58}Co for samples on the right side (UA).

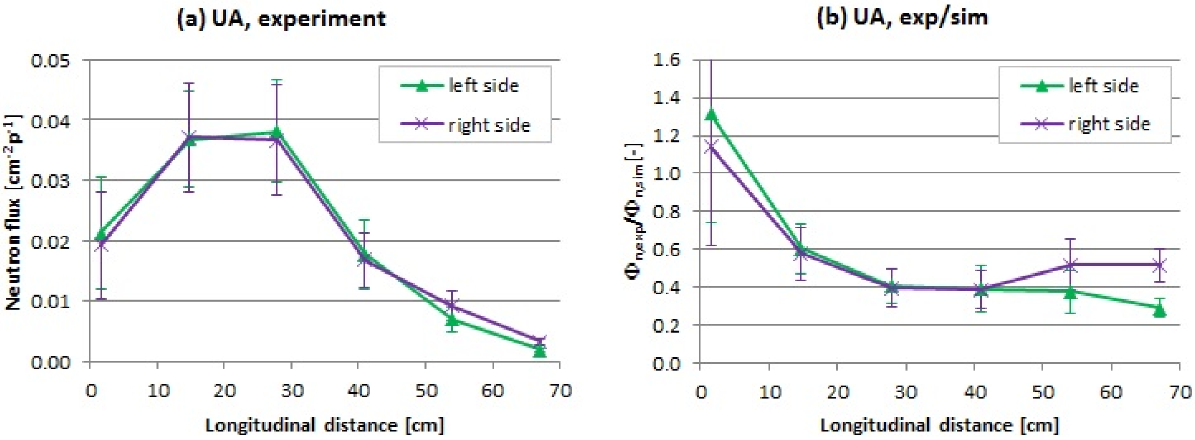

Figure 34: Experimental neutron flux (a) and experiment-to-simulation ratios (b) on the left and right side (UA).

indicates a higher sensitivity of the experiment-to-simulation agreement to the primary proton beam because the bismuth production is not influenced by the generated neutrons. This is natural and could be expected. Neutrons are formed in a large area, while protons are dominant only in or near the beam. Thus the production of radionuclides produced only in proton reactions happens only in the case of samples affected by the beam.

From the experimental values of neutron flux in Fig. 34.a, one can notice that the neutron distributions are similar on the left and right side because the neutron field is not too sensitive on the primary beam geometry. The experiment-to-simulation ratios in Fig. 34.b have similar trends. The highest disagreement can be seen in the last point on the left side, where the simulation overestimates the experiment by a factor of 3.5.

4.3.2 660 MeV proton irradiation with activation detectors closer to centre (CC)

The experimental reaction rates and experiment-to-simulation ratios of nuclei production of ^{57}Co and ^{58}Co in the ^{59}Co samples and ^{205}Bi and ^{206}Bi in the ^{nat}Pb samples are given in Figs. 35 and 36. The numerical values (including ^{60}Co) are given in Tabs. 30 and 31 in Appendix E.

From Figs. 35.a and 36.a, one can notice that the experimental values both for cobalt and bismuth production on the right side are relatively high compared to the left side and that there is only a decreasing tendency with greater longitudinal distance. This means that the samples on the right side were hit more by the primary proton beam due to beam centre position and 2-degree QUINTA rotation.

In Fig. 35.b of the experiment-to-simulation ratios of ^{57}Co and ^{58}Co, a good agreement was reached for the first four positions (disagreement for ^{57}Co did not exceed over 13 %), but not for the last two positions, where the simulations underestimate the experiment by a factor of 2.5. The disagreement on the last two positions is higher for the ^{205}Bi and ^{206}Bi case in Fig. 36.b, where the simulations in the last position underestimate the experiment almost by a factor of 6. This is because the cobalt isotopes are also formed by neutron-induced reactions.

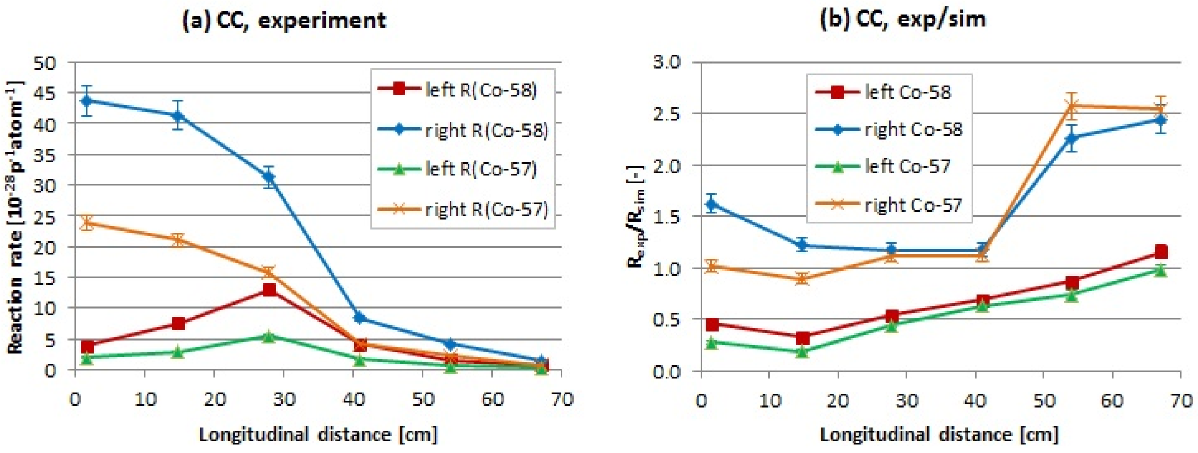

Figure 35: Experimental reaction rates (a) and experiment-to-simulation ratios (b) of production of ^{57}Co and ^{58}Co for samples on the left and right side (CC).

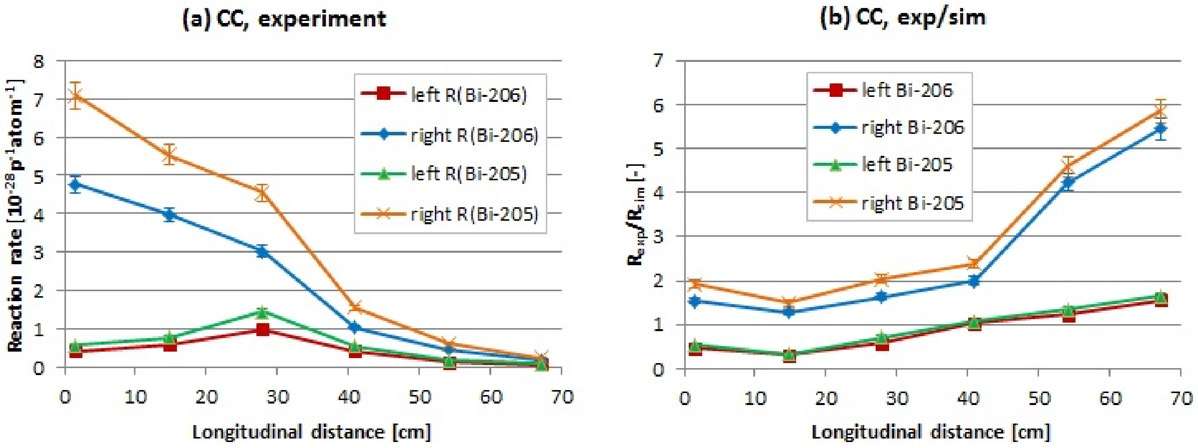

Figure 36: Experimental reaction rates (a) and experiment-to-simulation ratios (b) of production of ^{205}Bi and ^{206}Bi for samples on the left and right side (CC).

4.3.3 660 MeV proton irradiation without lead shielding (WS)

The experimental reaction rates of nuclei production of ^{57}Co, ^{58}Co, ^{205}Bi and ^{206}Bi are given in Fig. 37. The numerical values (including ^{60}Co) are given in Tabs. 30 and 31 in Appendix E. The comparison between the experimental reaction rates of ^{57}Co and ^{60}Co for the UA and WS experiments for the left side is shown in Fig. 38.

In Fig. 38.a, one can notice that there are no significant differences between the experiment with shielding (UA) and without shielding (WS). The effect of the lead shielding proved to be negligible for threshold reactions (threshold of the ^{59}Co(n,3n)^{57}Co reaction is 10.63 MeV, differences are mostly caused due to different beam settings). The shielding effect is more critical for non-threshold reactions, like (n,γ), as shown in Fig. 38.b, where one can notice clearly higher values of ^{60}Co production for the experiment with shielding. Mostly low-energy neutrons after moderation return to the setup in the case of the lead shielding.

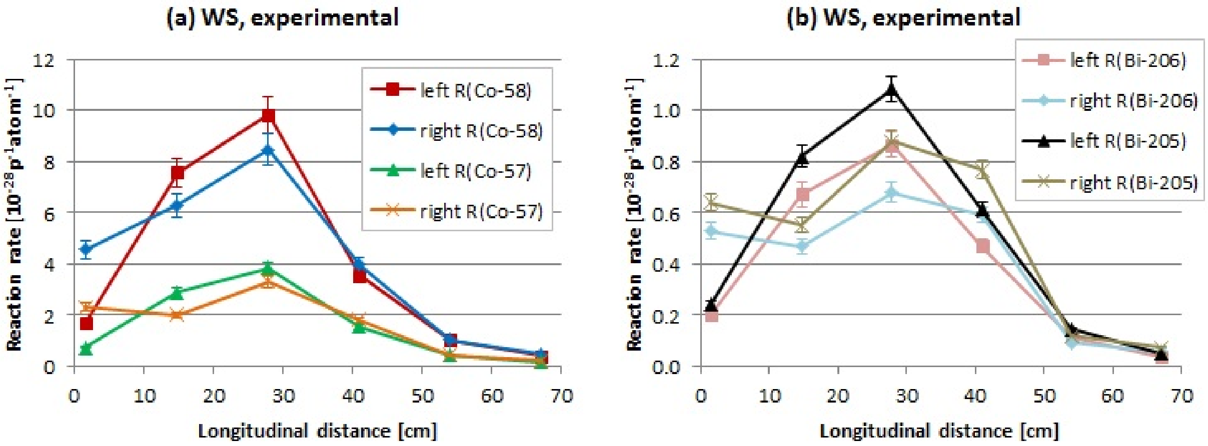

Figure 37: Experimental reaction rates of production of ^{57}Co, ^{58}Co (a) and ^{205}Bi, ^{206}Bi (b) for samples on the left and right side (WS).

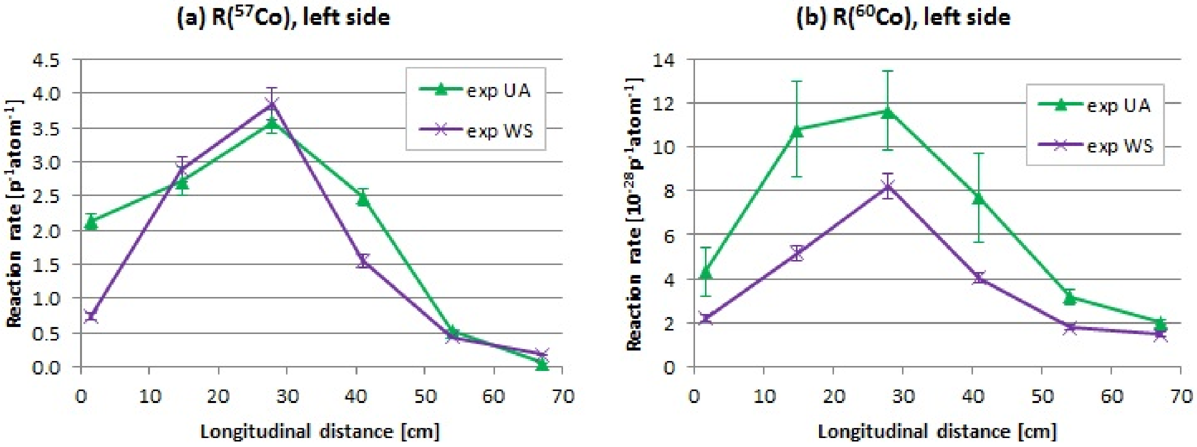

Figure 38: Experimental reaction rates of ^{57}Co (a) and ^{60}Co (b) production for the UA and WS experiments for samples on the left side.

4.4 Summary of the QUINTA results

As was assumed, the results of this chapter show that the agreement between experimental data and simulations in the central region of the QUINTA setup is very sensitive to the beam accelerator settings. The agreement was relatively good especially for simulations of neutron field in the Nuclotron experiments (^{27}Al activation detectors), where the average disagreement was around 33 %. The agreement was worse for the Phasotron case (^{59}Co activation detectors), where simulations can be used to some extent, but one has to worry especially of the edge positions. It has to be noted that reaction rates of the studied radionuclides for neutron field characterisation are also influenced by proton and deuteron contributions to the reaction rates. Therefore while using these reaction rates for characterisation of neutron field, neutron field is more precisely characterised in more remote QUINTA radial positions, where neutron contribution to reaction rates prevail [100].

The agreement of experimental and simulated data of the proton- (and deuteron- in the Nuclotron irradiations) induced reactions proved to be worse than for neutron field, and therefore more sensitive to the accelerator beam settings. In the Phasotron experiments, registered protons are given predominantly by the primary protons (direct hit of activation samples by the protons). Beyond the range of flight of the primary protons, the proton contributions are given by secondary processes.

In the Nuclotron experiments, registered protons are mostly protons emerging from spallation reactions of deuteron beam and target nuclei, and registered deuterons are mostly primary beam deuterons. In general, the activation detectors (registering mostly protons) close to the beam can not too contribute to the benchmarking of the Monte Carlo simulation codes due to the beam geometry inaccuracies. However, they can be beneficial in the study of correction of the beam geometry and influence of its uncertainty on neutron data not close to the beam.

5 Sensitivity analysis of simulation results

In the previous chapters, it was discovered that the results for activation samples close to the central beam axis are very sensitive to the beam accelerator settings, especially to the beam centre coordinates and angle of the QUINTA rotation. It can be supposed, that the 2-degree QUINTA rotation was better determined for the Nuclotron experiments due to a special laser positioning system, which is missing in the Phasotron experimental hall.

I decided to perform the sensitivity analysis of simulation results for the QUINTA UA and CC experiments to assess the measure of sensitivity. The original coordinate d_x (see Fig. 24 and Tab. 4) in the UA experiment was being systematically changed from 0.4 up to 3.0 cm (Figs. 39 and 41), and the beam was being rotated from angle $\alpha = 0°$ up to 4° (Figs. 40 and 42). In the CC experiment, the coordinate d_x was being changed from 1.4 up to 2.4 cm (Figs. 43 and 45), and the beam was being rotated from $\alpha = 0°$ up to 3° (Figs. 44 and 46). The simulations were performed in MCNPX 2.7.0 and reaction rates of ^{58}Co and ^{206}Bi production were evaluated by convolutions with cross-sections extracted from TALYS 1.6, as described in section 2.3. In this chapter, only representative results are shown. More results are given in Appendix F. Note that the angle of beam rotation $\alpha = 2°$ corresponds to the QUINTA 2-degree rotation, and from this position, the beam was being deflected in the plane xz, i.e. up to ±2° in the UA experiment.

From Figs. 39, 41, 43 and 45, where the beam angle was at a constant value of 2° and the beam position was being shifted, one can notice that reaction rate maxima on the left side graphs are being shifted forward (in the direction of greater longitudinal distance) with raising coordinate d_x of the beam centre. On the right side graphs, the situation is the opposite. It is a consequence of the 2-degree QUINTA rotation. However, the maxima shift was not observed on the right-side graphs of the CC experiment (Figs. 43.b and 45.b) where the values of reaction rates are similar for different beam settings. It is caused by the very close location of the samples to the QUINTA central axis, great FWHM of the beam ($\text{FWHM}_x = 3.11$ cm) and that the shift of the coordinate d_x is investigated just for higher values than its original position.

I also investigated the beam parameters sensitivity for activation samples not close to the beam passage. For this purpose, I redefined the studied samples in the MCNPX model of the UA experiment to more remote positions and performed simulations in the same way as mentioned above. The imaginary ^{59}Co and ^{nat}Pb samples were placed 12 cm in the vertical direction above their original positions. The results for ^{58}Co production are given in Figs. 47 and 48. The beam parameters sensitivity is much smaller than in Figs. 39 and 40, where the samples were situated close to the central beam passage. The average change in reaction rate derived from the values in Fig. 47 is around 1.4 % per 1 mm beam shift. The influence of protons can be considered negligible in the positions remote from the primary beam axis, because of absence of the primary protons. Also, the intensity of neutron field in these positions is not very sensitive to the neutron source location changes. The usage of MCNPX 2.7.0 for simulations of QUINTA positions not close to the central beam axis was also demonstrated in paper [100] for ^{59}Co, ^{197}Au and ^{209}Bi activation detectors.

Based on the knowledge that the influence of inaccuracies of beam parameters settings do not affect in considerable measure the neutron production in the QUINTA remote radial positions, it can be concluded that activation detectors not close to the beam can be advantageously used for the simulation codes benchmarking. It can be assumed then that the future BURAN experiments will be suitable for benchmarks considering the fact that in the experiments activation samples will be situated not close to the primary beam passage. To verify this hypothesis, I performed simulations at BURAN irradiated by the 660 MeV proton beam. Cylindrical volumes of 30 mm in diameter and 10 mm in length representing ^{59}Co activation samples were added to the BURAN geometry model into the first air channel in the upward direction to every measurement position, i.e., 20 ^{59}Co volumes were situated 14 cm above the central longitudinal axis in line A (see section 1.3.5). Simulations were performed for BURAN equipped with a lead spallation target of 200 mm in diameter and 1000 mm in length. A beam channel of 100 mm in diameter and 200 mm in length was defined in the lead target front. The coordinates of the beam centre (d_x, d_y) on the BURAN entrance and full widths at half maximum of the 2D Gaussian profile used as input parameters for the simulations were set to $d_x = d_y = 0$ cm and $FWHM_x = FWHM_y = 3.5$ cm (orientation of the axes is identical to the E+T and QUINTA experiments, see Figs. 4 and 24). The coordinate d_x was being changed from 0 up to 0.9 cm. The simulation results for the ^{58}Co production given in Fig. 49 show minimal differences in reaction rates for the considered beam displacements. The average change in reaction rate derived from the given values is around 0.6 % per 1 mm beam shift.

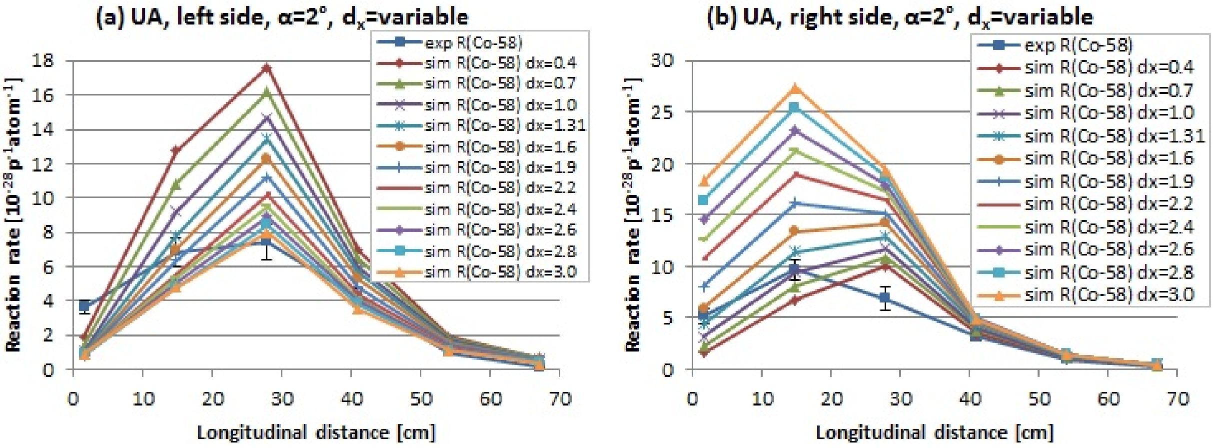

Figure 39: Simulated reaction rates with variable coordinate d_x and angle $\alpha = 2°$ of ^{58}Co production for samples on the left (a) and right (b) side (UA).

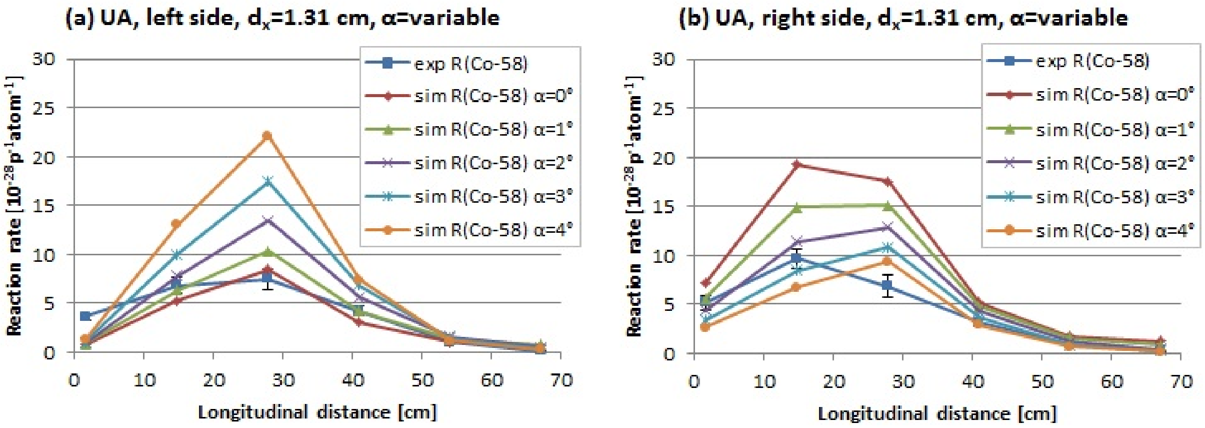

Figure 40: Simulated reaction rates with coordinate $d_x = 1.31$ cm and variable angles α of ^{58}Co production for samples on the left (a) and right (b) side (UA).

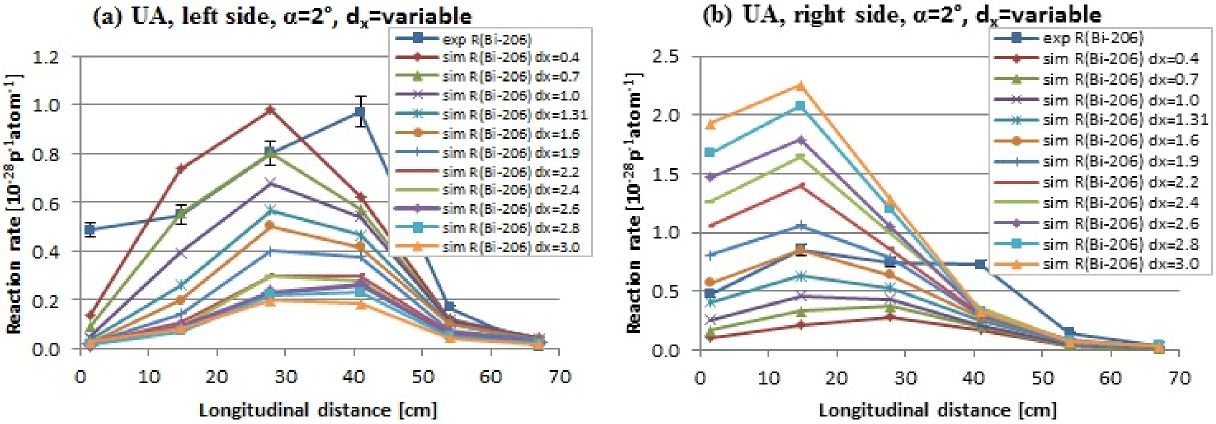

Figure 41: Simulated reaction rates with variable coordinate d_x and angle α = 2° of ^{206}Bi production for samples on the left (a) and right (b) side (UA).

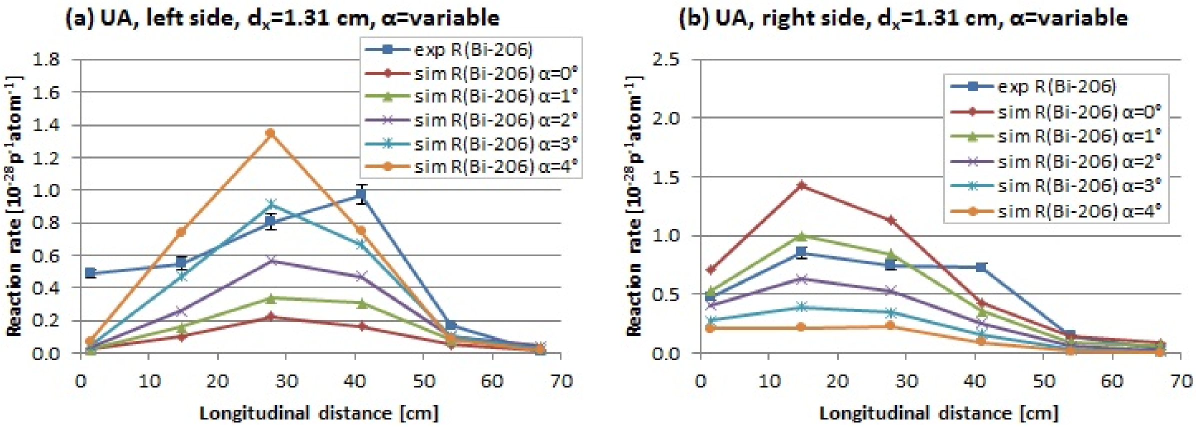

Figure 42: Simulated reaction rates with coordinate $d_x = 1.31$ cm and variable angles α of ^{206}Bi production for samples on the left (a) and right (b) side (UA).

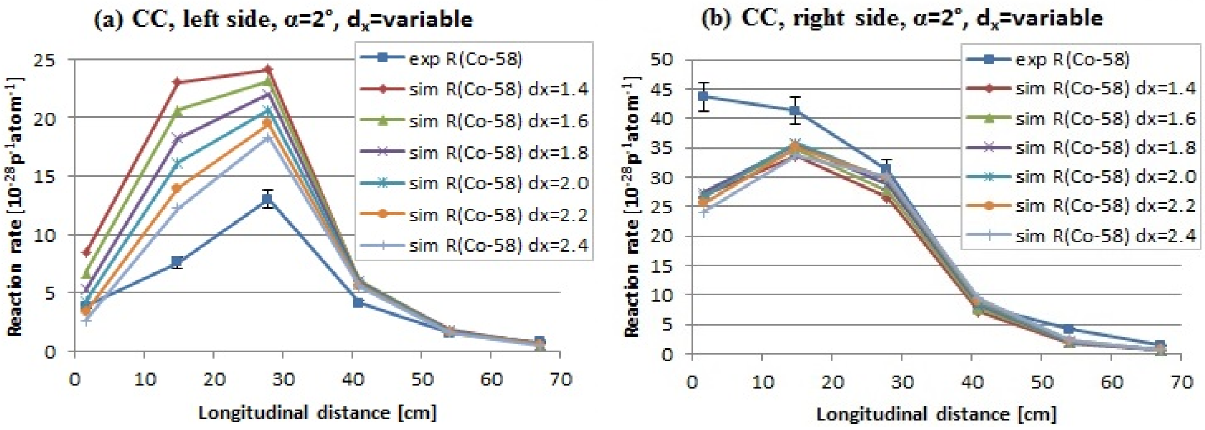

Figure 43: Simulated reaction rates with variable coordinate d_x and angle α = 2° of ^{58}Co production for samples on the left (a) and right (b) side (CC).

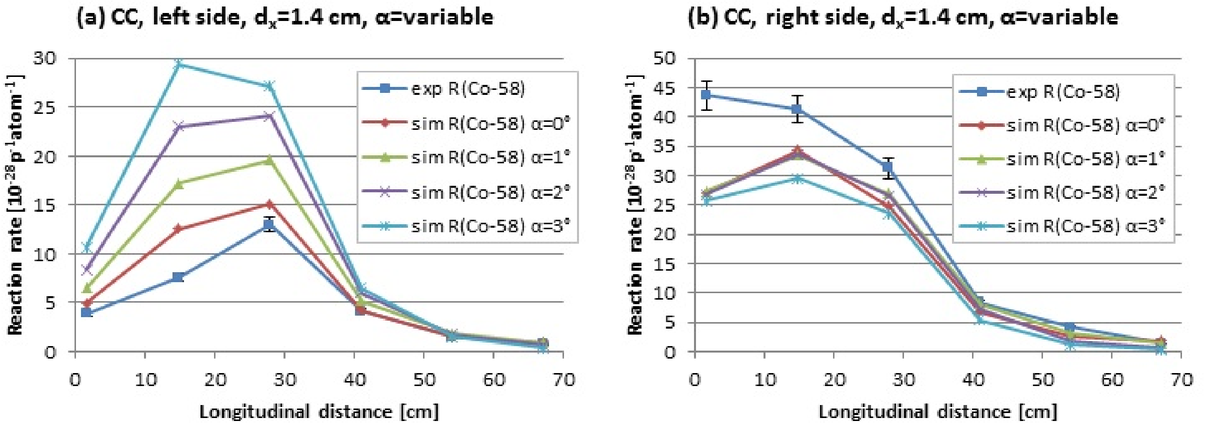

Figure 44: Simulated reaction rates with coordinate d_x = 1.4 cm and variable angles α of ^{58}Co production for samples on the left (a) and right (b) side (CC).

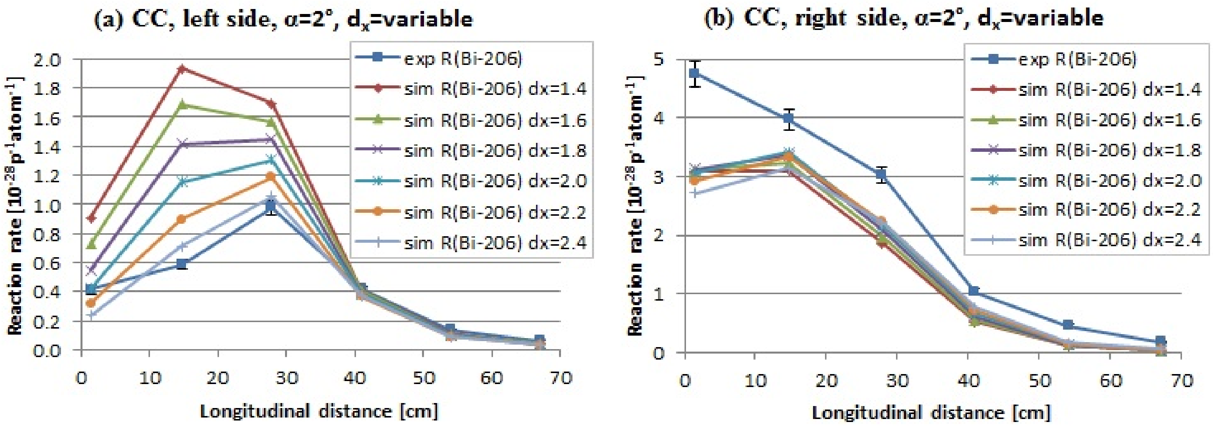

Figure 45: Simulated reaction rates with variable coordinate d_x and angle α = 2° of ^{206}Bi production for samples on the left (a) and right (b) side (CC).

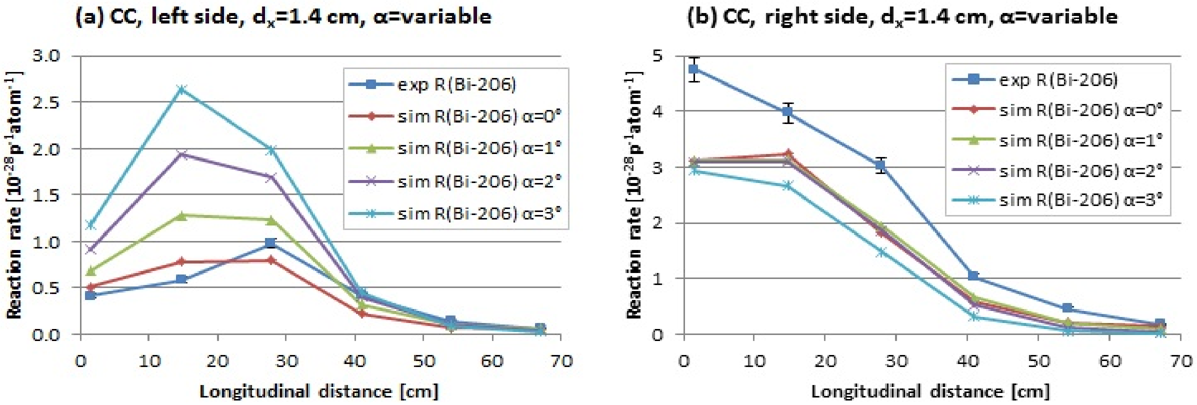

Figure 46: Simulated reaction rates with coordinate d$_x$ = 1.4 cm and variable angles α of ^{206}Bi production for samples on the left (a) and right (b) side (CC).

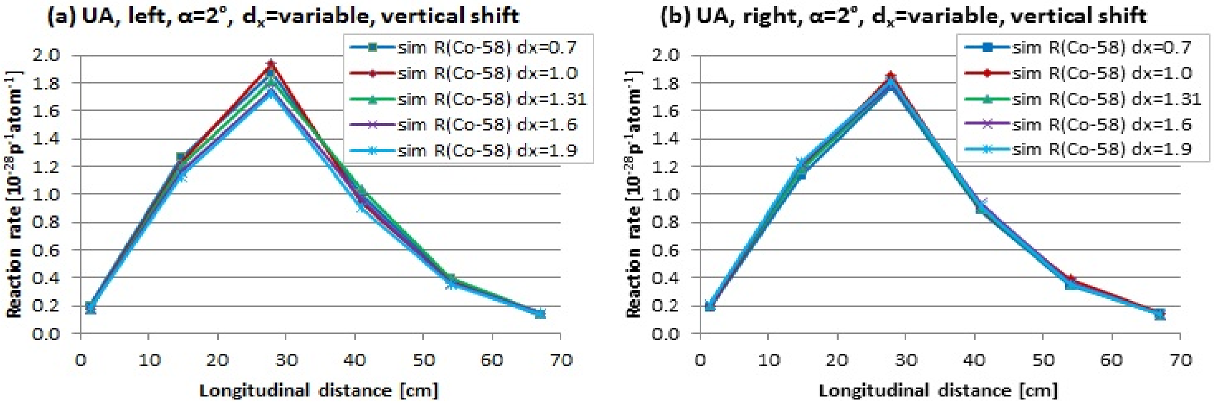

Figure 47: Simulated reaction rates with variable coordinate d$_x$ and angle α = 2° of ^{58}Co production for imaginary samples (vertically shifted 12 cm above their original positions) on the left (a) and right (b) side (UA).

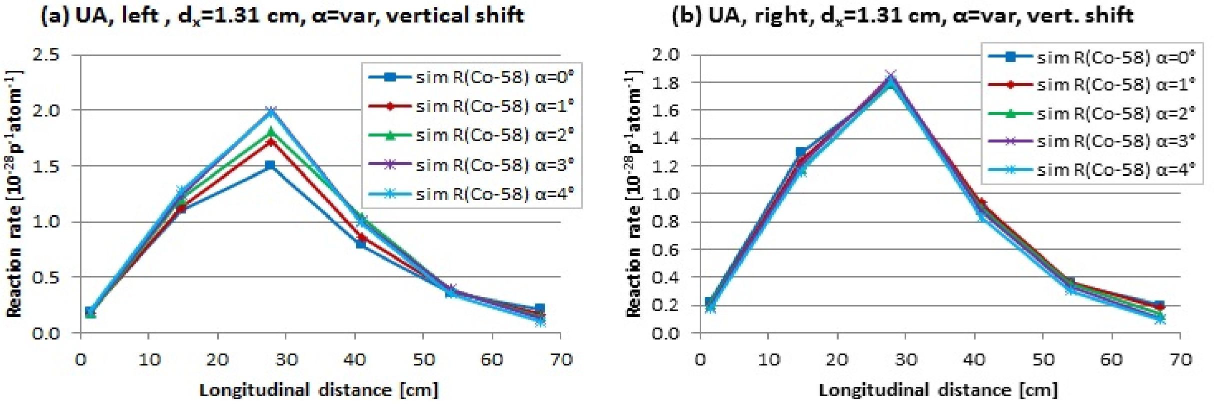

Figure 48: Simulated reaction rates with coordinate d$_x$ = 1.31 cm and variable angles α of ^{58}Co production for imaginary samples (vertically shifted 12 cm above their original positions) on the left (a) and right (b) side (UA).

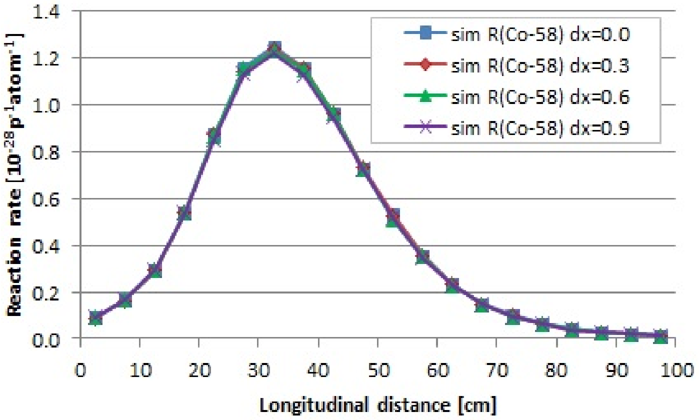

Figure 49: Simulated reaction rates with variable coordinate d_x of ^{58}Co production for imaginary samples in BURAN.

It was demonstrated that the intensity of the mixed neutron-proton field close to the primary beam passage is very sensitive to accelerator beam settings. Monte Carlo simulation benchmarks in this region are, therefore, possible only under the condition of a very accurate primary beam geometry description. The beam proximity influence is more significant for the ^{206}Bi isotope produced in ^{nat}Pb samples than for the ^{58}Co isotope produced in ^{59}Co samples, due to the fact that ^{206}Bi is mostly produced by the primary beam protons.

The results confirm that there exist inaccuracies in the primary beam geometry description, and developing of universal correction factors for the beam settings that could be applied to the experiments in order to make the settings more precise is a challenge for future investigation. The more in-depth research in the problematics can also help to determine beam parameters of the Phasotron WS experiment.

It was proven that the influence of inaccuracies of the beam parameter settings for neutron production is less significant for remote radial positions in the QUINTA assembly. Also, the significance of a possible beam displacement in the future BURAN experiments on the reaction rate activation measurements would be negligible. Therefore, the experiments at BURAN will be beneficial for benchmark studies of Monte Carlo simulation codes.

A sensitivity analysis of QUINTA simulation results using MCNPX 2.7.0 was also carried out by M. Suchopár [88]. The author considered 2 GeV deuteron beam with beam parameters $d_x = d_y = 0$ cm and $FWHM_x = FWHM_y = 1.5$ cm, and beam rotation $\alpha = 0°$. He studied yields of ^{24}Na isotope produced in ^{27}Al activation samples. The samples were positioned in the centre of the aluminium plates 2-5 (see Fig. 7) at radial distances of 0, 4, 8 and 12 cm. The beam was being shifted in 3 mm intervals in horizontal and vertical directions. He discovered that the most significant influence is for the samples positioned on the setup central axis and that the influence becomes less significant for samples placed in greater radial distances. This corresponds to my research. He concluded that the average change in the yield is about 1.5 % per 1 mm beam shift, while for the samples located on the central longitudinal axis it can be up to 5 % per 1 mm beam shift.

6 Subcritical assembly BURAN simulations

The new BURAN assembly is a successor of the subcritical QUINTA setup. Experiments with this setup are supposed to start soon at the Joint Institute for Nuclear Research.

6.1 Description and approach

Since it has not been decided yet which spallation target should be used in the BURAN setup, a study of neutron characteristics of the BURAN setup with different spallation targets irradiated with high-energy proton and deuteron beams was performed using the MCNPX 2.7.0 code. This research can give an insight into which spallation target material would be the most suitable for which kind of the future BURAN experiments, as well as highly contribute to the planning and course strategy of future experiments.

The first experiments with the BURAN assembly are supposed to be performed at the Phasotron accelerator (where BURAN is located at present), which is able to provide us with the 660 MeV proton beam. In the future, when the BURAN experiments at Phasotron are finished, BURAN can also be moved to the Nuclotron accelerator in order to be irradiated with proton and deuteron beams in order of magnitude of GeV energies. Therefore the BURAN characteristics were investigated for three different beams (660 MeV proton beam, 1 GeV proton beam and 1 GeV deuteron beam) impinging three potential spallation targets (depleted uranium, lead and carbon). Some results of this chapter were published in [157].

6.1.1 Measuring points marking system

For purposes of this work, let us mark the measuring points by numbers. In view of the fact that BURAN can be considered homogeneous and symmetrical, it would be useless to mark and perform simulations in all of the 1440 measuring points. Therefore, only a set of representative points of line A was chosen (see Fig. 50 and section 1.3.5).

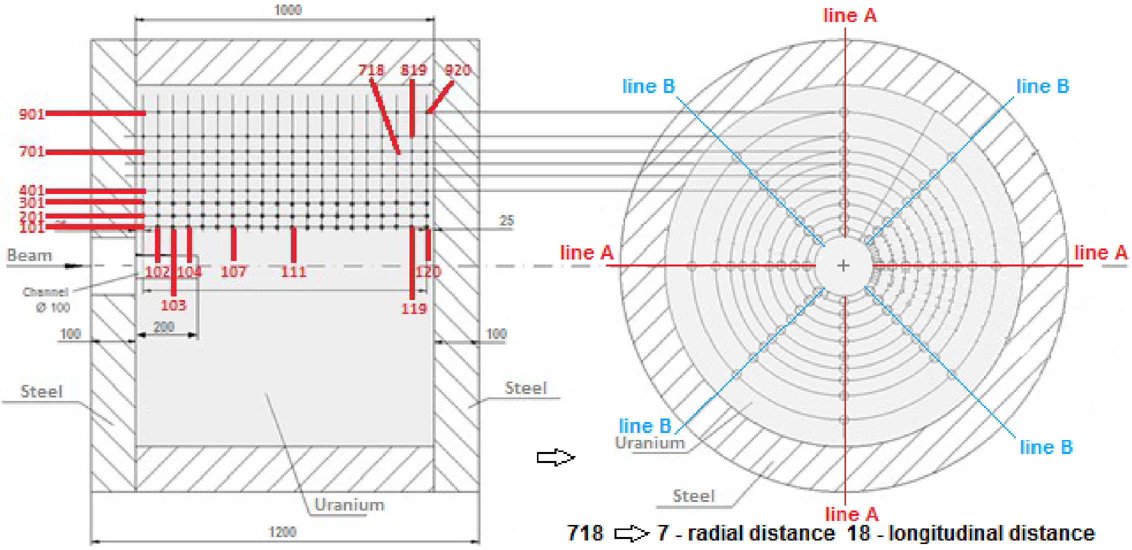

Figure 50: System of the BURAN measuring points marking [93].

In Fig. 50, one can also observe the points marking. Each number related to a point consists of three digits. The first digit represents the placement in a radial direction, while the next two digits in a longitudinal direction. By the term line, we will understand the longitudinal line. For instance, line 1 is formed by points 101 - 120, line 2 by points 201 - 220 etc.

6.1.2 Simulations

All simulations presented here were performed for the 660 MeV and 1 GeV proton beam, and 1 GeV deuteron beam incident perpendicularly on the BURAN setup (see section 1.3.5 and Fig. 11). The coordinates of the source beam centre (d_x, d_y) on the setup entrance were set to $d_x = d_y = 0$ cm and full widths at half maximums on axes x and y of the 2D Gaussian profile were set to $FWHM_x = FWHM_y = 2$ cm. Because dimensions of the possible real spallation targets (depleted uranium, lead, carbon) have not been decided yet, for purposes of the simulations, the dimensions were set to 1000 mm in length and 200 mm in diameter. The target channel was set to 200 mm in length and 100 mm in diameter. The steel shielding behind the spallation target was also taken into consideration. The simulations were performed in the MCNPX 2.7.0 Monte Carlo code (see section 2.3), and the results were normalised to one incident particle.

Average neutron flux (in the air in the measurement channels) in the setup was investigated. Position of neutron flux maximum in every longitudinal A line was determined by fitting the regions with the highest values of neutron flux of the spectra in Figs. 51, 53 and 55 by a polynomial function of degree 6 (e.g. the longitudinal distance region of 7.5 - 47.5 cm was used for the uranium target and 660 MeV proton beam, region 17.5 - 57.5 cm for the lead target and 1 GeV proton beam etc.). The individual values of the longitudinal maximums were calculated using WolframAlpha [158] and Polynomials & Scientific Calculator [159].

Further, energy neutron spectra were simulated. The results are presented for six selected measuring points (105, 110, 115, 305, 310 and 315).

Also, neutron spectra hardness along three longitudinal lines (1, 3 and 6) was investigated. In this thesis, hardness in each measuring point is defined as the ratio of the total flux of neutrons with energies higher than 10 MeV to the total flux of neutrons with energies less than or equal to 10 MeV.

According to MCNPX 2.7.0, the ranges of flights of the impinging particles in the target materials are: 19 cm (depleted uranium, 660 MeV protons), 34 cm (depleted uranium, 1 GeV protons), 25 cm (depleted uranium, 1 GeV deuterons), 31 cm (lead, 660 MeV protons), 55 cm (lead, 1 GeV protons), 41 cm (lead, 1 GeV deuterons), 89 cm (carbon, 660 MeV protons), 162 cm (carbon, 1 GeV protons) and 117 cm (carbon, 1 GeV deuterons).

6.2 Neutron flux results

6.2.1 Uranium target

The graphs of the average neutron flux in the BURAN setup equipped with the uranium target for the 660 MeV proton, 1 GeV proton and 1 GeV deuteron beams are given in Fig. 51. When comparing the neutron flux, one can observe the highest amount of neutrons formed for the 1 GeV deuteron beam, followed by 1 GeV proton beam, and the smallest amount for the 660 MeV proton beam, as it was supposed.

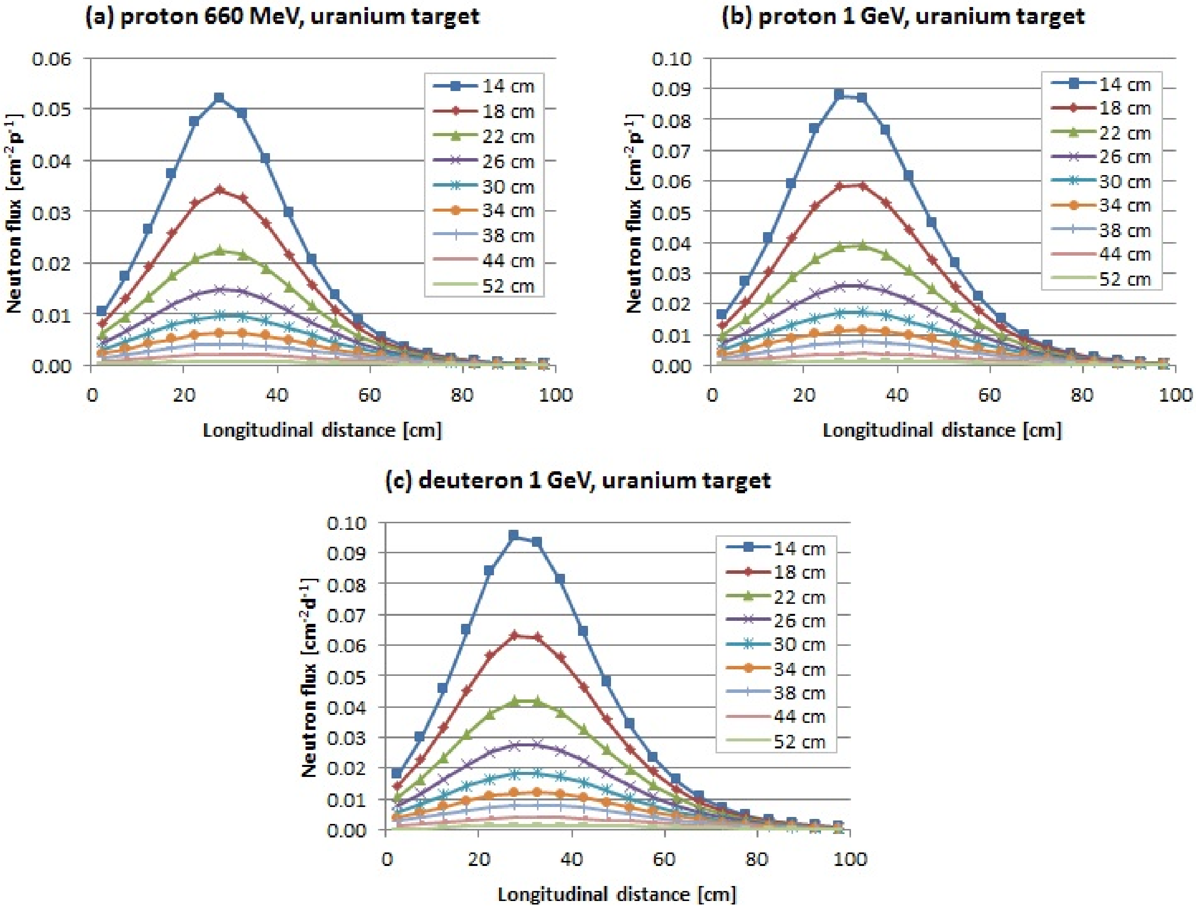

Figure 51: Average neutron flux in the BURAN setup for the 660 MeV proton (a), 1 GeV proton (b) and 1 GeV deuteron (c) beam, and the uranium target. Distances in the legends represent radial positions.

The results of the neutron flux longitudinal maximum investigation are shown in Tab. 6 and related Fig. 52. From there, one can notice that the positions of the longitudinal maximums increase towards greater radial distances. Moreover, one can observe the linear dependence of the maximum shifts (linear fits). The linear dependences found can be expressed by the equations

$$y = 0.078x + 26.756 \tag{22}$$

for the 660 MeV proton beam,

$$y = 0.0955x + 28.386 \tag{23}$$

for the 1 GeV proton beam, and

$$y = 0.1089x + 27.709 \tag{24}$$

for the 1 GeV deuteron beam. Longitudinal maximums for the 1 GeV proton and 1 GeV deuteron beams are of similar values. The course of the deuteron shift is a little steeper and positions of longitudinal maximums are of smaller values than for the 1 GeV proton beam until the radial distance of 50.52 cm where the dependences cross each other (intersection point of the linear fits). In the last investigated radial distance point of 52 cm the value of longitudinal maximum is higher for the 1 GeV deuteron beam than for the 1 GeV proton beam. One can also observe that the linearity for the 1 GeV beams is better than for the 660 MeV proton beam and that the 660 MeV dependence is less steep than for the 1 GeV beams.

Table 6: Positions of neutron flux longitudinal maximums (calculated from the polynomial function fits) for the 660 MeV proton, 1 GeV proton and 1 GeV deuteron beams in the uranium target. Dimensions are in cm.

Radial distance	proton 660 MeV	proton 1 GeV	deuteron 1 GeV
14 cm	28.01	29.73	29.28
18 cm	28.21	30.13	29.69
22 cm	28.46	30.53	30.13
26 cm	28.73	30.79	30.53
30 cm	28.89	31.25	30.92
34 cm	29.34	31.60	31.37
38 cm	29.59	32.01	31.76
44 cm	30.41	32.61	32.55
52 cm	30.86	33.37	33.44

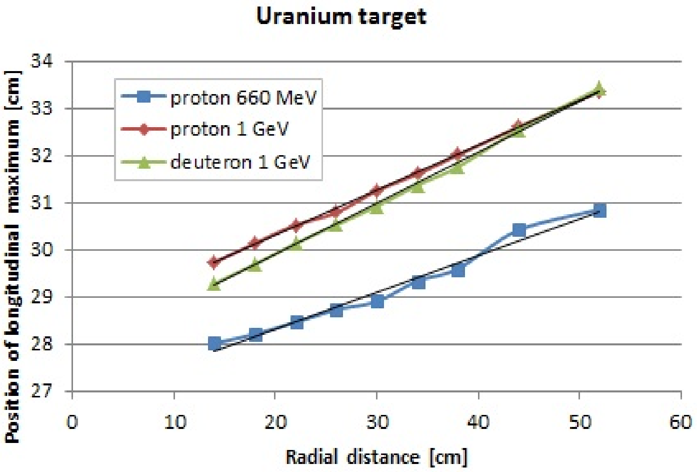

Figure 52: Longitudinal maximums in dependence on radial distance for the uranium target. Marks are corresponding to the data from Tab. 6.

6.2.2 Lead target

The graphs of the average neutron flux in the BURAN setup equipped with the lead target for the 660 MeV proton, 1 GeV proton and 1 GeV deuteron beams are shown in

Fig. 53. When comparing the graphs for the lead spallation target with the graphs for the uranium target, one can notice that the neutron flux is approximately one-third smaller for the lead target.

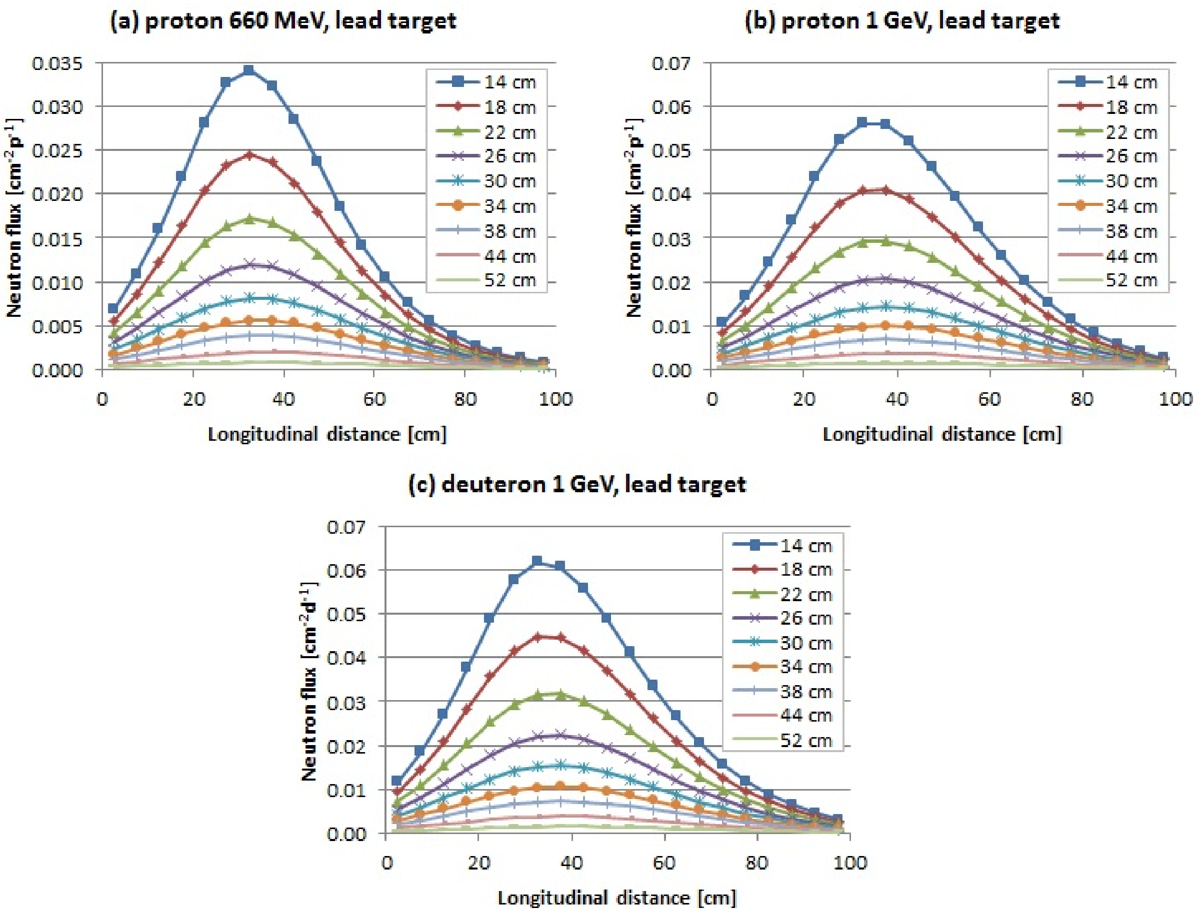

Figure 53: Average neutron flux in the BURAN setup for the 660 MeV proton (a), 1 GeV proton (b) and 1 GeV deuteron (c) beam, and the lead target. Distances in the legends represent radial positions.

The results of the neutron flux longitudinal maximum investigation are shown in Tab. 7 and related Fig. 54. From there, one can notice that the positions of the longitudinal maximums increase towards greater radial distances like in the uranium target case. A linear dependence can also be observed more or less like in the uranium target case. The linear dependences found can be expressed by the equations

$$y = 0.1112x + 30.754 \tag{25}$$

for the 660 MeV proton beam,

$$y = 0.1579x + 32.412 \tag{26}$$

for the 1 GeV proton beam, and

$$y = 0.1496x + 32.007 \tag{27}$$

for the 1 GeV deuteron beam. Again, like in the uranium target case, we can observe that the linearity for the 660 MeV proton beam is less steep than for the 1 GeV beams. But the linearity for the 1 GeV proton beam is steeper than for the 1 GeV deuteron beam and the positions of the longitudinal maximums are always smaller for the deuteron beam. Longitudinal maximums were also found at greater radial distances than in the uranium target case.

Table 7: Positions of neutron flux longitudinal maximums (calculated from the polynomial function fits) for the 660 MeV proton, 1 GeV proton and 1 GeV deuteron beams in the lead target. Dimensions are in cm.

Radial distance	proton 660 MeV	proton 1 GeV	deuteron 1 GeV
14 cm	32.18	34.53	33.77
18 cm	32.77	35.33	34.73
22 cm	33.22	36.03	35.44
26 cm	33.74	36.48	36.04
30 cm	34.04	37.17	36.58
34 cm	34.63	37.84	37.26
38 cm	34.93	38.14	37.54
44 cm	35.83	39.39	38.68
52 cm	36.36	40.71	39.60

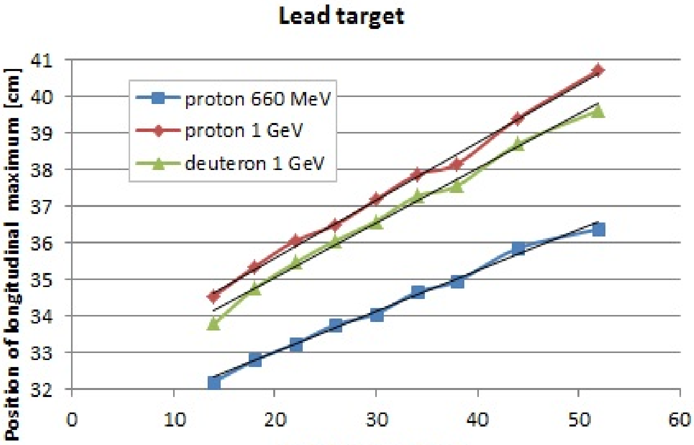

Figure 54: Longitudinal maximums in dependence on radial distance for the lead target. Marks are corresponding to the data from Tab. 7.

6.2.3 Carbon target

The graphs of the average neutron flux in the BURAN setup equipped with the carbon target for the 660 MeV proton, 1 GeV proton and 1 GeV deuteron beams are shown in Fig. 55. The neutron flux is approximately two times smaller than in the lead target case.

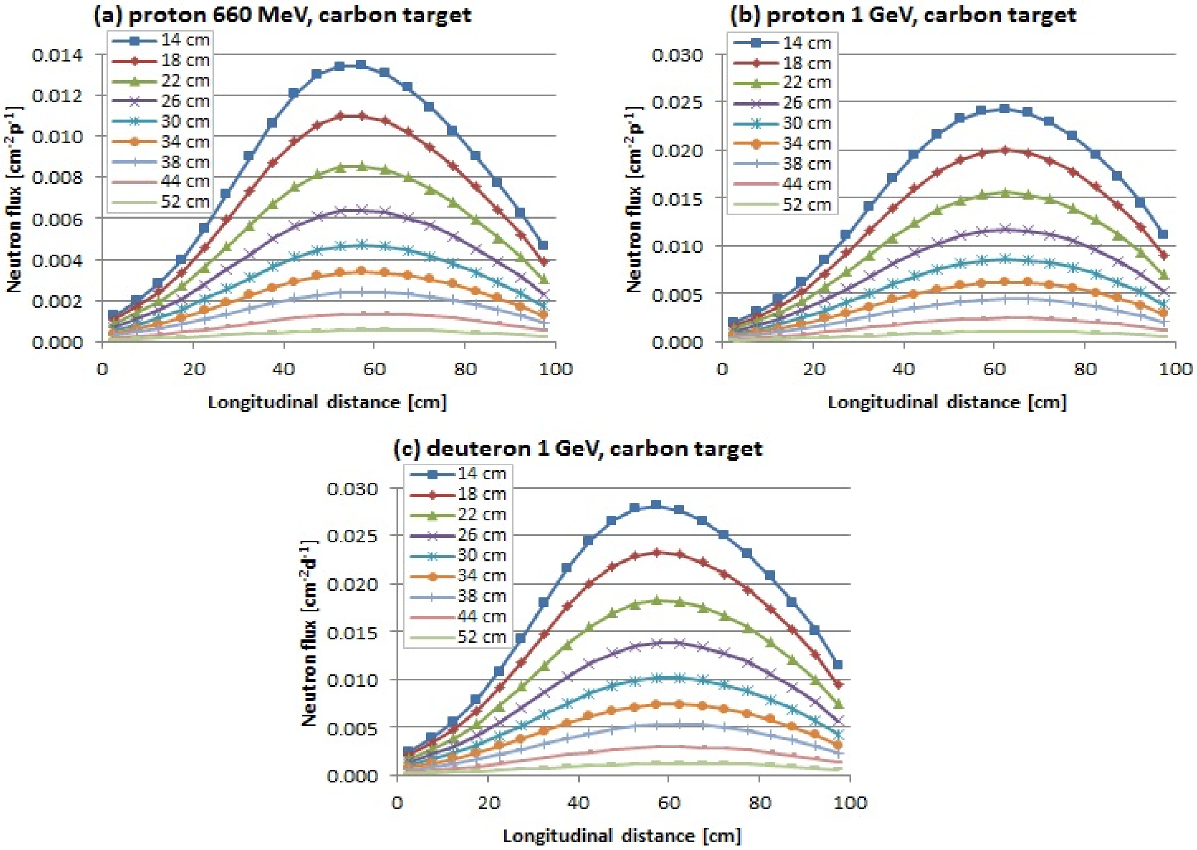

Figure 55: Average neutron flux in the BURAN setup for the 660 MeV proton (a), 1 GeV proton (b) and 1 GeV deuteron (c) beam, and the carbon target. Distances in the legends represent radial positions.

The results of the neutron flux longitudinal maximum investigation are shown in Tab. 8 and related Fig. 56. A linear dependence of the positions of the longitudinal maximums was not observed like in the uranium and lead target cases. It can be caused by the significant width of the maximums in the carbon case, and therefore there can exist a substantial inaccuracy in the positions determination. However, one can observe linearity for the 660 MeV proton beam between the radial distances of 14 cm and 30 cm, and for the 1 GeV deuteron beam between the distances of 14 cm and 44 cm, which can be expressed by the equations

$$y = 0.18x + 52.32 \tag{28}$$

for the 660 MeV proton beam, and

$$y = 0.1926x + 54.473 \tag{29}$$

for the 1 GeV deuteron beam. In the carbon target case, one can notice that the differences in the positions of the longitudinal maximums between the 1 GeV proton and 1 GeV deuteron beams are clearly much more significant than in the uranium and lead target cases. Longitudinal maximums were found at greater radial distances than in the uranium and lead target simulations. It can also be seen that in the 660 MeV proton and 1 GeV deuteron beam cases, the positions of longitudinal maximums seem to have a decreasing tendency with very high radial distances.

Table 8: Positions of neutron flux longitudinal maximums (calculated from the polynomial function fits) for the 660 MeV proton, 1 GeV proton and 1 GeV deuteron beams in the carbon target. Dimensions are in cm.

Radial distance	proton 660 MeV	proton 1 GeV	deuteron 1 GeV
14 cm	54.89	61.70	55.88
18 cm	55.49	62.38	57.98
22 cm	56.20	62.72	58.77
26 cm	57.17	62.67	59.73
30 cm	57.65	62.95	60.43
34 cm	57.22	64.19	60.95
38 cm	58.90	64.60	61.78
44 cm	58.86	64.20	62.79
52 cm	57.12	66.13	61.24

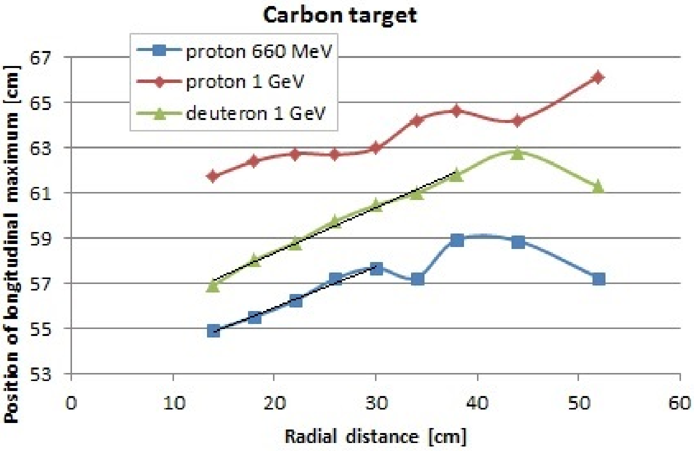

Figure 56: Longitudinal maximums in dependence on radial distance for the carbon target. Marks are corresponding to the data from Tab. 8.

6.3 Energy neutron spectra results

The energy neutron spectra for the 660 MeV proton, 1 GeV proton and 1 GeV deuteron beams and uranium target are shown in Figs. 57, 58 and 59. These spectra are formed predominantly by fission and moderated spallation neutrons from the evaporation and fission phases of the spallation reaction. High-energy spallation neutrons from the intranuclear cascade phase are mostly emitted into forward angles of the spallation reaction course. The maximal neutron flux for the uranium target case can be found around 40 keV. One can see that the graphs for the 1 GeV proton and 1 GeV deuteron beams are of a similar shape, even if values of neutron flux can be slightly higher for the deuteron beam. As supposed, the flux in the 660 MeV proton case reaches smaller values than for the 1 GeV beams. It can also be observed that in the 660 MeV proton case, the course and values of neutron flux are very similar in the points 110 and 305. The figures for the lead and carbon targets for all the three beams are given in Appendix G.

When comparing the shapes of neutron energy distributions in Fig. 60 in the longitudinal direction (points 105 - 115 and points 305 - 315), one can notice that the high-energy part of the spectra (above ∼ 60 keV) is more dominant for the low longitudinal distances. This is caused because of ionisation losses of the charged primary particles. The particles lose their energy with rising longitudinal distance, and therefore the energy of spallation neutrons is also decreasing. There are no significant differences in the spectra shapes for the different primary beams. The neutron flux is evidently higher for higher primary proton beam energy, and there is only a little increase of neutron flux between the 1 GeV proton and 1 GeV deuteron beams. Analogical figures to Fig. 60 for the lead and carbon targets are given in Appendix G.

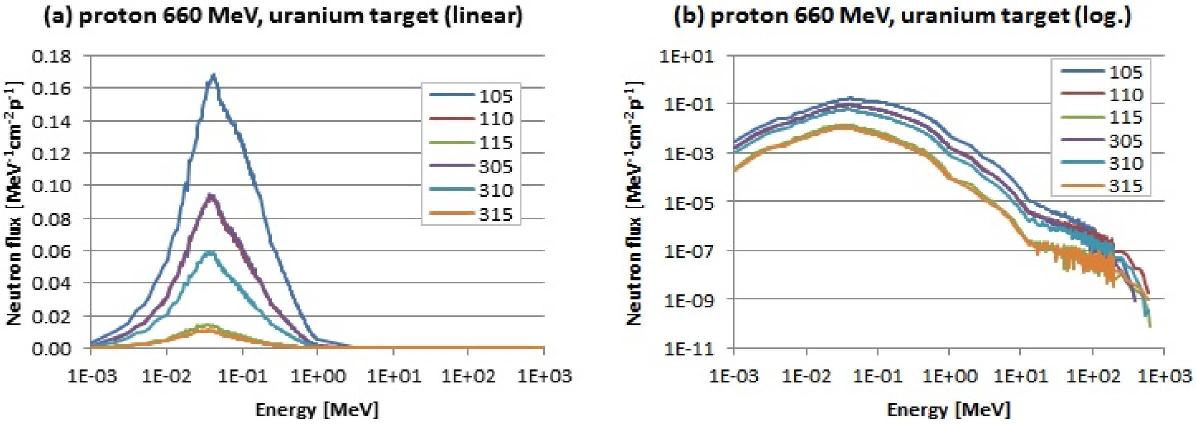

Figure 57: Energy neutron spectra in linear (a) and logarithmic (b) scale for the 660 MeV proton beam and the uranium target in the points 105, 110, 115, 305, 310 and 315.

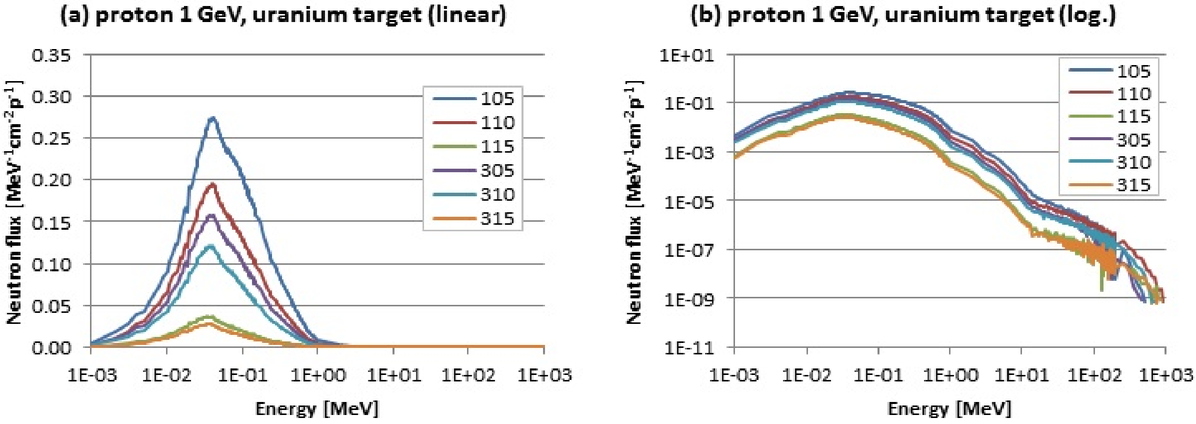

Figure 58: Energy neutron spectra in linear (a) and logarithmic (b) scale for the 1 GeV proton beam and the uranium target in the points 105, 110, 115, 305, 310 and 315.

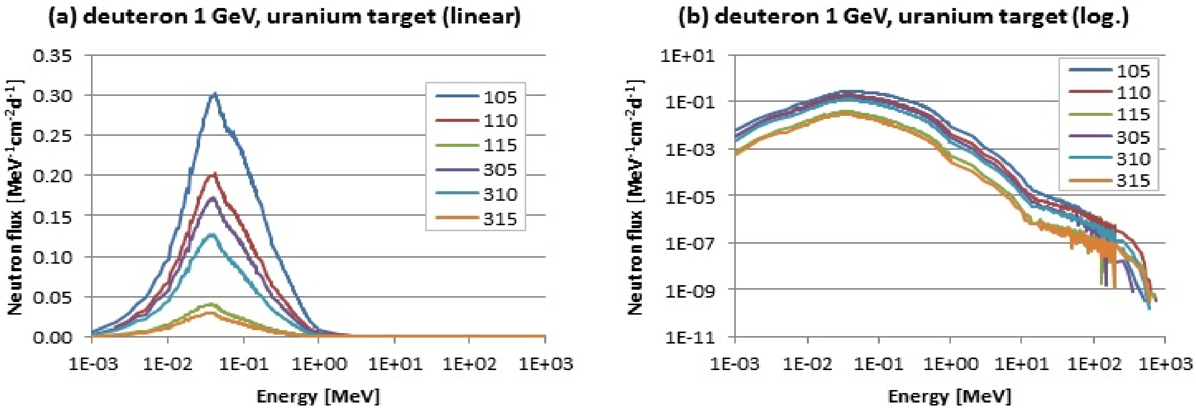

Figure 59: Energy neutron spectra in linear (a) and logarithmic (b) scale for the 1 GeV deuteron beam and the uranium target in the points 105, 110, 115, 305, 310 and 315.

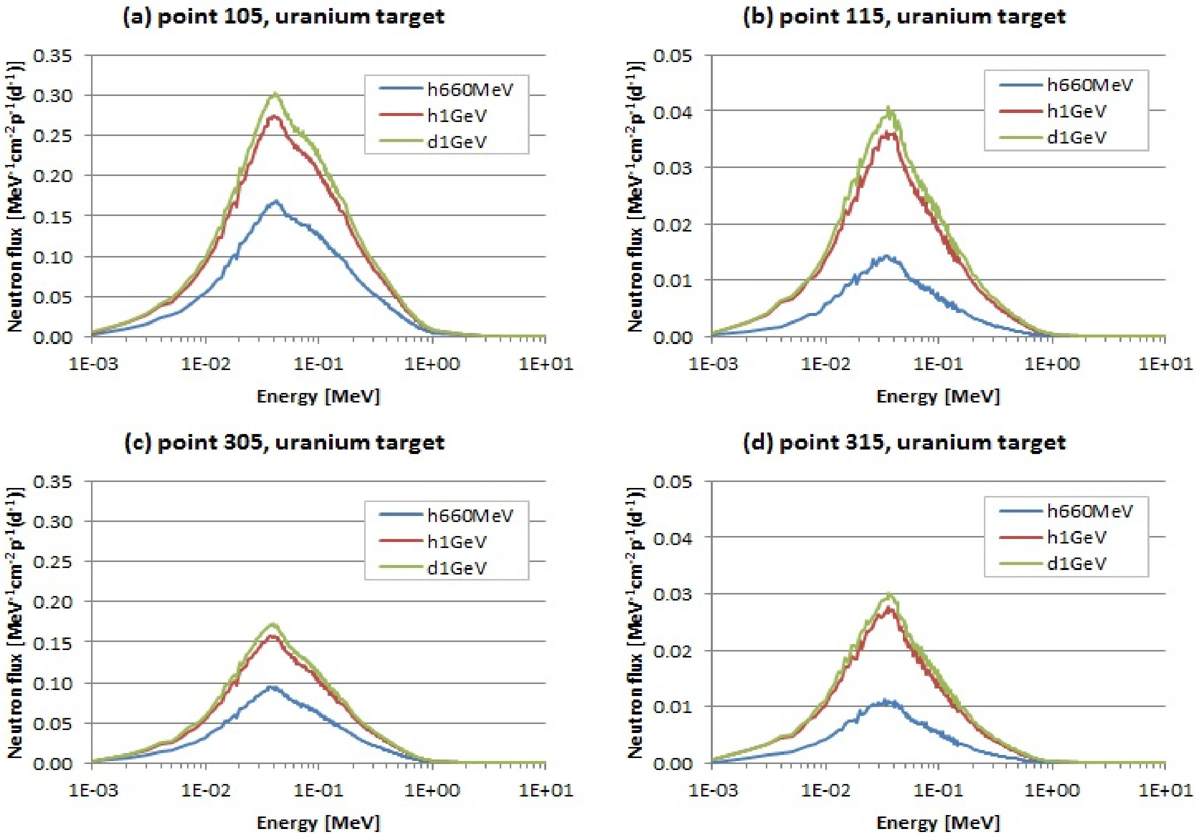

Figure 60: Energy neutron spectra for the 660 MeV proton, 1 GeV proton and 1 GeV deuteron beams and the uranium target in the points 105 (a), 115 (b), 305 (c) and 315 (d).

6.4 Neutron spectra hardness results

In this section, results of the neutron spectra hardness investigation is given. The hardness in each measuring point was calculated as the ratio of the simulated total flux of neutrons with energies higher than 10 MeV to the simulated total flux of neutrons with energies less than or equal to 10 MeV.

6.4.1 Uranium target

The dependences of the neutron spectra hardness on longitudinal distance with the use of uranium target are given in Fig. 61. At lower distances, significant differences in hardness both for the proton and deuteron beams are not visible (for the 660 MeV proton beam the values are a little smaller than for the 1 GeV proton beam). At higher distances, greater values of hardness for the 1 GeV deuteron beam can be found than for the 1 GeV proton beam. Further, the curves cross each other at longitudinal distances of about 14 and 60 cm. It can be concluded that around these values, the hardness is approximately identical for all radial distances. Furthermore, one can notice that the shape of dependences becomes more linear with increasing radial distance. This, in fact, confirms that the most remote distances are reached by the most energetic neutrons. For the line 6 of the 660 MeV proton beam, a very steep increase of hardness can be seen.

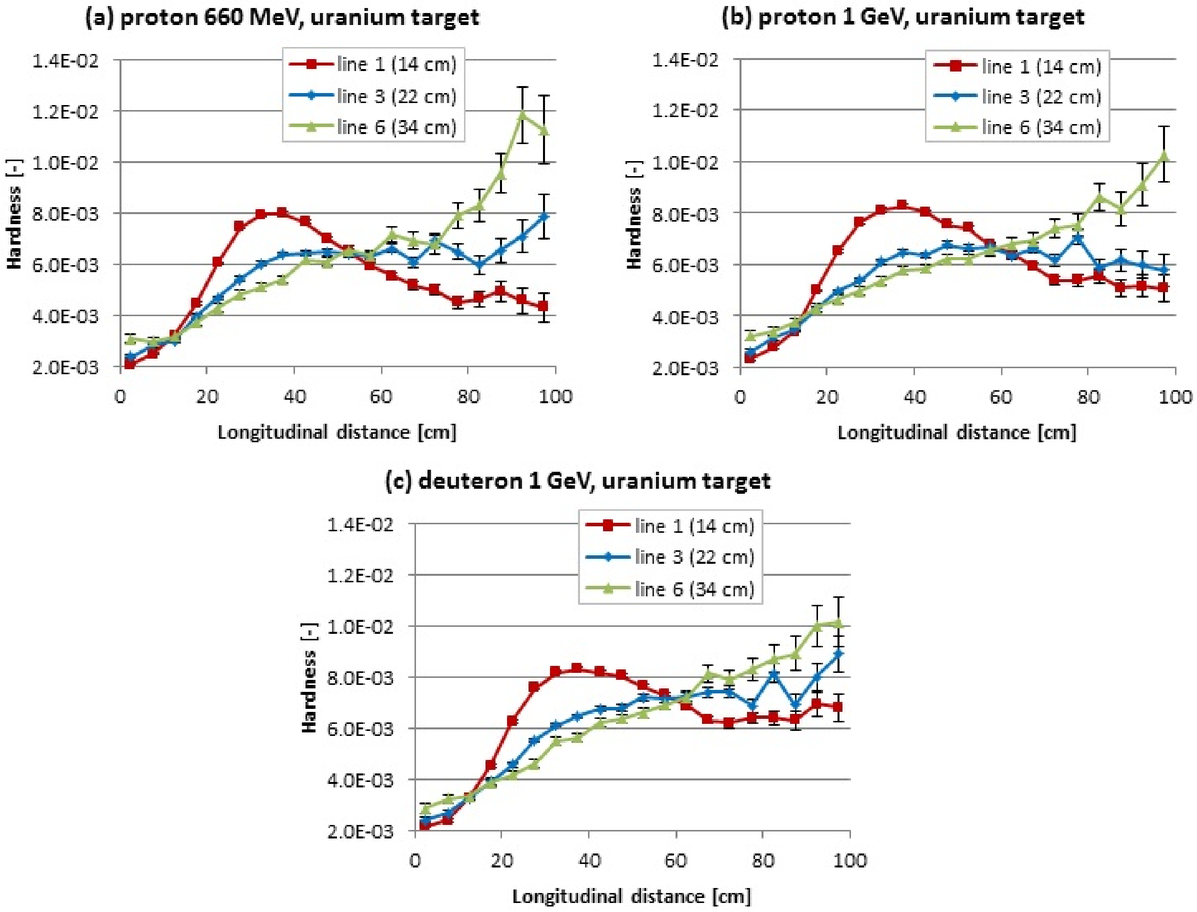

Figure 61: Neutron spectra hardness in dependence on longitudinal distance for the 660 MeV proton (a), 1 GeV proton (b) and 1 GeV deuteron (c) beam, and the uranium target. Hardness is shown for three longitudinal lines. Distances in the brackets mean radial positions of the lines.

6.4.2 Lead target

The dependences of the neutron spectra hardness on longitudinal distance with the use of lead target are given in Fig. 62. A better linearity with rising radial distances is also apparent like in the uranium target case. The first intersection of the curves is about 10 cm of longitudinal distance. The second intersection is not found around a similar value of longitudinal distance like in the uranium target case, but around the value of 70 cm for the 660 MeV proton beam, around 85 cm for the 1 GeV proton beam, and for the 1 GeV deuteron beam the intersection is not even found.

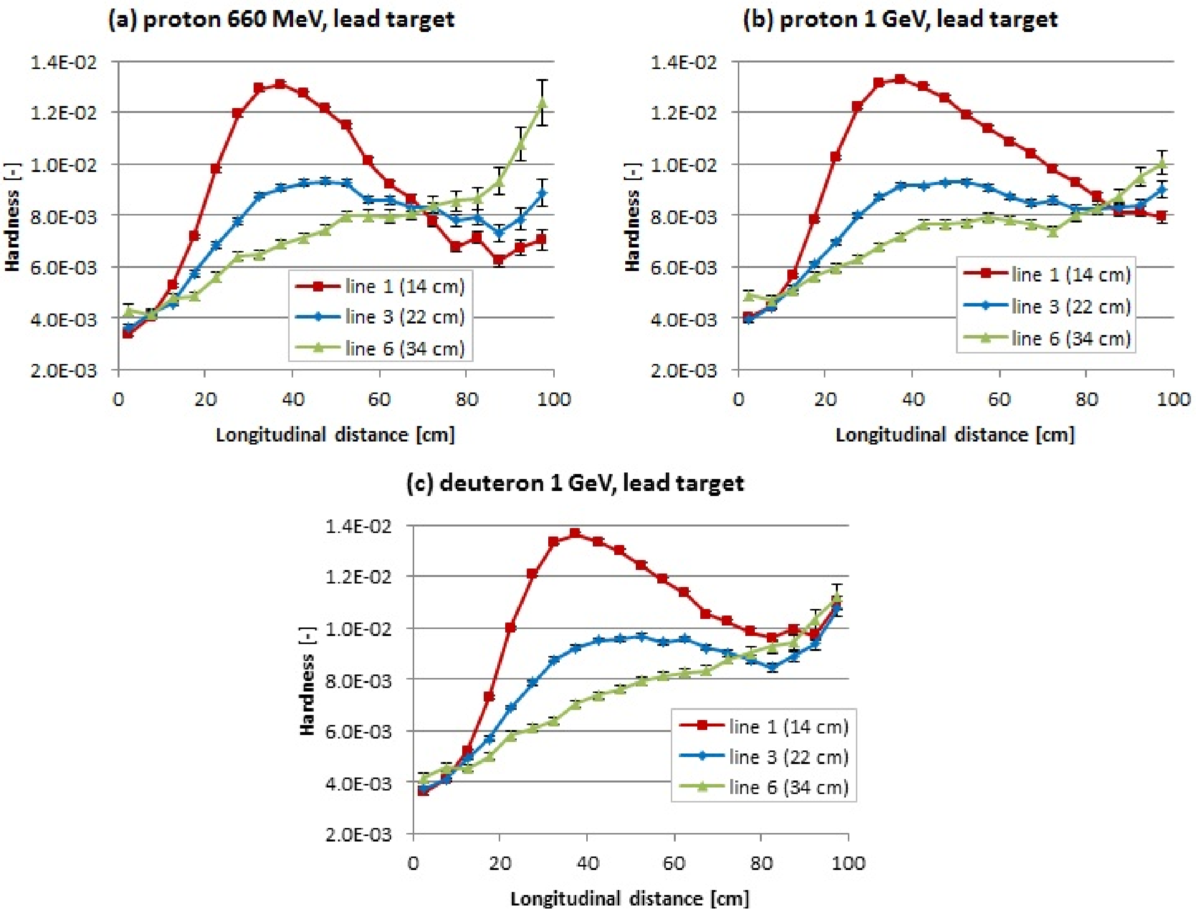

Figure 62: Neutron spectra hardness in dependence on longitudinal distance for the 660 MeV proton (a), 1 GeV proton (b) and 1 GeV deuteron (c) beam, and the lead target. Hardness is shown for three longitudinal lines. Distances in the brackets mean radial positions of the lines.

6.4.3 Carbon target

The dependences of the neutron spectra hardness with the use of carbon target on longitudinal distance are given in Fig. 63. The first intersection of the curves for all the beams can be found around 7 cm of longitudinal distance. The second intersection was not observed. The spectra tend to be more linear with rising radial distance like in the uranium and lead cases.

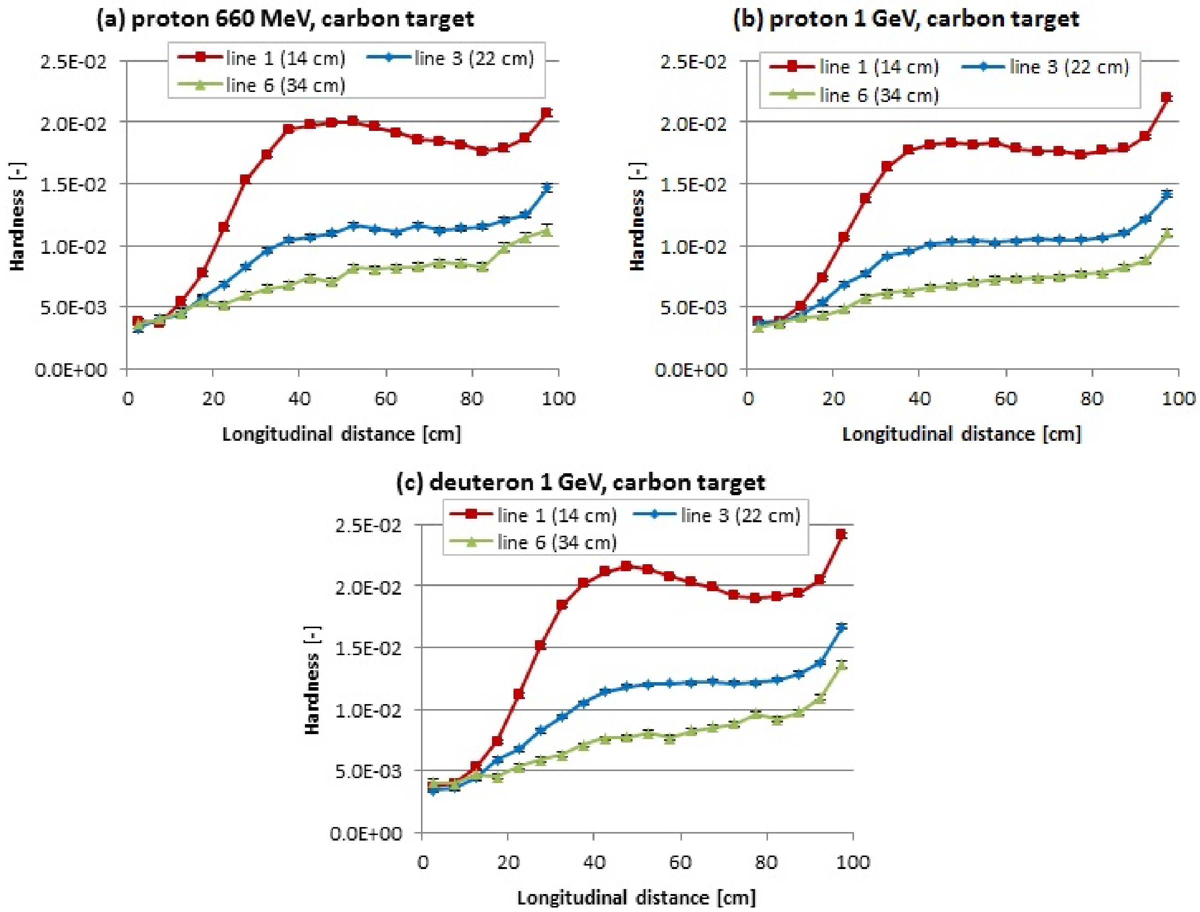

Figure 63: Neutron spectra hardness in dependence on longitudinal distance for the 660 MeV proton (a), 1 GeV proton (b) and 1 GeV deuteron (c) beam, and the carbon target. Hardness is shown for three longitudinal lines. Distances in the brackets mean radial positions of the lines.

7 Comparison of QUINTA and BURAN neutron flux simulations

The methodology of performing the QUINTA experiments is based on long-time experience and investigation of the E&T RAW collaboration. It can be supposed that the worked out methodology could be effectively applied also for the future BURAN experiments. Also, a question arose if the BURAN experiments would not be problematic from the radiation safety point of view. Therefore, I studied neutron distribution inside the setups and neutron leakage.

The simulations of neutron flux inside the uranium part (see Figs. 8 and 11) of QUINTA and BURAN were performed in MCNPX 2.7.0 (see section 2.3). Because BURAN is now awaiting long series of irradiations at Phasotron and also the QUINTA experiments were realised only at Phasotron since the end of 2014, I decided to study the neutron characteristics under the influence of the 660 MeV proton beam. For BURAN, the lead spallation target was chosen as the most likely option for future experiments. The beam parameters in the QUINTA simulations were set as in the UA experiment (see Tab. 4) and the 2-degree setup rotation was also taken into consideration. The beam parameters and MCNPX model of BURAN were used the same as written in section 6.1.2. For the simulations, the MESH tally function [80] of the MCNPX 2.7.0 code was applied. The uranium part of the QUINTA and BURAN models were divided into a net of small cubes and neutron flux inside these cubes was simulated. For easier description, let us denote xy plane as the plane that is perpendicular to the setup central axis (the x-axis is horizontal and y-axis is vertical), and the setup central axis as the z-axis.

The neutron flux distributions on the central axes and 2D distributions on the xz planes in the centre of the setups are given in Figs. 64, 65 and 66. Based on these results, 1D neutron flux distributions on the central x-axes and 2D distributions on the xy planes are given in Figs. 67, 68 and 69. The coordinates z for the distributions were chosen according to the highest values of neutron flux found. The most intensive neutron flux for QUINTA was around 0.31 $\mathrm{cm}^{-2}\mathrm{p}^{-1}$ for z = 16.5 cm, and for BURAN around 0.27 $\mathrm{cm}^{-2}\mathrm{p}^{-1}$ for z = 24.5 cm.

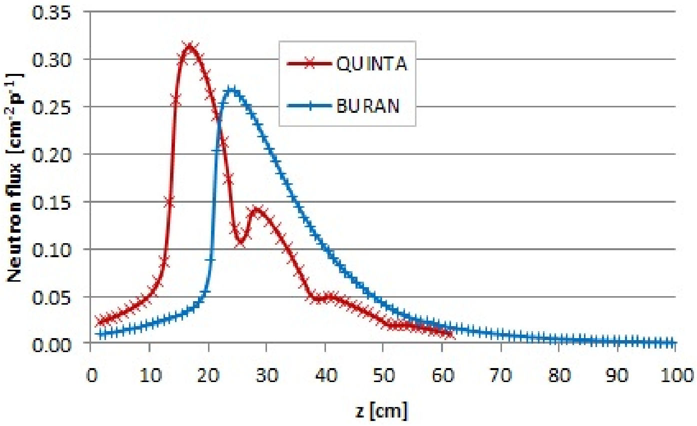

Figure 64: Longitudinal neutron flux on the central axis of the QUINTA and BURAN uranium part.

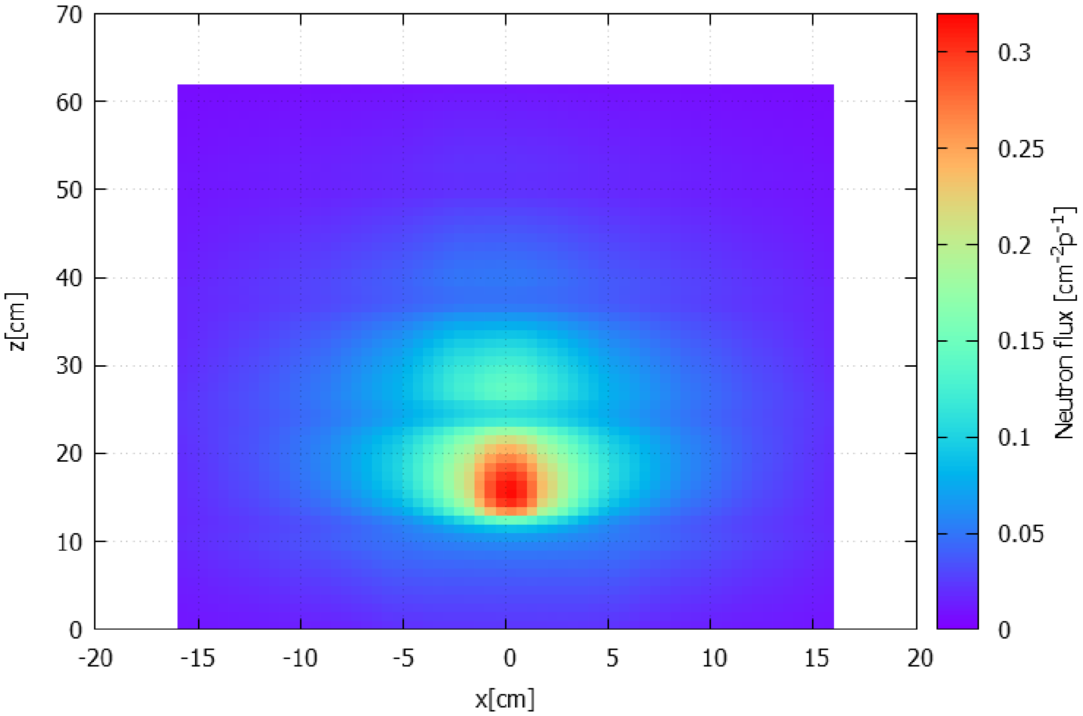

Figure 65: 2D neutron flux distribution on the central xz plane of the QUINTA uranium part.

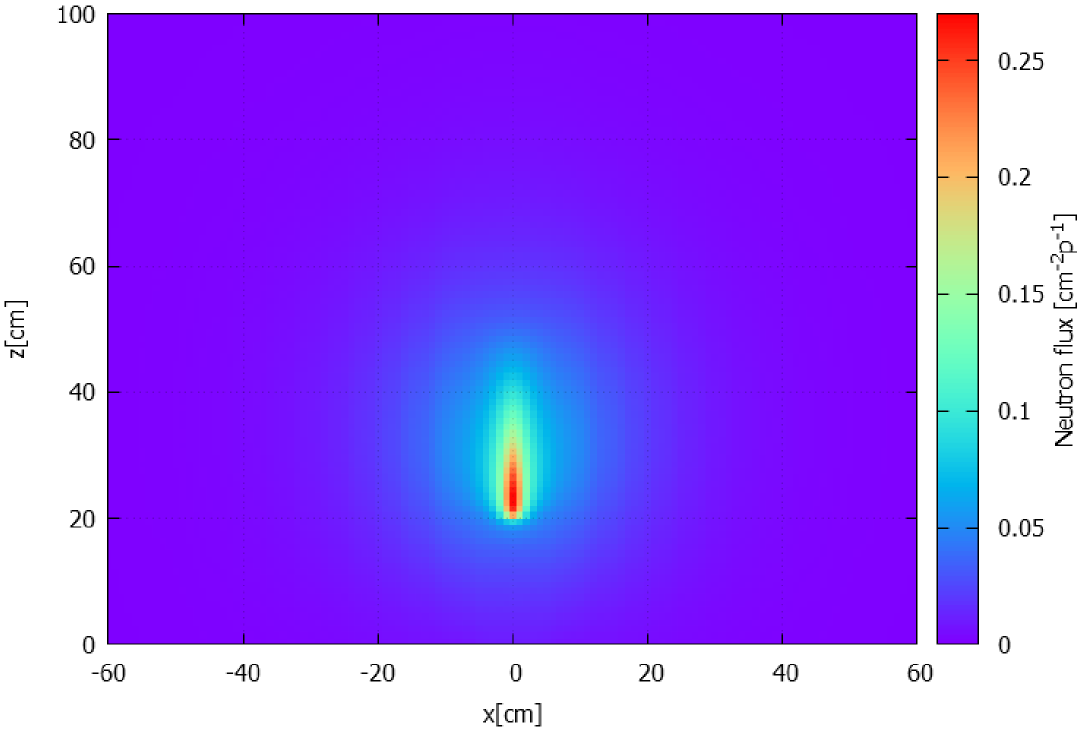

Figure 66: 2D neutron flux distribution on the central xz plane of the BURAN uranium part.

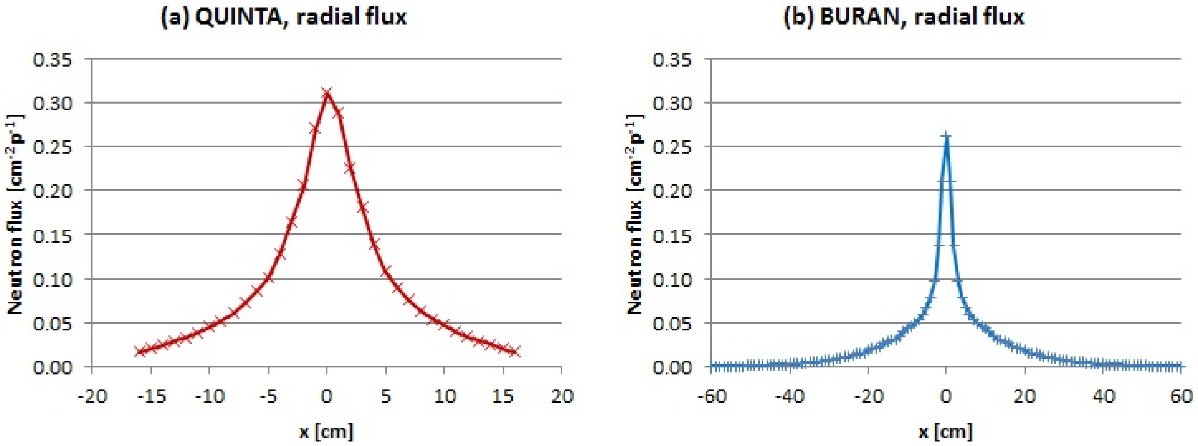

Figure 67: Radial neutron flux on the x-axis of the QUINTA uranium part for y = 0 and z = 16.5 cm (a), and BURAN uranium part for y = 0 and z = 24.5 cm (b).

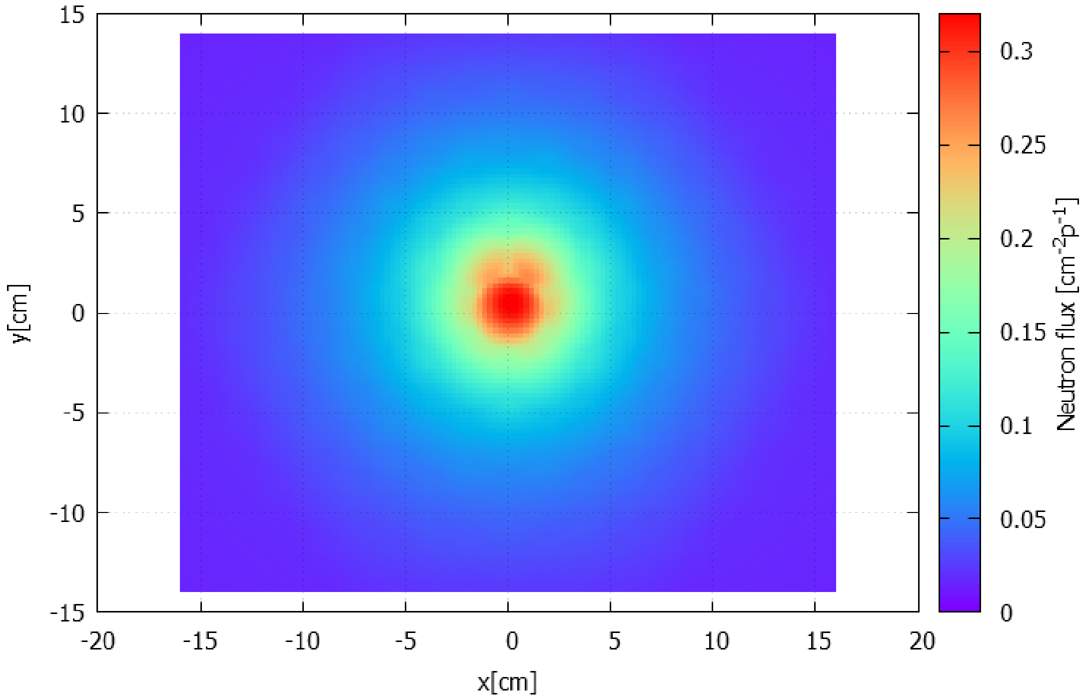

Figure 68: 2D neutron flux distribution on the xy plane of the QUINTA uranium part for z = 16.5 cm.

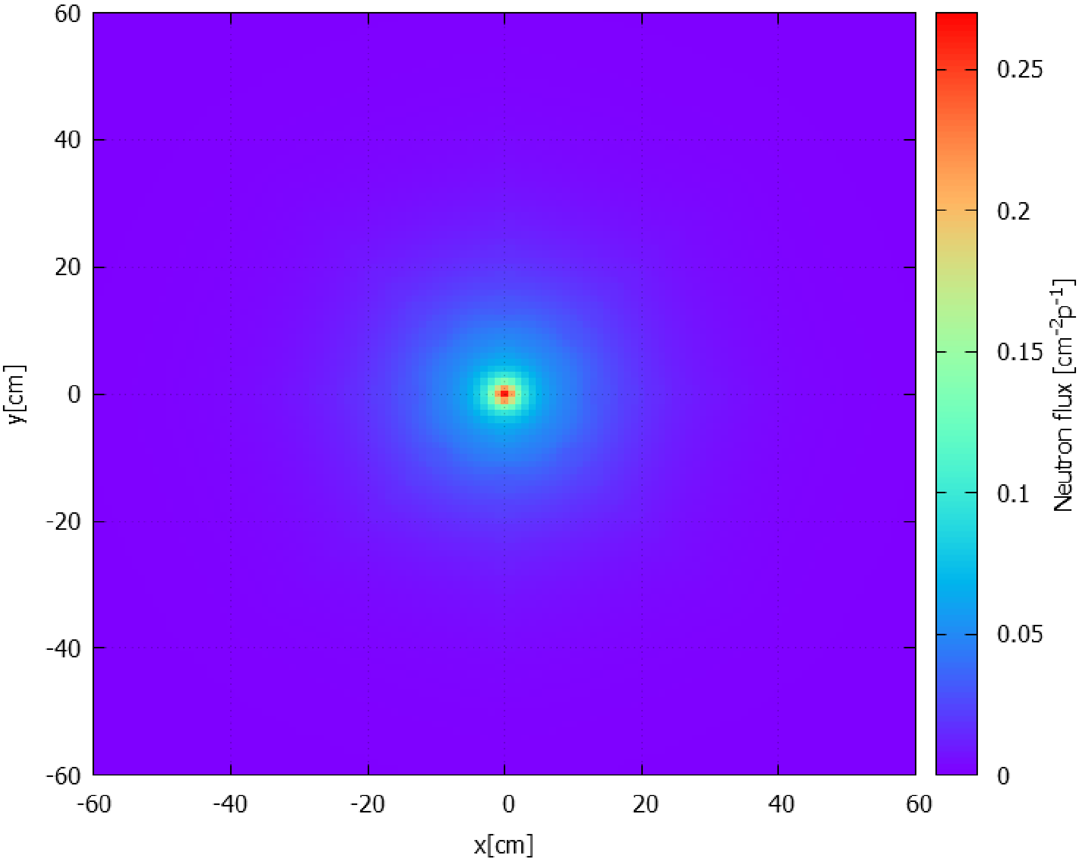

Figure 69: 2D neutron flux distribution on the xy plane of the BURAN uranium part for z = 24.5 cm.

In Figs. 64 and 65, one can notice a steep increase of the QUINTA longitudinal neutron flux around z = 12 cm and three decreases around z = 24 cm, z = 38.5 cm and z = 50.5 cm. These four areas correspond to the air gaps between the QUINTA uranium sections. In Figs. 64 and 66 for BURAN, there is a steep increase around z = 20 cm. This value corresponds to the site, where the primary proton beam travelling through the 200 mm target channel enters the BURAN lead target. The neutron flux in the air is of smaller values than the neutron flux in the uranium, and therefore it proves that neutron flux in spallation setups is also material dependent.

In Figs. 67.a and 68, a light asymmetry in the QUINTA radial neutron flux can be observed. This asymmetry is the greatest around x = 0 cm, and it gradually fades away with higher coordinate x. It is caused by the primary beam settings and 2-degree QUINTA rotation, and it confirmes the conclusion from chapter 5 that activation detectors close to the central axis are influenced by the inaccuracies of the beam settings more than detectors remote from the axis. On the contrary, no asymmetry can be observed in the BURAN case in Figs. 67.b and 69 because there is no setup rotation, and the beam position coordinates were set to $d_x = d_y = 0$ cm.

The large dimensions of the BURAN depleted uranium cylinder (1000 mm in length and 1200 mm in diameter) also help to minimalise the neutron leakage. The neutron leakage was also simulated with MCNPX 2.7.0. The result was that for 1E7 incident primary protons, approximately 1.8E9 neutrons were created in QUINTA and 3.9E8 neutrons were created in BURAN. The numbers of escaping neutrons were 1.4E9 for QUINTA and 5.6E7 for BURAN. Based on the simulations, the neutron escape for QUINTA was assessed as 76.1 % and for BURAN as 14.5 %.

Due to the comparable neutron flux in QUINTA and BURAN, I conclude that the experimental methodology used for QUINTA can also be applied to the forthcoming BURAN irradiations (i.e. the neutron flux in BURAN will be measurable when using the same methodology for various threshold activation detectors). Considering that BURAN is composed of depleted uranium (and not of natural uranium like QUINTA) and due to big BURAN size, I would recommend to enlarge activation detectors dimensions (e.g. to increase sample thickness), especially at very remote radial and/or longitudinal distances.

8 Experiment with lead target

To experimentally test a potential target for the future BURAN setup (see section 1.3.5 and chapter 6), 20 ^{nat}Pb cylinder blocks with a diameter of 19 cm and approximate length of 5.2 cm were purchased. The blocks, therefore, formed a lead spallation target with 19 cm in diameter and approximate length of 104 cm. The 19 cm diameter of the target (compared to the BURAN simulations with the potential lead target of 20 cm in diameter) was chosen in order to avoid problems of insertion the lead target into the BURAN central opening. Another difference compared to the presented BURAN simulations is that in this case, there was no target channel.

8.1 Description and approach

In June 2018, an experiment with the lead target at Phasotron was performed. The target was irradiated with the 660 MeV proton beam aiming perpendicularly at the centre of the first lead cylinder (see Fig. 70). The coordinates of the source beam centre (d_x, d_y) on the target entrance were d_x = -0.29 cm and d_y = -0.06 cm, and full widths at half maximums on axes x and y of the 2D Gaussian profile were $FWHM_x$ = 3.38 cm and $FWHM_y$ = 3.71 cm (orientation of the axes is identical to the E+T and QUINTA experiments, see Figs. 4 and 23). The beam characteristics were measured by the ionisation chamber. The integral number of protons impinging on the target was 2.15(18)E15. The number was determined using aluminium monitoring foil and ^{27}Al(p,3pn)^{24}Na reaction. The irradiation time was 5 hours.

Figure 70: Lead target with its stand. The proton beam hits the target from the right side. The locations of the ^{nat}Pb activation samples are marked.

In this experiment, there were 5 ^{nat}Pb activation samples placed inside and at the end of the lead target, and 16 depleted U samples placed on the surface of the target to study spatial and energy distribution of the generated mixed neutron-proton field, radionuclide production, fission reactions, and to perform benchmark tests of Monte Carlo simulation codes. There were also 11 plastic ampoules filled with NaCl powder placed on the surface of the lead target (white ampoules in Fig. 70) to investigate radionuclide production in NaCl as a potential heat conducting material for spallation targets. I was involved in the Monte Carlo simulation benchmarks for the 5 ^{nat}Pb samples. Simulation results of the produced radionuclides were also published in [160].

Five ^{nat}Pb activation samples with dimensions 5×5×0.05 cm^3 were placed to the centre and between the lead target cylinders (see Fig. 71) into longitudinal distances of 10.4, 20.8, 31.2, 41.6 and 104 cm, and they were denoted as APb, BPb, CPb, DPb and EPb, respectively. The average weight of a single ^{nat}Pb sample was 14.75 g. The weights of the individual samples are listed in Tab. 27 in Appendix D. The gamma-ray spectra were measured with HPGe detectors and reaction rates of produced radionuclides were evaluated by the activation techniques the way described in chapter 2. The experimental results were compared to the simulations. The simulation results (reaction rates) were obtained by convolutions of neutron and proton flux simulated with MCNPX 2.7.0 [80] and cross-sections calculated with TALYS 1.8 [148], as described in section 2.3. Some of the studied activation products have a significant contribution to the reaction rate from the products that undergo the β decay. This cumulative effect has also been taken into consideration, and the reaction rates of these products (calculated according to the equation 16) were added to the reaction rate of the studied products generated directly by the reactions of neutrons and protons with the ^{nat}Pb samples.

I participated in the experiment, its preparation, course of irradiation and measurement. The experimental reaction rates were evaluated by my colleague J. H. Khushvaktov. All simulations presented in this chapter, including the preparation of the MCNPX geometry model, were performed and evaluated by myself.

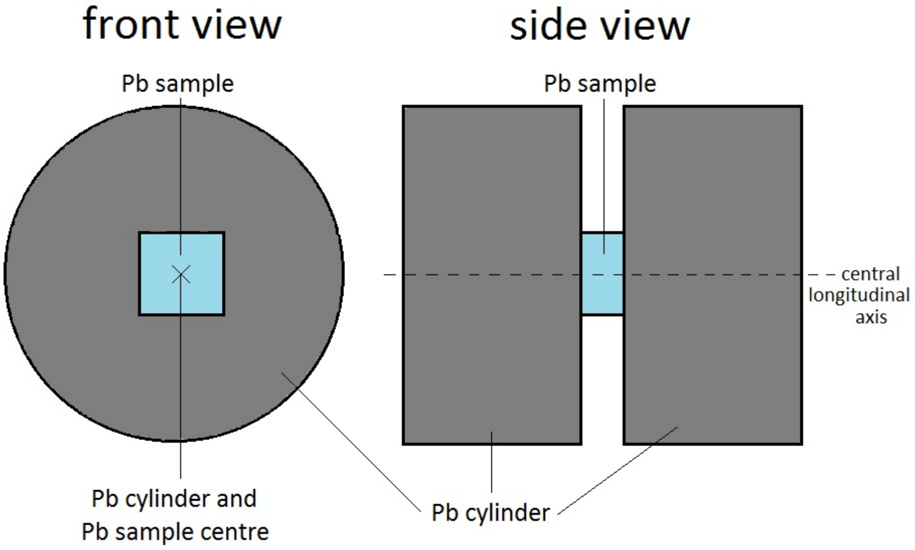

Figure 71: Placement of the ^{nat}Pb samples on the surface and between the lead target cylinders.

8.2 Results of the lead target experiment

At the first stage of the simulation process, the dimensions of the lead cylinders were carefully measured. Considering that the thickness of the lead cylinders varied between 5 and 5.4 cm, the approximate thickness of a single lead cylinder was set to 5.2 cm. Due to the simplification of the MCNPX geometry model, this value was then used as the thickness of each lead cylinder in the model. After the performance and evaluation of the first simulations, it was shown that simulated reaction rates for the CPb sample were highly overestimated compared to the experimental results. The reason for the disagreement was caused by the fact that the CPb sample was positioned in the region of the primary proton range of flight, as shown in Fig. 72.a. From the figure, one can notice that the proton range of flight is around a longitudinal distance of 31 cm. Therefore, a slight change in the longitudinal thickness of the lead target can have a significant effect on the simulation results as demonstrated in Fig. 72.b.

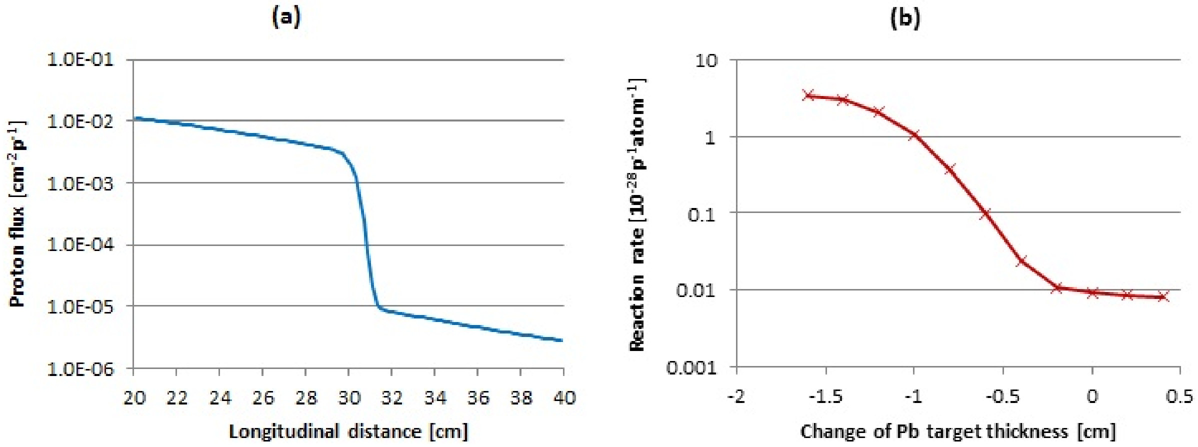

Figure 72: (a) Simulated proton flux on the central longitudinal axis of the lead target (MCNPX input file of this simulation is given in Appendix B) (b) Dependence of the simulated reaction rate of ^{206}Bi for the CPb sample on change of lead target longitudinal thickness.

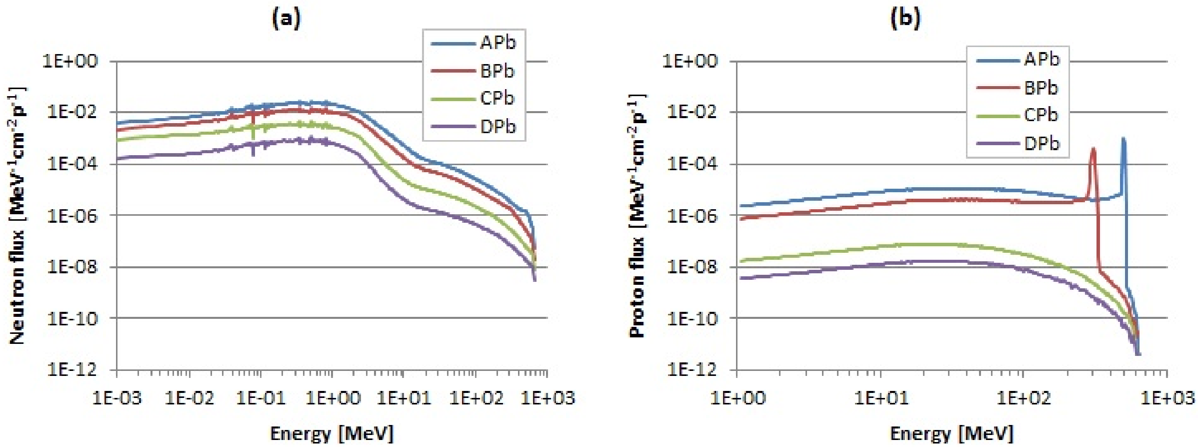

Figure 73: Simulated neutron (a) and proton (b) energy spectra in the ^{nat}Pb samples.

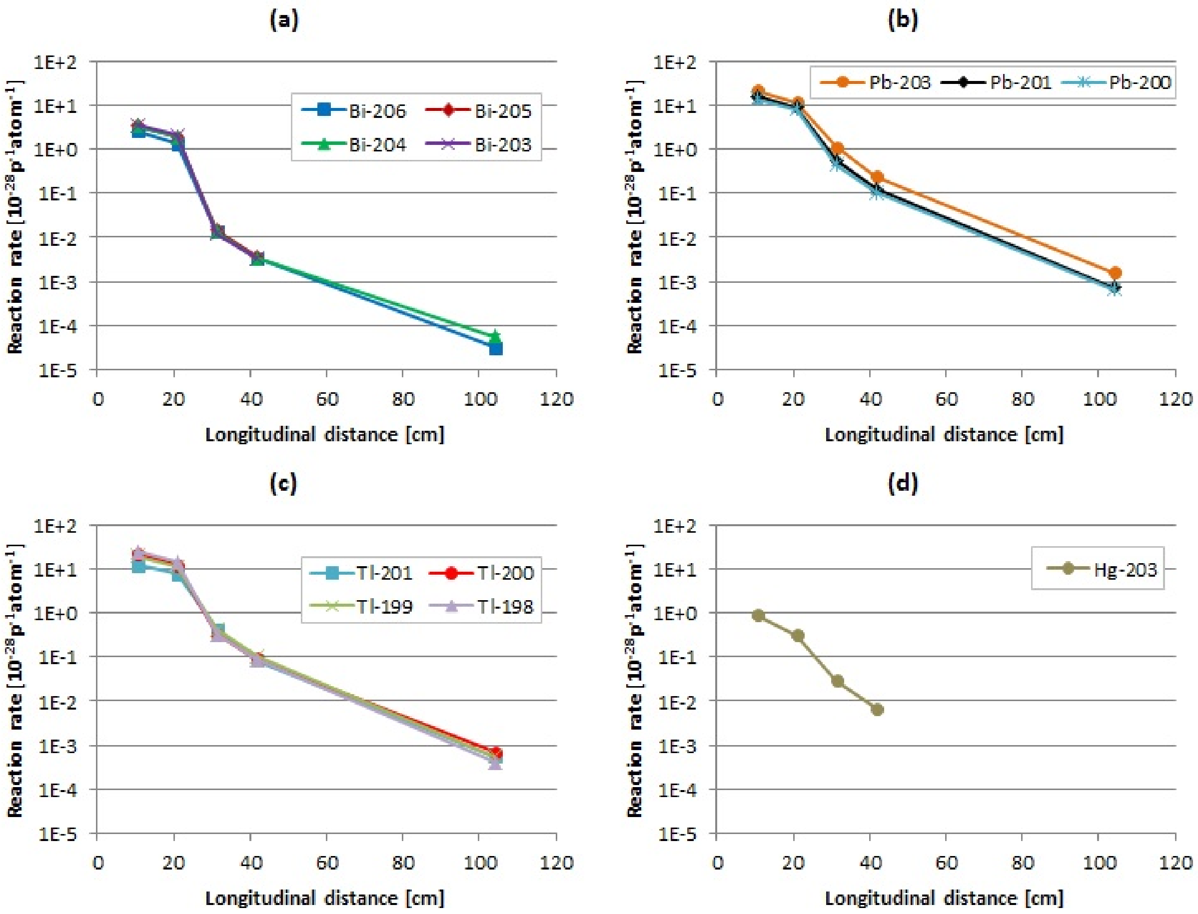

Figure 74: Experimental reaction rates of Bi (a), Pb (b) and Tl (c) isotopes, and ^{203}Hg (d) produced in the APb, BPb, CPb, DPb and EPb lead samples.

The geometry model was then redefined, and the exact dimensions of the lead cylinders were included. After the new performance of the simulation procedure, the ratios of the experiment-to-simulation results gave right results for the CPb lead sample.

The simulated neutron and proton energy spectra are given in Fig. 73. In Fig. 73.b, the peaks at energies 495 and 303 MeV in the APb and BPb samples, respectively, are composed mostly of primary protons. These protons lost their energy by ionization losses at the lead target. The proton spectra in the CPb and DPb samples are formed dominantly by protons produced in secondary processes, because these samples are situated beyond the range of flight of the primary protons.

The experimental reaction rates of the studied isotopes produced in the APb, BPb, CPb, DPb and EPb lead samples are given in Fig. 74. The ratios of experiment-to-simulation reaction rates are given in Fig. 75. The numerical values of the experimental and simulated reaction rates are given in Tab. 32 in Appendix H. The simulations for the EPb sample were not carried out due to low statistics.

In Fig. 74, one can notice the drop of reaction rates beyond the proton range of flight due to the lack of proton contributions in this region. The most significant drop is observed for the isotopes of bismuth, which are formed only by proton-induced reactions. From Fig. 75, one can see that the simulations describe the experiment relatively well.

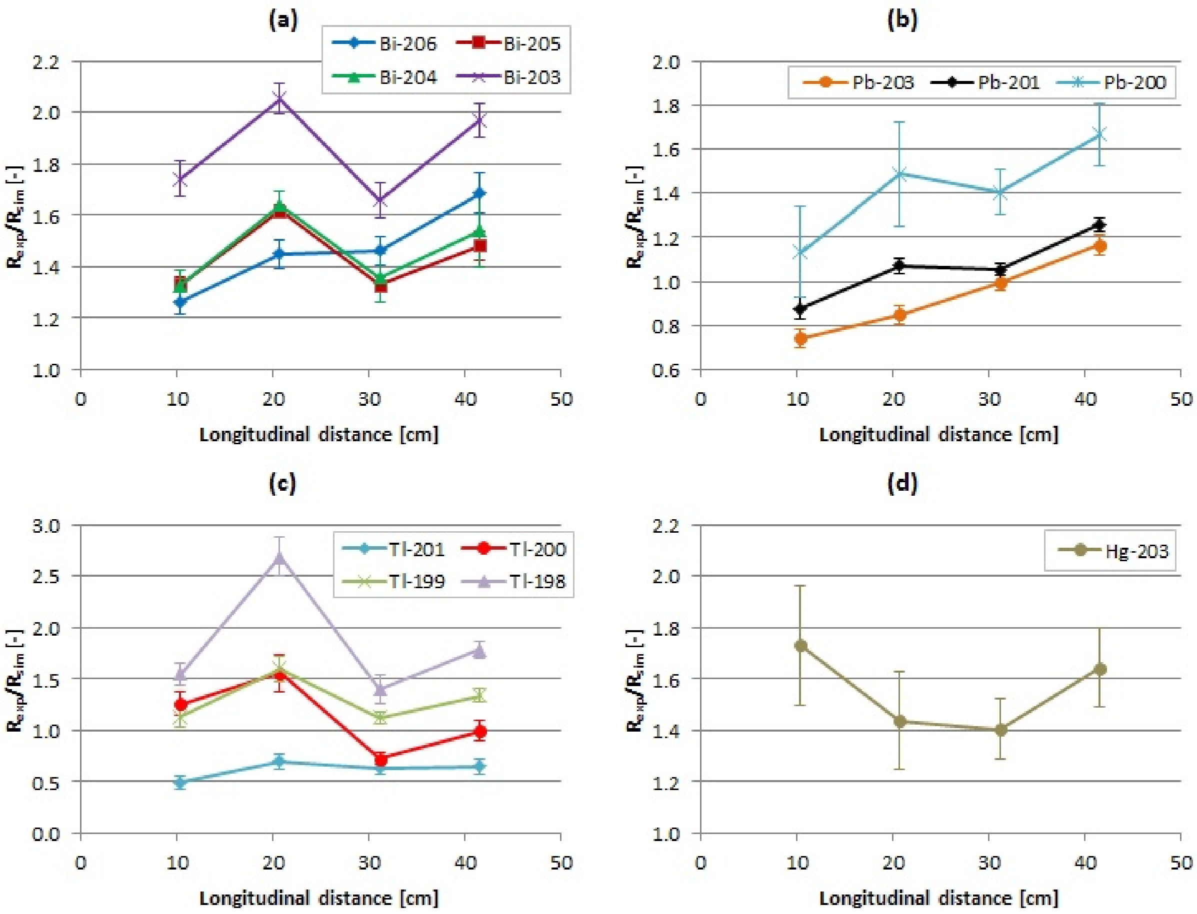

Figure 75: Experiment-to-simulation reaction rate ratios of Bi (a), Pb (b) and Tl (c) isotopes, and ^{203}Hg (d) produced in the APb, BPb, CPb and DPb lead samples.

When comparing the radionuclides of Bi, Pb and Tl with different mass numbers, it can be noticed that the worst experiment-to-simulation agreement was reached for the isotopes with the lowest mass number (e.g., the typical experiment-to-simulation ratio for ^{203}Bi is around 1.9, while for the other bismuth isotopes it is around 1.5). It is caused mainly by the insufficient knowledge of cross-sections for reactions with high thresholds.

9 Conclusions

The accelerator-driven systems represent a perspective solution of the future spent nuclear fuel management. Although before the systems are ready for commercial use, much research has to be done. Description of fast neutron, proton and deuteron interactions and transport are still suffering for missing nuclear data like cross-sections. This, in a significant measure, also influence the precision of the Monte Carlo simulation codes. Even though the codes are able to provide us with reasonable results in many cases, there are still some cases in which the results are far from being satisfactory. Therefore, the codes need to be continuously enhanced together with a considerable portion of benchmark tests.

The aim of the thesis was to deal with specific tasks concerning ADS experiments at uranium setups, which are conducted at JINR in the framework of the broad E&T RAW collaboration. My research was focused on the last uranium setups E+T and QUINTA irradiated by high-energy proton and deuteron beams of the JINR accelerators Phasotron and Nuclotron, and also on the newest transmutation setup BURAN, which is now being prepared for its first irradiations.

I prepared brand new Monte Carlo simulations with the MCNPX 2.7.0 code for experiments at the E+T setup. That involved irradiations at Nuclotron by 0.7, 1, 1.5 and 2 GeV proton beams, and 1.6, 2.52 and 4 GeV deuteron beams. Threshold reactions on activation samples of ^{27}Al, ^{197}Au and ^{209}Bi were studied. The samples were chosen because of their presence in all of the mentioned experiments. Furthermore, they were located in the identical or similar positions in the E+T setup, and therefore the results can be easily compared between each other throughout the series of irradiations. Generally, the simulations were in good agreement with the experimental data. But the agreement was worse for reactions with high-energy neutron thresholds ($E_{thr} > 30$ MeV). The primary source of discrepancies is in the insufficient knowledge of neutron cross-sections and uncertainties of the hard part of spallation neutron spectra. The systematical process of the performance of the new simulations also revealed a systematical error related to the activation samples positions in the 1.5 GeV proton experiment. Therefore, the error was corrected based on the new data. Also, an apparent mistake in the experimental evaluation of reaction rates of isotopes of bismuth in the 2 GeV proton experiment was discovered and corrected. In the E+T results, a dependence of the experiment-to-simulation agreement on the samples radial position in the setup was observed. Worse results were generally given for samples situated close to the primary beam passage. This was caused due to the stronger influence of proton- (deuteron-) induced reactions. This indicates that the precise description of the primary beam geometry is an essential factor. For this reason, I got involved in the investigation of the accelerator beam settings and primary beam geometry description in the experiments with the QUINTA setup by focusing on the mixed neutron-proton (deuteron) fields in regions close to the primary beam. The new simulations at the E+T setup are a vital part of a newly prepared systematics of the E+T experiments, which is still ongoing at NPI.

I focused on the QUINTA irradiations by the 4 and 8 GeV deuteron beams of Nuclotron, and on three irradiations by the 660 MeV proton beam of Phasotron. Combinations of ^{27}Al and ^{nat}Pb (Nuclotron experiments), and ^{59}Co and ^{nat}Pb (Phasotron experiments) activation samples were used due to their characteristics. ^{27}Al and ^{59}Co samples are mainly sensitive to neutrons, but ^{nat}Pb samples are sensitive just to protons and deuterons. The pairs of samples were located close to the primary beam passage, on the left and right sides of each QUINTA aluminium holders, and I studied the production of ^{57}Co, ^{58}Co, ^{60}Co, ^{205}Bi and ^{206}Bi isotopes using the activation techniques and the MCNPX 2.7.0 simulation code. The influence of the precision of the beam geometry description was confirmed. The simulation results for the bismuth products were generally worse than for the ^{24}Na product and cobalt isotopes. Bismuth products are formed mainly by reactions with the primary beam particles, and beyond the primary particles range of flight by reactions with charged particles from secondary processes. An excellent experiment-to-simulation agreement was reached for the ^{24}Na production in the Nuclotron experiments, where the average disagreement was around 33 %. Using the ^{27}Al and ^{59}Co samples for characterisation of neutron field is better in positions not close to the beam. In more remote positions, the contributions of charged particles are diminished and neutron contributions prevail [100]. Due to inaccuracies of the beam geometry, the activation samples positioned close to the beam are unsuitable for benchmarking of the Monte Carlo simulation codes. But they are very suitable for investigation of the beam geometry precision and study of its influence on neutron data not close to the primary beam.

The detected sensitivity to the precision of the primary beam geometry description naturally led to the need to quantify it. Therefore, I worked out the sensitivity analysis of simulation results for activation samples close to the primary beam using MCNPX 2.7.0. The analysis was performed for two of the QUINTA experiments at Phasotron by systematical changes of the beam position, by the beam shifting and deflecting. I also performed the analysis for samples located not close to the beam passage in QUINTA. It was proved that the neutron field in the remote positions could be advantageously studied using the activation samples because the effect of beam description inaccuracies is minimal. For this reason, these positions are also very suitable for Monte Carlo codes benchmarking. Based on the gained knowledge, by following simulation performances at the newly prepared BURAN setup, it was proved that the beam description inaccuracies would not seriously affect the future BURAN experiments and that the experiments would be very suited for the Monte Carlo simulation codes benchmarking. Predictions of the neutron behaviour characteristics in the future BURAN irradiations were also described using simulations. I studied average neutron flux in the setup, energy neutron spectra and neutron spectra hardness for different spallation targets and different high-energy beams.

Using MCNPX 2.7.0, neutron distributions inside QUINTA and BURAN and neutron leakage from the setups were studied and compared. Based on the results, it can be concluded that the experimental methodology used for QUINTA can also be applied to the future BURAN experiments due to comparable neutron fluxes inside the setups. Although, given that BURAN is composed of depleted uranium and due to its size, I would recommend enlarging dimensions of activation samples in the BURAN experiments, especially in very remote radial and/or longitudinal positions. The neutron leakage from BURAN irradiated by the 660 MeV protons of Phasotron was calculated as 14.5 % compared to 76.1 % for QUINTA.

A preparatory experiment for the forthcoming BURAN irradiations was performed. A potential lead spallation target of the setup was irradiated by the 660 MeV protons of Phasotron. I focused on the MCNPX 2.7.0 benchmarking by performing simulations for isotopes production in ^{nat}Pb activation samples placed inside the target. The experimental data were well described by the MCNPX 2.7.0 code.

The simulation results from the experiment with the lead target were also published in the peer-reviewed journal Nuclear Instruments and Methods in Physics Research Section A [160]. Some of my results from the E+T, QUINTA, sensitivity analysis and also BURAN investigations are supposed to be published in the peer-reviewed journal Indian Journal of Pure and Applied Physics. I submitted the manuscript of the paper and received a positive reviewer's report with a decision of recommendation for publication with minor revision needed. During my PhD study, I also regularly presented my results at international physics conferences. Some of the QUINTA and BURAN results were published in the conference papers [153, 154, 157].

Subsequently, the systematics of the E+T experiments, based on the simulation results given in this thesis, is supposed to be completed in the framework of our group at NPI. Another challenge is to expand the study of sensitivity analysis and to develop universal correction factors for the accelerator settings for the QUINTA experiments. Considering that all simulations presented in this thesis were performed employing the intranuclear cascade physics model INCL4.2, fission-evaporation model ABLA-KHSv3p, and standard cross-section data library ENDF/B-VII.1, it would be worthy of repeating the simulations employing different models and libraries and study the sensitivity to the simulation results. Likewise, to study the effect of usage of different sets of cross-sections used for evaluation of reaction rates by convolutions with simulated particle fluxes.

The experiments conducted at JINR are very beneficial for the ADS Research & Development. Investigation of the neutron behaviour and transport inside the model uranium setups irradiated by high-energy particle beams can provide us with essential nuclear neutron data. They also present an excellent possibility for the Monte Carlo codes benchmarking. Especially the future experiments at the BURAN setup are supposed to be ideal for such purpose because the accelerator settings uncertainties will not be critical, as was proved in this thesis. Testing of the simulation codes is vital for the ADS research because the precise description of the neutron characteristics is a cornerstone in the realisation of larger-scale ADS projects. The results presented in this thesis can also help the future ADS Research & Development.

References

[1] *Status of Accelerator Driven Systems Research and Technology Development*, IAEA TECDOC series, IAEA-TECDOC-1766, 2015. <https://www-pub.iaea.org/MTCD/Publications/PDF/TE-1766_web.pdf> (18.3.2020)

[2] Bowman C.D. et al., *Nuclear energy generation and waste transmutation using an accelerator-driven intense thermal neutron source*, Nuclear Instruments and Methods in Physics Research A, 320 (1992) 336.

[3] Rubbia C. et al., *Conceptual design of a fast neutron operated high power energy amplifier*, European Organization for Nuclear Research, 1995.

[4] *Accelerator Based Conversion of Surplus Plutonium*, < https://www.fas.org/sgp/othergov/doe/lanl/pubs/00326021.pdf > (18.3.2020)

[5] Lisowski P.W., *The Accelerator Production of Tritium Project*, in Proceedings of the Particle Accelerator Conference, Vancouver, British Columbia, Canada, IEEE, 97CB36167 (1997) 3780.

[6] *Euratom*, < https://ec.europa.eu/programmes/horizon2020/en/h2020-section/euratom > (18.3.2020)

[7] *FP5 - Fifth RTD Framework Programme*, < https://cordis.europa.eu/programme/id/FP5 > (18.3.2020)

[8] *n-TOF: The neutron time-of-flight facility at CERN*, < https://ntof-exp.web.cern.ch/ntof-exp/ > (18.3.2020)

[9] Meulders J.P. et al., *High and Intermediate Energy Nuclear Data for Accelerator Driven Systems - The HINDAS Project*, in Proceedings of the 6th Information Exchange Meeting on Actinide and Fission Product Partitioning and Transmutation, Madrid, Spain, Citeseer, 2000.

[10] Wallenius J., *CONFIRM: Collaboration on Nitride Fuel Irradiation and Modelling,* in Proceedings of the Nuclear Applications in the New Millenium, Reno, Nevada, USA, (2001) 11.

[11] Hugon M. et al., *Advanced concepts for waste management and nuclear energy production in the EURATOM Fifth Framework Programme*, in Proceedings of the Second Workshop on Advanced Reactors with Innovative Fuels, OECD, (2002) 481.

[12] *Sixth Framework Programme*, < https://ec.europa.eu/growth/sectors/space/research/fp6_en > (18.3.2020)

[13] Barreau G., *EFNUDAT, a network of European Facilities for NUclear DATa measurements devoted to nuclear waste transmutation*, in Proceedings of the International Conference on Nuclear Data for Science and Technology, EDP Sciences, (2007) 449.

[14] Knebel J.U., Fazio C., *European research programme for the transmutation of high level nuclear waste in an accelerator driven system (EUROTRANS)*, Kerntechnik, (2007) 22.

[15] Madic C., et al., *EUROPART: European Research Programme for Partitioning of Minor Actinides within High Active Wastes Issuing from the Reprocessing of Spent Nuclear Fuels*, in Proceedings of the Pacific Basin Nuclear Conference, Australian Nuclear Association, (2006) 710.

[16] Gudowski W. et al., *Impact of Partitioning, Transmutation and Waste Reduction Technologies on the Final Nuclear Waste Disposal (Red-Impact)*, in Proceedings of the 6th International Conference on EU Research and Training in Reactor Systems, Luxembourg, (2006) 13.

[17] *Seventh Framework Programme*, < https://wayback.archive-it.org/12090/20191127213419/https:/ec.europa.eu/research/fp7/index_en.cfm > (18.3.2020)

[18] Bruyn D. et al., *The FP7 Central Design Team Project: towards a fast-spectrum Transmutation experimental Facility*, in Proceedings of the 2010 International Congress on Advances in Nuclear Power Plants, San Diego, CA, USA, (2010) 10114.

[19] *FAbrication, Irradiation and Reprocessing of FUELS and targets for transmutation*, < https://cordis.europa.eu/project/id/232624 > (18.3.2020)

[20] *Horizon 2020*, < https://ec.europa.eu/programmes/horizon2020/en > (18.3.2020)

[21] *Commission Implementing Decision of 14.12.2018*, < https://ec.europa.eu/research/participants/data/ref/h2020/wp/2018-2020/euratom/h2020-wp1920-euratom_en.pdf > (18.3.2020)

[22] *Horizon 2020 projects - Euratom*, < https://cordis.europa.eu/search/en?q=content-type%3D%27project%27%20AND%20programme%2Fcode%3D%27H2020-Euratom%27&p=1&num=10&srt=Relevance:decreasing > (18.3.2020)

[23] *Spallation Neutron Source*, < https://neutrons.ornl.gov/sns > (18.3.2020)

[24] Fomin N. et al., *Fundamental Neutron Physics Beamline at the Spallation Neutron Source at ORNL*, Nuclear Instruments and Methods in Physics Research A, 773 (2015) 45.

[25] *European Spallation Source*, < https://europeanspallationsource.se/ > (18.3.2020)

[26] Chen H. et al., *Target station status of China Spallation Neutron Source*, Neutron News, 29 (2018) 2.

[27] *China's first spallation neutron source goes into operation*, < http://www.ecns.cn/news/sci-tech/2018-08-24/detail-ifyxikfc9641531.shtml > (18.3.2020)

[28] Joshi S.C. et al., *Development of Superconducting Cavities and Related Infrastructure for High Intensity Proton Linac for Spallation Neutron Source*, in Proceedings of the 27th Linear Accelerator Conference, Geneva, Switzerland, (2014) 1140.

[29] *Indian Spallation Neutron Source (ISNS) - Accelerator Physics Design*, < http://www.rrcat.gov.in/technology/accel/abps/isns.html > (18.3.2020)

[30] Latge C. et al., *MEGAPIE: the world's first high-power liquid metal spallation neutron source*, Thorium Energy for the World, (2016) 279.

[31] Bauer G.S., Salvatores M., Heusener G., *MEGAPIE: a 1 MW pilot experiment for a liquid metal spallation target*, Journal of Nuclear Materials, 296 (2001) 17.

[32] Fazio C. et al., *The MEGAPIE-TEST project: Supporting research and lessons learned in first-of-a-kind spallation target technology,* Nuclear Engineering and Design, 238 (2008) 1471.

[33] Wohlmuther M., Wagner W., *PIE preparation of the MEGAPIE target*, Journal of Nuclear Materials, 431 (2012) 10.

[34] Hammer-Rotzler B. et al., *Distribution and surface enrichment of radionuclides in lead-bismuth eutectic from spallation targets*, The European Physical Journal Plus, 131 (2016) 233.

[35] *MYRRHA*, < https://myrrha.be/ > (18.3.2020)

[36] *SCK CEN: Technology*, < https://www.sckcen.be/en/expertises/technology > (18.3.2020)

[37] Abderrahim A.H. et al., *MYRRHA, a Multipurpose hYbrid Research Reactor for High-end Applications*, Nuclear Physics News, 20 (2010) 24.

[38] Mueller A.C., *Transmutation of Nuclear Waste and the future MYRRHA Demonstrator*, Journal of Physics: Conference Series, 420 (2013) 012059.

[39] *Transmutation Experimental Facility (TEF)*, < https://j-parc.jp/Transmutation/en/index.html > (18.3.2020)

[40] *Introduction to ADANES Research in China*, < http://english.imp.cas.cn/Work2017/CI2017/ > (18.3.2020)

[41] Yan X. et al., *Concept of an accelerator-driven advanced nuclear energy system*, Energies, 10 (2017) 944.

[42] Vasilkov R.G. et al., *Neutron yields and thermal neutron fluxes in a lead-water system bombarded by high energy protons*, Atomic Energy, 25 (1968) 1307.

[43] Chudoba P., *Využití aktivačních detektorů při měření neutronového pole v modelových sestavách ADTS*, Master thesis, Faculty of Mathematics and Physics, Charles University, Prague, Czech Republic, 2013. (in Czech)

[44] Adam J. et al., *Transmutation studies with GAMMA-2 setup using relativistic proton beams of the JINR Nuclotron*, Nuclear Instruments and Methods in Physics Research A, 562 (2006) 741.

[45] Westmeier W. et al., *Transmutation experiments on* ^{129}I*,* ^{139}La *and* ^{237}Np *using the Nuclotron accelerator*, Radiochimica Acta/International journal for chemical aspects of nuclear science and technology, 93 (2005) 65.

[46] Adam J. et al., *Свинцово-графитовая установка «Гамма-3» для исследования трансмутации долгоживущих радионуклидов на пучках частиц нуклотрона ЛФВЭ ОИЯИ. Ч.1. Конструкция. Определение потока нейтронов в расчете на один дейтрон с энергией 2,33 ГэВ*, JINR Preprint, P1-2010-102, 2010. (in Russian)

[47] Svoboda O., *Experimental study of neutron production and transport for ADTT*, Dissertation thesis, Faculty of Nuclear Sciences and Physical Engineering, Czech Technical University in Prague, Prague, Czech Republic, 2011.

[48] Krivopustov M.I. et al., *About the First Experiment on Investigation of* ^{129}I*,* ^{237}Np*,* ^{238}Pu *and* ^{239}Pu *Transmutation at the Nuclotron 2.52 GeV Deuteron Beam in Neutron Field Generated in U/Pb-Assembly "Energy plus Transmutation"*, JINR Preprint, E1-2007-7, 2007.

[49] Krása A., *Neutron Emission in Spallation Reactions of 0.7 - 2.0 GeV Protons on Thick Lead Target Surrounded by Uranium Blanket*, Dissertation thesis, Faculty of Nuclear Sciences and Physical Engineering, Czech Technical University in Prague, Prague, Czech Republic, 2008.

[50] Krivopustov M.I. et al., *First experiments with a large uranium blanket within the installation „Energy plus Transmutation“ exposed to 1.5 GeV protons*, Kerntechnik, 68 (2003) 48.

[51] Krivopustov M.I., Chultem D., *Experiments on electronuclear technology and transmutation of nuclear waste using synchrophasotron beams*, JINR News, 3 (1998) 27.

[52] Krivopustov M.I. et al., *Modeling of the Electronuclear Method of Energy Production and Study of Radioactive Waste Transmutation Using a Proton Beam of the JINR Synchrophasotron/Nuclotron*, JINR Communication, (1999) 135.

[53] Adam J. et al., *First nuclear activation experiments using the new accelerator NUCLOTRON in Dubna*, Kerntechnik, 68 (2003) 214.

[54] Zamani-Valasiadou M. et al., *Neutron Generation in the New Transmutation Setup "Energy plus Transmutation" in Dubna*, Nuclear Instruments and Methods in Physics Research A, 508 (2003) 454.

[55] Hashemi-Nezhad S.R. et al., *Experimental Studies and Monte-Carlo Computer Simulation of Space Distribution of Neutrons Generated in the Electronuclear System*, Radiation Measurements, 36 (2003) 295.

[56] Malakhov A.I. et al., *Relativistic nuclear physics at the Joint Institute for Nuclear Research*, Physics of Particles and Nuclei, 33 (2007) 407.

[57] Krása A. et al., *Neutron production in spallation reactions of 0.9 and 1.5 GeV protons on a thick lead target. Comparison between experimental data and Monte-Carlo simulations*, JINR Preprint, E1-2005-46, 2005.

[58] Svoboda O. et. al., *Study of Spallation Reactions, Neutron Production and Transport in Thick Lead Target and Uranium Blanket Irradiated with 0.7 GeV Protons*, JINR Preprint, E15-2009-177, 2009.

[59] Krása A. et al., *Neutron Emission in the Spallation Reactions of 1 GeV Protons on a Thick Lead Target Surrounded by Uranium Blanket*, JINR Preprint, E15-2007-81, 2007.

[60] Křížek F. et al., *The study of spallation reactions, neutron production, and transport in a thick lead target and a uranium blanket during 1.5 GeV proton irradiation*, Czechoslovak Journal of Physics, 56 (2006) 243.

[61] Krása A. et al., *Neutron Production in p + Pb/U at 2 GeV*, JINR Preprint, E1-2009-195, 2009.

[62] Svoboda O. et al., *Neutron production in Pb/U assembly irradiated by protons and deuterons at 0.7-2.52 GeV*, in Proceedings of the International Conference on Nuclear Data for Science and Technology, Nice, France, EDP Sciences, (2007) 1197.

[63] Zamani-Valasiadou M. et al., *Performance of a Pb-spallation target surrounded by a U-blanket during irradiations with 1.6 and 2.5 GeV deuteron beams: Comparison with relativistic proton beams*, Annals of Nuclear Energy, 37 (2010) 241.

[64] Borger J.J. et al., *Studies of the neutron field of the Energy plus Transmutation set-up under 4 GeV deuteron irradiation*, Radiation Measurements, 46 (2011) 1765.

[65] Svoboda O. et al., *The Study of Spallation Reactions, Neutron Production and Transport in a Thick Lead Target and Uranium Blanket during 1.6 and 2.52 GeV Deuteron Irradiation*, JINR Preprint, E15-2011-39, 2011.

[66] Suchopár M. et al., *Activation measurement of neutron production and transport in a thick lead target and a uranium blanket during 4 GeV deuteron irradiation*, Nuclear Instruments and Methods in Physics Research A, 908 (2018) 347.

[67] Krivopustov M.I. et al., *First results studying the transmutation of* ^{129}I, ^{237}Np, ^{238}Pu *and* ^{239}Pu *in the irradiation of an extended natU/Pb-assembly with 2.52 GeV deuterons*, Journal of Radioanalytical and Nuclear Chemistry, 279 (2008) 567.

[68] Adam J. et al., *A study of nuclear transmutation of Th and nat U with neutrons produced in a Pb target and U blanket irradiated by 1.6 GeV deuterons*, The European Physical Journal A, 43 (2010) 159.

[69] Krivopustov M.I. et al., *Investigation of Neutron Spectra and Transmutation of* ^{129}I*,* ^{237}Np *and Other Nuclides with 1.5 GeV Protons from the Nuclotron Using the Electronuclear "Energy plus Transmutation" Setup*, JINR Preprint, E1-2004-79, 2004.

[70] Brandt R. et al., *Accelerator driven systems for transmutation and energy production: challenges and dangers*, Kerntechnik, 69 (2004) 37.

[71] McKinney G. et al., *MCNPX 2.6x features*, LANL report, LA-UR-07-2053, 2007.

[72] Meer K. et al., *Spallation yields of neutrons produced in thick lead/bismuth targets by protons at incident energies of 420 and 590 MeV*, Nuclear Instruments and Methods in Physics Research B, 217 (2004) 202.

[73] Beckurts K.H., Wirtz K., *Neutron Physics*, Springer-Verlag, New York, USA, 1964.

[74] Waters L.S., *MCNPX User's Manual, Version 2.4.0*, LANL report, LA-CP-02-408, 2002.

[75] Hendricks J.S., *MCNPX User's Manual, Version 2.6.C*, LANL report, LA-UR-06-7991, 2006.

[76] Prael R.E., Lichtenstein H., *User Guide to LCS: The LAHET code system*, LANL report, LA-UR-89-3014, 1989.

[77] Briesmeister J.F., *MCNP - A General Monte Carlo N-Particle Transport Code Version 4B*, LANL report, LA-12625-M, 1997.

[78] Waters L.S., *MCNPX User's Manual, Version 2.3.0*, LANL report, LA-UR-02-2607, 2002.

[79] Pelowitz D.B., *MCNPX User's Manual, Version 2.7.A*, LANL report, LA-UR-08-07182, 2008.

[80] Pelowitz D.B., *MCNPX User's Manual Version 2.7.0*, LANL report, LA-CP-11-00438, 2011.

[81] Krása A. et al., *Neutron production in a Pb/U-setup irradiated with 0.7-2.5 GeV protons and deuterons*, Nuclear Instruments and Methods in Physics Research A, 615 (2010) 70.

[82] Majerle M. et al., *Monte Carlo Studies of the "Energy plus Transmutation" System*, JINR Preprint, E15-2007-82, 2007.

[83] Wagner V. et al., *Cross-section studies of important neutron and relativistic deuteron reactions*, Journal of Physics: Conference Series, 533 (2014) 012052.

[84] Vrzalová J. et al., *Studies of (n,xn) cross-sections in Al, Au, Bi, Cu, Fe, I, In, Mg, Ni, Ta, Y, and Zn by the activation method*, Nuclear Instruments and Methods in Physics Research A, 726 (2013) 84.

[85] Chudoba P. et al., *Activation Measurements of Cross Sections for Ground and Isomeric States Production in Neutron Threshold Reactions on Y and Au*, Nuclear Science and Engineering, 191 (2018) 150.

[86] Chudoba P., *Study of reaction cross-sections important for advanced nuclear systems*, Dissertation thesis, Faculty of Mathematics and Physics, Charles University, Prague, Czech Republic, 2018.

[87] Vrzalová J., *Experimentální určení účinných průřezů neutronových reakcí důležitých pro urychlovačem řízené transmutační systémy*, Dissertation thesis, Faculty of Nuclear Sciences and Physical Engineering, Czech Technical University in Prague, Prague, Czech Republic, 2015. (in Czech)

[88] Suchopár M., *Study of neutron production and transport in systems based on spallation reactions*, Dissertation thesis, Faculty of Nuclear Sciences and Physical Engineering, Czech Technical University in Prague, Prague, Czech Republic, 2016.

[89] Křížek F., *Studium tříštivých reakcí, produkce a transportu neutronů v terčích vhodných pro produkci neutronů k transmutacím*, Master thesis, Faculty of Mathematics and Physics, Charles University, Prague, Czech Republic, 2004. (in Czech)

[90] Svoboda O., *Stanovení rozložení neutronů v sestavě složené z olověného terče a uranového blanketu postavené na svazku protonů s energií 0.7 GeV*, Master thesis, Faculty of Nuclear Sciences and Physical Engineering, Czech Technical University in Prague, Prague, Czech Republic, 2006. (in Czech)

[91] Majerle M., *Monte Carlo methods in spallation experiments*, Dissertation thesis, Faculty of Nuclear Sciences and Physical Engineering, Czech Technical University in Prague, Prague, Czech Republic, 2009.

[92] Katovský K., *Studium sekundárních neutronů a jader vznikajících při reakcích protonů a neutronů v terčích z uranu a plutonia*, Dissertation thesis, Faculty of Nuclear Sciences and Physical Engineering, Czech Technical University in Prague, Prague, Czech Republic, 2008. (in Czech)

[93] Furman W.I. et al., *Recent results of the study of ADS with 500 kg natural uranium target assembly QUINTA irradiated by deuterons with energies from 1 to 8 GeV at JINR NUCLOTRON*, in Proceedings of the XXI International Baldin Seminar on High Energy Physics Problems, Dubna, Russia, PoS, 173 (2012) 086.

[94] Zeman M., *Experimentální výzkum urychlovačem řízených jaderných reaktorů pro thoriovou jadernou energetiku*, Master thesis, Faculty of Electrical Engineering and Communication, Brno University of Technology, Brno, Czech Republic, 2015. (in Czech)

[95] Voronko V.A. et al., *Estimation of the beam power gain for deep-subcritical uranium assembly QUINTA under relativistic proton, deuteron and carbon nuclei irradiation*, Вопросы атомной науки и техники, 115 (2018) 183.

[96] Adam J. et al., *Study of Deep Subcritical Electronuclear Systems and Feasibility of Their Application for Energy Production and Radioactive Waste Transmutation*, JINR Preprint, E10-2010-61, 2010.

[97] Artiushenko M.Yu. et al., *Monitoring of high energy deuteron beams in the experiments with massive targets*, Вопросы атомной науки и техники, 91 (2014) 186.

[98] Zhuk I.V. et al., *Off-line Technique for Deuteron Beam Parameters Determination using Solid State Nuclear Track Detectors. Experiments at the QUINTA Target (Dubna, Russia, VBLHEP JINR). Nuclotron RUN 46 results(December 2012)*, in Proceedings of the 12th International School-Seminar on The Actual Problems of Microworld Physics, Gomel, Belarus, 1 (2015) 181.

[99] Artiushenko M.Yu. et al., *Measuring deuteron beam parameters with solid-state track detectors in experiments with the QUINTA target assembly*, Physics of Particles and Nuclei Letters, 10 (2013) 544.

[100] Závorka L. et al., *Characterization of a mixed high-energy spallation neutron–proton field using monoisotopic activation detectors*, Nuclear Instruments and Methods in Physics Research A, 903 (2018) 246.

[101] Adam J. et al., *Secondary particle distributions in an extended uranium target under irradiation by proton, deuteron, and carbon beams*, Nuclear Instruments and Methods in Physics Research A, 872 (2017) 87.

[102] Asquith N.L. et al., *Activation of* ^{197}Au *and* ^{209}Bi *in a fast spectrum sub-critical assembly composed of 500 kg natural uranium irradiated with 1 and 4 GeV deuterons*, Annals of Nuclear Energy, 63 (2014) 742.

[103] Bielewicz M. et al., *Determining the Fast Neutron Flux Density and Transmutation Level Measurements in ADS by the Use of a Threshold Nuclear Reaction*, Physics of Particles and Nuclei Letters, 15 (2018) 516.

[104] Artiushenko M.Yu. et al., *Investigation of the spatial and energy distributions of neutrons in the massive uranium target irradiated by deuterons with energy of 1. . . 8 GeV*, Вопросы атомной науки и техники, 88 (2013) 170.

[105] Zeman M. et al., *Experimental investigation of the radionuclides produced in massive spallation target*, in Proceedings of the 19th International Scientific Conference on Electric Power Engineering, Brno, Czech Republic, IEEE, (2018) 532.

[106] Adam J. et al., *Study of secondary neutron interactions with* ^{232}Th *,* ^{129}I*, and* ^{127}I *nuclei with the uranium assembly "QUINTA" at 2, 4, and 8 GeV deuteron beams of the JINR Nuclotron accelerator*, Applied Radiation and Isotopes, 107 (2016) 225.

[107] Khushvaktov J.H. et al., *Interactions of secondary particles with thorium samples in the setup QUINTA irradiated with 6 GeV deuterons*, Nuclear Instruments and Methods in Physics Research B, 381 (2016) 84.

[108] Závorka L. et al., *Neutron-induced transmutation reactions in* ^{237}Np*,* ^{238}Pu*, and* ^{239}Pu *at the massive natural uranium spallation target*, Nuclear Instruments and Methods in Physics Research B, 349 (2015) 31.

[109] Hashemi-Nezhad S.R. et al., *Transmutation of uranium and thorium in the particle field of the Quinta sub-critical assembly*, Nuclear Instruments and Methods in Physics Research A, 883 (2018) 96.

[110] Suchopár M. et al., *Cross-section studies of relativistic deuteron reactions on copper by activation method*, Nuclear Instruments and Methods in Physics Research B, 344 (2015) 63.

[111] Wagner V. et al., *Nuclear data for advanced nuclear systems*, in Proceedings of the XXII International Baldin Seminar on High Energy Physics Problems, Dubna, Russia, PoS, 225 (2015) 057.

[112] Wagner V. et al., *Studies of deuteron and neutron cross-sections important for ADS research*, in Proceedings of the XXI International Baldin Seminar on High Energy Physics Problems, Dubna, Russia, PoS, 173 (2013) 090.

[113] Khushvaktov J.H. et al., *Monte Carlo simulations and experimental results on neutron production in the uranium spallation target QUINTA irradiated with 660 MeV protons*, Applied Radiation and Isotopes, 137 (2018) 102.

[114] Závorka L. et al., *Validation of Monte Carlo simulation of neutron production in a spallation experiment*, Annals of Nuclear Energy, 80 (2015) 178.

[115] Suchopár M. et al., *Monte carlo simulations of Yttrium reaction rates in Quinta uranium target*, in Proceedings of the XXIII International Baldin Seminar on High Energy Physics Problems, Dubna, Russia, EPJ, 138 (2017) 10003.

[116] Suchopár M. et al., *Monte Carlo Simulations of Natural Uranium Setups Irradiated With Relativistic Deuterons by Means of MCNPX Code*, in Proceedings of the XXI International Baldin Seminar on High Energy Physics Problems, Dubna, Russia, PoS, 173 (2013) 091.

[117] Adam J. et al., *Measurement of the high energy neutron flux on the surface of the natural uranium target assembly QUINTA irradiated by deuterons of 4 and 8 GeV energy*, Physics Procedia, 80 (2015) 94.

[118] Svoboda J. et al., *Process of heat generation and its transfer monitoring at uranium spallation target QUINTA*, in Proceedings of the 19th International Scientific Conference on Electric Power Engineering, Brno, Czech Republic, IEEE, (2018) 522.

[119] Svoboda J. et al., *Neutron Flux Determination by High Accuracy Temperature Measurement*, in Proceedings of the 26th International Nuclear Physics Conference, Adelaide, Australia, PoS, 281 (2017) 116.

[120] Svoboda, J., et al. *Determination of the neutron flux by the temperature differences at the massive spallation uranium target QUINTA*, in Proceedings of the 17th International Scientific Conference on Electric Power Engineering, Prague, Czech Republic, IEEE, (2016) 582.

[121] Král, D., *Studium využití thoria v jaderných reaktorech řízených urychlovačem*, Master thesis, Faculty of Electrical Engineering and Communication, Brno University of Technology, Brno, Czech Republic, 2017. (in Czech)

[122] Závorka L., *Transmutation of Actinides Using Spallation Reactions*, Dissertation thesis, Faculty of Nuclear Sciences and Physical Engineering, Czech Technical University in Prague, Prague, Czech Republic, 2015.

[123] Wagner V. et al., *The intensity of the deuteron beams on Quinta setup during 2011/2012/2013 experimental campaign*, E&T RAW internal reports, 2011-2013.

[124] Zhuk I.V. et al., *Deuteron beam parameters measurements of the Nuclotron using SSNTD*, E&T RAW internal reports, 2011-2013.

[125] Vespalec R. et al., *The Beam Intensity Determination - QUINTA Phasotron*, E&T RAW internal reports, 2015-2017.

[126] Adam J. et al., *Positions of Samples*, E&T RAW internal documents, 2013-2017.

[127] Artiushenko M.Yu. et al., *Comparison of neutron-physical characteristics of uranium target of assembly "QUINTA" irradiated by relativistic deuterons and* ^{12}C *nuclei*, Вопросы атомной науки и техники, 103 (2016) 74.

[128] Schwarz A.L., Schwarz R.A., Carter L.L., *MCNP/MCNPX Visual Editor Computer Code Manual for Vised Version 24E*, LANL, 2011.

[129] Adam J. et al., *Spallation neutron spectrum on a massive lead/paraffin target irradiated with 1 GeV protons*, European Physics Journal A, 23 (2005) 61.

[130] Kadykov M.G. et al., *Восстановление спектра быстрых нейтронов методом деформации опорного спектра, представляемой в виде функции разложения по полиномам лежандра*, Писма в ЭЧАЯ, 10 (2013) 936. (in Russian)

[131] Dem'yanov A.V. et al., *JINR Phasotron and its Beams*, in Proceedings of the XIII Meeting on Particle Accelerators, Dubna, Russia, JINR, D9-92-380, 1992.

[132] Malakhov A.I., *Research program for the Nuclotron*, Nuclear Physics A, 743 (2004) 82.

[133] Smirnov A.A., Kovalenko A.D., *НУКЛОТРОН - Сверхпроводящий ускоритель ядер в ЛВЭ ОИЯИ (создание, работа и развитие)*, Писма в ЭЧАЯ, 1 (2004) 11. (in Russian)

[134] *Genie 2000 Spectroscopy Software, version 3.3, Operations Manual*, Canberra Industries, 2012.

[135] *MAESTRO-32, MCA Emulator for Microsoft Windows 2000 Professional and XP Professional, version 6.0, Software User's Manual*, Advanced Measurement Technology, ORNL, 2006.

[136] Debertin K., Helmer R.G., *Gamma-and X-ray spectrometry with semiconductor detectors*, Science Publishers B.V., 1988.

[137] Sudár S., *USER GUIDE TrueCoinc: A program for calculation of true coincidence correction for gamma rays*, Institute of Experimental Physics, University of Debrecen, Debrecen, Hungary, 1999-2009. < http://kisfiz.phys.klte.hu/kisfiz/sudar/TrueCoinc/UserGuide.pdf > (18.3.2020)

[138] Majerle M. et al., *Monte Carlo method in neutron activation analysis*, JINR Preprint, E11-2009-178, 2009.

[139] Frána J., *Program DEIMOS32 for gamma-ray spectra evaluation*, Journal of Radioanalytical and Nuclear Chemistry, 257 (2003) 583.

[140] Vespalec R. et al., *YASNAPP-2 Program Package for Data Analysis 1.4 (YAp.1.4): User's Manual*, E&T RAW internal document, 2016.

[141] Adam J. et al., *Software for Calculating Nuclear Reaction Cross Sections*, Measurement Techniques, 44 (2001) 93.

[142] Flanagan D., Matsumoto Y., *The Ruby Programming Language*, O'Reilly Media, 2008.

[143] Boudard A. et al., *Intranuclear cascade model for a comprehensive description of spallation reaction data*, Physical Review C, 66 (2002) 044615.

[144] Gaimard J.J., Schmidt K.H., *A reexamination of the abrasion-ablation model for the description of the nuclear fragmentation reaction*, Nuclear Physics A, 531 (1991) 709.

[145] Junghans A.R. et al., *Projectile-fragment yields as a probe for the collective enhancement in the nuclear level density*, Nuclear Physics A, 629 (1998) 635.

[146] Chadwick M. et al., *ENDF/B-VII.1 Nuclear data for science and technology: Cross sections, covariances, fission product yields and decay data*, Nuclear Data Sheets, 112 (2011) 2887.

[147] Koning A., Hilaire S., Goriely S., *TALYS-1.6: A Nuclear Reaction Program*, User Manual, NRG, 2003.

[148] Koning A., Hilaire S., Goriely S., *TALYS-1.8: A Nuclear Reaction Program*, User Manual, NRG, 2015.

[149] *Experimental Nuclear Reaction Data (EXFOR)*, < https://www-nds.iaea.org/exfor/exfor.htm > (18.3.2020)

[150] Mashnik S.G. et al., *CEM03.03 and LAQGSM03.03 Event Generators for the MCNP6, MCNPX, and MARS15 Transport Codes*, LANL report, LA-UR-08-2931, 2008.

[151] Zhuk I.V. et al., *Determination of high-energy deuteron beam profile and spatial distribution of high-energy neutrons in a U/Pb assembly under 1.26 GeV/nucleon deuteron irradiation*, Radiation Measurements, 43 (2008) 199.

[152] Westmeier W. et al., *Experiment S: 4.00 GeV deuterons on E+T, Technical Report*, Internal publication for E&T RAW collaboration, 2011.

[153] Tichý P. et al., *Determination and Monte Carlo Simulations of Neutron Flux inside Spallation Target QUINTA*, in Proceedings of the 26th International Nuclear Physics Conference, Adelaide, Australia, PoS, 281 (2017) 115.

[154] Tichý P. et al., *Experimental Investigation and Monte Carlo Simulations of Radionuclide Production inside the Uranium Spallation Target QUINTA Irradiated with a 660-MeV Proton Beam*, in Proceedings of the XXIV International Baldin Seminar on High Energy Physics Problems, Dubna, Russia, EPJ, 204 (2019) 04003.

[155] Wan J.S. et al., *Transmutation of radioactive waste by means of relativistic heavy ions*, Kerntechnik, 63 (1998) 167.

[156] Adam J., personal communication (5.10.2016)

[157] Tichý P., Suchopár M., *Future usage of quasi-infinite depleted uranium target (BURAN) for benchmark studies*, in Proceedings of the XXII International Baldin Seminar on High Energy Physics Problems, Dubna, Russia, PoS, 225 (2015) 065.

[158] *WolphramAlpha: Computational Knowledge Engine*, < http://www.wolframalpha.com > (18.3.2020)

[159] *Polynomials & Scientific Calculator*, < https://xrjunque.nom.es/polycalc.aspx > (18.3.2020)

[160] Khushvaktov J.H., Tichý P. et al., *Study of the residual nuclei generation in a massive lead target irradiated with 660 MeV protons*, Nuclear Instruments and Methods in Physics Research A, 959 (2020) 163542.

[161] Saloman E.B., Hubbell J.H., *X-ray attenuation coefficients (total cross sections): Comparison of the experimental data base with the recommended values of Henke and the theoretical values of Scofield for energies between 0. 1-100 keV*, National Bureau of Standards, Center for Radiation Research, Washington DC, USA, 1986.

[162] Chu S.Y.F., Ekström L.P., Firestone R.B., *The Lund/LBNL Nuclear Data Search, version 2.0*, 1999. < http://nucleardata.nuclear.lu.se/toi/ > (18.3.2020)

Appendix A - Program package for reaction rate determination

TailCor This program deals with the problem of fitting one peak in the spectrum as a composition of a full-energy peak and a tail generated by improper charge collection in a detector. TailCor counts impulses in the two fits and considers them as one peak. Other parameters of the new summed peak are taken from the peak fit with greater area.

TimeConst TimeConst reads the DEIMOS32 output files and creates an RBScripts.INP file from which the following programs take data. The user inserts date and time of the beginning and irradiation end and TimeConst calculates the time between the irradiation end and start of measurement. Then the user needs to write down some other parameters into the created RBScripts.INP file such as the integral beam intensity, integral beam intensity uncertainty, time of irradiation and beam correction data file.

NonLin64 Because the linear description of energy-channel dependence (described in section 2.1) is just approximate and not as accurate as it should be, there is a need to perform non-linearity corrections for that deviations. The NonLin64 program uses linearity deviation functions and non-linearity function parameters of every individual detector.

Puregam Puregam deals with the background radioactivity. The program package also includes a background library file Background.lib, which contains previously measured background radiation in the laboratory. Puregam compares the peaks from the *.cor output files from NonLin64 with the peaks from the Background.lib library and subtracts the background from every peak from the *.cor output files that meet at least one of the following conditions

$$\mid E_\gamma - E_\gamma^{bcg} \mid < n \cdot \sqrt{a^2 + (\Delta E_\gamma)^2 + (\Delta E_\gamma^{bcg})^2} \tag{30}$$

and/or

$$\mid E_\gamma - E_\gamma^{bcg} \mid < m \cdot FWHM(E_\gamma) \tag{31}$$

where E_γ is the energy of the *.cor gamma peak, $\Delta\mathrm{E}_\gamma$ is its relative uncertainity, FWHM(E_γ) is the full energy width at half maximum of the gamma peaks, E_γ^{bcg} is the background peak energy with uncertainity $\Delta\mathrm{E}_\gamma^{bcg}$, a = 0.15 keV stands for the non-linearity correction factor (the value of a was assessed based on the previous experience of the JINR work-group), n ≈ 2 is the variable taking statistics into consideration and the constant m ≈ 2 deals with non-Gaussian profile of the fitted peaks.

The background of the peaks is calculated according to the following equations

$$S_{bcg}^{cnt}(E_\gamma) = K_{norm} \cdot S_{bcg}(E\gamma) \tag{32}$$

$$K_{norm} = \frac{t_{live,spec}}{t_{live,bcg}} \tag{33}$$

where $S_{bcg}^{cnt}(E_\gamma)$ is the background peak contribution, $S_{bcg}(E_\gamma)$ is the area of the background peak, K_{norm} represents the normalisation constant calculated as a ratio of the background measurement time $t_{live,spec}$ to spectrum measurement time $t_{live,bcg}$.

SepDepe When a gamma-ray energy is higher than 1022 keV, interactions by electron-positron pairs come into existence. The newly formed particles are decelerated in the matter, and when the kinetic energy of the positron becomes nearly zero, the positron annihilates and two photons of energy 511 keV are created. At HPGe detectors, there is always a high probability that at least one of the photons leaves detector. When one photon leaves, the total absorption peak is shifted 511 keV towards lower energies and we observe single-escape peak (SEP) in the spectrum. When both formed photons leave, the energy peak is shifted 1022 keV towards lower energies and we observe double-escape peak (DEP).

For the SEP $S(E_{SEP})$ and DEP $S(E_{DEP})$ areas, the following equations are valid

$$S(E_{SEP}) = S(E_\gamma) \cdot \epsilon_{SEP}(E_\gamma) \tag{34}$$

$$S(E_{DEP}) = S(E_\gamma) \cdot \epsilon_{DEP}(E_\gamma) \tag{35}$$

where $S(E_\gamma)$ is the the full-energy peak area, $\epsilon_{SEP}(E_\gamma)$ is the single-escape peak to full-energy peak ratio and $\epsilon_{DEP}(E_\gamma)$ is the double-escape peak to full-energy peak ratio. Energy dependence of the $\epsilon_{SEP}(E_\gamma)$ to $\epsilon_{DEP}(E_\gamma)$ ratios were investigated in individual experiments. According to the functions found, it is possible to determine the $S(E_{SEP})$ and $S(E_{DEP})$ areas for every measured $S(E_\gamma)$ area. It was also noticed that the $\epsilon_{SEP}(E_\gamma)$ to $\epsilon_{DEP}(E_\gamma)$ ratios are independent on the distance of the sample to detector.

SepDepe determines the single-escape and double-escape peak areas and subtracts them from the measured spectrum.

EffCor The EffCor program determines the correction factor $\varepsilon_p(E_\gamma)$ for the full-energy peak efficiency of the detector

$$\varepsilon_p(E_\gamma) = exp\left(a_0 + \sum_{i=1}^{N} a_i ln^i(E_\gamma)\right) \tag{36}$$

where E_γ is the gamma peak energy, a_i stand for parameters of the efficiency function, and N is the polynomial function degree. The coefficients a_i are calculated by the EFFEKT5 program using results of calibration standards measurements.

AttCor Some gamma rays emitted by a sample can be self-absorbed due to the sample thickness. Another factor influencing the number of self-absorbed gamma rays is the sample material. Let us consider a plain gamma source with homogeneous distribution emitting particles into a solid angle. Let t is the source thickness and A_0 the source activity. Then the number of gamma particles N emitted can be expressed as

$$N = \int_0^t \frac{A_0 \cdot exp\left(-\mu(E_\gamma) \cdot x\right)}{t} dx = A_0 \cdot \frac{1 - exp\left(-\mu(E_\gamma) \cdot x\right)}{\mu(E_\gamma) \cdot t} \tag{37}$$

where $\mu(E_\gamma)$ is the linear attenuation coefficient (values are given for various gamma energies E_γ in [161]). The correction factor $C_{abs}(E_\gamma)$ is then given as

$$C_{abs}(E_\gamma) = 1 - \frac{1 - exp\,(-\mu(E_\gamma) \cdot t)}{\mu(E_\gamma) \cdot t} \tag{38}$$

Because linear attenuation coefficients cannot be tabulated for all gamma energies used, there is a need to make an interpolation. AttCor calculates the self-absorption factors $C_{abs}(E_\gamma)$ for tabulated energies E_γ and creates a self-absorption function by fitting the factors

$$C_{abs}(E_\gamma) = exp\left(k_0 + \sum_{i=1}^{N} k_i ln^i(E_\gamma)\right) \tag{39}$$

MidLit7 The program identifies the individual gamma lines from the AttCor *.rss output files. The user has to prepare a library *.lib containing gamma line energies E_γ^{lib} and their uncertainties ΔE_γ^{lib}, intensities I_γ and uncertainties ΔI_γ, and half-life times $T_{1/2}$ (these data were taken from [162]). In the library, there also have to be pointed the gamma line $E_{\gamma,max}^{lib}$ with the highest intensity $I_{\gamma,max}$ for every isotope from the library.

If the gamma line $E_{\gamma,max}^{lib}$ for a particular library isotope is not found in the spectrum, then it is assumed that the other gamma lines cannot be found too. In such case, Midlit7 concludes that the isotope is not present in the spectrum. In the opposite case, when the gamma line $E_{\gamma,max}^{lib}$ is found, the program looks for the other gamma lines. A particular gamma line E_γ is denoted as $E_{\gamma,max}^{lib}$ or E_γ^{lib} under the following condition

$$\mid E_\gamma - E_{\gamma,max}^{lib} \mid < 0.2 \cdot \left(1 + \frac{E_\gamma}{3000}\right) + 2 \cdot \sqrt{\left(\Delta E_{\gamma,max}^{lib}\right)^2 + (\Delta E_\gamma)^2} + FWHM(E_\gamma) \tag{40}$$

where $FWHM(E_\gamma)$ is the full energy width at half maximum of the E_γ line.

BeamCor If the accelerator beam is unstable during irradiation, the correction factor is calculated by the BeamCor program. The correction has to be performed in case of using the JINR Nuclotron accelerator. In case of the JINR Phasotron accelerator, the correction can be neglected due to the high beam stability during the whole irradiation time. The correction factor calculation is based on dividing the total beam time into short time intervals.

TransCs9 The TransCs9 program calculates the reaction rates R according to the equations (5) and (6).

SigmaJ7 The last program from the JINR workgroup package is SigmaJ7. The program searches for the same gamma lines of the isotopes created in the sample from different sets of the sample measurements and puts them together. From the groups found, it calculates weighted averages of the TransCs9 reaction rates according to the equations (12) - (15). Also, total weighted averages from all reaction rates of a certain isotope are calculated.

Appendix B - Example of MCNPX input file

This is an example of an MCNPX input file used in this thesis. Specifically, the proton flux simulation on the central longitudinal axis of the lead target in the longitudinal range from 20 to 40 cm. For this particular simulation, the MCNPX lead target model was simplified to a continuous lead cylinder of 100 cm in length and 19 cm in diameter, and the MESH tally function [80] was applied. The results are given in Fig. 72.a.

```
c cell card
1 2 -11.35 -1 2 -3 $ Pb target
99 1 -1.292e-3 (1:-2:3) -99 $ air outside
100 0 99

c surface card
1 cz 9.5
2 pz 0
3 pz 100
99 so 200

c data card
mode n h / d
imp:n,h,/,d 1 1r 0
phys:n 800 3j -1
phys:h 800 j -1
phys:d 800
phys:/ 800
m1 7014 -0.755 8016 -0.232 18000.42c -0.013 hlib=70h nlib=70c $ air
m2 82204 1.4 82206 24.1 82207 22.1 82208 52.4 hlib=70h nlib=70c $ Pb
tmesh
rmesh1:h flux
cora1 -2 2
corb1 -2 2
corc1 20 99i 40
endmd
c physics models INCL4+ABLA
lca 6j 1 j 2
lea 6j 2
stop nps 5e8
prdmp j 1e8 1 j 1e8
c 660 MeV proton beam, gaussian spatial profile
sdef dir 1 vec 0 0 1 x d1 y d2 z -100 tr 3 par h erg 660
sp1 -41 3.38 0
sp2 -41 3.71 0
tr3 0 0 0  1 0 0  0 1 0  0 0 1
```

Appendix C - Experimental and simulated reaction rates from the E+T experiments

The values given in the following tables are meant to be used for further calculations. Their format (number of valid digits), therefore, does not follow the standard guidelines.

Table 9: Experimental and simulated reaction rates of studied isotopes in the ^{209}Bi samples from the experiment of irradiation the E+T setup with the 0.7 GeV proton beam.

E+T, 0.7 GeV protons, ^{209}Bi samples - experimental and simulation results

Reaction	(n,4n)	(n,6n)	(n,7n)	(n,8n)
Isotope	^{206}Bi	^{204}Bi	^{203}Bi	^{202}Bi
E_{thr} [MeV]	22.6	38.2	45.4	54.3
$T_{1/2}$	6.24 d	11.22 h	11.76 h	1.72 h
l [cm], exp-sim	Longitudinal reaction rates for r = 3 cm [10^{-28}proton^{-1}atom^{-1}]			
0.0 (exp)	20.82 ± 3.47	7.29 ± 2.43	8.33 ± 4.16	9.68 ± 0.45
0.0 (sim)	12.19	5.47	4.61	2.39
11.8 (exp)	8.43 ± 0.56	5.55 ± 1.39	5.00 ± 0.35	5.03 ± 0.24
11.8 (sim)	17.38	8.23	6.46	3.89
24.0 (exp)	4.82 ± 0.35	3.33 ± 0.24	3.19 ± 0.24	3.69 ± 0.10
24.0 (sim)	8.27	4.05	3.42	2.03
36.2 (exp)	n/a	n/a	n/a	n/a
36.2 (sim)	1.71	0.81	0.59	0.38
48.4 (exp)	0.38 ± 0.06	0.32 ± 0.02	0.27 ± 0.03	0.30 ± 0.04
48.4 (sim)	0.63	0.31	0.24	0.15
r [cm], exp-sim	Radial reaction rates for l = 11.8 cm [10^{-28}proton^{-1}atom^{-1}]			
3.0 (exp)	8.43 ± 0.56	5.55 ± 1.39	5.00 ± 0.35	5.03 ± 0.24
3.0 (sim)	17.38	8.23	6.46	3.89
6.0 (exp)	5.97 ± 0.38	4.16 ± 0.14	3.54 ± 0.21	2.98 ± 0.10
6.0 (sim)	7.10	3.26	2.37	1.51
8.5 (exp)	2.81 ± 0.14	1.62 ± 0.10	1.35 ± 0.08	1.42 ± 0.35
8.5 (sim)	3.49	1.55	1.05	0.69

Table 10: Experimental and simulated reaction rates of studied isotopes in the ^{197}Au and ^{27}Al samples from the experiment of irradiation the E+T setup with the 0.7 GeV proton beam.

E+T, 0.7 GeV protons, ^{197}Au and ^{27}Al samples - experimental and simulation results										
Sample	^{197}Au				^{27}Al	^{197}Au				^{27}Al
Reaction	(n,2n)	(n,4n)	(n,5n)	(n,6n)	(n,α)	(n,2n)	(n,4n)	(n,5n)	(n,6n)	(n,α)
Isotope	^{196}Au	^{194}Au	^{193}Au	^{192}Au	^{24}Na	^{196}Au	^{194}Au	^{193}Au	^{192}Au	^{24}Na
E_{thr} [MeV]	8.1	23.3	30.2	38.9	3.2	8.1	23.3	30.2	38.9	3.2
$T_{1/2}$	6.2 d	38 h	17.7 h	4.9 h	15 h	6.2 d	38 h	17.7 h	4.9 h	15 h
l [cm], exp-sim	Longitudinal reaction rates for r = 3 cm [10^{-28}proton^{-1}atom^{-1}]					Longitudinal reaction rates for r = 8.5 cm [10^{-28}proton^{-1}atom^{-1}]				
0.0 (exp)	31.40 ± 1.31	11.38 ± 0.46	38.92 ± 2.29	7.62 ± 0.49	3.54 ± 0.31	6.44 ± 0.26	1.64 ± 0.20	1.24 ± 0.49	0.74 ± 0.09	0.54 ± 0.13
0.0 (sim)	25.09	7.12	6.74	3.40	1.96	4.77	1.05	0.73	0.41	0.35
11.8 (exp)	36.63 ± 2.62	14.59 ± 0.49	29.76 ± 2.62	9.91 ± 0.65	3.72 ± 0.31	9.45 ± 0.36	3.07 ± 0.75	1.86 ± 0.78	1.77 ± 0.13	0.73 ± 0.10
11.8 (sim)	33.22	11.80	9.64	5.58	2.58	7.80	2.34	1.69	0.99	0.59
24.0 (exp)	16.91 ± 0.46	7.85 ± 2.29	13.08 ± 13.08	5.72 ± 0.39	1.54 ± 0.07	4.91 ± 0.78	1.90 ± 0.46	1.80 ± 0.78	0.88 ± 0.16	0.44 ± 0.02
24.0 (sim)	14.32	5.95	4.82	2.87	1.12	4.37	1.47	1.07	0.64	0.33
36.2 (exp)	4.28 ± 0.13	2.03 ± 0.46	3.27 ± 0.98	1.05 ± 0.13	0.32 ± 0.08	2.29 ± 0.98	0.95 ± 0.59	0.39 ± 0.10	0.63 ± 0.08	0.182 ± 0.008
36.2 (sim)	3.37	1.24	0.93	0.57	0.26	1.81	0.65	0.47	0.28	0.139
48.4 (exp)	1.31 ± 0.33	0.75 ± 0.16	1.47 ± 0.49	0.37 ± 0.08	0.09 ± 0.03	0.88 ± 0.13	0.39 ± 0.06	0.07 ± 0.05	0.36 ± 0.10	0.061 ± 0.006
48.4 (sim)	0.99	0.41	0.32	0.20	0.08	0.57	0.22	0.17	0.10	0.044
l [cm], exp-sim	Longitudinal reaction rates for r = 6 cm [10^{-28}proton^{-1}atom^{-1}]					Longitudinal reaction rates for r = 10.7 cm [10^{-28}proton^{-1}atom^{-1}]				
0.0 (exp)	12.46 ± 0.43	3.24 ± 0.65	4.58 ± 0.98	2.19 ± 0.23	1.15 ± 0.10	3.86 ± 0.13	0.85 ± 0.16	3.04 ± 0.78	0.36 ± 0.05	0.32 ± 0.01
0.0 (sim)	9.41	2.18a	1.69	0.90	0.70	2.91	0.70	0.47	0.26	0.22
11.8 (exp)	16.68 ± 1.64	6.74 ± 0.29	5.69 ± 0.92	3.86 ± 0.20	1.50 ± 0.09	4.84 ± 0.43	2.29 ± 0.98	n/a	0.75 ± 0.98	0.41 ± 0.03
11.8 (sim)	14.33	4.52	3.38	2.01	1.09	4.83	1.44	1.03	0.61	0.37
24.0 (exp)	9.58 ± 0.33	3.92 ± 2.29	5.79 ± 0.69	2.94 ± 0.26	0.83 ± 0.02	3.79 ± 0.49	1.08 ± 0.20	3.60 ± 1.64	0.82 ± 0.10	0.26 ± 0.02
24.0 (sim)	7.36	2.60	1.99	1.18	0.57	2.87	0.97	0.72	0.43	0.22
36.2 (exp)	4.19 ± 0.10	2.16 ± 0.56	6.21 ± 1.31	1.57 ± 0.20	0.36 ± 0.01	2.03 ± 0.26	0.59 ± 0.10	0.69 ± 0.26	0.46 ± 0.13	0.13 ± 0.04
36.2 (sim)	2.81	1.05	0.80	0.49	0.22	1.28	0.45	0.33	0.20	0.10
48.4 (exp)	1.44 ± 0.10	0.78 ± 0.13	0.29 ± 0.26	0.75 ± 0.13	0.13 ± 0.07	0.62 ± 0.07	0.30 ± 0.06	0.49 ± 0.23	0.11 ± 0.05	0.050 ± 0.004
48.4 (sim)	0.82	0.35	0.27	0.17	0.06	0.41	0.16	0.13	0.08	0.032

Table 11: Experimental and simulated reaction rates of studied isotopes in the ^{197}Au and ^{27}Al samples from the experiment of irradiation the E+T setup with the 1 GeV proton beam.

E+T, 1 GeV protons, ^{197}Au and ^{27}Al samples - experimental and simulation results						
Sample	^{197}Au					^{27}Al
Reaction	(n,2n)	(n,4n)	(n,5n)	(n,6n)	(n,7n)	(n,α)
Isotope	^{196}Au	^{194}Au	^{193}Au	^{192}Au	^{191}Au	^{24}Na
E_{thr} [MeV]	8.1	23.3	30.2	38.9	46.0	3.2
$T_{1/2}$	6.2 d	38 h	17.7 h	4.9 h	3.2 h	15 h
l [cm], exp-sim	Longitudinal reaction rates for r = 6 cm [10^{-28}proton^{-1}atom^{-1}]					
0.0 (exp)	14.29 ± 0.20	3.03 ± 0.07	1.86 ± 0.26	1.23 ± 0.06	0.43 ±0.13	1.03 ± 0.02
0.0 (sim)	16.60	3.48	2.45	1.34	1.01	1.22
11.8 (exp)	25.25 ± 0.29	6.93 ± 0.16	5.63 ± 0.33	5.63 ± 0.10	1.50 ± 0.20	1.90 ± 0.03
11.8 (sim)	29.45	8.31	6.21	3.69	2.98	2.22
24.0 (exp)	13.80 ± 0.26	4.35 ± 0.13	3.34 ± 0.39	2.35 ± 0.13	1.44 ± 0.20	1.10 ± 0.02
24.0 (sim)	17.07	5.20	3.93	2.33	1.90	1.30
36.2 (exp)	6.93 ± 0.20	2.32 ± 0.10	2.03 ± 0.26	1.34 ± 0.08	0.82 ± 0.13	0.60 ± 0.01
36.2 (sim)	8.36	2.77	2.15	1.27	1.04	0.64
48.4 (exp)	2.45 ± 0.10	1.09 ± 0.06	0.95 ± 0.23	0.66 ± 0.05	0.36 ± 0.10	0.197 ± 0.004
48.4 (sim)	2.93	1.23	0.98	0.59	0.50	0.227
r [cm], exp-sim	Radial reaction rates for l = 11.8 cm [10^{-28}proton^{-1}atom^{-1}]					
3.0 (exp)	65.97 ± 0.56	19.92 ± 0.26	19.17 ± 0.88	13.44 ± 0.52	6.15 ± 0.62	5.76 ± 0.06
3.0 (sim)	82.77	25.91	22.27	12.46	10.20	6.39
6.0 (exp)	25.25 ± 0.29	6.93 ± 0.16	5.63 ± 0.33	5.63 ± 0.10	1.50 ± 0.20	1.90 ± 0.03
6.0 (sim)	29.45	8.31	6.21	3.69	2.98	2.22
8.5 (exp)	12.72 ± 0.23	3.70 ± 0.10	2.91 ± 0.43	1.67 ± 0.10	0.88 ± 0.16	0.96 ± 0.02
8.5 (sim)	15.02	4.13	3.01	1.79	1.41	1.13
10.7 (exp)	7.82 ± 0.23	2.29 ± 0.10	2.19 ± 0.52	1.08 ± 0.07	0.75 ± 0.20	0.56 ± 0.01
10.7 (sim)	9.36	2.57	1.87	1.09	0.87	0.70

Table 12: Experimental and simulated reaction rates of studied isotopes in the ^{209}Bi samples from the experiment of irradiation the E+T setup with the 1 GeV proton beam.

E+T, 1 GeV protons, ^{209}Bi samples - experimental and simulation results

Reaction	(n,4n)	(n,5n)	(n,6n)	(n,7n)	(n,8n)	(n,9n)
Isotope	^{206}Bi	^{205}Bi	^{204}Bi	^{203}Bi	^{202}Bi	^{201}Bi
E$_{thr}$ [MeV]	22.6	29.6	38.2	45.4	54.3	61.7
T$_{1/2}$	6.24 d	15.31 d	11.22 h	11.76 h	1.72 h	1.8 h
l [cm], exp-sim	Longitudinal reaction rates for r = 6 cm [10^{-28}proton^{-1}atom^{-1}]					
0.0 (exp)	2.00 ± 0.23	1.62 ± 0.03	1.41 ± 0.03	1.10 ± 0.06	1.12 ± 0.02	0.69 ± 0.04
0.0 (sim)	4.10	2.64	1.60	1.03	0.63	0.43
11.8 (exp)	8.02 ± 0.06	5.48 ± 0.14	3.45 ± 0.03	2.43 ± 0.06	2.19 ± 0.03	1.10 ± 0.06
11.8 (sim)	9.57	6.44	4.28	2.91	1.93	1.40
24.0 (exp)	5.56 ± 0.06	3.89 ± 0.14	2.61 ± 0.04	1.93 ± 0.07	1.78 ± 0.02	1.04 ± 0.05
24.0 (sim)	6.03	4.15	2.74	1.90	1.25	0.90
36.2 (exp)	2.69 ± 0.04	2.05 ± 0.10	1.34 ± 0.02	1.02 ± 0.03	0.93 ± 0.02	0.59 ± 0.02
36.2 (sim)	3.21	2.27	1.49	1.06	0.69	0.50
48.4 (exp)	1.26 ± 0.03	1.03 ± 0.08	0.71 ± 0.01	0.63 ± 0.03	0.59 ± 0.01	0.36 ± 0.02
48.4 (sim)	1.41	1.05	0.70	0.55	0.34	0.25

Table 13: Experimental and simulated reaction rates of studied isotopes in the ^{197}Au and ^{27}Al samples from the experiment of irradiation the E+T setup with the 1.5 GeV proton beam.

E+T, 1.5 GeV protons, ^{197}Au and ^{27}Al samples - experimental and simulation results							
Sample	^{197}Au						^{27}Al
Reaction	(n,2n)	(n,4n)	(n,5n)	(n,6n)	(n,7n)	(n,9n)	(n,α)
Isotope	^{196}Au	^{194}Au	^{193}Au	^{192}Au	^{191}Au	^{189}Au	^{24}Na
E$_{thr}$ [MeV]	8.1	23.3	30.2	38.9	46.0	62.4	3.2
T$_{1/2}$	6.2 d	38 h	17.7 h	4.9 h	3.2 h	28.7 min	15 h
l [cm], exp-sim	Longitudinal reaction rates for r = 3 cm [10^{-28}proton^{-1}atom^{-1}]						
0.0 (exp)	40.56 ± 1.96	8.60 ± 0.39	3.24 ± 0.23	4.51 ± 0.23	2.19 ± 0.49	1.34 ± 0.13	3.58 ± 0.18
0.0 (sim)	67.43	15.52	15.08	7.07	5.72	2.22	4.91
11.8 (exp)	82.42 ± 3.92	23.22 ± 0.98	9.88 ± 0.59	14.26 ± 0.72	7.56 ± 0.72	6.77 ± 0.46	7.66 ± 0.36
11.8 (sim)	109.64	30.42	25.36	14.24	11.70	5.45	8.26
24.0 (exp)	51.35 ± 2.29	14.78 ± 0.69	6.15 ± 0.36	10.11 ± 0.49	5.53 ± 0.65	4.78 ± 0.29	4.12 ± 0.18
24.0 (sim)	60.89	17.52	14.44	8.16	6.68	3.14	4.62
36.2 (exp)	31.73 ± 1.64	9.19 ± 0.43	4.22 ± 0.29	6.80 ± 0.33	3.76 ± 0.43	3.63 ± 0.26	2.64 ± 0.12
36.2 (sim)	28.73	8.56	6.99	3.97	3.27	1.54	2.19
48.4 (exp)	11.15 ± 0.52	4.22 ± 0.20	2.22 ± 0.16	3.47 ± 0.20	2.00 ± 0.36	2.13 ± 0.16	1.06 ± 0.05
48.4 (sim)	9.36	3.27	2.74	1.59	1.32	0.64	0.73
r [cm], exp-sim	Radial reaction rates for l = 11.8 cm [10^{-28}proton^{-1}atom^{-1}]						
3.0 (exp)	82.42 ± 3.92	23.22 ± 0.98	9.88 ± 0.59	14.26 ± 0.72	7.56 ± 0.72	6.77 ± 0.46	7.66 ± 0.36
3.0 (sim)	109.64	30.42	25.36	14.24	11.70	5.45	8.26
6.0 (exp)	50.37 ± 2.29	14.00 ± 0.65	5.85 ± 0.39	9.32 ± 0.49	5.23 ± 0.98	3.99 ± 0.29	4.26 ± 0.18
6.0 (sim)	40.62	10.55	7.76	4.62	3.73	1.76	3.04
8.5 (exp)	31.40 ± 1.31	8.34 ± 0.39	3.40 ± 0.29	5.17 ± 0.26	2.98 ± 0.49	2.13 ± 0.16	2.53 ± 0.12
8.5 (sim)	21.49	5.55	4.01	2.36	1.90	0.89	1.61
10.7 (exp)	19.98 ± 0.95	5.53 ± 0.26	1.93 ± 0.23	3.40 ± 0.20	2.03 ± 0.56	1.41 ± 0.13	1.20 ± 0.06
10.7 (sim)	13.13	3.50	2.51	1.50	1.21	0.55	0.98

Table 14: Experimental and simulated reaction rates of studied isotopes in the ^{209}Bi samples from the experiment of irradiation the E+T setup with the 1.5 GeV proton beam.

E+T, 1.5 GeV protons, ^{209}Bi samples - experimental and simulation results									
Reaction	(n,4n)	(n,5n)	(n,6n)	(n,7n)	(n,8n)	(n,9n)	(n,10n)	(n,11n)	(n,12n)
Isotope	^{206}Bi	^{205}Bi	^{204}Bi	^{203}Bi	^{202}Bi	^{201}Bi	^{200}Bi	^{199}Bi	^{198}Bi
E_{thr} [MeV]	22.6	29.6	38.2	45.4	54.3	61.7	70.9	78.6	88.1
$T_{1/2}$	6.24 d	15.31 d	11.22 h	11.76 h	1.72 h	1.8 h	36.4 min	27 min	10.3 min
l [cm], exp-sim	Longitudinal reaction rates for r = 3 cm [10^{-28}proton^{-1}atom^{-1}]								
0.0 (exp)	13.67 ± 0.62	8.71 ± 0.49	4.48 ± 0.21	2.67 ± 0.14	3.23 ± 0.14	1.18 ± 0.07	1.71 ± 0.08	0.66 ± 0.03	0.75 ± 0.03
0.0 (sim)	19.47	16.62	8.65	6.93	3.75	2.43	1.76	2.18	0.96
11.8 (exp)	29.84 ± 1.39	18.50 ± 0.94	12.77 ± 0.59	8.50 ± 0.42	14.26 ± 0.69	5.76 ± 0.35	6.56 ± 0.42	1.97 ± 0.10	2.91 ± 0.14
11.8 (sim)	35.80	26.68	16.70	12.27	7.76	5.53	4.14	4.63	2.23
24.0 (exp)	19.36 ± 0.90	12.94 ± 0.66	8.71 ± 0.42	6.07 ± 0.28	9.30 ± 0.45	3.96 ± 0.24	4.89 ± 0.21	1.43 ± 0.08	2.15 ± 0.10
24.0 (sim)	20.44	15.25	9.57	6.92	4.43	3.13	2.39	2.68	1.30
36.2 (exp)	12.63 ± 0.59	8.95 ± 0.52	5.83 ± 0.28	4.13 ± 0.21	6.66 ± 0.31	2.57 ± 0.17	3.86 ± 0.02	1.17 ± 0.06	1.84 ± 0.09
36.2 (sim)	9.95	7.38	4.66	3.35	2.15	1.53	1.17	1.32	0.65
48.4 (exp)	4.96 ± 0.24	3.78 ± 0.21	2.67 ± 0.14	1.69 ± 0.09	3.09 ± 0.17	1.21 ± 0.09	1.78 ± 0.08	0.37 ± 0.02	0.70 ± 0.03
48.4 (sim)	3.74	2.81	1.81	1.33	0.85	0.63	0.48	0.55	0.27
r [cm], exp-sim	Radial reaction rates for l = 11.8 cm [10^{-28}proton^{-1}atom^{-1}]								
3.0 (exp)	29.84 ± 1.39	18.50 ± 0.94	12.77 ± 0.59	8.50 ± 0.42	14.26 ± 0.69	5.76 ± 0.35	6.56 ± 0.42	1.97 ± 0.10	2.91 ± 0.14
3.0 (sim)	35.80	26.68	16.70	12.27	7.76	5.53	4.14	4.63	2.23
6.0 (exp)	17.25 ± 0.80	10.03 ± 0.56	7.11 ± 0.35	4.41 ± 0.21	8.78 ± 0.42	3.23 ± 0.28	3.05 ± 0.14	0.95 ± 0.05	1.33 ± 0.07
6.0 (sim)	11.85	7.89	5.33	3.56	2.38	1.72	1.26	1.24	0.70
8.5 (exp)	10.76 ± 0.49	6.84 ± 0.38	4.13 ± 0.21	2.57 ± 0.14	4.41 ± 0.21	1.56 ± 0.17	1.75 ± 0.08	0.45 ± 0.03	0.64 ± 0.03
8.5 (sim)	6.33	4.10	2.72	1.78	1.20	0.85	0.62	0.58	0.34
10.7 (exp)	7.77 ± 0.38	4.72 ± 0.28	2.91 ± 0.14	1.79 ± 0.09	2.91 ± 0.14	0.97 ± 0.10	1.05 ± 0.05	0.32 ± 0.02	0.42 ± 0.02
10.7 (sim)	4.03	2.61	1.76	1.17	0.77	0.55	0.40	0.36	0.22

Table 15: Experimental and simulated reaction rates of studied isotopes in the ^{197}Au and ^{27}Al samples from the experiment of irradiation the E+T setup with the 2 GeV proton beam.

E+T, 2 GeV protons, ^{197}Au and ^{27}Al samples - experimental and simulation results

Sample	^{197}Au				^{27}Al
Reaction	(n,2n)	(n,4n)	(n,5n)	(n,6n)	(n,α)
Isotope	^{196}Au	^{194}Au	^{193}Au	^{192}Au	^{24}Na
E_{thr} [MeV]	8.1	23.3	30.2	38.9	3.2
$T_{1/2}$	6.2 d	38 h	17.7 h	4.9 h	15 h
l [cm], exp-sim	Longitudinal reaction rates for r = 5.2 cm [10^{-28}proton^{-1}atom^{-1}]				
11.8 (exp)	61.82 ± 2.62	16.81 ± 0.78	4.12 ± 0.72	6.87 ± 0.95	6.34 ± 0.17
11.8 (sim)	62.14	15.86	12.21	7.05	4.61
24.0 (exp)	39.90 ± 1.96	11.58 ± 0.92	3.04 ± 1.21	7.46 ± 1.05	3.79 ± 0.10
24.0 (sim)	41.89	11.21	8.73	5.07	3.14
36.2 (exp)	20.31 ± 1.18	6.08 ± 0.56	1.41 ± 0.49	4.06 ± 0.75	1.50 ± 0.06
36.2 (sim)	25.06	6.98	5.52	3.14	1.89
48.4 (exp)	8.24 ± 0.65	3.17 ± 0.33	0.65 ± 0.23	1.90 ± 0.20	0.89 ± 0.04
48.4 (sim)	10.33	3.42	2.84	1.62	0.79

Table 16: Experimental and simulated reaction rates of studied isotopes in the ^{209}Bi samples from the experiment of irradiation the E+T setup with the 2 GeV proton beam.

E+T, 2 GeV protons, ^{209}Bi samples - experimental and simulation results

Reaction	(n,4n)	(n,5n)	(n,6n)	(n,7n)	(n,8n)	(n,9n)	(n,10n)
Isotope	^{206}Bi	^{205}Bi	^{204}Bi	^{203}Bi	^{202}Bi	^{201}Bi	^{200}Bi
E_{thr} [MeV]	22.6	29.6	38.2	45.4	54.3	61.7	70.9
$T_{1/2}$	6.24 d	15.31 d	11.22 h	11.76 h	1.72 h	1.8 h	36.4 min
l [cm], exp-sim	Longitudinal reaction rates for r = 5.2 cm [10^{-28}proton^{-1}atom^{-1}]						
11.8 (exp)	14.33 ± 0.31	17.66 ± 2.78	5.58 ± 0.07	4.96 ± 0.11	2.06 ± 0.04	1.10 ± 0.15	1.39 ± 0.60
11.8 (sim)	18.36	12.72	8.24	5.80	3.79	2.72	2.00
24.0 (exp)	10.79 ± 0.17	11.34 ± 1.29	4.23 ± 0.05	3.90 ± 0.09	1.92 ± 0.04	0.83 ± 0.11	5.00 ± 1.89
24.0 (sim)	12.98	9.12	5.92	4.17	2.71	1.95	1.45
36.2 (exp)	7.07 ± 0.19	9.08 ± 1.21	2.81 ± 0.05	2.50 ± 0.08	1.26 ± 0.04	0.66 ± 0.10	n/a
36.2 (sim)	8.02	5.71	3.67	2.62	1.69	1.21	0.90
48.4 (exp)	3.58 ± 0.12	2.63 ± 0.64	1.55 ± 0.03	1.46 ± 0.06	0.78 ± 0.03	0.34 ± 0.07	n/a
48.4 (sim)	3.88	2.93	1.87	1.38	0.88	0.64	0.48

Table 17: Experimental and simulated reaction rates of studied isotopes in the ^{197}Au and ^{27}Al samples from the experiment of irradiation the E+T setup with the 1.6 GeV deuteron beam.

E+T, 1.6 GeV deuterons, ^{197}Au and ^{27}Al samples - experimental and simulation results										
Sample	^{197}Au				^{27}Al	^{197}Au				^{27}Al
Reaction	(n,2n)	(n,4n)	(n,5n)	(n,6n)	(n,α)	(n,2n)	(n,4n)	(n,5n)	(n,6n)	(n,α)
Isotope	^{196}Au	^{194}Au	^{193}Au	^{192}Au	^{24}Na	^{196}Au	^{194}Au	^{193}Au	^{192}Au	^{24}Na
E_{thr} [MeV]	8.1	23.3	30.2	38.9	3.2	8.1	23.3	30.2	38.9	3.2
$T_{1/2}$	6.2 d	38 h	17.7 h	4.9 h	15 h	6.2 d	38 h	17.7 h	4.9 h	15 h
l [cm], exp-sim	Longitudinal reaction rates for r = 3 cm [10^{-28}deuteron^{-1}atom^{-1}]					Longitudinal reaction rates for r = 8.5 cm [10^{-28}deuteron^{-1}atom^{-1}]				
0.0 (exp)	49.39 ± 5.89	10.30 ± 0.46	5.82 ± 0.82	4.25 ± 0.16	5.10 ± 0.07	15.27 ± 0.43	3.30 ± 0.16	2.68 ± 0.69	1.50 ± 0.29	1.45 ± 0.03
0.0 (sim)	53.52	10.06	6.60	3.71	3.83	12.14	2.58	1.79	1.00	0.88
11.8 (exp)	110.22 ± 3.92	34.34 ± 1.64	31.07 ± 1.64	19.79 ± 0.43	11.74 ± 0.13	28.78 ± 1.64	8.31 ± 0.49	5.00 ± 0.72	4.09 ± 0.23	2.87 ± 0.27
11.8 (sim)	97.33	26.77	19.98	11.96	7.21	23.26	6.15	4.42	2.63	1.73
24.0 (exp)	66.40 ± 2.29	21.59 ± 0.98	17.99 ± 1.64	13.05 ± 0.52	6.98 ± 0.09	19.98 ± 0.95	6.51 ± 0.39	5.00 ± 0.82	3.57 ± 0.20	2.08 ± 0.04
24.0 (sim)	54.40	16.09	12.19	7.32	4.09	15.97	4.63	3.40	2.02	1.21
36.2 (exp)	33.36 ± 1.31	11.97 ± 0.62	13.08 ± 0.98	7.00 ± 0.23	3.39 ± 0.05	11.45 ± 0.36	4.15 ± 0.16	2.16 ± 0.49	2.39 ± 0.33	1.08 ± 0.02
36.2 (sim)	26.85	8.56	6.57	3.97	2.06	8.76	2.69	1.99	1.19	0.66
48.4 (exp)	12.13 ± 0.78	5.43 ± 0.29	5.63 ± 0.59	3.43 ± 0.23	1.25 ± 0.06	4.78 ± 0.26	2.00 ± 0.13	1.83 ± 0.52	1.83 ± 0.72	0.47 ± 0.01
48.4 (sim)	9.08	3.53	2.83	1.72	0.72	3.29	1.19	0.93	0.57	0.25
l [cm], exp-sim	Longitudinal reaction rates for r = 6 cm [10^{-28}deuteron^{-1}atom^{-1}]					Longitudinal reaction rates for r = 10.7 cm [10^{-28}deuteron^{-1}atom^{-1}]				
0.0 (exp)	25.12 ± 0.36	5.27 ± 0.13	2.75 ± 0.43	2.65 ± 0.16	2.36 ± 0.04	9.62 ± 0.29	2.49 ± 0.13	1.86 ± 0.43	0.95 ± 0.23	0.87 ± 0.02
0.0 (sim)	22.09	4.48	2.98	1.68	1.59	7.79	1.74	1.20	0.69	0.56
11.8 (exp)	48.73 ± 5.56	14.49 ± 0.56	10.14 ± 1.31	8.05 ± 0.29	4.70 ± 0.07	18.64 ± 0.98	6.21 ± 0.36	4.25 ± 0.98	2.81 ± 0.16	1.68 ± 0.03
11.8 (sim)	41.56	11.06	8.09	4.83	3.10	14.71	3.95	2.86	1.67	1.09
24.0 (exp)	35.32 ± 1.31	11.38 ± 0.49	6.97 ± 0.95	6.02 ± 0.23	3.33 ± 0.05	14.06 ± 0.98	4.38 ± 0.43	2.94 ± 1.31	2.26 ± 0.16	1.30 ± 0.03
24.0 (sim)	26.58	7.74	5.74	3.45	2.00	10.52	3.16	2.34	1.39	0.79
36.2 (exp)	19.17 ± 0.39	6.31 ± 0.20	4.91 ± 0.92	3.79 ± 0.26	1.67 ± 0.03	8.27 ± 0.29	3.04 ± 0.13	1.80 ± 0.52	1.50 ± 0.33	0.69 ± 0.02
36.2 (sim)	14.05	4.35	3.27	1.97	1.06	6.05	1.94	1.44	0.87	0.46
48.4 (exp)	7.62 ± 0.29	2.91 ± 0.20	1.50 ± 0.39	2.45 ± 0.36	0.75 ± 0.01	3.66 ± 0.33	1.28 ± 0.16	1.18 ± 0.39	1.11 ± 0.39	0.32 ± 0.01
48.4 (sim)	5.14	1.87	1.45	0.89	0.40	2.30	0.87	0.67	0.41	0.18

Table 18: Experimental and simulated reaction rates of studied isotopes in the ^{209}Bi samples from the experiment of irradiation the E+T setup with the 1.6 GeV deuteron beam.

E+T, 1.6 GeV deuterons, ^{209}Bi samples - experimental and simulation results

Reaction	(n,4n)	(n,5n)	(n,6n)	(n,7n)	(n,8n)	(n,9n)
Isotope	^{206}Bi	^{205}Bi	^{204}Bi	^{203}Bi	^{202}Bi	^{201}Bi
E_{thr} [MeV]	22.6	29.6	38.2	45.4	54.3	61.7
$T_{1/2}$	6.24 d	15.31 d	11.22 h	11.76 h	1.72 h	1.8 h
l [cm], exp-sim	Longitudinal reaction rates for r = 3 cm [10^{-28}deuteron^{-1}atom^{-1}]					
0.0 (exp)	16.31 ± 1.04	18.39 ± 10.06	7.18 ± 0.21	4.27 ± 0.66	6.21 ± 0.76	5.90 ± 1.04
0.0 (sim)	13.84	8.41	5.54	3.58	2.43	2.07
11.8 (exp)	50.66 ± 4.16	58.99 ± 48.58	24.29 ± 5.21	21.86 ± 4.16	21.03 ± 0.62	11.80 ± 1.39
11.8 (sim)	35.34	24.14	16.34	11.32	7.63	5.73
24.0 (exp)	26.72 ± 1.39	38.17 ± 17.35	14.57 ± 1.39	11.83 ± 0.45	12.77 ± 0.52	9.37 ± 1.04
24.0 (sim)	20.78	14.34	9.67	6.78	4.57	3.42
36.2 (exp)	15.62 ± 1.04	17.00 ± 8.33	8.68 ± 1.04	6.98 ± 0.66	8.40 ± 0.52	6.28 ± 0.59
36.2 (sim)	10.62	7.43	5.00	3.60	2.42	1.83
48.4 (exp)	5.76 ± 0.59	7.29 ± 6.59	3.50 ± 0.10	3.23 ± 0.17	3.44 ± 0.45	1.91 ± 0.21
48.4 (sim)	4.20	3.04	2.10	1.53	1.05	0.81
r [cm], exp-sim	Radial reaction rates for l = 11.8 cm [10^{-28}deuteron^{-1}atom^{-1}]					
3.0 (exp)	50.66 ± 4.16	58.99 ± 48.58	24.29 ± 5.21	21.86 ± 4.16	21.03 ± 0.62	11.80 ± 1.39
3.0 (sim)	35.34	24.14	16.34	11.32	7.63	5.73
6.0 (exp)	16.90 ± 0.69	16.66 ± 3.47	7.53 ± 0.17	6.14 ± 0.76	5.34 ± 0.28	3.30 ± 0.31
6.0 (sim)	13.51	8.91	5.98	3.98	2.69	1.96
8.5 (exp)	8.36 ± 0.49	7.04 ± 0.76	3.25 ± 0.09	2.64 ± 0.24	2.33 ± 0.14	1.18 ± 0.14
8.5 (sim)	7.18	4.68	3.15	2.06	1.38	1.00
11.5 (exp)	4.72 ± 0.35	4.72 ± 0.52	1.87 ± 0.06	1.70 ± 0.45	1.21 ± 0.07	0.68 ± 0.09
11.5 (sim)	3.98	2.58	1.73	1.11	0.76	0.54

Table 19: Experimental and simulated reaction rates of studied isotopes in the ^{197}Au and ^{27}Al samples from the experiment of irradiation the E+T setup with the 2.52 GeV deuteron beam.

E+T, 2.52 GeV deuterons, ^{197}Au and ^{27}Al samples - experimental and simulation results										
Sample	^{197}Au				^{27}Al	^{197}Au				^{27}Al
Reaction	(n,2n)	(n,4n)	(n,5n)	(n,6n)	(n,α)	(n,2n)	(n,4n)	(n,5n)	(n,6n)	(n,α)
Isotope	^{196}Au	^{194}Au	^{193}Au	^{192}Au	^{24}Na	^{196}Au	^{194}Au	^{193}Au	^{192}Au	^{24}Na
E_{thr} [MeV]	8.1	23.3	30.2	38.9	3.2	8.1	23.3	30.2	38.9	3.2
$T_{1/2}$	6.2 d	38 h	17.7 h	4.9 h	15 h	6.2 d	38 h	17.7 h	4.9 h	15 h
l [cm], exp-sim	Longitudinal reaction rates for r = 3 cm [10^{-28}deuteron^{-1}atom^{-1}]					Longitudinal reaction rates for r = 8.5 cm [10^{-28}deuteron^{-1}atom^{-1}]				
0.0 (exp)	72.94 ± 1.31	15.93 ± 0.52	7.52 ± 1.31	7.13 ± 0.46	5.21 ± 0.09	21.91 ± 2.29	4.58 ± 3.60	n/a	n/a	1.75 ± 0.63
0.0 (sim)	72.54	13.50	8.94	5.06	5.11	17.60	3.75	2.52	1.44	1.27
11.8 (exp)	114.47 ± 13.08	34.83 ± 0.59	26.17 ± 3.27	17.17 ± 0.75	9.32 ± 1.30	34.18 ± 0.62	10.89 ± 0.46	7.52 ± 1.96	4.84 ± 0.39	2.75 ± 0.06
11.8 (sim)	139.32	35.72	26.37	15.72	10.22	35.31	8.94	6.39	3.75	2.61
24.0 (exp)	65.41 ± 16.35	20.93 ± 2.94	22.24 ± 2.62	14.62 ± 0.92	6.76 ± 0.13	25.38 ± 0.59	7.85 ± 6.21	3.60 ± 1.64	4.25 ± 1.31	2.03 ± 0.05
24.0 (sim)	86.07	23.40	17.54	10.40	6.39	26.45	7.22	5.28	3.15	1.99
36.2 (exp)	48.73 ± 0.98	15.60 ± 0.62	18.32 ± 1.64	8.31 ± 0.39	4.01 ± 0.07	16.81 ± 0.92	5.23 ± 3.27	5.89 ± 1.64	n/a	1.32 ± 0.04
36.2 (sim)	46.66	13.12	9.94	5.93	3.49	16.05	4.63	3.42	2.04	1.22
48.4 (exp)	18.28 ± 0.36	6.93 ± 0.46	6.90 ± 0.95	3.92 ± 0.39	1.55 ± 0.04	6.80 ± 0.46	2.78 ± 0.36	n/a	n/a	0.55 ± 0.03
48.4 (sim)	17.20	5.78	4.55	2.73	1.32	6.36	2.16	1.66	1.01	0.49
l [cm], exp-sim	Longitudinal reaction rates for r = 6 cm [10^{-28}deuteron^{-1}atom^{-1}]					Longitudinal reaction rates for r = 10.7 cm [10^{-28}deuteron^{-1}atom^{-1}]				
0.0 (exp)	32.18 ± 0.92	6.54 ± 3.27	7.52 ± 2.29	n/a	2.30 ± 0.13	12.49 ± 0.36	3.92 ± 4.58	n/a	n/a	0.94 ± 0.04
0.0 (sim)	31.81	6.33	4.24	2.41	2.25	11.33	2.52	1.77	1.01	0.81
11.8 (exp)	56.29 ± 0.65	16.88 ± 0.78	12.43 ± 1.64	7.82 ± 0.56	4.57 ± 0.11	21.03 ± 0.59	6.21 ± 0.85	n/a	2.62 ± 0.39	1.60 ± 0.08
11.8 (sim)	62.56	15.65	11.35	6.73	4.61	22.50	5.85	4.20	2.46	1.66
24.0 (exp)	42.00 ± 0.49	13.74 ± 8.50	8.18 ± 1.64	9.81 ± 1.31	3.42 ± 0.07	16.55 ± 0.69	5.89 ± 3.27	n/a	n/a	1.21 ± 1.70
24.0 (sim)	44.02	11.89	8.76	5.23	3.28	17.55	4.94	3.61	2.14	1.31
36.2 (exp)	24.46 ± 0.56	6.54 ± 9.81	4.91 ± 1.64	n/a	2.70 ± 0.06	11.09 ± 0.52	3.27 ± 1.96	n/a	n/a	0.89 ± 0.02
36.2 (sim)	25.35	7.17	5.33	3.17	1.91	11.06	3.22	2.41	1.45	0.83
48.4 (exp)	10.66 ± 0.56	3.92 ± 5.56	2.68 ± 0.88	n/a	0.85 ± 0.13	4.09 ± 0.33	2.09 ± 0.92	n/a	n/a	0.39 ± 0.01
48.4 (sim)	9.91	3.28	2.55	1.54	0.75	4.49	1.55	1.20	0.73	0.34

Table 20: Experimental and simulated reaction rates of studied isotopes in the ^{209}Bi samples from the experiment of irradiation the E+T setup with the 2.52 GeV deuteron beam.

E+T, 2.52 GeV deuterons, ^{209}Bi samples - experimental and simulation results

Reaction	(n,4n)	(n,5n)	(n,6n)	(n,7n)	(n,8n)	(n,9n)
Isotope	^{206}Bi	^{205}Bi	^{204}Bi	^{203}Bi	^{202}Bi	^{201}Bi
E_{thr} [MeV]	22.6	29.6	38.2	45.4	54.3	61.7
$T_{1/2}$	6.24 d	15.31 d	11.22 h	11.76 h	1.72 h	1.8 h
l [cm], exp-sim	Longitudinal reaction rates for r = 3 cm [10^{-28}deuteron^{-1}atom^{-1}]					
0.0 (exp)	40.60 ± 4.51	32.97 ± 3.82	18.74 ± 1.39	14.85 ± 0.97	27.73 ± 1.01	13.53 ± 2.78
0.0 (sim)	46.55	29.16	20.48	13.93	9.85	10.67
11.8 (exp)	104.11 ± 13.88	95.78 ± 7.29	58.99 ± 83.28	57.26 ± 4.51	45.11 ± 1.39	30.88 ± 3.12
11.8 (sim)	102.36	72.09	48.17	34.52	23.09	18.21
24.0 (exp)	41.99 ± 3.47	37.48 ± 4.51	21.52 ± 2.43	18.74 ± 1.74	19.64 ± 0.87	9.02 ± 1.04
24.0 (sim)	57.30	40.76	26.93	19.32	12.84	9.91
36.2 (exp)	17.70 ± 1.39	20.82 ± 20.82	9.37 ± 2.43	8.33 ± 2.43	9.30 ± 0.38	6.07 ± 0.83
36.2 (sim)	28.34	20.22	13.33	9.53	6.33	4.83
48.4 (exp)	7.98 ± 1.39	13.88 ± 10.41	4.48 ± 0.94	5.55 ± 2.08	5.17 ± 0.73	2.01 ± 0.49
48.4 (sim)	10.86	8.01	5.34	3.89	2.61	2.00
r [cm], exp-sim	Radial reaction rates for l = 11.8 cm [10^{-28}deuteron^{-1}atom^{-1}]					
3.0 (exp)	104.11 ± 13.88	95.78 ± 7.29	58.99 ± 83.28!!!	57.26 ± 4.51	45.11 ± 1.39	30.88 ± 3.12
3.0 (sim)	102.36	72.09	48.17	34.52	23.09	18.21
6.0 (exp)	29.84 ± 1.74	26.37 ± 4.51	14.23 ± 5.90	10.79 ± 0.56	9.47 ± 0.69	4.68 ± 0.69
6.0 (sim)	30.36	20.10	13.53	9.15	6.14	4.47
8.5 (exp)	14.12 ± 0.73	13.88 ± 13.88	7.11 ± 0.83	5.24 ± 0.21	3.81 ± 0.08	2.43 ± 0.24
8.5 (sim)	14.94	9.75	6.52	4.31	2.90	2.11
11.5 (exp)	7.98 ± 0.21	6.91 ± 1.01	3.12 ± 1.04	2.81 ± 0.59	1.98 ± 0.21	1.04 ± 0.14
11.5 (sim)	7.83	5.08	3.40	2.23	1.49	1.09

Table 21: Experimental and simulated reaction rates of studied isotopes in the ^{197}Au samples from the experiment of irradiation the E+T setup with the 4 GeV deuteron beam. (Part I)

E+T, 4 GeV deuterons, ^{197}Au samples - experimental and simulation results											
Reaction	(n,2n)	(n,3n)	(n,4n)	(n,5n)	(n,6n)	(n,7n)	(n,8n)	(n,9n)	(n,10n)	(n,12n)	(n,14n)
Isotope	^{196}Au	^{195}Au	^{194}Au	^{193}Au	^{192}Au	^{191}Au	^{190}Au	^{189}Au	^{188}Au	^{186}Au	^{184}Au
E_{thr} [MeV]	8.1	14.8	23.3	30.2	38.9	46.0	55.0	62.4	71.9	88.7	106.3
$T_{1/2}$	6.2 d	186.1 d	38 h	17.7 h	4.9 h	3.2 h	42.8 min	28.7 min	8.8 min	10.7 min	53 s
r [cm], exp-sim	Radial reaction rates for l = 0 cm [10^{-28}deuteron^{-1}atom^{-1}]										
3.0 (exp)	161.90±3.27	73.92 ±3.92	38.04 ±0.49	28.78±1.64	21.26±3.60	15.70±0.98	14.39±8.50	10.14±3.27	7.20±1.64	5.27±0.78	n/a
3.0 (sim)	129.83	54.27	24.05	15.93	9.18	7.09	3.82	3.48	2.43	1.21	2.937
6.0 (exp)	76.86±1.31	41.21 ±3.92	17.69 ±0.29	7.20 ±1.31	7.52 ±0.56	4.97±0.59	1.64±1.31	n/a	n/a	n/a	n/a
6.0 (sim)	59.22	25.28	11.42	7.61	4.32	3.32	1.73	1.44	0.97	0.49	0.328
8.5 (exp)	42.85±1.31	23.55±2.62	10.99±0.52	4.28 ±0.95	3.92 ±0.20	3.63 ±0.88	2.03±0.72	n/a	n/a	n/a	n/a
8.5 (sim)	32.59	14.44	6.65	4.47	2.58	1.98	1.03	0.87	0.59	0.30	0.203
10.7 (exp)	27.60±0.85	15.05±2.94	7.13 ±0.29	2.52±0.85	2.68 ±0.33	3.27 ±3.27	0.98±0.98	n/a	n/a	n/a	n/a
10.7 (sim)	20.73	9.56	4.47	3.02	1.75	1.33	0.71	0.59	0.40	0.21	0.141
r [cm], exp-sim	Radial reaction rates for l = 11.8 cm [10^{-28}deuteron^{-1}atom^{-1}]										
3.0 (exp)	387.25±9.16	209.65±7.20	117.75±1.64	65.41±2.94	73.59±2.94	78.50±13.08	54.29±7.20	42.19±6.21	36.63±8.50	18.32±1.64	1.024±0.049
3.0 (sim)	261.43	126.77	65.33	49.00	29.02	23.81	12.55	11.55	8.12	4.64	7.787
6.0 (exp)	158.30±2.62	80.79±4.91	46.90±0.62	33.36±2.94	26.17±1.64	16.26±0.92	11.45±3.92	10.47±2.29	9.81±1.64	5.40±0.69	0.298±0.039
6.0 (sim)	124.42	59.59	30.37	22.13	13.15	10.68	5.65	5.07	3.54	1.97	2.504
8.5 (exp)	84.38±1.64	48.73±4.25	24.56±0.72	18.32±2.29	13.15±0.72	8.86±0.75	5.89±1.64	5.89±1.64	3.60±1.31	2.55±0.26	0.157±0.029
8.5 (sim)	69.29	33.44	17.01	12.20	7.24	5.84	3.11	2.77	1.92	1.04	1.174
10.7 (exp)	54.95±1.64	29.76±4.25	16.26±0.23	8.83±1.31	7.62±0.52	5.23±2.94	1.96±0.98	n/a	n/a	n/a	n/a
10.7 (sim)	43.34	21.32	10.87	7.83	4.65	3.72	1.99	1.76	1.21	0.65	0.683
r [cm], exp-sim	Radial reaction rates for l = 24.0 cm [10^{-28}deuteron^{-1}atom^{-1}]										
3.0 (exp)	194.28±8.50	104.99±4.25	61.65±0.43	50.04±2.62	34.02±4.25	27.15±0.98	20.61±4.58	19.62±2.62	13.41±4.25	8.24±0.59	0.432±0.043
3.0 (sim)	168.71	83.10	43.66	33.27	19.51	16.07	8.42	7.77	5.47	3.15	5.370
6.0 (exp)	104.66±2.62	52.33±3.92	31.63±0.49	21.59±1.96	17.99±0.75	12.43±0.98	8.83±1.64	7.85±1.96	6.87±1.96	3.37±0.29	0.177±0.029
6.0 (sim)	91.13	44.55	23.37	17.32	10.28	8.38	4.45	4.02	2.81	1.57	2.194
8.5 (exp)	63.78±1.31	35.32±4.25	19.30±0.56	14.06±1.64	10.47±0.98	7.00±0.95	1.96±1.96	4.71±0.69	n/a	2.16±0.23	n/a
8.5 (sim)	54.77	27.26	14.23	10.42	6.17	5.03	2.68	2.40	1.67	0.91	1.148
10.7 (exp)	42.52±1.31	24.53±3.60	13.28±0.43	7.52±1.31	7.36±0.39	4.55±0.78	2.62±1.31	n/a	n/a	n/a	n/a
10.7 (sim)	35.70	18.12	9.53	7.00	4.18	3.40	1.81	1.59	1.12	0.61	0.731

Table 22: Experimental and simulated reaction rates of studied isotopes in the ^{197}Au samples from the experiment of irradiation the E+T setup with the 4 GeV deuteron beam. (Part II)

E+T, 4 GeV deuterons, ^{197}Au samples - experimental and simulation results											
Reaction	(n,2n)	(n,3n)	(n,4n)	(n,5n)	(n,6n)	(n,7n)	(n,8n)	(n,9n)	(n,10n)	(n,12n)	(n,14n)
Isotope	^{196}Au	^{195}Au	^{194}Au	^{193}Au	^{192}Au	^{191}Au	^{190}Au	^{189}Au	^{188}Au	^{186}Au	^{184}Au
E_{thr} [MeV]	8.1	14.8	23.3	30.2	38.9	46.0	55.0	62.4	71.9	88.7	106.3
$T_{1/2}$	6.2 d	186.1 d	38 h	17.7 h	4.9 h	3.2 h	42.8 min	28.7 min	8.8 min	10.7 min	53 s
r [cm], exp-sim	Radial reaction rates for l = 36.2 cm [10^{-28}deuteron^{-1}atom^{-1}]										
3.0 (exp)	105.97±2.29	61.49±4.58	32.64±0.62	28.46±2.29	19.53±0.62	16.35 ±1.31	10.79 ±1.64	9.81 ±1.96	9.49 ±2.29	4.74±0.85	0.258±0.023
3.0 (sim)	97.16	48.27	25.68	19.76	11.61	9.57	4.98	4.60	3.24	1.86	3.250
6.0 (exp)	58.87±1.31	38.27±4.25	17.99±0.36	12.76±1.31	10.92±0.46	8.50±0.72	4.91±1.31	5.89±0.98	n/a	2.35±0.26	0.105±0.026
6.0 (sim)	56.93	28.16	14.95	11.28	6.66	5.44	2.87	2.62	1.84	1.04	1.491
8.5 (exp)	38.59±0.98	25.18±3.27	11.84±0.65	7.52±1.31	7.10±0.33	5.10±0.62	2.62±0.98	2.13±0.65	n/a	1.77±0.26	n/a
8.5 (sim)	35.97	18.11	9.65	7.17	4.27	3.47	1.84	1.66	1.16	0.64	0.851
10.7 (exp)	26.98±0.69	17.01±5.23	8.47±0.33	7.20±1.64	5.27±0.29	4.58±1.96	1.31±0.98	n/a	n/a	n/a	n/a
10.7 (sim)	23.95	12.44	6.65	4.94	2.96	2.41	1.28	1.15	0.80	0.44	0.569
r [cm], exp-sim	Radial reaction rates for l = 48.4 cm [10^{-28}deuteron^{-1}atom^{-1}]										
3.0 (exp)	47.13±0.59	34.02±3.60	16.42±0.75	17.66±1.31	11.28±0.49	9.52 ±0.88	8.50 ±1.64	6.21±0.69	4.91±0.98	2.78±0.56	0.160±0.023
3.0 (sim)	36.92	20.32	11.49	9.22	5.44	4.57	2.41	2.26	1.60	0.94	1.793
6.0 (exp)	26.85±0.69	23.88±5.23	10.24±0.49	6.87±1.31	6.77±0.72	5.00±0.85	4.58±1.31	n/a	n/a	n/a	n/a
6.0 (sim)	23.13	12.80	7.18	5.61	3.35	2.81	1.49	1.37	0.97	0.56	0.878
8.5 (exp)	16.88±0.43	11.12±3.60	5.95±0.20	4.38±0.88	4.09±0.26	3.57±0.85	0.59±0.85	2.75±0.65	n/a	0.95 ±0.26	n/a
8.5 (sim)	15.14	8.46	4.73	3.66	2.22	1.83	0.98	0.90	0.63	0.36	0.533
10.7 (exp)	12.04±0.36	13.41±5.23	4.45±0.16	3.43±0.98	2.81±0.26	5.23±2.29	1.93±0.88	n/a	n/a	n/a	n/a
10.7 (sim)	10.21	5.87	3.31	2.57	1.56	1.31	0.69	0.63	0.45	0.25	0.366

Table 23: Experimental and simulated reaction rates of studied isotopes in the ^{209}Bi samples from the experiment of irradiation the E+T setup with the 4 GeV deuteron beam.

E+T, 4 GeV deuterons, ^{209}Bi samples - experimental and simulation results									
Reaction	(n,4n)	(n,5n)	(n,6n)	(n,7n)	(n,8n)	(n,9n)	(n,10n)	(n,11n)	(n,12n)
Isotope	^{206}Bi	^{205}Bi	^{204}Bi	^{203}Bi	^{202}Bi	^{201}Bi	^{200}Bi	^{199}Bi	^{198}Bi
E_{thr} [MeV]	22.6	29.6	38.2	45.4	54.3	61.7	70.9	78.6	88.1
$T_{1/2}$	6.24 d	15.31 d	11.22 h	11.76 h	1.72 h	1.8 h	36.4 min	27 min	10.3 min
l [cm], exp-sim	Longitudinal reaction rates for r = 3 cm [10^{-28}deuteron^{-1}atom^{-1}]								
0.0 (exp)	22.04 ± 0.31	17.04 ± 0.56	8.22 ± 0.28	5.52 ± 0.28	10.10 ± 0.83	5.52 ± 0.10	3.82 ± 0.49	3.68 ± 0.17	2.85 ± 0.07
0.0 (sim)	21.96	13.09	8.39	5.26	3.45	2.51	1.87	1.52	1.04
11.8 (exp)	64.20 ± 1.39	59.34 ± 2.08	32.97 ± 1.39	25.92 ± 0.49	25.68 ± 1.39	28.70 ± 0.31	19.43 ± 1.39	20.44 ± 0.56	13.39 ± 0.52
11.8 (sim)	60.41	40.43	26.95	18.49	12.38	9.04	6.76	6.90	3.72
24.0 (exp)	43.38 ± 0.59	38.52 ± 1.74	21.86 ± 0.87	17.35 ± 0.45	24.99 ± 1.74	18.67 ± 0.21	12.42 ± 0.87	13.74 ± 0.52	10.65 ± 0.31
24.0 (sim)	42.20	28.59	18.99	13.10	8.75	6.37	4.78	4.95	2.62
36.2 (exp)	24.74 ± 0.42	22.31 ± 0.94	12.53 ± 0.59	10.06 ± 0.49	16.31 ± 1.04	11.04 ± 0.17	7.18 ± 0.56	8.54 ± 0.42	6.84 ± 0.17
36.2 (sim)	25.49	17.40	11.53	8.00	5.33	3.88	2.92	3.05	1.61
48.4 (exp)	10.03 ± 0.14	9.16 ± 0.52	5.45 ± 0.21	4.37 ± 0.21	7.74 ± 0.45	5.00 ± 0.07	3.50 ± 0.28	4.27 ± 0.21	3.16 ± 0.10
48.4 (sim)	11.70	8.31	5.57	3.94	2.64	1.94	1.48	1.59	0.82
r [cm], exp-sim	Radial reaction rates for l = 11.8 cm [10^{-28}deuteron^{-1}atom^{-1}]								
3.0 (exp)	64.20 ± 1.39	59.34 ± 2.08	32.97 ± 1.39	25.92 ± 0.49	25.68 ± 1.39	28.70 ± 0.31	19.43 ± 1.39	20.44 ± 0.56	13.39 ± 0.52
3.0 (sim)	60.41	40.43	26.95	18.49	12.38	9.04	6.76	6.90	3.72
6.0 (exp)	32.93 ± 0.69	28.80 ± 1.74	15.06 ± 0.62	12.15 ± 0.35	15.27 ± 1.04	12.60 ± 0.17	8.36 ± 0.87	7.84 ± 0.24	5.97 ± 0.24
6.0 (sim)	30.25	19.79	13.23	8.91	5.99	4.36	3.22	3.16	1.78
8.5 (exp)	17.94 ± 0.24	15.44 ± 0.59	7.74 ± 0.35	6.21 ± 0.21	7.36 ± 0.76	5.52 ± 0.10	3.75 ± 0.35	3.40 ± 0.17	2.67 ± 0.10
8.5 (sim)	17.48	11.35	7.60	5.05	3.38	2.46	1.80	1.71	1.00
11.5 (exp)	10.34 ± 0.17	8.85 ± 0.35	4.48 ± 0.17	3.40 ± 0.21	4.13 ± 0.42	3.02 ± 0.07	1.94 ± 0.21	1.74 ± 0.10	1.18 ± 0.03
11.5 (sim)	9.84	6.38	4.26	2.79	1.89	1.37	1.00	0.94	0.56

Table 24: Experimental and simulated reaction rates of ^{24}Na production in the ^{27}Al samples from the experiment of irradiation the E+T setup with the 4 GeV deuteron beam.

E+T, 4 GeV deuterons, ^{27}Al samples - experimental and simulation results					
	Radial reaction rates of ^{24}Na [10^{-28}deuteron^{-1}atom^{-1}]				
r [cm], exp-sim	l = 0.0 cm	l = 11.8 cm	l = 24.0 cm	l = 36.2 cm	l = 48.4 cm
3.0 (exp)	12.90 ± 0.18	31.90 ± 0.36	15.50 ± 0.10	8.46 ± 0.11	3.76 ± 0.06
3.0 (sim)	9.32	19.20	12.51	7.24	2.81
6.0 (exp)	5.60 ± 0.06	11.87 ± 0.13	8.19 ± 0.09	4.71 ± 0.06	2.13 ± 0.04
6.0 (sim)	4.19	9.13	6.77	4.26	1.75
8.5 (exp)	3.20 ± 0.05	6.56 ± 0.08	4.94 ± 0.07	3.80 ± 0.05	1.33 ± 0.03
8.5 (sim)	2.32	5.10	4.09	2.71	1.15
10.7 (exp)	1.97 ± 0.04	4.00 ± 0.05	3.34 ± 0.04	2.03 ± 0.04	0.95 ± 0.02
10.7 (sim)	1.48	3.20	2.66	1.79	0.78

Appendix D - Weights of activation samples

Table 25: Weights of aluminium and lead samples in the Nuclotron experiments. Uncertainty in weight is 0.01 %.

d4GeV			d8GeV		
	^{27}Al	^{nat}Pb		^{27}Al	^{nat}Pb
No.	weight [g]	weight [g]	No.	weight [g]	weight [g]
1	0.19	0.52	1	0.51	0.66
2	0.20	0.53	2	0.48	0.69
3	0.21	0.49	3	0.47	0.70
4	0.21	0.48	4	0.44	0.63
5	0.20	0.53	5	0.46	0.63
6	0.21	0.52	6	0.46	0.58
7	0.20	0.53	7	0.48	1.22
8	0.20	0.52	8	0.44	1.27
9	0.21	0.53	9	0.48	1.25
10	0.20	0.50	10	0.49	1.10
11	0.22	0.52	11	0.45	1.22
12	0.22	0.50	12	0.42	1.17

Table 26: Weights of cobalt and lead samples in the Phasotron experiments. Uncertainty in weight is 0.01 %.

UA			CC			WS		
	^{59}Co	^{nat}Pb		^{59}Co	^{nat}Pb		^{59}Co	^{nat}Pb
No.	weight [g]	weight [g]	No.	weight [g]	weight [g]	No.	weight [g]	weight [g]
1	1.87	0.52	1	1.78	3.10	1	1.89	3.10
2	1.35	0.53	2	1.84	2.80	2	1.90	2.80
3	1.92	0.48	3	1.82	2.83	3	1.92	2.83
4	2.06	0.48	4	1.81	2.67	4	1.81	2.67
5	1.98	0.53	5	1.86	2.79	5	1.78	2.79
6	2.09	0.52	6	1.92	2.81	6	1.91	2.81
7	1.94	0.53	7	1.89	2.77	7	1.83	2.77
8	1.82	0.52	8	1.91	2.84	8	1.90	2.84
9	1.99	0.53	9	1.84	2.73	9	1.90	2.73
10	1.77	0.50	10	1.76	2.78	10	1.84	2.78
11	2.03	0.52	11	1.89	2.78	11	1.78	2.78
12	1.98	0.50	12	1.82	2.75	12	1.77	2.75

Table 27: Weights of lead samples in the experiment with lead target. Uncertainty in weight is 0.01 %.

^{nat}Pb sample	weight [g]
APb	14.77
BPb	14.67
CPb	14.73
DPb	15.00
EPb	14.57

Appendix E - Experimental and simulated reaction rates from the QUINTA experiments

Table 28: Experimental reaction rates of the ^{24}Na production in the ^{27}Al foils of the Nuclotron experiments. Results are given for the left and right side of the QUINTA plates. l is the longitudinal distance.

Experiment	d4GeV	d8GeV	d4GeV	d8GeV
l [cm], exp-sim	R(^{24}Na) [10^{-28}deuteron^{-1}atom^{-1}], left		R(^{24}Na) [10^{-28}deuteron^{-1}atom^{-1}], right	
1.50 (exp)	1.37 ± 0.08	1.58 ± 0.11	1.22 ± 0.07	1.79 ± 0.11
1.50 (sim)	0.83	1.37	1.09	1.15
14.75 (exp)	7.71 ± 0.48	n/a	6.74 ± 0.41	12.35 ± 0.73
14.75 (sim)	6.16	12.81	7.53	7.24
27.85 (exp)	18.83 ± 1.01	27.64 ± 1.52	13.12 ± 0.77	29.63 ± 1.81
27.85 (sim)	14.25	35.40	15.06	16.59
40.95 (exp)	13.66 ± 0.90	19.10 ± 1.14	8.10 ± 0.43	17.99 ± 1.04
40.95 (sim)	10.46	28.25	9.23	11.86
54.05 (exp)	7.59 ± 0.45	11.08 ± 0.65	4.22 ± 0.27	8.63 ± 0.51
54.05 (sim)	6.64	17.59	5.02	7.41
67.15 (exp)	3.83 ± 0.22	5.99 ± 0.31	1.98 ± 0.12	4.19 ± 0.24
67.15 (sim)	3.26	8.67	2.26	3.78

Table 29: Experimental reaction rates of studied isotopes in the ^{nat}Pb foils of the Nuclotron experiments. Results are given for the left and right side of the QUINTA plates. l is the longitudinal distance.

Experiment	d4GeV	d8GeV	d4GeV	d8GeV
l [cm], exp-sim	R(^{206}Bi) [10^{-28}deuteron^{-1}atom^{-1}], left		R(^{206}Bi) [10^{-28}deuteron^{-1}atom^{-1}], right	
1.50 (exp)	0.33 ± 0.05	0.21 ± 0.04	0.21 ± 0.14	0.60 ± 0.10
1.50 (sim)	0.03	0.26	0.28	0.04
14.75 (exp)	1.02 ± 0.06	0.97 ± 0.09	0.70 ± 0.06	2.16 ± 0.13
14.75 (sim)	0.28	1.80	0.52	0.25
27.85 (exp)	4.66 ± 0.22	5.60 ± 0.28	2.39 ± 0.12	6.28 ± 0.40
27.85 (sim)	1.47	6.08	1.62	1.17
40.95 (exp)	3.63 ± 0.19	4.05 ± 0.20	1.31 ± 0.07	3.25 ± 0.17
40.95 (sim)	1.20	5.17	0.88	0.79
54.05 (exp)	2.11 ± 0.12	2.75 ± 0.22	0.61 ± 0.05	1.43 ± 0.14
54.05 (sim)	0.80	3.22	0.44	0.49
67.15 (exp)	1.21 ± 0.08	1.98 ± 0.38	0.30 ± 0.03	0.79 ± 0.14
67.15 (sim)	0.50	1.62	0.20	0.29
l [cm], exp-sim	R(^{205}Bi) [10^{-28}deuteron^{-1}atom^{-1}], left		R(^{205}Bi) [10^{-28}deuteron^{-1}atom^{-1}], right	
1.50 (exp)	n/a	n/a	n/a	n/a
1.50 (sim)	0.03	0.29	0.30	0.04
14.75 (exp)	1.33 ± 0.21	n/a	0.92 ± 0.12	2.52 ± 0.35
14.75 (sim)	0.34	2.11	0.63	0.31
27.85 (exp)	5.74 ± 0.46	6.89 ± 0.68	2.53 ± 0.27	7.87 ± 0.50
27.85 (sim)	1.82	7.33	2.04	1.45
40.95 (exp)	4.29 ± 0.30	5.12 ± 0.30	1.68 ± 0.20	4.12 ± 0.25
40.95 (sim)	1.48	6.23	1.09	0.97
54.05 (exp)	2.78 ± 0.20	3.09 ± 0.28	0.78 ± 0.10	1.69 ± 0.18
54.05 (sim)	0.99	3.88	0.54	0.60
67.15 (exp)	1.48 ± 0.16	2.04 ± 0.28	n/a	n/a
67.15 (sim)	0.61	1.96	0.25	0.35

Table 30: Experimental and simulated reaction rates of studied isotopes in the ^{59}Co foils of the Phasotron experiments. Results are given for the left and right side of the QUINTA plates. l is the longitudinal distance.

Experiment	UA	CC	WS	UA	CC	WS
l [cm], exp-sim	R(^{58}Co) [10^{-28}proton^{-1}atom^{-1}], left			R(^{58}Co) [10^{-28}proton^{-1}atom^{-1}], right		
1.50 (exp)	3.60 ± 0.38	3.87 ± 0.22	1.68 ± 0.13	5.17 ± 0.69	43.69 ± 2.47	4.55 ± 0.34
1.50 (sim)	0.90	8.40	n/a	4.38	26.87	n/a
14.75 (exp)	6.84 ± 0.82	7.58 ± 0.43	7.58 ± 0.57	9.66 ± 1.04	41.29 ± 2.33	6.30 ± 0.47
14.75 (sim)	7.80	23.03	n/a	11.39	33.70	n/a
27.85 (exp)	7.44 ± 1.04	12.98 ± 0.73	9.83 ± 0.73	6.86 ± 1.10	31.27 ± 1.76	8.46 ± 0.63
27.85 (sim)	13.45	24.09	n/a	12.88	26.57	n/a
40.95 (exp)	4.20 ± 0.50	4.14 ± 0.23	3.54 ± 0.26	3.11 ± 0.36	8.30 ± 0.47	3.97 ± 0.30
40.95 (sim)	5.59	5.96	n/a	4.25	7.10	n/a
54.05 (exp)	0.96 ± 0.14	1.53 ± 0.09	1.04 ± 0.08	0.90 ± 0.11	4.17 ± 0.24	1.03 ± 0.08
54.05 (sim)	1.59	1.76	n/a	1.19	1.84	n/a
67.15 (exp)	0.13 ± 0.02	0.73 ± 0.04	0.39 ± 0.03	0.25 ± 0.03	1.38 ± 0.08	0.47 ± 0.04
67.15 (sim)	0.53	0.63	n/a	0.40	0.56	n/a
l [cm], exp-sim	R(^{57}Co) [10^{-28}proton^{-1}atom^{-1}], left			R(^{57}Co) [10^{-28}proton^{-1}atom^{-1}], right		
1.50 (exp)	2.13 ± 0.12	1.91 ± 0.10	0.73 ± 0.04	3.21 ± 0.17	23.88 ± 1.28	2.31 ± 0.14
1.50 (sim)	0.33	6.84	n/a	3.47	23.41	n/a
14.75 (exp)	2.71 ± 0.20	2.83 ± 0.15	2.88 ± 0.18	4.31 ± 0.22	21.00 ± 1.13	2.00 ± 0.13
14.75 (sim)	2.73	14.63	n/a	5.50	23.51	n/a
27.85 (exp)	3.58 ± 0.17	5.46 ± 0.28	3.84 ± 0.24	3.33 ± 0.17	15.73 ± 0.80	3.31 ± 0.21
27.85 (sim)	5.31	12.24	n/a	4.99	14.12	n/a
40.95 (exp)	2.48 ± 0.12	1.67 ± 0.08	1.55 ± 0.10	1.69 ± 0.08	4.12 ± 0.21	1.81 ± 0.11
40.95 (sim)	2.64	2.64	n/a	1.72	3.66	n/a
54.05 (exp)	0.52 ± 0.03	0.60 ± 0.03	0.43 ± 0.03	0.48 ± 0.02	2.18 ± 0.11	0.43 ± 0.03
54.05 (sim)	0.73	0.80	n/a	0.46	0.85	n/a
67.15 (exp)	0.054 ± 0.003	0.29 ± 0.01	0.17 ± 0.01	0.12 ± 0.01	0.65 ± 0.03	0.21 ± 0.01
67.15 (sim)	0.243	0.29	n/a	0.16	0.26	n/a
l [cm], exp-sim	R(^{60}Co) [10^{-28}proton^{-1}atom^{-1}], left			R(^{60}Co) [10^{-28}proton^{-1}atom^{-1}], right		
1.50 (exp)	4.34 ± 1.11	7.30 ± 1.28	2.19 ± 0.14	6.94 ± 2.38	88.22 ± 9.49	2.28 ± 0.16
14.75 (exp)	10.80 ± 2.19	10.78 ± 1.52	5.16 ± 0.35	11.89 ± 2.88	48.70 ± 12.38	5.29 ± 0.35
27.85 (exp)	11.64 ± 1.77	15.09 ± 2.00	8.21 ± 0.54	12.85 ± 1.63	32.70 ± 7.24	8.33 ± 0.57
40.95 (exp)	7.71 ± 2.03	6.59 ± 0.43	4.04 ± 0.26	6.70 ± 0.62	10.04 ± 1.55	4.07 ± 0.27
54.05 (exp)	3.19 ± 0.35	3.41 ± 0.21	1.75 ± 0.11	3.36 ± 0.23	5.87 ± 0.99	1.82 ± 0.11
67.15 (exp)	2.00 ± 0.10	2.19 ± 0.21	1.47 ± 0.09	2.13 ± 0.11	2.96 ± 0.29	1.49 ± 0.09

Table 31: Experimental reaction rates of studied isotopes in the ^{nat}Pb foils of the Phasotron experiments. Results are given for the left and right side of the QUINTA plates. l is the longitudinal distance.

Experiment	UA	CC	WS	UA	CC	WS
l [cm], exp-sim	R(^{206}Bi) [10^{-28}proton^{-1}atom^{-1}], left			R(^{206}Bi) [10^{-28}proton^{-1}atom^{-1}], right		
1.50 (exp)	0.49 ± 0.03	0.42 ± 0.03	0.20 ± 0.01	0.47 ± 0.03	4.76 ± 0.22	0.53 ± 0.03
1.50 (sim)	0.04	0.91	n/a	0.40	3.08	n/a
14.75 (exp)	0.55 ± 0.04	0.59 ± 0.03	0.67 ± 0.05	0.86 ± 0.05	3.98 ± 0.18	0.47 ± 0.03
14.75 (sim)	0.26	1.94	n/a	0.63	3.11	n/a
27.85 (exp)	0.80 ± 0.05	0.98 ± 0.05	0.87 ± 0.05	0.75 ± 0.04	3.03 ± 0.14	0.68 ± 0.04
27.85 (sim)	0.57	1.69	n/a	0.53	1.86	n/a
40.95 (exp)	0.97 ± 0.06	0.42 ± 0.02	0.47 ± 0.02	0.73 ± 0.03	1.03 ± 0.05	0.59 ± 0.03
40.95 (sim)	0.47	0.41	n/a	0.25	0.52	n/a
54.05 (exp)	0.17 ± 0.01	0.14 ± 0.01	0.12 ± 0.01	0.14 ± 0.01	0.46 ± 0.02	0.09 ± 0.01
54.05 (sim)	0.10	0.11	n/a	0.05	0.11	n/a
67.15 (exp)	0.004 ± 0.001	0.063 ± 0.003	0.038 ± 0.002	0.028 ± 0.002	0.18 ± 0.01	0.056 ± 0.003
67.15 (sim)	0.04	0.04	n/a	0.021	0.03	n/a
l [cm], exp-sim	R(^{205}Bi) [10^{-28}proton^{-1}atom^{-1}], left			R(^{205}Bi) [10^{-28}proton^{-1}atom^{-1}], right		
1.50 (exp)	0.55 ± 0.03	0.58 ± 0.03	0.24 ± 0.01	0.58 ± 0.03	7.08 ± 0.35	0.64 ± 0.03
1.50 (sim)	0.04	1.09	n/a	0.48	3.68	n/a
14.75 (exp)	0.72 ± 0.05	0.77 ± 0.05	0.82 ± 0.04	0.98 ± 0.05	5.54 ± 0.27	0.55 ± 0.03
14.75 (sim)	0.32	2.33	n/a	0.75	3.71	n/a
27.85 (exp)	0.90 ± 0.04	1.44 ± 0.07	1.09 ± 0.05	0.85 ± 0.04	4.55 ± 0.21	0.88 ± 0.04
27.85 (sim)	0.71	2.04	n/a	0.65	2.25	n/a
40.95 (exp)	1.21 ± 0.06	0.56 ± 0.03	0.61 ± 0.03	0.85 ± 0.04	1.55 ± 0.07	0.77 ± 0.04
40.95 (sim)	0.59	0.52	n/a	0.33	0.65	n/a
54.05 (exp)	0.19 ± 0.01	0.19 ± 0.01	0.15 ± 0.01	0.17 ± 0.01	0.62 ± 0.03	0.12 ± 0.01
54.05 (sim)	0.13	0.14	n/a	0.07	0.13	n/a
67.15 (exp)	n/a	0.086 ± 0.004	0.050 ± 0.003	0.031 ± 0.002	0.24 ± 0.01	0.072 ± 0.003
67.15 (sim)	0.05	0.052	n/a	0.027	0.04	n/a

Appendix F - Sensitivity analysis of simulation results for the Phasotron experiments

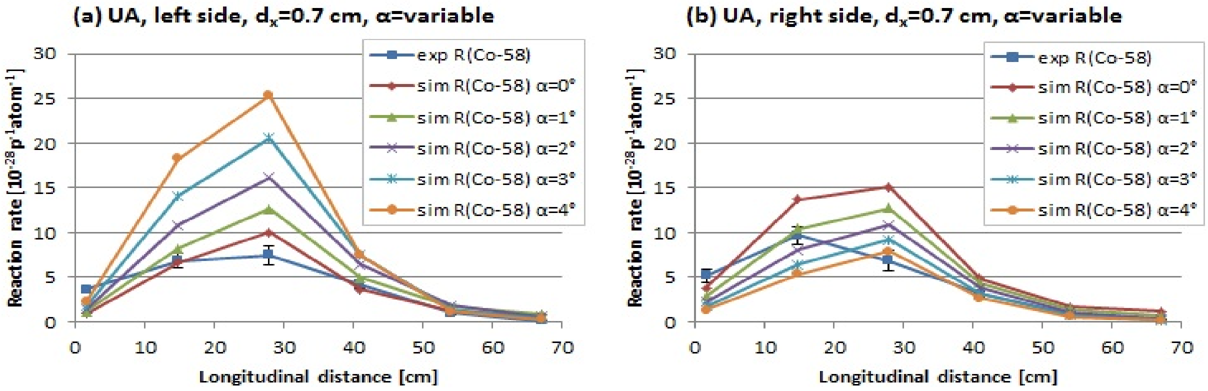

Figure 76: Simulated reaction rates with coordinate $d_x = 0.7$ cm and variable angles α of ^{58}Co production for samples on the left (a) and right (b) side (UA).

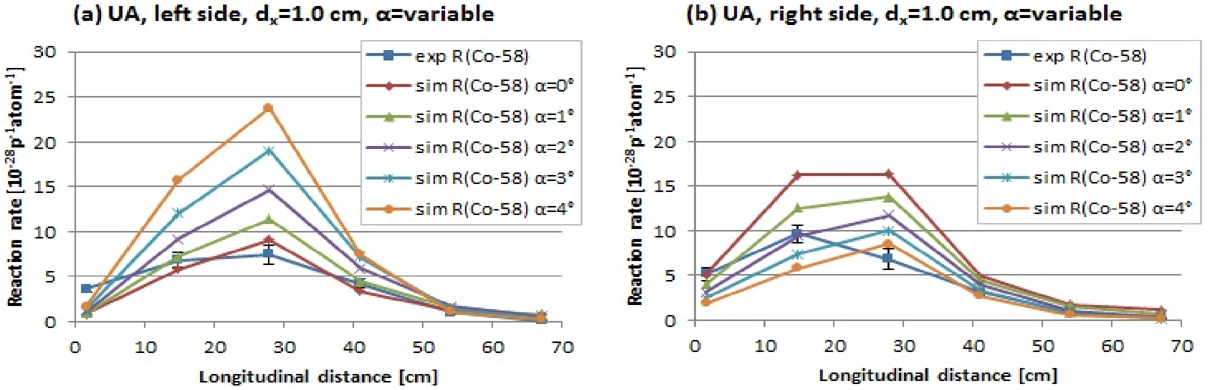

Figure 77: Simulated reaction rates with coordinate $d_x = 1$ cm and variable angles α of ^{58}Co production for samples on the left (a) and right (b) side (UA).

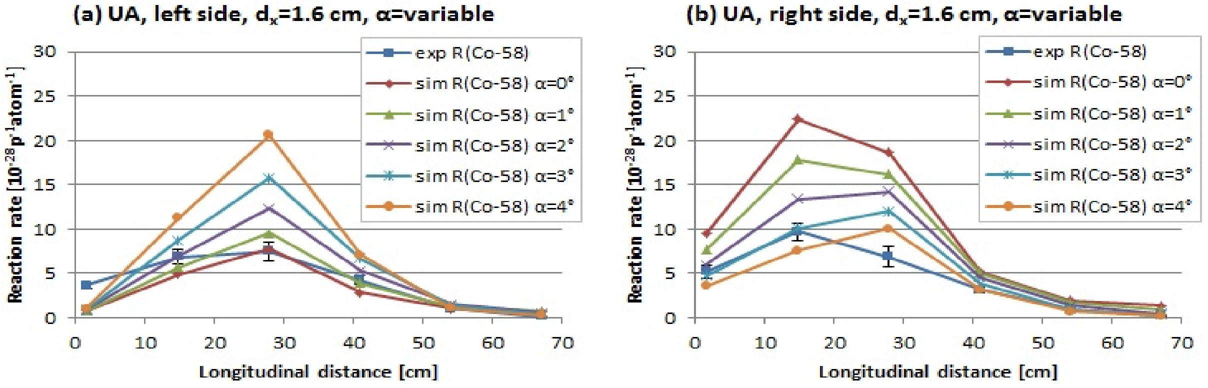

Figure 78: Simulated reaction rates with coordinate $d_x = 1.6$ cm and variable angles α of ^{58}Co production for samples on the left (a) and right (b) side (UA).

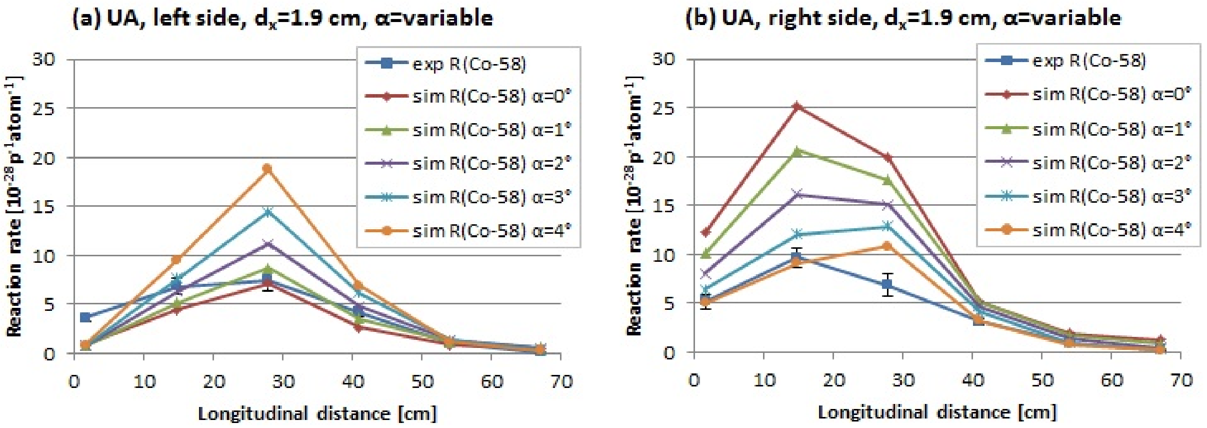

Figure 79: Simulated reaction rates with coordinate d_x = 1.9 cm and variable angles α of ^{58}Co production for samples on the left (a) and right (b) side (UA).

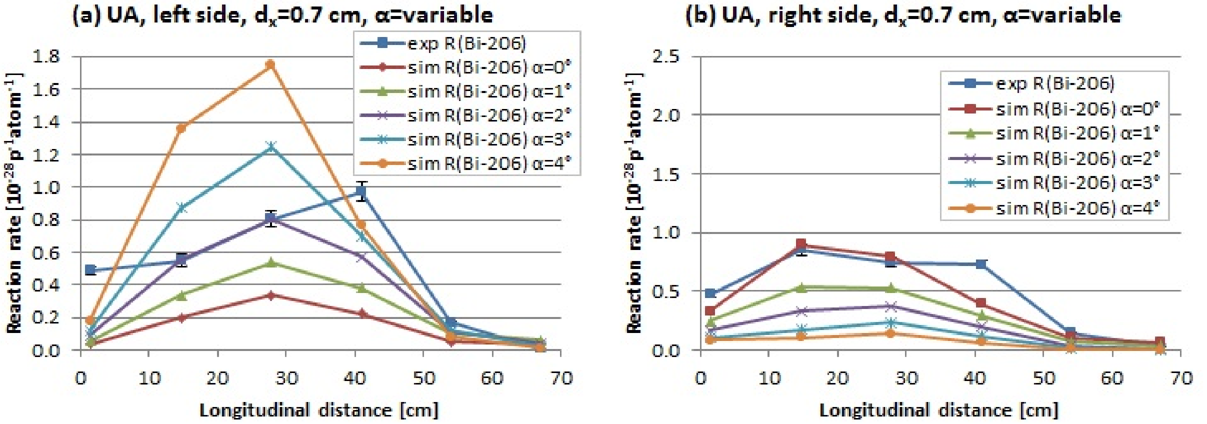

Figure 80: Simulated reaction rates with coordinate d_x = 0.7 cm and variable angles α of ^{206}Bi production for samples on the left (a) and right (b) side (UA).

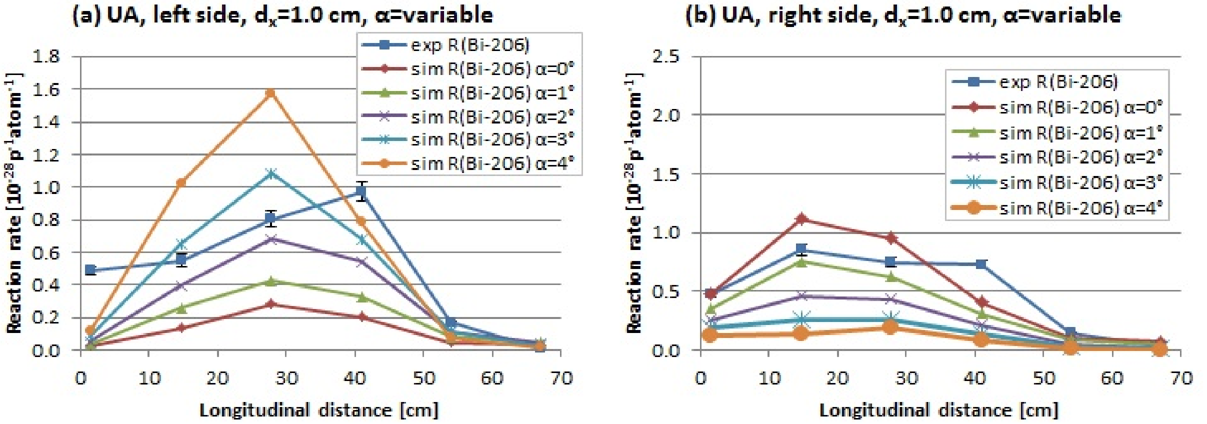

Figure 81: Simulated reaction rates with coordinate d_x = 1.0 cm and variable angles α of ^{206}Bi production for samples on the left (a) and right (b) side (UA).

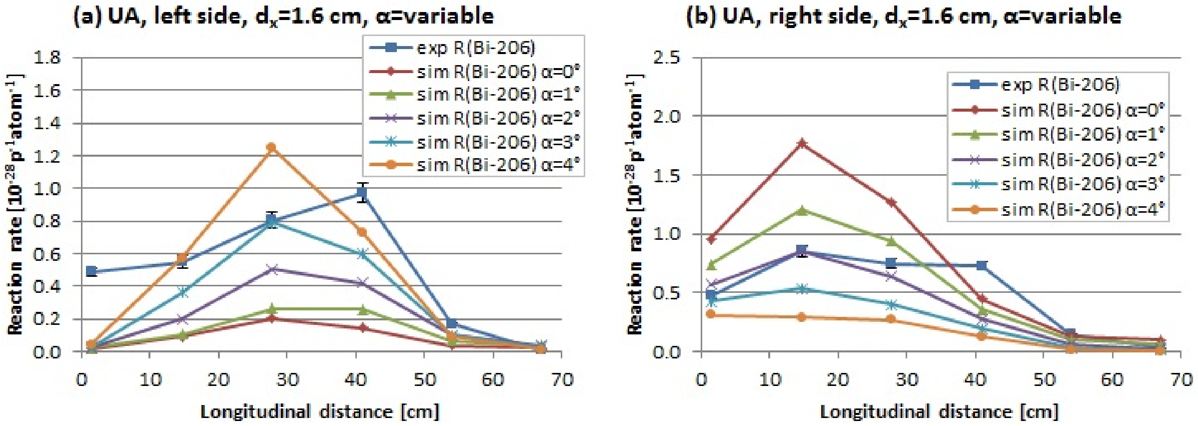

Figure 82: Simulated reaction rates with coordinate $d_x = 1.6$ cm and variable angles α of ^{206}Bi production for samples on the left (a) and right (b) side (UA).

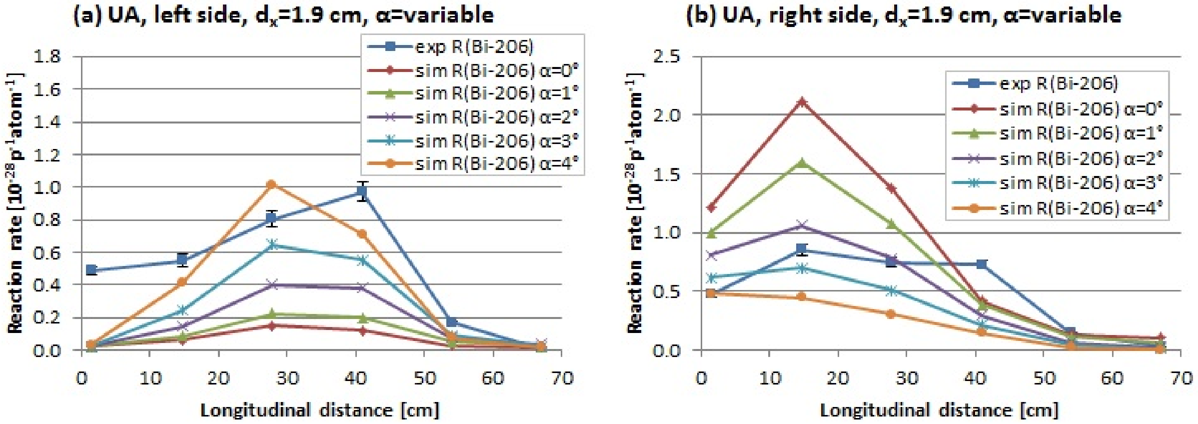

Figure 83: Simulated reaction rates with coordinate $d_x = 1.9$ cm and variable angles α of ^{206}Bi production for samples on the left (a) and right (b) side (UA).

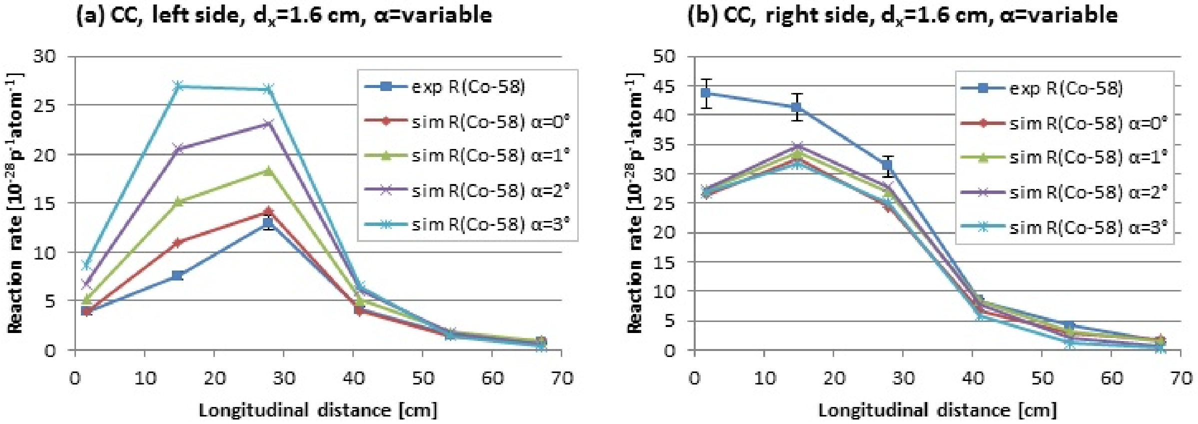

Figure 84: Simulated reaction rates with coordinate $d_x = 1.6$ cm and variable angles α of ^{58}Co production for samples on the left (a) and right (b) side (CC).

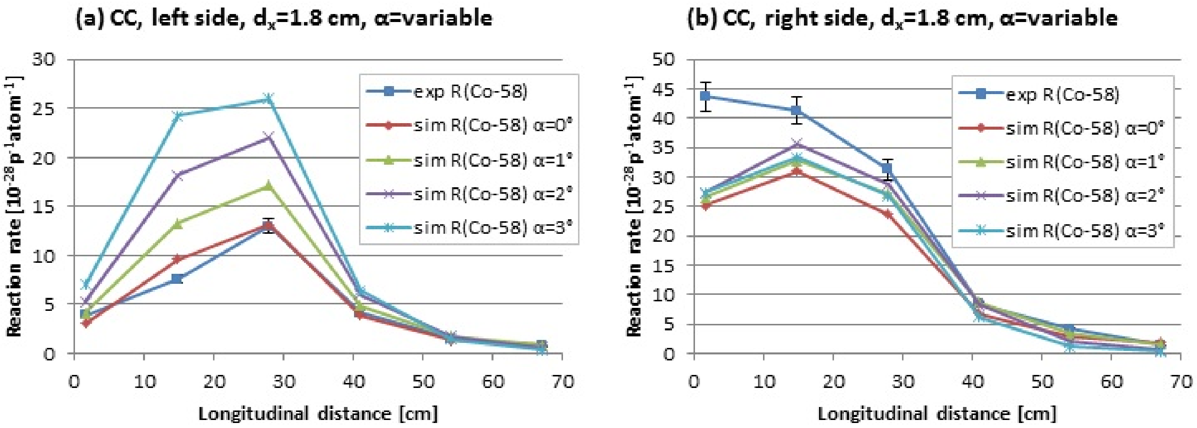

Figure 85: Simulated reaction rates with coordinate $d_x = 1.8$ cm and variable angles α of ^{58}Co production for samples on the left (a) and right (b) side (CC).

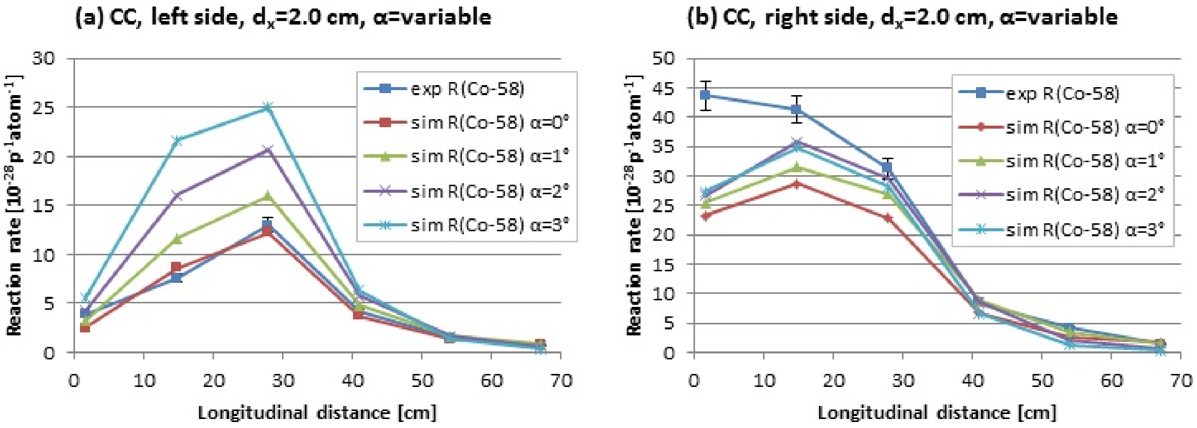

Figure 86: Simulated reaction rates with coordinate $d_x = 2.0$ cm and variable angles α of ^{58}Co production for samples on the left (a) and right (b) side (CC).

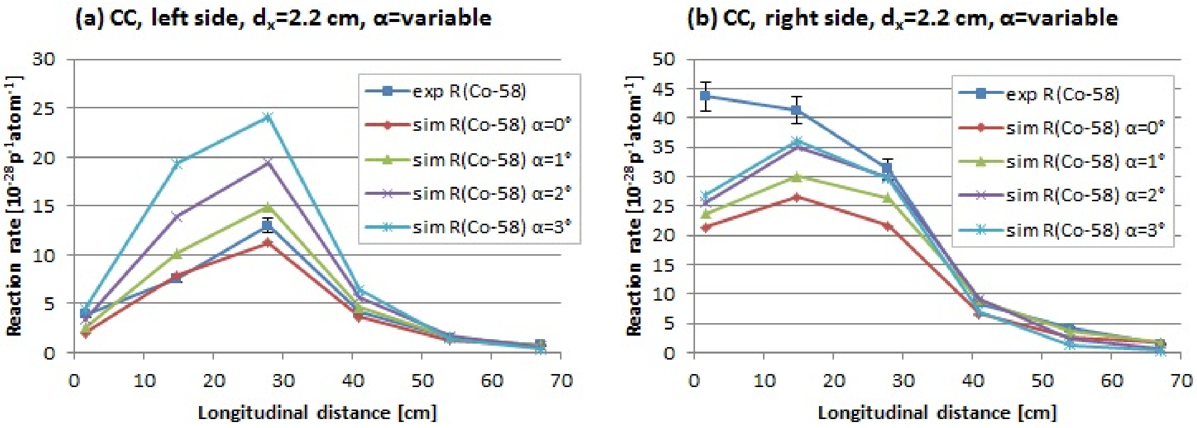

Figure 87: Simulated reaction rates with coordinate $d_x = 2.2$ cm and variable angles α of ^{58}Co production for samples on the left (a) and right (b) side (CC).

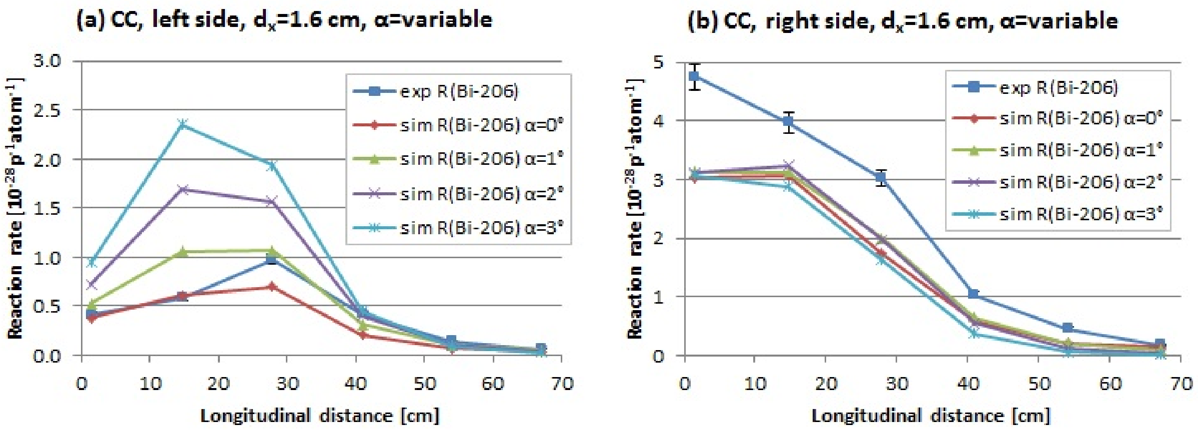

Figure 88: Simulated reaction rates with coordinate $d_x = 1.6$ cm and variable angles α of ^{206}Bi production for samples on the left (a) and right (b) side (CC).

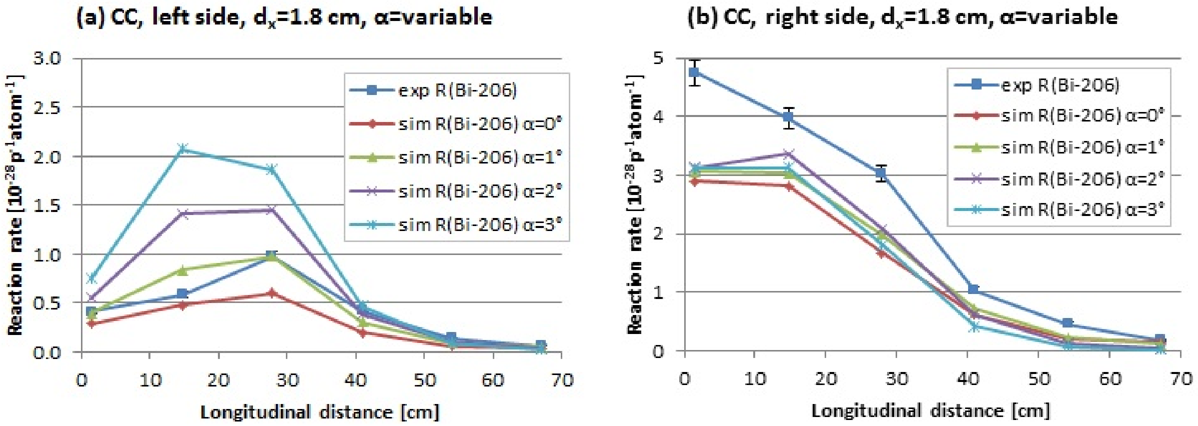

Figure 89: Simulated reaction rates with coordinate $d_x = 1.8$ cm and variable angles α of ^{206}Bi production for samples on the left (a) and right (b) side (CC).

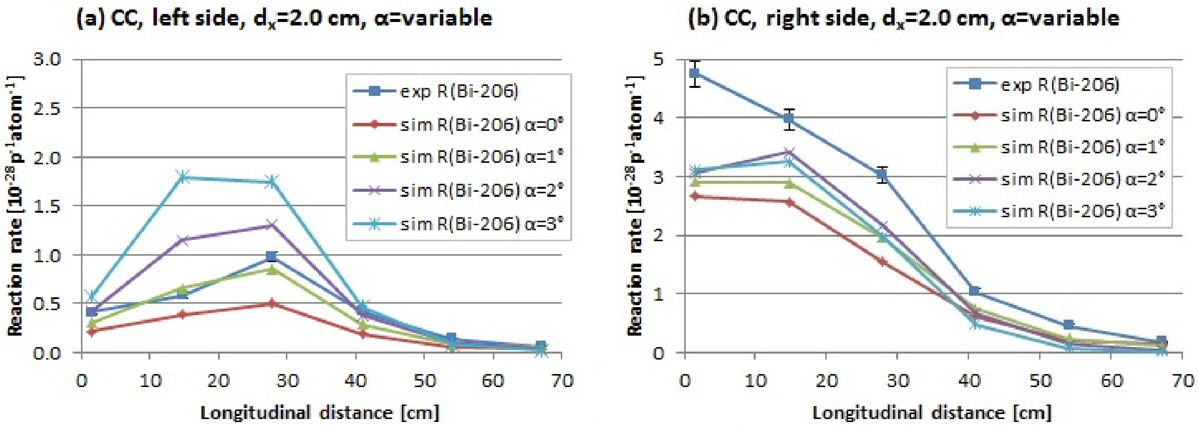

Figure 90: Simulated reaction rates with coordinate $d_x = 2.0$ cm and variable angles α of ^{206}Bi production for samples on the left (a) and right (b) side (CC).

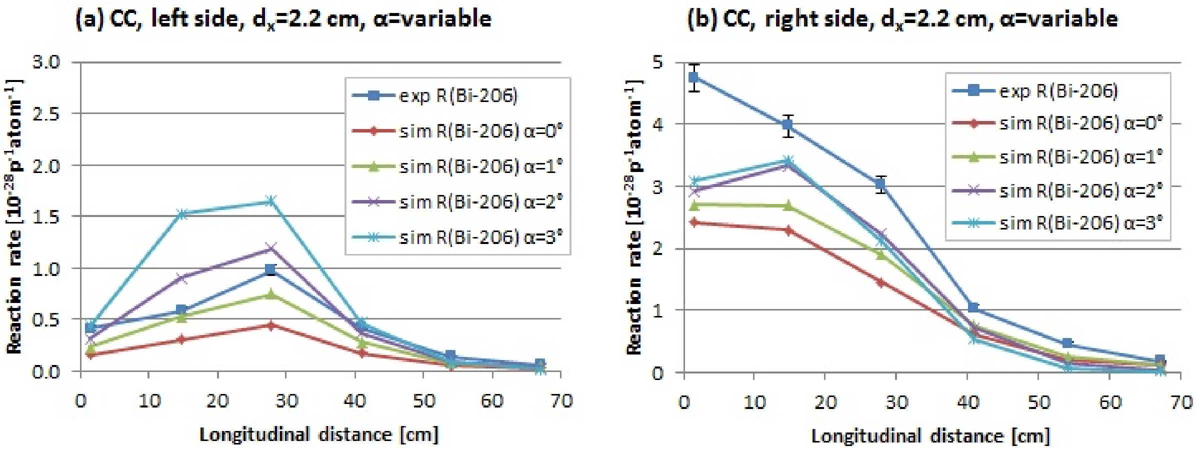

Figure 91: Simulated reaction rates with coordinate $d_x = 2.2$ cm and variable angles α of ^{206}Bi production for samples on the left (a) and right (b) side (CC).

Appendix G - Energy neutron spectra in BURAN equipped with lead and carbon targets

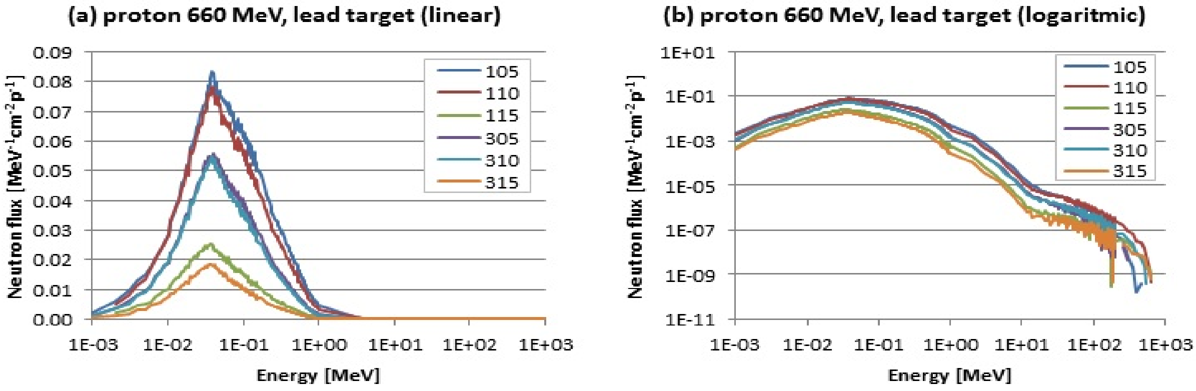

Figure 92: Energy neutron spectra in linear (a) and logarithmic (b) scale for the 660 MeV proton beam and the lead target in the points 105, 110, 115, 305, 310 and 315.

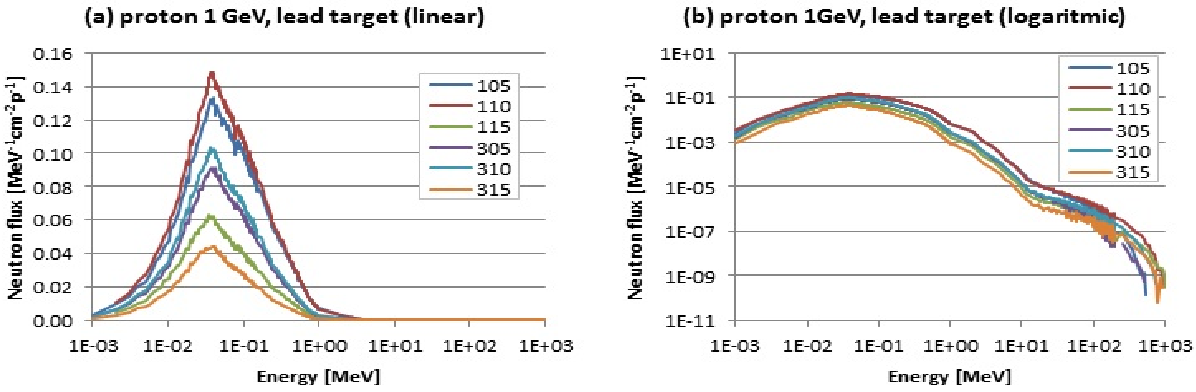

Figure 93: Energy neutron spectra in linear (a) and logarithmic (b) scale for 1 GeV the proton beam and the lead target in the points 105, 110, 115, 305, 310 and 315.

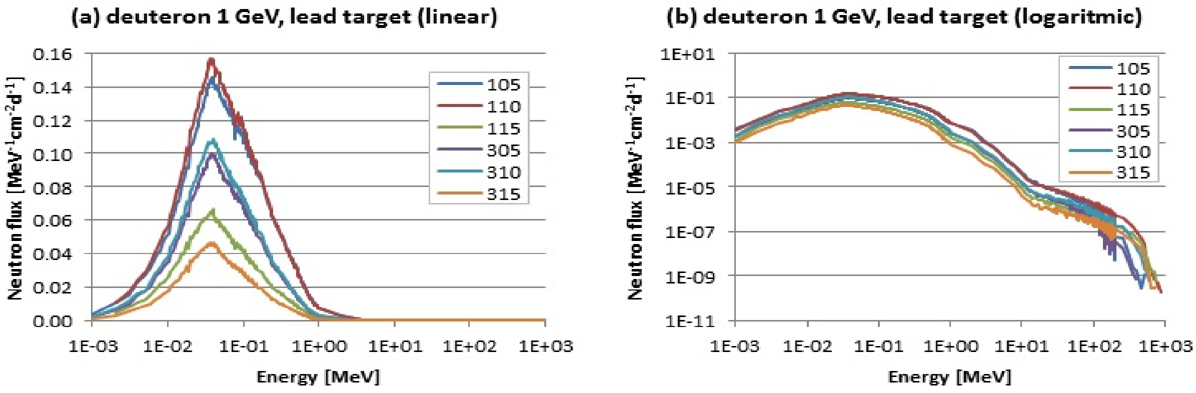

Figure 94: Energy neutron spectra in linear (a) and logarithmic (b) scale for the 1 GeV deuteron beam and the lead target in the points 105, 110, 115, 305, 310 and 315.

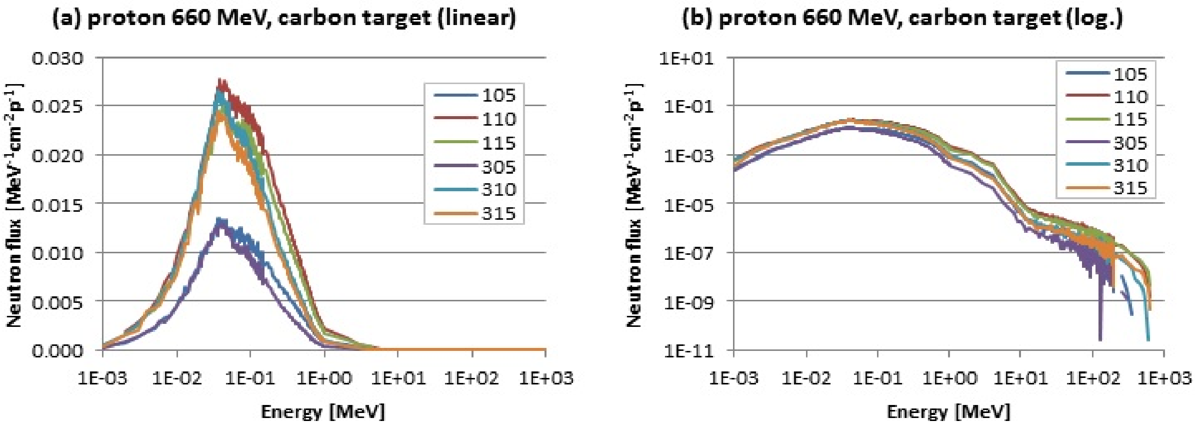

Figure 95: Energy neutron spectra in linear (a) and logarithmic (b) scale for the 660 MeV proton beam and the carbon target in the points 105, 110, 115, 305, 310 and 315.

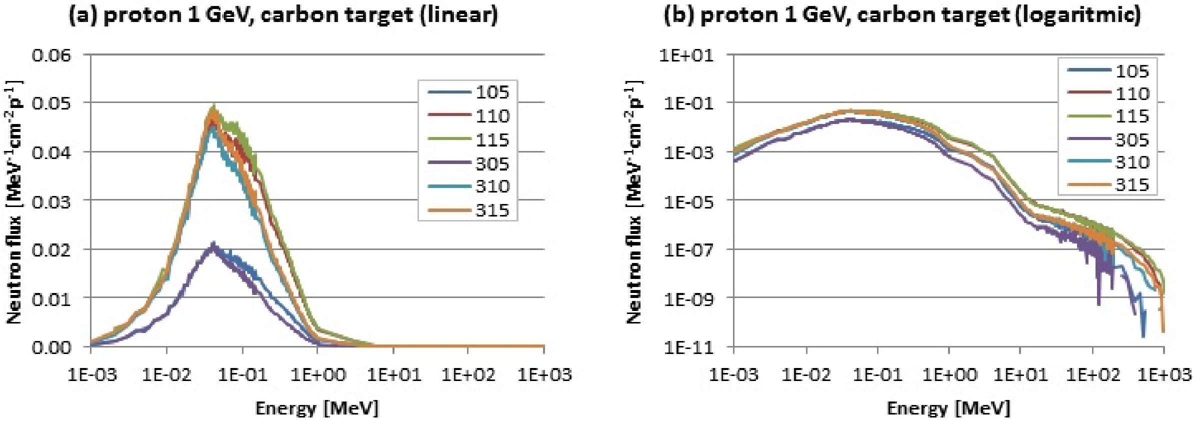

Figure 96: Energy neutron spectra in linear (a) and logarithmic (b) scale for the 1 GeV proton beam and the carbon target in the points 105, 110, 115, 305, 310 and 315.

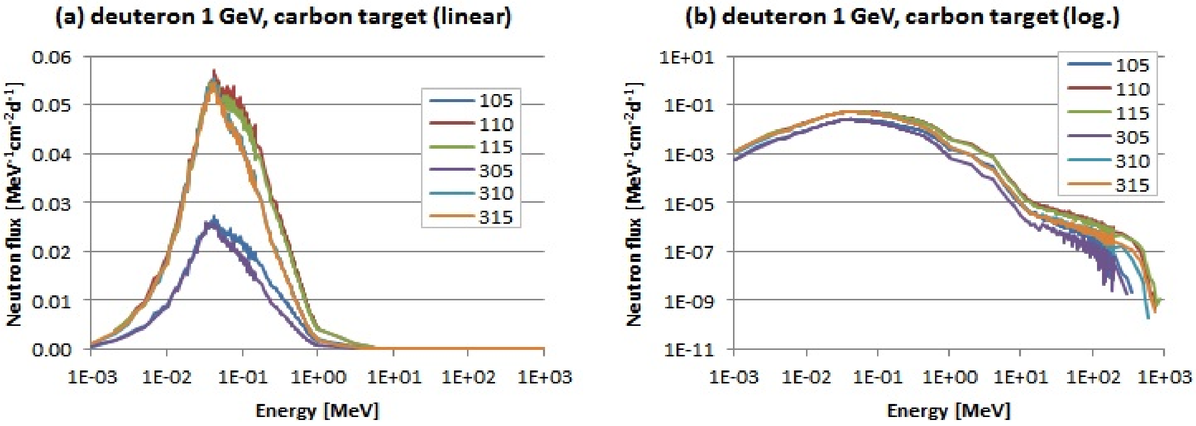

Figure 97: Energy neutron spectra in linear (a) and logarithmic (b) scale for the 1 GeV deuteron beam and the carbon target in the points 105, 110, 115, 305, 310 and 315.

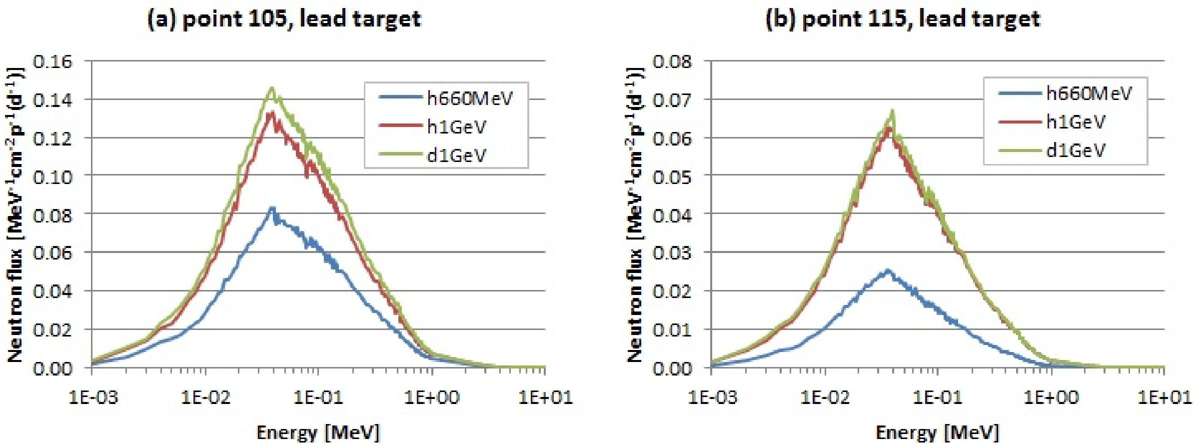

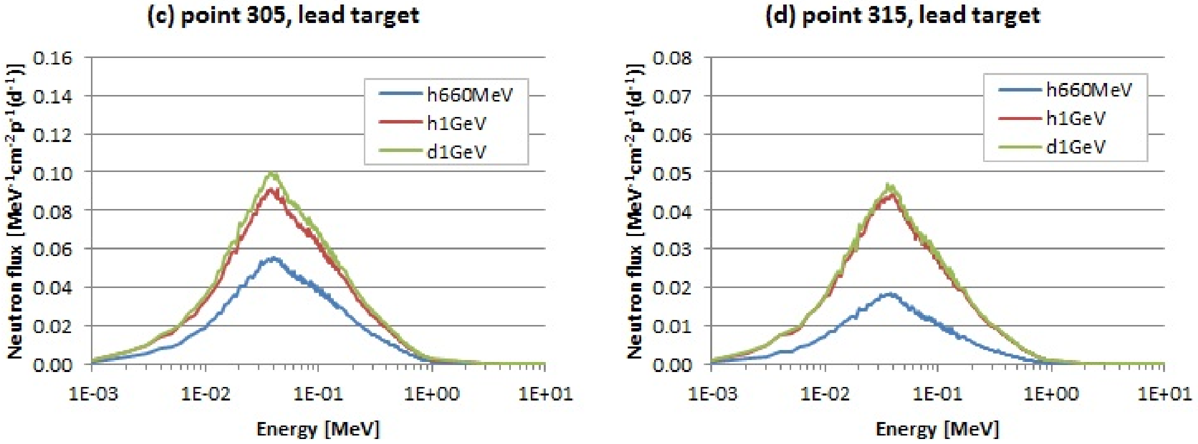

Figure 98: Energy neutron spectra for the 660 MeV proton, 1 GeV proton and 1 GeV deuteron beams and the lead target in the points 105 (a), 115 (b), 305 (c), and 315 (d).

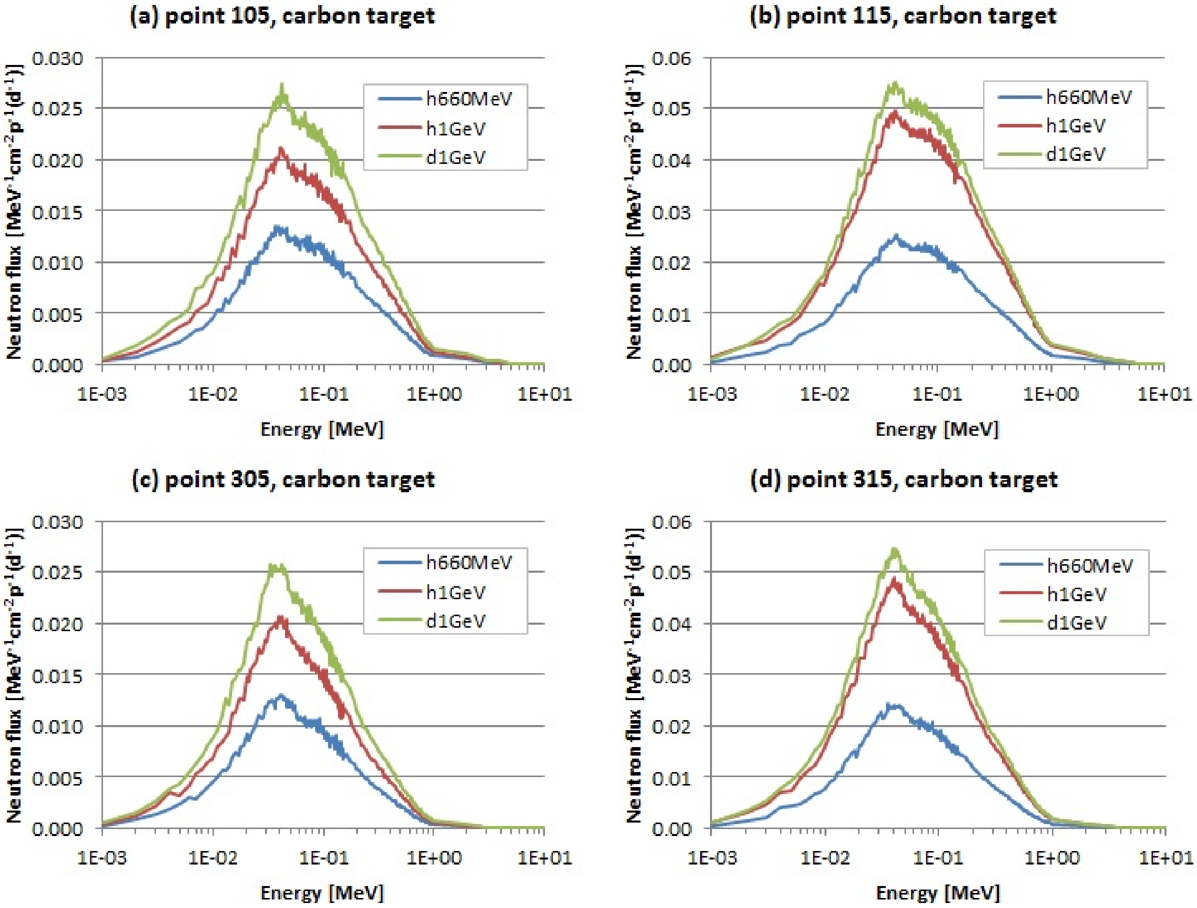

Figure 99: Energy neutron spectra for the 660 MeV proton, 1 GeV proton and 1 GeV deuteron beams and the carbon target in the points 105 (a), 115 (b), 305 (c), and 315 (d).

Appendix H - Experimental and simulated reaction rates from the experiment with lead target

Table 32: Experimental and simulated reaction rates of studied isotopes in the ^{nat}Pb samples (APb, BPb, CPb, DPb, EPb) from the experiment with the lead target. Index i symbolises indipendent value and index c cumulative value of reaction rate.

^{nat}Pb sample		APb	BPb	CPb	DPb	EPb
Isotopes		R [proton^{-1}atom^{-1}]				
^{206}Bi^{i}	Exp.	2.60(10)E-28	1.37(5)E-28	1.33(5)E-30	3.44(16)E-31	3.23(61)E-33
	Sim.	2.06E-28	9.46E-29	9.09E-31	2.04E-31	n/a
^{205}Bi^{i}	Exp.	3.36(7)E-28	1.89(3)E-28	1.45(3)E-30	3.70(14)E-31	n/a
	Sim.	2.52E-28	1.17E-28	1.09E-30	2.50E-31	n/a
^{204}Bi^{i}	Exp.	3.36(15)E-28	1.92(6)E-28	1.30(9)E-30	3.42(31)E-31	5.5(10)E-33
	Sim.	2.53E-28	1.17E-28	9.58E-31	2.22E-31	n/a
^{203}Bi^{i}	Exp.	3.52(14)E-28	2.07(6)E-28	1.21(5)E-30	3.36(11)E-31	n/a
	Sim.	2.02E-28	1.01E-28	7.29E-31	1.71E-31	n/a
^{203}Pb^{c}	Exp.	2.15(12)E-27	1.16(6)E-27	1.13(4)E-28	2.45(9)E-29	1.59(6)E-31
	Sim.	2.90E-27	1.37E-27	1.14E-28	2.10E-29	n/a
^{201}Pb^{c}	Exp.	1.62(9)E-27	8.86(31)E-28	5.47(13)E-29	1.26(3)E-29	7.35(25)E-32
	Sim.	1.85E-27	8.28E-28	5.20E-29	1.00E-29	n/a
^{200}Pb^{c}	Exp.	1.37(25)E-27	8.1(13)E-28	4.54(33)E-29	1.06(9)E-29	6.58(61)E-32
	Sim.	1.21E-27	5.44E-28	3.23E-29	6.35E-30	n/a
^{203}Hg^{c}	Exp.	8.9(12)E-29	3.14(41)E-29	2.91(24)E-30	6.74(64)E-31	n/a
	Sim.	5.14E-29	2.18E-29	2.07E-30	4.10E-31	n/a
^{201}Tl^{c}	Exp.	1.23(16)E-27	7.86(87)E-28	4.23(46)E-29	8.54(97)E-30	5.62(84)E-32
	Sim.	2.49E-27	1.13E-27	6.68E-29	1.31E-29	n/a
^{200}Tl^{c}	Exp.	2.25(21)E-27	1.23(14)E-27	3.26(26)E-29	8.99(88)E-30	6.81(53)E-32
	Sim.	1.79E-27	7.90E-28	4.52E-29	9.06E-30	n/a
^{199}Tl^{c}	Exp.	1.99(18)E-27	1.12(9)E-27	4.34(22)E-29	1.05(5)E-29	5.51(31)E-32
	Sim.	1.76E-27	7.01E-28	3.87E-29	7.83E-30	n/a
^{198}Tl^{c}	Exp.	2.45(17)E-27	1.46(10)E-27	3.35(33)E-29	8.88(42)E-30	4.04(19)E-32
	Sim.	1.58E-27	5.42E-28	2.39E-29	4.96E-30	n/a